The Dynamics of a Small Model Glass Former as Viewed from Its Potential Energy Landscape

Dissertation
zur Erlangung des Grades
„Doktor der Naturwissenschaften“

am Fachbereich Physik
der Johannes Gutenberg–Universität
in Mainz

vorgelegt von

Burkhard Doliwa
geboren in Hadamar

Mainz 2002

Tag der mündlichen Prüfung: 25.2.2003

Contents

Introduction

In our every-day life, we are surrounded by amorphous solids. This does not only cover the ordinary window glass or the optical fiber which we use for short and long-range communications. Among other things, most of the engineering plastics and also –honey– belong to this kind of material.

Although the technical processing of glasses has been known for millennia now, the physical principles behind glass formation are still not fully understood. What is clear is that the melt, upon sufficiently rapid cooling, remains in the liquid state instead of crystallizing. Due to the low temperature, then, molecular motion becomes very sluggish, e.g. happens on the time scale of seconds rather than picoseconds. For this reason, the liquid is extremely viscous, thus acting very much like a solid. Although the underlying crystal is the thermodynamically stable state, the system is too slow to reach it within the experimental time scale; the liquid is said to be metastable or supercooled.

On a phenomenological basis, one defines the glass transition temperature (T_g) as the point where characteristic molecular relaxation times reach 10^2 s, or alternatively, where the shear viscosity exceeds $\eta = 10^{13}$ poise. To get an impression of the order of magnitude, consider a cubic centimeter of a substance with exactly this viscosity, where a shear force of 100 N is constantly applied. After one day, the deformation of the probe is ca. 1 mm.

For the development of glasses and their industrial application, it is highly desirable to understand *why* certain compositions of materials readily form glasses on cooling a melt while others have a strong tendency to crystallize. This remains one of the great unsolved mysteries of glass science, although empirical descriptions have been developed which successfully account for the glass-forming ability in certain specific cases. Nevertheless, choosing the right composition for a glass former with some desired properties is still in an 'alchemy' stage. Of course, the question of the ease of glass formation on cooling a melt is intimately related to the problem of *how* do glasses form.

One puzzling observation is that the dramatic slowdown of dynamics is accom-

panied by no more than subtle changes in structure. One also says that the glass transition is a kinetic phenomenon. Moreover, the mobility of particles can vary by orders of magnitude between different regions of the same sample, which is referred to as dynamic heterogeneity. These, and other aspects of glass formation, like the jump in specific heat at T_g, are not fully understood. The major goal would be to predict dynamic (and also thermodynamic) properties of the system in question from first principles, i.e. from the microscopic interaction potentials. The problem is that the lacking periodicity of the inter-molecular structure complicates the application of the classical tools of theoretical physics.

The physics of glass-forming liquids is a complex many-body problem. This shows up, e.g., in the non-exponential decay of dynamic response functions or in the non-Arrhenius behavior of viscosities in many glass formers. Apart from phenomenological models as that of (Adam and Gibbs, 1965) and analytical theories like mode-coupling theory (Götze and Sjogren, 1992) or the theory of spin glasses (Mezard et al., 1987), computer simulations are having an increasing impact on this field of research. In particular, the potential energy landscape approach (PEL) proposed by Goldstein over thirty years ago (Goldstein, 1969) could be implemented numerically with considerable success (Stillinger and Weber, 1982). The idea is to consider the high-dimensional vector of all particle coordinates as a point moving on the surface of the total potential energy. At low temperatures, the system stays near the local minima of the PEL, the so-called inherent structures. Using only their local properties one is then able to predict all *thermodynamic* quantities. At high temperatures, this attempt breaks down since the system is no longer confined to the very vicinity of the local minima. In recent years, important pieces of information have been gained about the PEL of different glass-forming systems via extended computer simulations (Sastry, 2001; Sastry et al., 1998; Sciortino et al., 2000; Sciortino et al., 1999). It has turned out that the PEL description starts to work when cooling below $T \approx 2T_c$, where T_c is the critical temperature of mode-coupling theory (MCT). In this regime the equation of state could be expressed completely in terms of a few parameters that characterize the statistical properties of PEL minima (La Nave et al., 2002a).

The current understanding of *dynamics* in terms of the PEL structure is much less satisfying. However, it is felt that the molecular slowing down, as expressed, e.g., by the diffusion coefficient $D(T)$, should be related to the hopping over PEL barriers which separate the minima. The quantification of this idea will be the main subject of this thesis. The first question that arises is

- *Is there a simple relation between $D(T)$ and the hopping between minima?*

We shall demonstrate in chapter 4 that there is, if one considers whole superstruc-

tures of many PEL minima (metabasins), rather than single minima. The existence of metabasins has been hypothesized some years ago (Stillinger, 1995) and recently been demonstrated within simulations (Büchner and Heuer, 2000; Middleton and Wales, 2001). Metabasins are reminiscent of protein folding funnels (Bryngelson et al., 1995) or related structures in the energy landscape of small clusters (Ball et al., 1996). Next, one could ask

- *How is the hopping rate between metabasins connected to their depth, i.e. to the barriers that surround them?*

This will be the subject of chapter 5, where we will prove that the mean residence time inside deep metabasins can be quantitatively related to the local PEL structure. We will then be able to express $D(T)$ by the depths of metabasins and their population at a given temperature. A question which is important with respect to the current view on supercooled liquids is

- *What is the temperature regime where the hopping description can be applied?*

Mode-coupling theory predicts a power-law behavior of the form $D(T) \propto (T - T_c)^\gamma$ above the MCT critical temperature T_c. Since T_c is found to be higher than the glass transition temperature T_g, the MCT divergence of $1/D(T)$ at T_c is not observed in practice. The common explanation for this shortcoming of MCT is that the theory neglects 'activated processes', or 'hopping', which is supposed to come into play around and below T_c. In chapter 7, we will see that the temperature dependence of $D(T)$ is governed by activated processes (barriers larger than $5k_\mathrm{B}T$) already significantly above T_c. This is in contrast to many of the conclusions that have been drawn in recent numerical studies of the PEL above T_c.

An important technical point concerns the choice of system size. In order to optimize the information that can be extracted from a simulation, it is essential to use small systems. Due to the experimentally observed, finite length scales of correlated motion (Tracht et al., 1998; Russell and Israeloff, 2000) down to T_g, different subsystems of a macroscopic sample are essentially independent of each other. Thus, considering many of these quasi-independent subsystems in parallel, one washes out much of the interesting PEL information about a single one. Guided by this simple argument, we will mainly consider a small system of 65 particles in this thesis. In order to show that no finite-size related artifacts arise, we give a detailed comparison to larger systems of the same type in chapter 6.

The outline of the thesis is as follows. In chapter 1, we describe the salient features of supercooled liquids from our point of view, together with some background information about experimental and theoretical techniques. Chapter 2 defines the

model system under investigation and the simulation technique applied. For reasons of completeness, we give detailed results on the static PEL aspects in chapter 3. Especially, we would like to draw the reader's attention to sections 3.2 and 3.3, where we present some interesting findings about the total number of minima and the configurational entropy. Chapters 4 to 7 contain the main results of this thesis as described above. They correspond to the following publications (in that order): (Doliwa and Heuer, 2002c), (Doliwa and Heuer, 2002a), and (Doliwa and Heuer, 2002b).[1]

For the hasty reader we note that chapter 7 gives a compact summary of the main results of the preceding chapters. Then, further aspects of metabasins will be given (e.g., the differentiation between solid- and liquid-like metabasins), together with a final comparison of the present work to that of other groups.

[1] Chapter 7 is still to be published.

Chapter 1

Supercooled Liquids and the Glass Transition

Meßkunst wird und Forscherlust
einst noch Glas und Baum befragen:
und der Wissenschaft wird tagen,
was der Weisheit längst bewußt.

frei nach Christian Morgenstern

We begin with a brief overview of the salient features of supercooled liquids and their current theoretical understanding. Of course, we will not attempt to cover all the interesting developments in this field that have been achieved during the last decades. In view of the large number of comprehensive review articles, we restrict ourselves to the aspects of supercooling and glass formation, which are of direct relevance for the present study.

1.1 Phenomenology.

The glass transition is the transition from the viscoelastic liquid to the amorphous solid state. For many materials, e.g. oxidic melts, low-molecular organic substances or alloys, one can avoid crystallization via rapid cooling (quenching) or other special techniques (like vapor deposition or solid evaporation), so that a supercooled liquid and finally a glass is formed (Angell, 1995). Supercooling is the more easy, the more irregular the molecular structure. For that reason, the glass transition of polymers is of special importance. The more complicated molecular structure as compared to low-molecular substances and the entanglements in the polymeric melt prevent

the efficient self-organization into a crystal, in favor of the amorphous solid. If a substance can readily be supercooled at normal cooling rates without being trapped in the crystalline state, one speaks of a good glass former. The glassy state is characterized both by liquid-like and solid-like properties, since the structure of a glass is isotropic, without long-range order, although its macroscopic mechanical properties are similar to those of a solid.

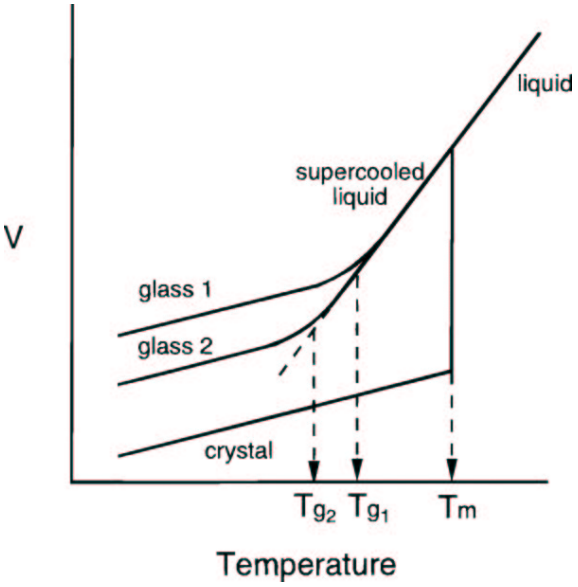

Figure 1.1: Schematic representation of the specific volume as a function of temperature (Ediger, 1996). Glass 1 corresponds to a higher cooling rate than glass 2. See text for details.

Figure 1.1 illustrates the temperature dependence of a liquid's volume at constant pressure. If crystallization below the freezing temperature T_{m} is avoided by sufficiently fast cooling, the liquid stays in a metastable state which is characterized by a volume higher than that of the crystal. Upon further cooling, its viscosity increases and the molecules' motion becomes more and more sluggish. At some temperature, consequently, the molecules do not have a chance to rearrange significantly before the temperature is lowered further. Since these rearrangements are necessary to reach equilibrium at that temperature, the experimentally observed volume starts to deviate from the equilibrium value. At still lower temperatures, the time scale of single molecular rearrangements becomes comparable to the time scale of experimental observation. The molecular structure is then frozen from the practical view and we call the material a glass. Upon further cooling, the volume continues to drop, but according to a much smaller thermal expansion coefficient than in the supercooled liquid regime. As one can see from the figure, the thermal expansion is similar in the glass and the crystal. This can be explained by the fact that the volume changes are dominated by atomic vibrations, which are similar for glass and crystal.

One way to define the glass transition temperature T_{g} is to use the change in the thermal expansion coefficient, as seen in Fig. 1.1. Since this change is by no means sharp, the location of T_{g} has some intrinsic arbitrariness. Moreover, if cooled

more slowly, the supercooled liquid is able to reach a much smaller volume, and the bend in the volume curve appears at a lower temperature. This dependence of T_g upon cooling rate, though disturbing from a theoretical view, is relatively weak; changing the cooling rate by one order of magnitude typically affects T_g by no more than $3-5$ K. For practical purposes, thus, T_g serves as an important material property, which, for instance, is the most useful parameter for estimating mechanical properties of polymers. By extrapolating T_g towards zero cooling rate, one obtains the so-called ideal glass transition temperature T_0. Alternatively, one often uses the jump in the specific heat to determine T_g, which is then called the calorimetric glass transition temperature, $T_{g,cal}$, see below.

The slowing down.

As mentioned in the introduction, another definition for T_g is the temperature at which the shear viscosity reaches a value of 10^{13} poise (10^{12} Nsm^{-2}). As illustrated in the Arrhenius plot of Fig. 1.2, the viscosity is very sensitive to temperature changes near T_g. For some substances, which mostly are covalent network glass formers like SiO_2, the temperature dependence of the viscosity is well described by a simple Arrhenius law, $\eta(T) \propto \exp(E/k_B T)$ (a straight line in the Arrhenius plot). Here E is a constant activation energy and k_B is Boltzmann's constant. Other liquids exhibit an even stronger slow-down close to T_g, which can be expressed by a temperature dependent activation energy $E(T)$ in the above formula. After (Angell, 1988), the former substances are called *strong* glass formers, the latter are termed *fragile*. An empiric law which often fits experimental data very well is given by

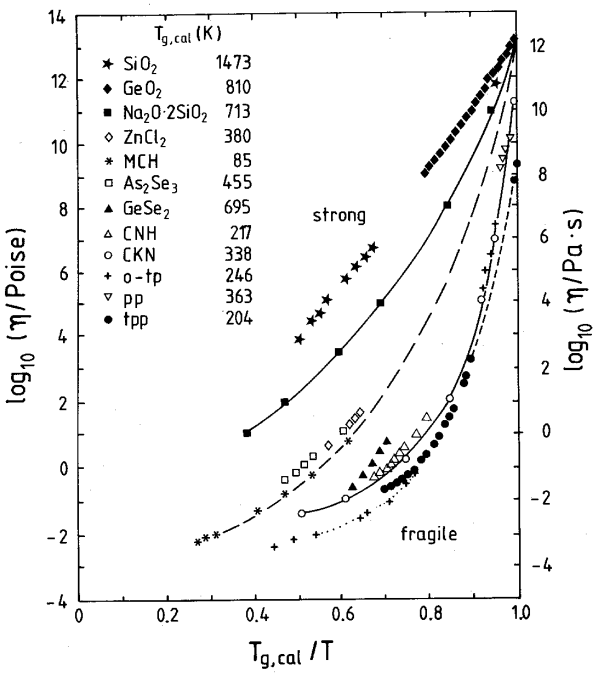

Figure 1.2: Arrhenius plot of the viscosity of different glass formers over inverse temperature $T_{g,cal}/T$, from (Richert and Blumen, 1993).

$$\eta(T) \propto \exp\left(\frac{A}{T - T_{VFT}}\right),$$

the so-called VFT relation with a constant A (Vogel, 1921; Fulcher, 1925; Tammann and Hesse, 1926). Interestingly, the temperature $T_{\rm VFT}$ thus introduced often turns out to be nearly identical to the 'ideal' glass transition temperature T_0.

The comprehension of $\eta(T)$ from first principles is one of the big unsolved problems in glass research. In the case of strong glass formers, the constant activation energy E suggests that a simple molecular mechanism governs the temperature dependence of $\eta(T)$. Indeed, for the network-forming SiO_2, there are some indications that E directly corresponds to the breaking of Si-O bonds (McMillan et al., 1994; Horbach and Kob, 1999). Thus, the energetic cost of structural relaxation seems to be dominated by these simple bond-breaking events, while possible subsequent rearrangements are comparably 'cheap'. The situation is less clear for fragile glass formers. There, nearest-neighbor interactions are generally weaker but more numerous. Thus, more complicated, highly collective rearrangements are expected to determine the temperature dependence of the viscosity. Some of the theoretical approaches which try to incorporate these complex many-particle effects will be described below.

Dynamic Heterogeneities and Length Scales. The presence of strong variations in mobility throughout a supercooled sample is a well-established fact (Sillescu, 1999). By numerous experimental techniques, like multi-dimensional NMR or nonresonant dielectric hole burning (Bohmer et al., 1998), it could be shown that the selection of intrinsically slow (or fast) sub-ensembles is feasible, in the sense that the selected particles remain slow (or fast) for a certain time after selection. Particularly fragile glass formers exhibit this so-called dynamic heterogeneity. Of course, the different mobility is expected to have a spatial aspect, meaning that, at a given time, whole regions of a probe behave extremely sluggish, while other parts are very mobile. The length scale of dynamic heterogeneity could indeed be measured in multi-dimensional NMR experiments through spin diffusion (Tracht et al., 1998; Reinsberg et al., 2002). The result is that at $T \approx T_{\rm g} + 10$ K, dynamical correlations are of an average range of ca. 4 nm in polyvinylacetate, 3 nm in *o*-terphenyl, and 1 nm in glycerol. The growth of dynamical length scales with decreasing temperature has clearly been demonstrated in computer simulations (Yamamoto and Onuki, 1998; Donati et al., 1999; Doliwa and Heuer, 2000). The divergence of length scales at a temperature near the glass transition is still controversial. Some theories, which claim the existence of an underlying phase transition, predict such a divergence. However, the observation of this phenomenon in practice would be difficult since the finiteness of cooling rates prevents the direct study of the putative phase transition.

For the present study, the aspect of dynamic length scales is of importance. Since in our approach we consider rather small systems, the common large-scale dynamic heterogeneity is certainly not captured. However, we shall demonstrate that the essential physics of the viscous slowing is already contained in the energy landscape of quite small model systems (chapter 6). This suggests that the occurrence of large-scale dynamic heterogeneity is merely a concomitant of the molecular slowing down.

Configurational entropy.

The specific entropy, $s(T)$, of a supercooled liquid is usually calculated by integrating over the measured specific heat,

$$s(T) = s(T_1) + \int_{T_1}^{T} \frac{c_p(T')}{T'} \mathrm{d}T'. \tag{1.1}$$

A typical specific heat curve is illustrated in Fig. 1.3(a) for the liquid, supercooled liquid, glass, and crystal. $c_p(T)$ is largest in the supercooled liquid and drops to some value close to the crystal near T_g. In fact, the calorimetric glass transition temperature, $T_\mathrm{g,cal}$, is defined by this drop in $c_p(T)$. Again, we find a certain sensitivity of $T_\mathrm{g,cal}$ on cooling rate. From such data, $s(T)$ can be obtained via Eq. 1.1. The crystal entropy $s(T)$, $T \leq T_\mathrm{m}$, can be calculated after measuring $c_p(T)$ from $T_1 = 0$ K to T. We then obtain the entropy of the liquid by adding the entropy of fusion to the crystal entropy at T_m. By further heating and measuring $c_p(T)$, we find $s(T)$ at higher liquid temperatures. Upon sufficiently rapid re-cooling, we enter the supercooled liquid regime and determine $s(T)$ in the same way as before. The resulting $s(T)$, schematically shown in Fig. 1.3(b), resembles very much the $V(T)$ of Fig. 1.1. It is interesting to compare the $s(T)$'s of the supercooled and crystalline states. Neglecting

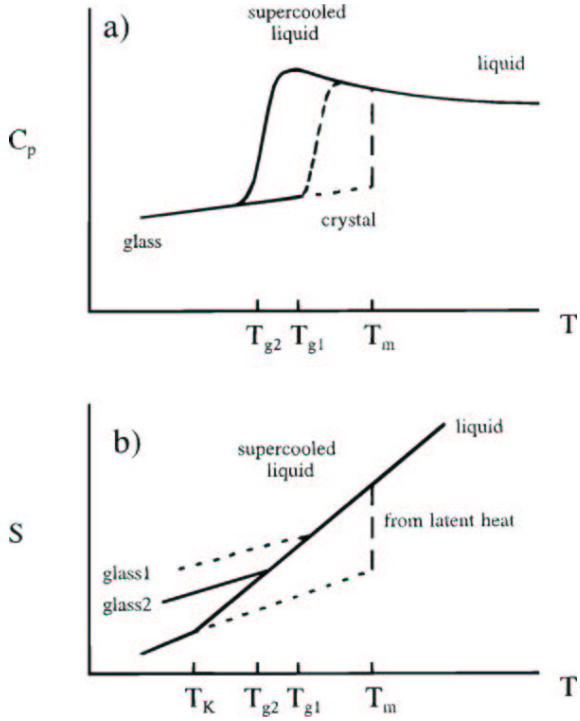

Figure 1.3: Schematic of (a) the temperature dependence of the specific heat, $c_p(T)$, and (b) the specific entropy, s(T), of crystal, liquid, supercooled liquid, and glass. Again, different cooling rates lead to different glasses 1 and 2 (Ediger, 1996).

defects, the configuration of the crystal is unique.[1] Hence, the crystal entropy just arises from lattice vibrations. The supercooled liquid, due to structural relaxation, is still able to visit a large number of distinct configurations. The corresponding 'configurational' entropy,

$$s_{\mathrm{c}}(T) = s(T) - s_{\mathrm{vib}}(T). \tag{1.2}$$

is a central quantity in many studies of the glass transition. Assuming that the vibrational entropy, $s_{\mathrm{vib}}(T)$, is similar to the one of the crystal, one is able to obtain $s_{\mathrm{c}}(T)$ from experiment.[2]

Due to the larger value of $c_p(T)$, the decrease of $s(T)$ upon cooling is larger in the supercooled liquid than in the crystal, see Fig. 1.3(b). Ignoring the bend in the curve, the extrapolation of $s(T)$ from the supercooled regime towards lower temperatures yields a temperature, T_{K}, where the supercooled $s(T)$ equals that of the crystal. Under the above assumption of equal vibrational entropies, one concludes that $s_{\mathrm{c}}(T_{\mathrm{K}}) = 0$, meaning that the glass is trapped in a unique configuration. Pushing the extrapolation of the liquid $s(T)$ still further, one clearly reaches a contradiction since $s_{\mathrm{c}}(T)$ would become smaller than zero. In a slightly different formulation, the occurrence of a negative configurational entropy below T_{K} was already noted by Kauzmann (the 'Kauzmann paradox'), which is why T_{K} bears his name (Kauzmann, 1948). However, the situation is not paradoxical at all. Due to the drop of $c_p(T)$ near T_{g}, the liquid entropy in practice never falls below that of the crystal. In the literature, this is often expressed by saying that 'the entropy crisis is thwarted by the glass transition'. Nonetheless, Fig. 1.3(b) suggests that in the limit of small cooling rates one might be able to reach a liquid entropy equal to that of the crystal at T_{K}. In section 3.3, though, we will give evidence that this is only possible if $T_{\mathrm{K}} = 0$.

1.2 Theories Describing the Viscous Slowing Down.

The theoretical understanding of the glass transition is still far from being complete. To date, no theory has been presented that captures all the prominent features of supercooled liquids and the glass transition. During the last years, though, considerable progress has been made both from the analytical and the numerical side. For a comprehensive review see, e.g., (Jäckle, 1986) or (Debenedetti and Stillinger, 2001). Here we concentrate on theories that describe the viscous slowing down of molecular motion.

[1] apart from particle permutations

[2] In simulations, we can directly compute the vibrational part of the entropy of the liquid without this assumption, see section 3.3.

Theories involving a low-temperature phase transition. Some of the early theories of the glass transition predicted a true phase transition at T_{K} or T_{VFT}. The first among them related the viscosity to the free volume within in the system (Cohen and Turnbull, 1959). One assumed that a minimum of local free volume is needed for particle transport to happen. If, by some fluctuation, this threshold value is exceeded, some molecules may rearrange. Under simple assumptions about the distribution function of these fluctuations and the mean free volume per particle, one arrived at the VFT relation for the viscosity. Later on, the free-volume model was extended by some elements from percolation theory (Cohen and Grest, 1979). By intuitive arguments, the authors related the glass transition to the percolation of liquid-like clusters (i.e. those with sufficient free volume) through the sample, which corresponds to a first-order phase transition.

In a rival theory, developed for polymers on a lattice, a second-order phase transition was predicted if the number of occupied sites becomes sufficiently large, leading to the vanishing of the configurational entropy (Gibbs and DiMarzio, 1958). Later, Adam and Gibbs explained the temperature dependence of relaxation times in glass-forming liquids in terms of the temperature variation of the size of 'cooperatively rearranging regions' (CRRs). Their work is certainly one of the most cited in the field of glass research (Adam and Gibbs, 1965). The important outcome is the Adam-Gibbs relation of relaxation times with configurational entropy, namely

$$\tau(T) = \tau_0 \exp\left(\frac{A}{T s_{\mathrm{c}}(T)}\right), \tag{1.3}$$

with constants τ_0 and A. If s_{c} goes to zero at T_{K} like $s_{\mathrm{c}}(T) \propto (T - T_{\mathrm{K}})/T$, one ends up again with the VFT equation, where we may then identify T_{K} with T_{VFT}. This is supported by the common observation of similar T_{K} and T_{VFT}. Moreover, Eq. 1.3 with $\tau(T)$ replaced by the diffusion coefficient has recently been verified for several model glass formers in numerical simulations (Saika-Voivod et al., 2001; Scala et al., 2000; Starr et al., 2001; Sastry, 2001) and experimentally over a broad range of substances (Richert and Angell, 1998; Casalini et al., 2002; Comez et al., 2002).

Thus, Eq. 1.3 provides a suggestive connection between kinetics and thermodynamics which seems to be more than coincidental. According to this equation, the viscous slow-down originates from the decreasing number of configurations that the system may sample. At the Kauzmann temperature, where $s_{\mathrm{c}} = 0$, the liquid would reside in a unique, non-crystalline state which is termed the ideal glass. A shortcoming of the treatment that leads to Eq. 1.3 is that no information about the size of CRRs is given. Recent simulation results, which connect the number of particles in collectively relaxing clusters to configurational entropy, seem to be

a first step towards a better real-space understanding of Eq. 1.3 (Giovambattista et al., 2002a).

We have mentioned the entropy theory by Adam and Gibbs because of two reasons. First, in section 3.3, we provide evidence that the concept of a vanishing configurational entropy at T_K should be revised. Second, the results presented in chapter 4 and chapter 5 might directly lead to a better understanding of Eq. 1.3 in terms of the potential energy landscape. However, the latter problem must be left unsolved in this thesis.

Mode-coupling theory. An alternative viewpoint to the concept of an underlying phase transition is provided by mode-coupling theory (MCT), where one assumes a purely dynamical viewpoint. Without invoking diverging correlation lengths, the theory provides a way of understanding diverging correlation times at low temperatures, starting from first principles (Götze, 1989). The basic idea is a quantitative formulation of a non-linear feedback of dynamic density correlations. Using static density correlations as an input, one is able to deduce a detailed picture for the dynamics, which comprises a two-step decay and certain factorization properties. Later, the MCT of simple liquids was generalized to molecular substances, incorporating their rotational degrees of freedom (Schilling and Scheidsteger, 1997).

The 'idealized' version of the theory predicts a divergence of correlation times at a critical temperature T_c. Since T_c is significantly higher than the laboratory glass transition, it is now widely understood that ideal MCT cannot be a theory for the glass transition itself. As already noted in the introduction, this is generally attributed to the fact that activated processes are not included in the theory. By a subsequent modification (Franosch et al., 1997), these 'hopping' contributions could be built into the theory, so that relaxation could continue down to much lower temperatures. Unfortunately, this improved version of MCT is not acknowledged much in the glass community today, possibly due to its too complex character.

We briefly note that the structure of the MCT equations is reproduced by some mean-field spin-glass models (Bouchaud et al., 1996). In general, the theory of spin glasses has had a large impact on the field of supercooled liquids and the glass transition. We do not attempt to discuss this here, but rather refer the reader to the extensive literature on the subject; see, e.g., (Mezard et al., 1987; Mezard and Parisi, 2000).

The generally presumed crossover of relaxation mechanism, from fluid-like above T_c to activated hopping below T_c, will be discussed in detail in chapter 7. The result will be that, upon cooling, activated barrier crossing becomes the dominant relaxation mechanism much above T_c. Whether this is consistent with the ideal

MCT picture or not shall be left open for discussion.

Chapter 2

On the Simulations

To capture the behavior of supercooled metal alloys, Stillinger and Weber have introduced a simple model potential of Lennard-Jones form (Weber and Stillinger, 1985a). As they have shown by an appropriate set of potential parameters, it is possible to reproduce the experimental findings, e.g., for amorphous $Ni_{80}P_{20}$ quite accurately (Weber and Stillinger, 1985b). Since these systems belong to the simplest liquids exhibiting a glass transition, they are an obvious choice for a numerical study.

In section 2.1, we present the details of the interparticle potentials and discuss the aspect of possible crystallization. Then we describe the equations of motion and their integration within the simulations (section 2.2), before turning to the issue of units (section 2.3).

2.1 Interaction Potentials.

In this thesis, we investigate a binary mixture of Lennard-Jones particles (BMLJ), as introduced by Kob and Andersen (Kob and Andersen, 1995). This system has only a weak tendency towards crystallization when cooled below the melting temperature of its crystal. In the numerical investigation of supercooled liquids this is quite essential. When trying to set up a simple system with spherical interaction potentials, $V_{ij}(|\boldsymbol{x}_{ij}|)$, one makes the experience that the driving force towards phase separation or crystallization is often strong.

One way to avoid these ordering effects is to introduce a large polydispersity of particle sizes. In systems of hard spheres with a gaussian distribution of particle diameters, for example, one needs a width of ca. 10% of the average size to hamper formation of large crystallites in the sample. For two-dimensional hard discs, one even has to go to a relative width of 25% (Doliwa and Heuer, 2000). If we intend to perform energy-landscape analyses, such large polydispersity has a drawback:

Since the motion of the smallest particles is much faster than the average, most IS transitions are related to the hopping of these small particles. This disturbs the analysis of the relaxation of average particles.

Another way to avoid ordering is to work with a small number of particle species and to carefully tune interaction potentials. The system of Kob and Andersen consists of two components, A and B, which are characterized by the interaction potentials of Lennard-Jones type ($a, b \in \{A, B\}$)

$$V_{ab}^{\mathrm{LJ}}(r) = 4\epsilon_{ab}\left\{\left(\frac{\sigma_{ab}}{r}\right)^{12} - \left(\frac{\sigma_{ab}}{r}\right)^{6}\right\}. \tag{2.1}$$

One applies standard periodic boundary conditions. The minimum of the potential is located at $2^{-1/6}\sigma_{ab}$. The following choice of parameters has proved to yield a stable supercooled liquid:

$$\begin{aligned} N = N_A + N_B, &\qquad N_A/N_B = 80/20, \\ \sigma_{\mathrm{BB}} = 0.8\sigma_{\mathrm{AA}}, &\qquad \sigma_{\mathrm{BB}} = 0.88\sigma_{\mathrm{AA}}, \\ \epsilon_{\mathrm{AB}} = 1.5\epsilon_{AA}, &\qquad \epsilon_{\mathrm{BB}} = 0.5\epsilon_{AA}, \\ \rho = N/V = 1.2. & \end{aligned} \tag{2.2}$$

The remaining σ_{AA} and ϵ_{AA} serve as units of length and energy. Of special importance is the large value of ϵ_{AB}. It favors the formation of $A-B$ next neighbors, thus preventing phase separation.

This type of system has now become the drosophila of supercooled computer liquids. Many results on the binary mixture Lennard-Jones (BMLJ) are available today, ranging from large-scale simulations of dynamical heterogeneities (Kob et al., 1997), over detailed PEL investigations (Sastry, 2001; Sciortino et al., 2000), to aging phenomena (Kob and Barrat, 1997). In order to achieve a maximum comparability with existing work, we try to stick as closely to Kob's BMLJ as possible.

For reasons of continuity at the cutoff, the original potential is modified,

$$V_{ab}(r) = V_{ab}^{\mathrm{LJ}}(r) + C_{ab}(r). \tag{2.3}$$

In the initial version of the potential (Kob and Andersen, 1995), the cutoff depended on particle species, by $r_{c,ab} = 2.5\sigma_{ab}$. The potential was simply shifted, $C_{ab}(r) = -V_{ab}(r_{c,ab})$, and set to zero for $r > r_{c,ab}$.

Generally, it is advisable to use a simulation box with dimensions larger than twice the cutoff. In this way, one avoids self interactions of particles and multiple interactions between pairs of particles.[1] The maximum cutoff length in Kob's BMLJ

[1] In the case of long-ranged interactions, like the Coulomb one, sophisticated techniques like the Ewald summation have to be used.

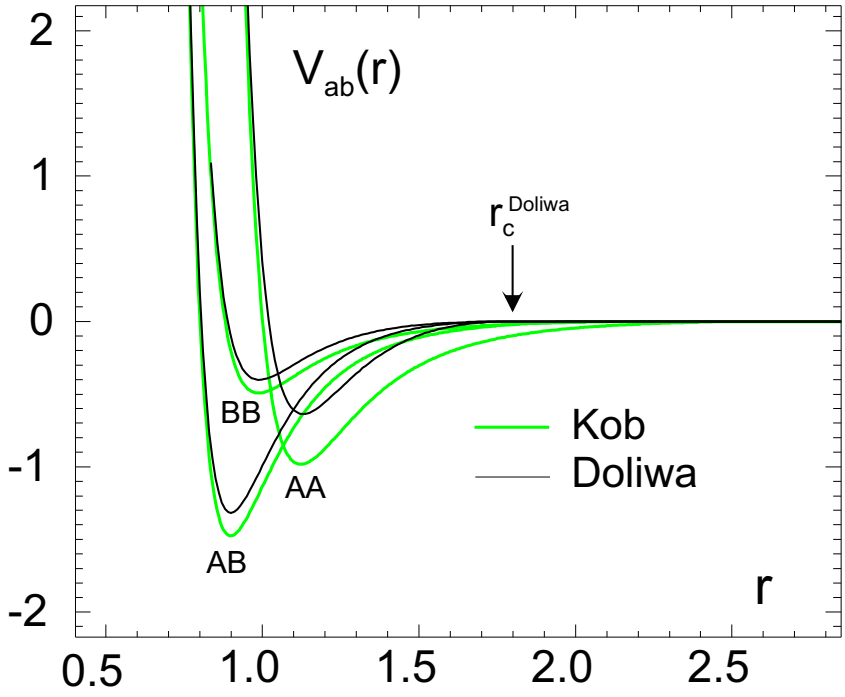

Figure 2.1: Comparison of the BMLJ potential by Kob and Andersen with the one used in the present work.

is $r_{c,AA} = 2.5$. Thus, the smallest possible system has the volume $V = (2 \times 2.5)^3$, corresponding to a minimum of $N = \rho V = 150$ particles at density $\rho = 1.2$. In this thesis, we are interested in the PEL of small systems, so that the limitation of $N \geq 150$ is a bit too strong. The work of Büchner and Heuer has shown that BMLJs of the size of 60 particles are very suitable for a PEL investigation (Büchner and Heuer, 1999). We therefore modify the original BMLJ by using a smaller cutoff, $r_c = 1.8$, which is independent of species. In this way, we can have systems as small as 56 particles.

So far, the introduction of a new cutoff only affects the shifting constants, whereas the shape of the potential remains untouched. However, a further proviso is needed. Some of the analyses carried out here need the continuity of interparticle *forces*. This can be achieved by adding a linear term to the potential (Allen and Tildesley, 1996),

$$C_{ab}(r) = -V_{ab}^{\mathrm{LJ}}(r_c) - V_{ab}^{\mathrm{LJ}\,\prime}(r_c)(r - r_c). \tag{2.4}$$

The expressions for the interparticle forces and for the Hessian, the second derivative matrix of the potential, are detailed in appendix B. Exactly the latter system has recently been treated by two groups (Broderix et al., 2000; Hernandez-Rojas and Wales, 2001). A comparison between the Kob-Andersen potential and our

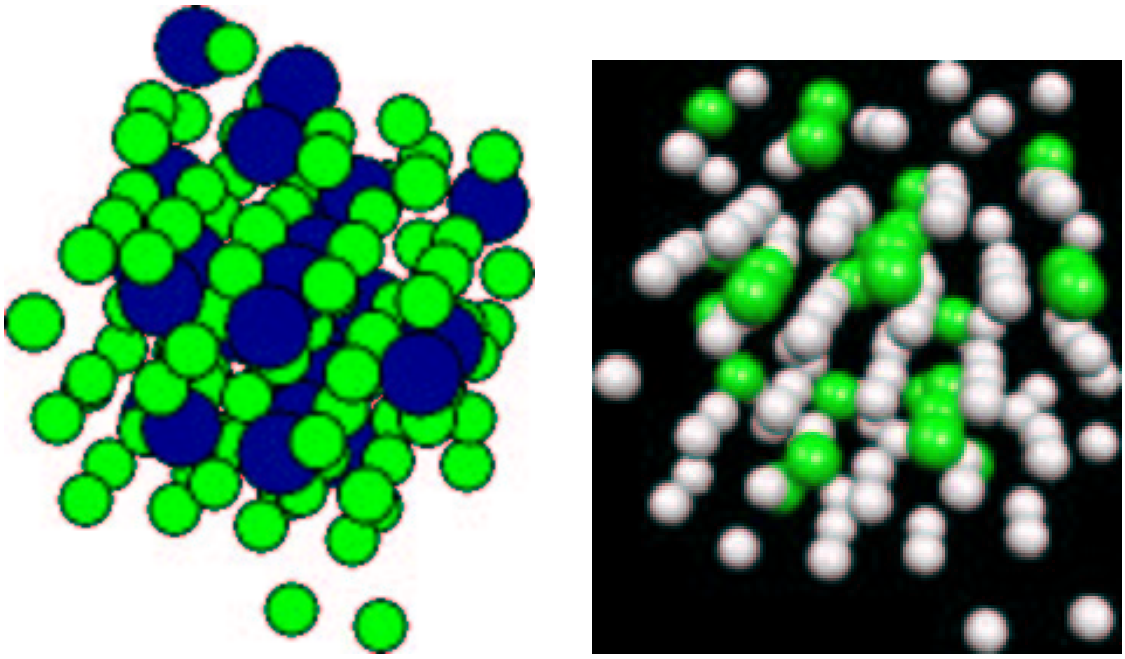

Figure 2.2: Two perspectives on the same crystal of a BMLJ with 130 particles. The stacking of A and B particles and the alternating arrangement of columns are nicely visible. For reasons of visualization, the A particles are depicted smaller than the B particles. The potential energy of this configuration is ca. $-616\epsilon_{\mathrm{AA}}$.

modified version is given in Fig. 2.1. Obviously, the $A-B$ and $B-B$ interactions are close to the original potential, whereas the $A-A$ interaction is considerably weaker than the one chosen by Kob and Andersen. Since the $A-A$ interaction predominates, we will find massively higher values of potential energies. For instance, the lowest amorphous minima found in our system have an energy of ca. $-4.65\epsilon_{\mathrm{AA}}$ per particle. In the Kob-Andersen system, Sciortino et al. find values down to $-7.7\epsilon_{\mathrm{AA}}$. Due to these deviations, a quantitative comparison between both models should be undertaken with care. Nonetheless, we will find that our brand of BMLJ has qualitatively the same behavior as its cousins.

Recently, crystallization of this computer model system has been reported by Wales and coworkers (Middleton et al., 2001). While these authors have used a global optimization strategy, we very rarely encounter crystalline configurations also in our regular simulations. It is interesting so see how the system finds a way to establish a long-range order despite our precautions. A typical crystal can be seen in Fig. 2.2. One finds columns of A particles, as well as of B particles, which are arranged parallely. Due to the strong $A-B$ interaction, A columns alternate with B columns. We found this crystal in a simulation run of a BMLJ130 system

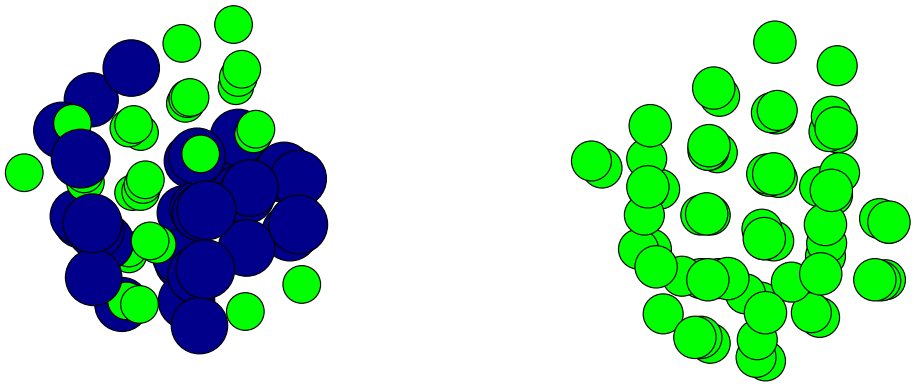

Figure 2.3: Two of the many crystalline configurations found in the binary soft-sphere system with 70 particles. On the left, the stacking of particles and the separation of A and B particles is visible. On the right, A and B particles have been plotted with the same size to better see the ordering.

(130 particles), after ca. 8×10^8 MD steps. This demonstrates that we really deal with a *supercooled* liquid here. Other runs at the same temperature ($T = 0.45$) have not crystallized. Since we are only interested in the amorphous phase, we sort out the rare simulation runs where crystallization occurs. These are easily detectable, since the minimum energies of the crystals lie well below the amorphous packings. For instance, the crystal depicted in the figure has a potential energy of $-4.74\epsilon_{\mathrm{AA}}$ per particle, whereas amorphous minima deeper than $-4.65\epsilon_{\mathrm{AA}}$ can hardly be found (see below). For a BMLJ60 with a nearly identical potential, Wales et al. report a crystal energy of $-4.71\epsilon_{\mathrm{AA}}$, which is still below the deepest amorphous packings. As a consequence, if the system is trapped in one of the crystalline structures, it normally stays there for the rest of the simulation run.

We note here that another well-known, simple model liquid - equimolar soft spheres with r^{-12} repulsions - does not have these convenient properties. Details of the soft-sphere system are given in appendix B.4. Long simulation runs of a small system (70 particle, see also (Grigera et al., 2002)) show crystalline, partly phase-separated configurations. These, however, are not stable but alternate with amorphous packings in the same run. The reason is that the minima energies of the ordered structures are not well-separated from the disordered ones. For example, the configurations shown in Fig. 2.3 have the energies $1.724\epsilon_{\mathrm{AA}}$ and $1.753\epsilon_{\mathrm{AA}}$ per particle, whereas also amorphous packings down to $1.75\epsilon_{\mathrm{AA}}$ exist. Thus, small soft-sphere systems have the serious drawback that crystallites are present in every low-temperature simulation run. In a larger system of 280 particles, we have not

found any crystalline configurations up to now. This indicates that the occurrence of crystallinity is an artifact of small soft-sphere systems. Further strong finite-size effects of soft-sphere systems are discussed in section 6.3; see also (Kim and Yamamoto, 2000).

2.2 Equation of Motion and its Integration.

Almost invariably, dynamics in supercooled liquids is generated by integrating Newton's equations of motion. From 'historical' but also from technical[2] reasons, we have made another choice, namely the position Langevin equation (Allen and Tildesley, 1996; Lax, 1966),

$$\dot{\boldsymbol{x}}_i(t) = \boldsymbol{F}_i(t)/m\zeta + \boldsymbol{g}_i(t), \tag{2.5}$$

where $\boldsymbol{x}_i(t)$ is the position vector of particle i, $\boldsymbol{F}_i(t)$ the force acting on particle i, m the mass, which is identical for all particles, and ζ the friction constant.[3][4] Thermal motion is induced by the last term in Eq. 2.5, $\boldsymbol{g}_i(t)$, which is a 'random velocity process', as usual for Brownian motion. The quantity $\boldsymbol{g}_i(t)$ is taken to be δ-correlated (Allen and Tildesley, 1996),

$$\left\langle g_i^\alpha(0) g_i^\beta(t) \right\rangle = \frac{2k_\mathrm{B}T}{m\zeta}\delta_{\alpha\beta}\delta_{ij}\delta(t). \tag{2.6}$$

A simple integration scheme for Eq. 2.5 has been given by Ermak and Yeh (Ermak and Yeh, 1974),

$$\boldsymbol{x}_i(t+\Delta t) = \boldsymbol{x}_i(t) + \Delta t \boldsymbol{F}_i(t)/m\zeta + \Delta\boldsymbol{g}_i(t). \tag{2.7}$$

Here Δt is the integration time step and

$$\Delta\boldsymbol{g}_i(t) = \int_t^{t+\Delta t} \mathrm{d}t' \boldsymbol{g}_i(t')$$

[2]Upon using the position Langevin equation, the instantaneous state during dynamics is specified solely by the particle coordinates and the random generator seed. Thus momenta do not have to be stored.

[3]not to be confused with the energy elevation $\zeta(x)$ of section 3.2 or the transition state ζ of chapter 5

[4]Henceforth, we will mainly use a short-hand notation which merges all the N particle positions into a $3N$-dimensional vector,

$$x = \{\boldsymbol{x}_1, ..., \boldsymbol{x}_N\}.$$

Similarly, the forces present in a given configuration x are combined to the vector $F(x)$, which we write as $F(x) = -\partial V(x)$. Components of vectors $\boldsymbol{x}_i$ are denoted by Greek letters, x_i^α.

are gaussian random variables with zero mean and width given by $\left\langle (\Delta g_i^\alpha)^2 \right\rangle = 2k_\mathrm{B}T/m\zeta \equiv \lambda^2$. Alternatively, one may specify the width λ instead of Δt,

$$\boldsymbol{x}_i(t+\Delta t) = \boldsymbol{x}_i(t) + \frac{\beta\lambda^2}{2}\boldsymbol{F}_i(t) + \lambda\Delta\boldsymbol{n}_i(t). \tag{2.8}$$

where, additionally, we switched to the *normal*-distributed random variables $\Delta\boldsymbol{n}_i(t)$. At fixed λ, the time step in Eq. 2.8 is given by

$$\Delta t = \beta\lambda^2 m\zeta/2, \tag{2.9}$$

which means that it grows longer upon cooling. As can be seen from the above equations, the choice of ζ sets the absolute time scale.

The dynamics generated by Eq. 2.8 might seem a bit artificial: On a short time scale, e.g., particles move as if they were freely diffusing, which is clearly unphysical. Nonetheless, there are arguments that this kind of propagation is equally pertinent for the study of supercooled liquids as solving Newton's equations. First, Gleim et al. have demonstrated that stochastic dynamics simulations lead to the same results in the BMLJ as does regular MD at low-enough temperatures (Gleim et al., 1998). This was shown for a momentum-space Langevin equation which is more general than our ansatz Eq. 2.8. Second, mode-coupling theory, which to a large degree describes the viscous slowing down upon cooling, makes no assumptions concerning the microscopic dynamics. This indicates that the interesting physics begins beyond the short-time regime. Third, Newtonian dynamics trajectories in a many-particle system are highly chaotic. It is easy to imagine that the momenta are completely randomized after a few collisions of each particle. We shall see later on that the activated crossing of potential energy barriers is the mechanism for the long-time dynamics at low temperatures. Although the durations of barrier crossing events are much smaller than the waiting times before them, they typically take several hundred MD steps. Within this time, an initial concentration of kinetic energy along the configuration-space direction of the transition will certainly dissipate into the remaining degrees of freedom. Hence, the crossing of potential barriers in Newtonian dynamics simulations should be considered as a pseudo-stochastic effect, which is qualitatively the same as in purely stochastic simulations. Thus, Langevin and Newtonian dynamics should lead to the same result in the regime of barrier crossing.

The choice of the elementary step size, λ, is essential. On the one hand, λ should be as small as possible in order to obtain an accurate integration of Eq. 2.5. On the other hand, due to the diffusive character of short-time dynamics (Eq. 2.9), reducing λ by a factor of two will lead to a fourfold computational cost. Throughout the thesis we use $\lambda = 0.015$, which is a good compromise between performance and precision.

For reasons of convenience, we set the friction constant to $\zeta = 2/0.015^2\sqrt{m\sigma_{\rm AA}^2/\epsilon_{\rm AA}}$, which results in the elementary time step $\Delta t = \beta\sqrt{m\sigma_{\rm AA}^2\epsilon_{\rm AA}}$. We checked that the dynamics (e.g., the long-time diffusion coefficients) for $\lambda = 0.0075$ is identical to that found at $\lambda = 0.015$. However, care must be taken if one looks for very precise values of the potential energy: Since the integration scheme Eq. 2.8 assumes constant forces during the elementary time step, a larger step size λ leads to the penetration of regions of higher energy, which would be avoided in the limit $\lambda \to 0$. Thus, a finite step size produces slightly elevated instantaneous energies (up to 5%) and also elevated forces and pressures. A way to access these quantities accurately is to combine the above dynamics with a second sampling scheme: Starting from configurations obtained via Langevin dynamics, one performs a short Metropolis sampling of configuration space. Since local equilibration is fast (e.g., in a potential energy minimum), the Metropolis algorithm yields correct local averages of the above quantities - without the shortcomings of a finite λ.

For completeness, we note that a small fraction of the simulations were performed with regular Newtonian dynamics, as is commonly used in studies of supercooled liquids. In this way, we have checked that the Langevin approach does not yield very different results (see section 4.1). To this end, we implemented the original BMLJ FORTRAN code of Walter Kob into our program package. There, he made use of the 'velocity verlet' algorithm (Allen and Tildesley, 1996) to integrate the equations of motion, i.e.

$$x(t+\Delta t) = x(t) + \Delta t v(t) + \frac{(\Delta t)^2}{2m}F(t)$$
$$v(t+\Delta t) = v(t) + \frac{\Delta t}{2m}\left(F(t) + F(t+\Delta t)\right),$$

where $v(t)$ is the high-dimensional vector formed by the N velocity vectors of the individual particles.

2.3 Units.

In computer simulations it is often convenient to express quantities such as temperature, density, pressure, and the like in reduced units. This means that we choose a pertinent unit of energy, length and mass and then express all other quantities in terms of these basic units. In our BMLJ, a natural (though not unique) choice for the basic units is the following:

- Unit of length; $\sigma_{\rm AA}$
- Unit of energy; $\epsilon_{\rm AA}$

- Unit of mass; m.

From these, we derive the other units needed:

- Unit of time; $\sqrt{m\sigma_{\mathrm{AA}}^2/\epsilon_{\mathrm{AA}}}$
- Unit of temperature; $\epsilon_{\mathrm{AA}}/k_{\mathrm{B}}$,

where k_{B} is Boltzmann's constant. Throughout the thesis, however, we will drop units completely, which is a matter of convenience.

If desired, we can also express our quantities in experimentally relevant units. For the case of $Ni_{80}P_{20}$, the translation can be done with the help of the following table.

Quantity	LJ units	$Ni_{80}P_{20}$
length	σ_{AA}	2.218 Å
energy	ϵ_{AA}	1.289 10^{-20} J
mass	m	1.028×10^{-25} kg
time	$\sqrt{m\sigma_{\mathrm{AA}}^2/\epsilon_{\mathrm{AA}}}$	0.626 ps
temperature	$k_{\mathrm{B}}^{-1}\epsilon_{\mathrm{AA}}$	934 K

Table 2.1: Transformation from LJ to $Ni_{80}P_{20}$ units.

Chapter 3

The Energy Landscape Approach

As a consequence of the amorphous structure of supercooled liquids, an accurate theoretical description of their dynamic and thermodynamic properties is very difficult. Although the physical principles behind the process of glass formation seem to be understood qualitatively today, there is still much disputation on their appropriate quantitative formulation. For example, the concept of growing molecular cooperativity for $T \to T_g$ is widely viewed as the reason for the slowing down of dynamics. However, it is not clear whether the corresponding dynamic correlation lengths diverge at T_g or not.

One of the possible approaches to a better understanding of glass-forming liquids has been proposed by Goldstein many years ago (Goldstein, 1969), and is at the basis of the present thesis.

To explain the idea, we first need some notation. Starting from the pair potentials $V_{ij}(\boldsymbol{x}_{ij})$, where $\boldsymbol{x}_{ij} = \boldsymbol{x}_j - \boldsymbol{x}_i$ is the distance vector between particle i and j, one writes the total potential energy

$$V(x) = \sum_{i,j=1,i<j}^{N} V_{ij}(\boldsymbol{x}_{ij})$$

as a function of the high-dimensional coordinate $x = (\boldsymbol{x}_1, ..., \boldsymbol{x}_N)$. The latter is an Nd-dimensional vector, since it comprises the positions of all particles. Throughout this thesis, we will only deal with three-dimensional systems, so that $d = 3$. The function $V(x)$ describes an extremely complex surface over configuration space,

$$\mathrm{PEL} = \left\{(x, V(x)), x \in \mathbb{R}^{Nd}\right\},$$

which we will call the *potential energy landscape (PEL).* For future use, we also define the force $F(x) = -\partial V(x)$ and the Hessian matrix $H(x) = \partial\partial V(x)$ of second derivatives (see appendix B for a detailed description of these objects).

By definition, the full complexity of the system is contained in $V(x)$. At low temperatures, however, the high-energetic details of the PEL become irrelevant. Therefore, the idea of the PEL approach is to reduce the information content of the PEL to few characteristic, low-energetic features; see Fig. 3.1. Local minima, in short minima, of $V(x)$ are the most useful information about the structure of the PEL (we denote the corresponding configuration by $\xi \in \mathbb{R}^{Nd}$). In the literature, they are also called inherent structures (Stillinger and Weber, 1982), and we sometimes use the abbreviation IS for them. Minima are characterized by a vanishing force and a positive definite Hessian. At low temperatures, the system will mainly reside in the very vicinity of minima, interrupted by rapid transitions among them. Under such circumstances, thermodynamic properties can be derived from the statistics of minima. From some configuration x, we obtain the nearby minimum by a steepest descent (SD) path, as given by the equation $\mathrm{d}x/\mathrm{d}s = F(x(s))$, where s is some curvilinear parameter. To every minimum ξ, we assign a *basin of attraction* $\Omega(\xi)$, or shortly basin, as the set of all configurations x that end up in ξ with their SD path.

Since at low temperatures the duration of inter-basin transitions is short compared to the average residence time inside basins, the contribution of transitions to thermodynamic (static) averages is negligible. For dynamics, however, they are of outstanding importance. Transition rates can be characterized by so-called saddles, i.e. configurations ζ on basin borders with vanishing forces. While minima are stable with respect to perturbations in all directions (the Hessian is positive), saddles also have unstable directions. This information is contained in the eigenvalues λ_ν of the Hessian matrix $H(\zeta)$. If $\lambda_\nu < 0$, the eigenvector v_ν points into an unstable direction, while $\lambda_\nu > 0$ implies stability along v_ν. The index $n(x)$ is defined as the number of negative eigenvalues of the Hessian $H(x)$. In the case of $n(\zeta) = 1$, we call ζ a *transition state (TS)*. It will turn out later on that the low-temperature dynamics is mainly governed by TSs instead of higher-order saddles, which is why we will mostly consider the former. A TS normally acts as a barrier between two minima and thus limits the transition rate among them. From the difference in potential energies one may estimate this rate.

At a higher level of sophistication where minima and transition states would not suffice, one could also include in the analysis whole reaction paths (RPs), starting at some minimum, passing through a TS and ending at another minimum. In this way, rate constants can be determined more accurately.

In recent years, important pieces of information have been gained about the PEL of different glass-forming systems via extended computer simulations. For a

review, see (Debenedetti and Stillinger, 2001) and references therein. In particular, it has turned out that the critical temperature T_c of mode-coupling theory serves as a good indicator for the temperature range where the PEL standpoint is appropriate: Below T_c (the so-called landscape-dominated regime), it is generally accepted that the temporal evolution of a system happens through activated jumps among PEL minima. Between T_c and $2T_c$ (the landscape-influenced regime), properties of minima are still deemed to be relevant for the thermodynamic description, whereas they are generally expected to be irrelevant for dynamics there. This has been concluded from the analysis of higher-order stationary points, which start to be populated above T_c. In this work, however, we provide evidence that this notion should be revised (see chapter 7). In any event, above $2T_c$ the PEL description breaks down due to the fact that the system no longer occupies the well-behaved vicinity of minima (Büchner and Heuer, 1999; Sciortino et al., 2000; Sastry et al., 1998).

In this chapter, we would like to present our results on the *thermodynamic* properties of the BMLJ65 system, based on the PEL approach. The analyses carried out in section 3.1 are largely well established in the field of supercooled liquids. In section 3.2, we report a new method for the computation of the total number of minima and give a comparison to standard techniques. Some new aspects of configurational entropy, $s_c(T)$, are reported in section 3.3. Due to a more rigorous treatment than commonly found in the literature, we reach the conclusion that $s_c(T)$ can only vanish at $T = 0$, so that the notion of the Kauzmann temperature as a relevant concept should be revised.

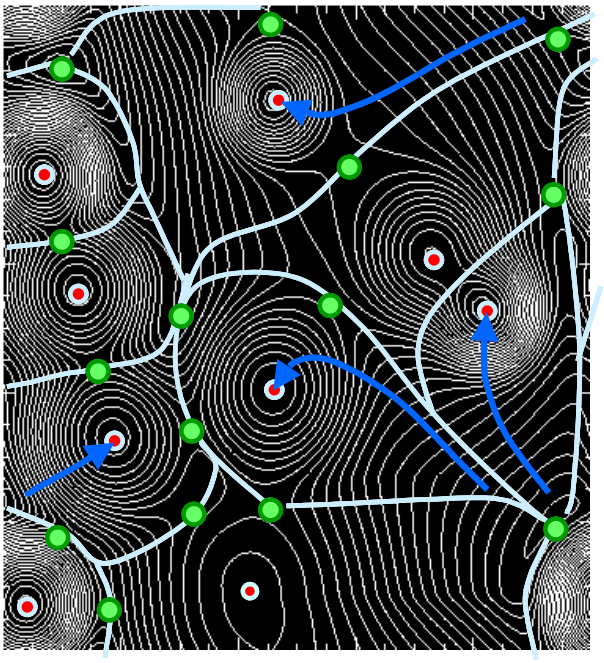

Figure 3.1: Two-dimensional sketch of the PEL, including contour lines, minima, transition states, saddles, basin borders, and steepest descent paths.

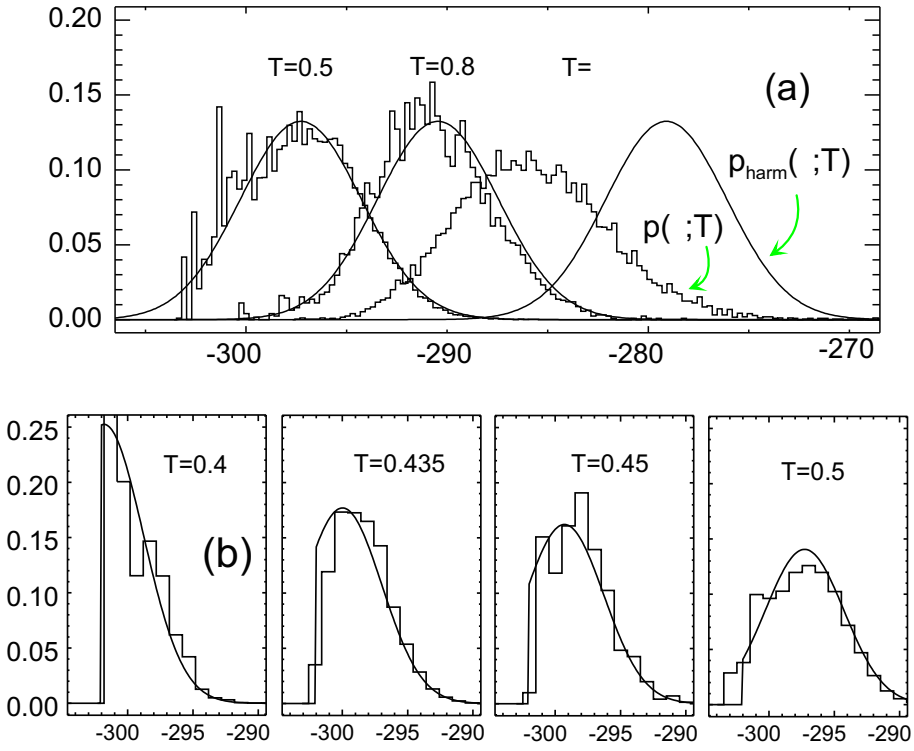

Figure 3.2: Population of minima energies ϵ at temperature T, $p(\epsilon;T)$, for the BMLJ65 system. (a) $T = 0.5, 0.8$, and ∞. (Equilibrium configurations for $T = \infty$ are generated by randomly choosing particle positions in the box.) (b) Low temperatures, where, *apparently*, the lower end of the PEL is reached. We will discuss this issue in section 5.5, where we will find that the apparent cutoff is probably due to insufficiently long simulation runs. Smooth lines: prediction from gaussian distribution of minima, Eq. 3.7, see below. In (a), we use $\epsilon_{\min} = -\infty$, whereas in (b), $\epsilon_{\min} = -302$ seems to be a good choice for the lower cutoff energy.

3.1 Statistics of Minima.

Since the set of all basins covers the configuration space, denoted Ω_{conf}, we can write the partition function

$$Z(T) = \frac{1}{N_A!N_B!}\int_{\Omega_{\text{conf}}} \frac{\mathrm{d}x}{u} e^{-\beta V(x)} = \sum_i \int_{\Omega_i} \frac{\mathrm{d}x}{u} e^{-\beta V(x)} = \sum_i Z_i(T). \tag{3.1}$$

Here, integration is over the $(Nd-d)$-dimensional configuration-space volume, where center-of-mass degrees of freedom are excluded, and u is a constant, high-dimensional reference volume. As will be assumed henceforth, we only sum over the basins, $\Omega_i \equiv \Omega(\xi_i)$, of *amorphous* minima, ξ_i. This will be the case throughout the thesis, unless otherwise stated. Since permutations of identical particles do not

change the geometry, every minimum is only one of $N_A!N_B!$ equivalent configurations. To eliminate the entropy of mixing, and hence make $\ln Z$ extensive, we have included the factorials in Eq. 3.1. Here and in the following, we adopt the convention that summation over basins i involves only geometrically distinct, non-crystalline, configurations. In a supercooled liquid, of course, the underlying crystal corresponds to the true thermodynamic equilibrium. We have already noted that its energy is considerably lower than that of the amorphous packings. Nonetheless, if the supercooled liquid remains sufficiently long in the amorphous state, we may apply equilibrium thermodynamics there.

The partition function is a dimensionless quantity, due to the normalization by the reference volume u. For convenience, we will omit u in the following, i.e. set it to unity. The population of basin i, $p_i(T) = Z_i(T)/Z(T)$, is generally a very small number, since the number of basins is large (see section 3.2). However, the population of minima of a certain energy ϵ,

$$p(\epsilon;T) = \sum_i \delta(\epsilon - \epsilon_i)\frac{Z_i(T)}{Z(T)},$$

can be measured directly in the simulations. From Fig. 3.2, we see that $p(\epsilon;T)$ shifts towards lower energies upon decreasing temperature, and that the distributions are approximately of gaussian shape, except for the very low temperatures. In what follows, we would like to show that some general properties of the PEL can be deduced from these distributions.

Harmonic approximation. The basins of attraction, Ω_i, may have a very complicated shape. Generally, we have no simple means to capture their structure. However, in the limit of low temperatures, we will mostly find the system close to the corresponding minima where the local PEL shape can be approximated by the harmonic curvature. Hence, the contributions of the so-called basin anharmonicities vanish in the limit $T \to 0$, and single-basin partition functions follow solely from the local information in the minima. An interesting question in this connection is from what temperature on this description works, in particular, whether this is already the case for temperatures above the glass transition. We will come back to this point later.

In the harmonic approximation, we can expand the potential around the minimum,

$$V(x) = \epsilon_i + \frac{1}{2}(x-\xi_i)^T H (x-\xi_i) + ...,$$

where H is the Hessian matrix evaluated at the minimum ξ_i, with $\epsilon_i = V(\xi_i)$. If we neglect contributions beyond the harmonic term, the basin partition functions can

be calculated,

$$\begin{aligned} Z_i(T) &\approx e^{-\beta\epsilon_i} \int_{\Omega_i} \mathrm{d}x \exp\left(-\frac{\beta}{2}\sum_\nu \lambda_{i,\nu} x_\nu^2\right) \\ &= e^{-\beta\epsilon_i} \prod_\nu \left(\frac{2\pi}{\beta\lambda_{i,\nu}}\right)^{1/2} = T^{(Nd-d)/2} Y_i e^{-\beta\epsilon_i} \equiv Z_{\mathrm{harm},i}(T), \end{aligned} \tag{3.2}$$

where

$$Y_i = \prod_\nu \left(\frac{2\pi}{\lambda_{i,\nu}}\right)^{1/2} = (2\pi)^{(Nd-d)/2} \exp\left(-\frac{1}{2}\sum \ln \lambda_{i,\nu}\right) \tag{3.3}$$

is the temperature-independent information about the harmonic modes around the minimum in question. By λ_ν we denote the eigenvalues of the Hessian, $\nu = 1, ..., (Nd-d)$. In systems without rotational degrees of freedom, like ours, d eigenvalues vanish since they correspond to center-of-mass motion. These are excluded from Eq. 3.3. Equivalently, the harmonic approximation can be written

$$p_i(T) \approx p_{\mathrm{harm},i}(T) = \frac{Y_i e^{-\beta\epsilon_i}}{\tilde{Z}(T)}, \tag{3.4}$$

where $\tilde{Z}(T) = \sum_i Y_i e^{-\beta\epsilon_i}$. In the presence of anharmonic contributions, we have to include a correction into Eq. 3.2,

$$Z_i(T) = z_{\mathrm{anh},i}(T) T^{(Nd-d)/2} Y_i e^{-\beta\epsilon_i}. \tag{3.5}$$

Anharmonic effects. The harmonic approximation is very attractive since it enables an exact calculation of the basin partition functions from local properties of the minima. Throughout the thesis, we will massively exploit this fact. We therefore have to take a closer look at the accuracy of the approximation, in that we find the temperature range where its accuracy is reasonable. In the literature on supercooled liquid simulations, it is the general point of view that anharmonic effects become negligible below $2T_c$ (Sciortino et al., 1999; Sastry, 2000).

The most direct test of the harmonic approximation is the comparison of the local PEL around a minimum ξ with the parabolic shape predicted from the eigenvalues of the Hessian matrix in ξ. It is clear from the high dimensionality of configuration space that only a limited number of directions from the minimum can be explicitly checked. Here, we limit ourselves to the directions of eigenvectors v_ν and compare the energy profile $V(\xi + x_\nu v_\nu) - V(\xi)$ with the prediction from the harmonic approximation, $\lambda_\nu x_\nu^2/2$. From Fig. 3.3, we see that the quality of the harmonic approximation strongly depends on the magnitude of the corresponding

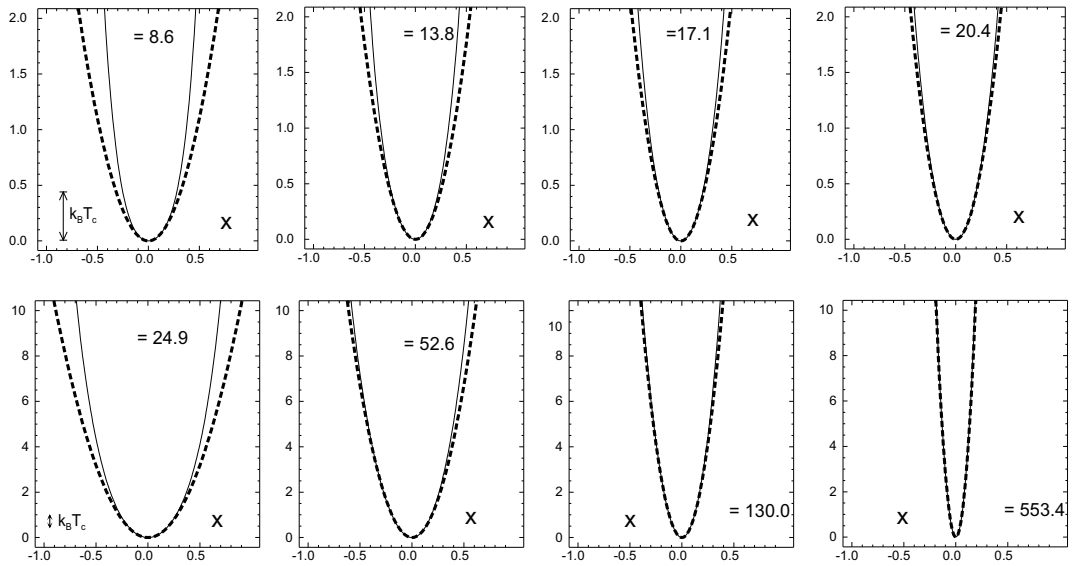

Figure 3.3: Potential energy difference $V(\xi + x_\nu v_\nu) - V(\xi)$ along some eigenvectors v_ν of the Hessian in one randomly chosen minimum ξ of the BMLJ65 (solid lines). The harmonic approximation $\lambda_\nu x_\nu^2/2$ of the potential is given as dashed lines. Eigenvectors to the four lowest, non-zero eigenvalues (top) and to four larger eigenvalues (bottom) were used. For comparison, we have indicated the magnitude of $k_{\mathrm{B}}T_c$.

eigenvalue. In 'soft' directions (small eigenvalues), the susceptibility of the potential to anharmonic effects is larger than along 'hard' vibrational modes. However, the data suggest that deviations from harmonic behavior should be small for $k_{\mathrm{B}}T < 1$. Clearly, from the pure inspection by eye of a single minimum we cannot make more quantitative statements. However, our later result that anharmonicities start to disturb around $T = 0.8$ - a conclusion also reached in the literature - is very plausible on the basis of the observations in Fig. 3.3.

Effective density of minima energies. Since in the harmonic approximation, a minimum is characterized by ϵ_i and Y_i, the partition function becomes

$$Z_{\mathrm{harm}}(T) = T^{(Nd-d)/2} \int \mathrm{d}\epsilon \int \mathrm{d}Y G(\epsilon, Y) Y e^{-\beta\epsilon},$$

where we have introduced the number density $G(\epsilon, Y)$ of minima ϵ with vibrational partition function $T^{(Nd-d)/2}Y$. In this expression, the effective density of minimum energies

$$G_{\mathrm{eff}}(\epsilon) \equiv \int \mathrm{d}Y G(\epsilon, Y) Y = \langle Y|\epsilon\rangle_G \, G(\epsilon) \tag{3.6}$$

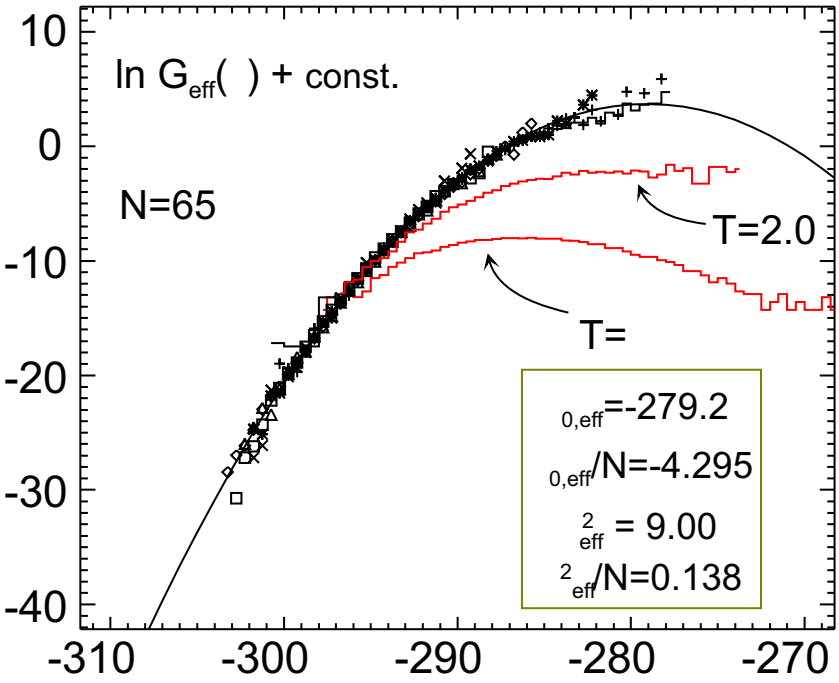

Figure 3.4: Natural logarithm of the effective density $G_{\text{eff}}(\epsilon)$ of minima, constructed from reweighted distributions $\langle \exp(\beta\epsilon)\delta(\epsilon - \epsilon')\rangle_T$, for the BMLJ65 at temperatures $T = 0.4, 0.435, 0.466, 0.48, 0.5, 0.6$, and 0.8 where the harmonic approximation is supposed to hold (landscape-influenced and landscape-dominated regimes). Higher temperatures ($T = 2$ and $T = \infty$) exhibit strong anharmonic effects, thus prohibiting an extension of $G_{\text{eff}}(\epsilon)$ towards high ϵ. The solid line is a gaussian fit to $G_{\text{eff}}(\epsilon)$, with variance σ^2_{eff} and mean $\epsilon_{0,\text{eff}}$. For the time being, the overall multiplicative constant $N_{0,\text{eff}}$ in $G_{\text{eff}}(\epsilon)$ remains unknown.

can be identified, which is different from the bare distribution

$$G(\epsilon) \equiv \int \mathrm{d}Y G(\epsilon, Y)$$

by the mean vibrational partition function of minima with energy ϵ

$$\langle Y|\epsilon\rangle_G \equiv \frac{1}{G(\epsilon)} \int \mathrm{d}Y G(\epsilon, Y) Y.$$

The probability of staying near a minimum of energy ϵ is given by

$$p_{\text{harm}}(\epsilon; T) = \frac{1}{\tilde{Z}(T)} \int \mathrm{d}Y G(\epsilon, Y) Y e^{-\beta\epsilon} = \frac{e^{-\beta\epsilon} G(\epsilon) \langle Y|\epsilon\rangle_G}{\tilde{Z}(T)} = \frac{e^{-\beta\epsilon} G_{\text{eff}}(\epsilon)}{\tilde{Z}(T)}, \qquad (3.7)$$

and, since $p(\epsilon; T) \approx p_{\text{harm}}(\epsilon; T)$ is a measurable distribution, we can invert this relation to obtain the effective density of states, up to a constant, i.e., $G_{\text{eff}}(\epsilon) \propto e^{\beta\epsilon} p(\epsilon; T)$. Clearly, from one temperature, one can only recover part of $G_{\text{eff}}(\epsilon)$

because a limited window of energies is sampled; see Fig. 3.2. Thus, a combination of runs with different T's is needed to obtain a larger part of $G_{\text{eff}}(\epsilon)$. The procedure is the so-called overlapping histogram method (Frenkel and Smit, 1996), where the distributions $ae^{\beta\epsilon}p(\epsilon;T)$ and $a'e^{\beta'\epsilon}p(\epsilon;T')$ are matched in the region of common energies ϵ by the appropriate choice of constants a and a'. In a logarithmic plot as Fig. 3.4, we just have to shift curves vertically until the overlap is optimum. For temperatures $T < 1.0$ the overlap is near perfect, whereas the distributions at $T = 2.0$ and $T = \infty$ do not fall onto the others. This is a direct indication for the presence of strong anharmonic effects at $T \geq 2.0$, and more importantly, of their dependence on ϵ, see below.

Note that the overall pre-factor in $G_{\text{eff}}(\epsilon)$, which is related to the total number of basins, N_0, remains unknown; it will be computed in section 3.2. As we see in Fig. 3.4, $G_{\text{eff}}(\epsilon)$ can be excellently fitted by a gaussian (mean $\epsilon_{0,\text{eff}}$, variance σ^2_{eff}). This property of $G_{\text{eff}}(\epsilon)$ was found in several model systems (Büchner and Heuer, 1999; Sciortino et al., 2000; Starr et al., 2001; La Nave et al., 2002a). Evidently, the small number of low-energy minima is compensated by the Boltzmann factor at low temperatures. Yet, the right, high-energetic wing of the distribution is not accessible by straightforward simulation, since both the Boltzmann factor and the number density are small there.

For huge systems, which, to a good approximation, are composed of many independent subsystems, the gaussianity of $G_{\text{eff}}(\epsilon)$ is an immediate consequence of the central limit theorem. However, as discussed in reference (Heuer and Büchner, 2000), a large degree of gaussianity must already be present in the subsystems that are considered elementary.

'Raw' density of minima energies. One may now ask in which way $G_{\text{eff}}(\epsilon)$ differs from the true number density $G(\epsilon)$ of minima with energy ϵ. From Eq. 3.6, we have $G(\epsilon) = G_{\text{eff}}(\epsilon)/\langle Y|\epsilon\rangle_G$, so we only need to know $\langle Y|\epsilon\rangle_G$. The simple calculation,

$$\langle Y|\epsilon\rangle_G = \frac{\int \mathrm{d}Y G(\epsilon,Y)Y}{\int \mathrm{d}Y Y^{-1} Y G(\epsilon,Y)} = \frac{1}{\langle Y^{-1}|\epsilon\rangle_T}, \tag{3.8}$$

shows that a canonical average[1] over Y^{-1} yields the desired quantity (in harmonic approximation). It turns out (Fig. 3.5) that $\ln\langle Y|\epsilon\rangle_G$ is to a great extent linear in ϵ, i.e., $\langle Y|\epsilon\rangle_G = e^{a+b\epsilon}$. With a gaussian $G_{\text{eff}}(\epsilon)$ (variance σ^2_{eff}, mean $\epsilon_{0,\text{eff}}$) this implies a gaussian shape for $G(\epsilon)$, too (variance $\sigma^2 = \sigma^2_{\text{eff}}$, mean $\epsilon_0 = \epsilon_{0,\text{eff}} - b\sigma^2$) (Sastry, 2001).

[1]Canonical averages $\langle ...\rangle_T$ are easy to compute in simulations by taking time averages.

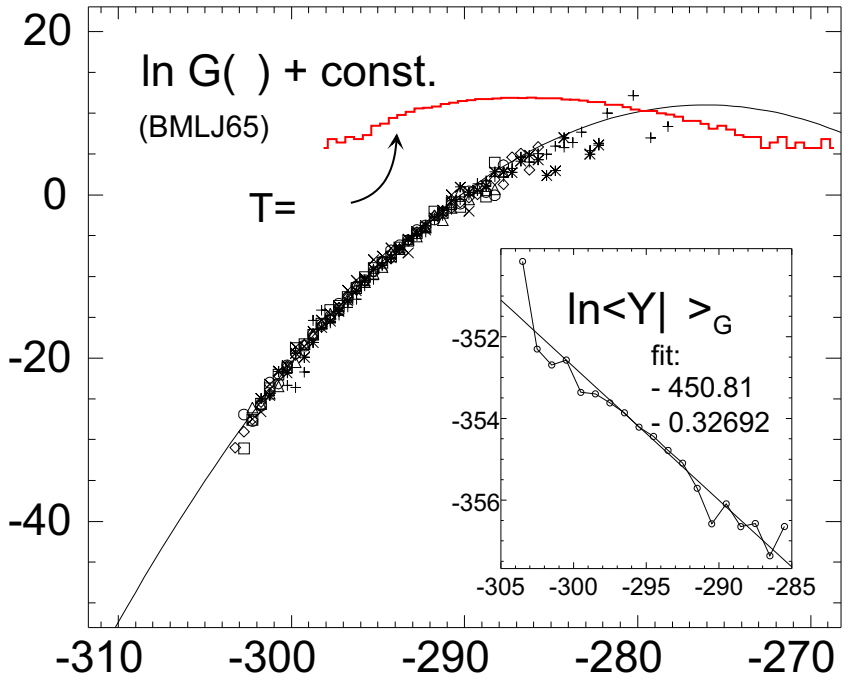

Figure 3.5: Natural logarithm of the density $G(\epsilon)$ of minima in the BMLJ65, constructed from reweighted distributions $\left\langle Y^{-1}\exp(\beta\epsilon)\delta(\epsilon-\epsilon')\right\rangle_T$, for temperatures $T = 0.4, 0.435, 0.45, 0.466, 0.5, 0.6$, and 0.8. Again, curves were shifted for maximum overlap and an overall constant remains unknown. The inverted parabola is $-(\epsilon-\epsilon_0)^2/2\sigma^2$ plus some constant, where $\sigma^2 = \sigma^2_{\rm eff} = 9.0$ and $\epsilon_0 = \epsilon_{0,\rm eff} - b\sigma^2_{\rm eff} = -276.3$. The curve for $T=\infty$ is $p(\epsilon; T=\infty)$ times some constant, see text. Inset: Mean harmonic basin volume $\ln\langle Y|\epsilon\rangle_G$ as a function of minimum energy ϵ. The straight line is the fit $a+b\epsilon$.

$G(\epsilon)$ can also be obtained by directly reweighting minima (ϵ_i, Y_i) in a histogram of ϵ. More precisely, in harmonic approximation, we have

$$G(\epsilon') \propto \left\langle Y^{-1} e^{\beta\epsilon}\delta(\epsilon-\epsilon')\right\rangle_T , \tag{3.9}$$

in the same way as the effective density $G_{\rm eff}(\epsilon)$ can be obtained by reweighting with the potential energy ϵ,

$$G_{\rm eff}(\epsilon') \propto \left\langle e^{\beta\epsilon}\delta(\epsilon-\epsilon')\right\rangle_T .$$

For different T, the respective parts of $G(\epsilon)$ were shifted to a maximum mutual overlap (see Fig. 3.5). Evidently, the gaussian approximation of $G(\epsilon)$ works well with the parameters ($\epsilon_0 = \epsilon_{0,\rm eff} - b\sigma^2$, and $\sigma^2 = \sigma^2_{\rm eff}$) derived from $G_{\rm eff}(\epsilon)$ and $\langle Y|\epsilon\rangle_G$.

Let us come back to the anharmonic effects which appear at high temperatures. We take $T=\infty$, where these are expected to be strongest. There, equilibrium configurations consist of completely random particle positions within the simulation

box, so that the population of basins is proportional to their (high-dimensional) volume,

$$p(\epsilon; T=\infty) \propto \sum_i \delta(\epsilon - \epsilon_i)\Omega_i = G(\epsilon)\,\langle\Omega|\epsilon\rangle_G\,.$$

In this expression, we have to use the number density $G(\epsilon, \Omega)$ of minima with energy ϵ and basin volume Ω. Figure 3.5 shows that the mean basin volume $\langle\Omega|\epsilon\rangle_G$ depends on the minimum energy ϵ, because $p(\epsilon; T=\infty)$ is not proportional to $G(\epsilon)$. Since the maximum of $p(\epsilon; T=\infty)$ is shifted to lower energies with respect to $G(\epsilon)$, we conclude that low-lying minima have larger volumes. More quantitatively, the relative mean basin volumes are fixed by the ratio of $p(\epsilon; T=\infty)$ and $G(\epsilon)$,

$$\frac{\langle\Omega_i|\epsilon\rangle_G}{\langle\Omega_i|\epsilon_0\rangle_G} = \frac{p(\epsilon; T=\infty)/G(\epsilon)}{p(\epsilon_0; T=\infty)/G(\epsilon_0)}.$$

The absolute value of the mean basin volumes, however, is not known, contrary to the basin partition function in harmonic approximation, $T^{(Nd-d)/2}Y_i$.

The difference between $G(\epsilon)$ and $G_{\text{eff}}(\epsilon)$ arises from the fact that low-energetic minima have larger vibrational entropies. This kind of dependence is expected from the mean basin volume $\langle\Omega|\epsilon\rangle$ which also increases with decreasing ϵ. A priori, there is no need for a relation between the volume Ω_i and the local vibrational properties Y_i at a minimum. Therefore it is interesting to know how strongly Ω_i and Y_i are coupled. Suppose that the simple relation $\Omega_i = aY_i$ holds, with some constant a. In this case, we would recover $G(\epsilon)$ from the reweighted population of minima energies at $T=\infty$, i.e., $\langle Y^{-1}\delta(\epsilon' - \epsilon)\rangle_{T=\infty} \propto G(\epsilon')$. As shown in Fig. 3.6, this behavior is not present. Interestingly, the relation $\Omega_i = aY_i^2$ is quite well fulfilled, since the ϵ'-dependence of $\langle Y^{-2}\delta(\epsilon' - \epsilon)\rangle_{T=\infty}$ is similar to that of $G(\epsilon)$. - Whether this relation has a deeper origin in PEL structure is not clear to us.

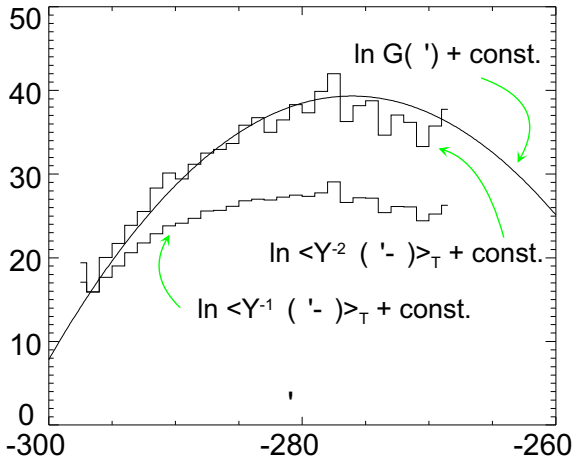

Figure 3.6: Distribution of minima energies in the BMLJ65, found at $T=\infty$, reweighted by Y_i and Y_i^2 (see text). Smooth line: $G(\epsilon')$.

Throughout the thesis, the number densities $G(\epsilon)$ and $G_{\text{eff}}(\epsilon)$ will serve as the basis for a statistical description of static PEL properties. It has to be checked in

every case which of either distribution must be used. Generally, if the vibrational part Y_i of the free energy is not explicitly considered, it is convenient to use $G_{\text{eff}}(\epsilon)$, since the weighting by $\langle Y|\epsilon\rangle_G$ is implicit,

$$p(\epsilon;T) \propto G_{\text{eff}}(\epsilon)e^{-\beta\epsilon} = G(\epsilon)\,\langle Y|\epsilon\rangle_G\, e^{-\beta\epsilon}.$$

It has to be noted that $G(\epsilon)$ and $G_{\text{eff}}(\epsilon)$ only count geometrically distinct minima. From every minimum, by interchanging particles of the same species, $N_A!N_B!$ configurations can be generated with exactly the same physical properties. It will turn out (section 3.2) that this multiplicity is in fact much larger than the number of different minima. If, for instance, $N = N_A + N_B = 52 + 13 = 65$, about $N_A!N_B! \approx 10^{77.7}$ permutations exist of one minimum, but only ca. 10^{22} different minima can be found. Although the BMLJ65 is a small system, we already have an astronomically large number of minima contributing to the partition function Eq. 3.1. Under such circumstances, it is clear that only statistical considerations of the PEL properties are sensible.

Since the number of minima is large but finite, $G(\epsilon)$ and $G_{\text{eff}}(\epsilon)$ cannot be exact gaussians. Below some minimum $\epsilon_{\min}$, no or at least negligibly few minima can be found, except for the crystalline states that lie far below $\epsilon_{\min}$ (Middleton et al., 2001). Moreover, deviations from a gaussian should be expected around $\epsilon_{\min}$, because there is no a priori reason that the few, highly optimized low-energetic states should be distributed according to the same law as the minima at high ϵ. For simplicity, however, we will model $G(\epsilon)$ and $G_{\text{eff}}(\epsilon)$ as gaussians with a cutoff, i.e.,

$$G(\epsilon) = \begin{cases} \frac{1}{I(\epsilon_{\min},0)} \frac{N_0}{\sqrt{2\pi\sigma^2}} \exp\left(-\frac{(\epsilon-\epsilon_0)^2}{2\sigma^2}\right) & \text{, if} \quad \epsilon > \epsilon_{\min} \\ 0 & \text{, if} \quad \epsilon < \epsilon_{\min} \end{cases} . \tag{3.10}$$

and analogously $G_{\text{eff}}(\epsilon)$. The integral $I(\epsilon_{\min}, 0)$, Eq. C.8, takes care of the proper normalization, $N_0 = \int \mathrm{d}\epsilon G(\epsilon)$. In the limit $\epsilon_{\min} = -\infty$, $I(\epsilon_{\min}, 0)$ is equal to unity, but even for a finite $\epsilon_{\min} < -300$, it can be neglected (e.g., $1 - I(\epsilon_{\min} = -302, 0) \approx 10^{-6}$).

Mean and variance of IS energies. Eq. 3.10 allows the calculation of the mean minimum energy $\langle\epsilon(T)\rangle$ and variance $\sigma^2(T) = \left\langle(\epsilon - \langle\epsilon\rangle)^2\right\rangle_T$, see Eq. C.13 and Eq. C.14. In the idealized case of a full gaussian, i.e. $\epsilon_{\min} = -\infty$, one gets the simple form $\langle\epsilon(T)\rangle = \epsilon_{0,\text{eff}} - \beta\sigma^2_{\text{eff}}$ and $\sigma^2(T) = \sigma^2_{\text{eff}} = \text{const}$. Corrections to these laws arise at low minima energies, where the end of the PEL, $\epsilon_{\min}$, is reached. Again, the cutoff energy $\epsilon_{\min} = -302$ seems to be in good agreement with the low-temperature values of $\langle\epsilon(T)\rangle$ and $\sigma^2(T)$ as seen from Fig. 3.7. However, as we have noted already in Fig. 3.2, the true PEL cutoff probably has a lower energy than

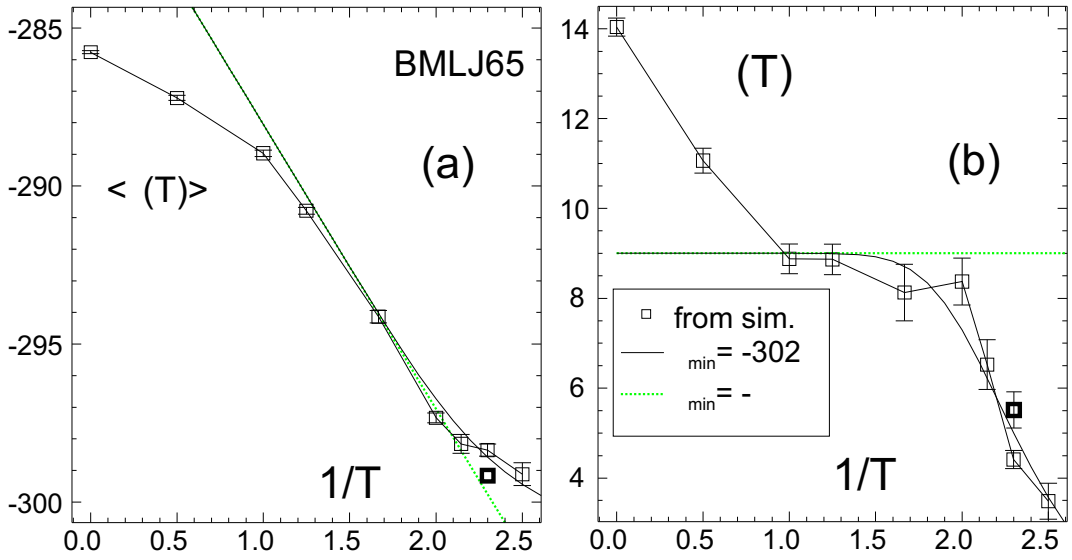

Figure 3.7: (a) Mean IS energy as a function of temperature (□). Predictions from gaussian $G_{\text{eff}}(\epsilon)$, with $\epsilon_{\min} = -\infty$ (dotted line) and $\epsilon_{\min} = -302$ (solid line). (b) Variance $\sigma^2(T) = \left\langle (\epsilon - \langle\epsilon\rangle)^2 | T \right\rangle$ of IS energies (□), again with the predictions from a gaussian distribution of ϵ. The deviations at temperatures $T < 0.5$ are probably due to insufficiently long simulation runs (for a thorough discussion see section 5.5). The fat squares at $T = 0.435$ ($1/T \approx 2.3$) have been calculated from a second run at this temperature which is six times longer. As can be seen, these data lie closer to the unrestricted gaussian prediction of $\epsilon_{\min} = -\infty$.

-302 in the BMLJ65. From the data presented here, we probably find a wrong, too high $\epsilon_{\min}$. The reason lies in insufficiently long simulation runs at temperatures $T < 0.5$. We will discuss in section 5.5 that this is less trivial than it might sound.

3.2 Total Number of Minima.

In this section, we would like to discuss three methods that allow the computation of N_0, the number of geometrically distinct minima. In general, it is not easy to get hold of N_0. As we have seen in the preceeding section, the distributions $p(\epsilon; T)$ of sampled minima permit the reconstruction of $G(\epsilon)$ up to the normalization constant. In order to obtain this constant, a more thorough sampling of the PEL is needed.

Lower Bound for N_0. A lower bound for N_0 can be given with the help of a simple reasoning. During a very long sampling of the PEL, some of the N_0 geometrically distinct minima will be found more than once. From the frequency of finding the same minima, then, one can deduce their total number. The probability of re-

visiting some minima is clearly largest for low temperatures, since there, low-lying minima are sampled, which are small in number. Let us therefore concentrate on the minima found below some $\hat{\epsilon}_1$. If the frequency of finding the same minimum below $\hat{\epsilon}_1$ is known, one can estimate the total number of minima below $\hat{\epsilon}_1$. In order to obtain uncorrelated configurations, we do not use a long, linear simulation run, but we proceed as follows. From a random configuration ($T = \infty$) of the BMLJ65 system, we initiate a simulation run at $T = 0.5$. Every 10^5 MD steps, minimization unveils the underlying minimum. Due to the low T, one observes the system descending within the PEL towards deeper and deeper minima. When a minimum of energy $\epsilon \in [\hat{\epsilon}_0, \hat{\epsilon}_1] = [-302, -300]$ is found, the run is stopped and the minimum is saved in a database. By repeated starts from uncorrelated configurations at $T = \infty$, we have found $n = 281$ minima $\epsilon \in [\hat{\epsilon}_0, \hat{\epsilon}_1]$ in a total simulation time of ca. 10^9 MD steps. Despite this enormous computational effort, no minimum has been found more than once. Thus, we are far from an exhaustive sampling of low-lying minima. This contrasts with an investigation of spin-glass inherent structures, where Crisanti and coworkers were able to estimate the configurational entropy (which is equivalent to the total number of inherent structures) by counting the frequency of sampling the same minimum (Crisanti et al., 2001). For the BMLJ65, seemingly, the number of minima is already too large to be susceptible to this method. Due to the slow dynamics at $T = 0.5$, a faster sampling of low-lying minima is not possible.

However, our negative result leads to a strong lower bound for N_0: Suppose that there is total of $\hat{N}$ minima in $[\hat{\epsilon}_0, \hat{\epsilon}_1]$. We have n times chosen one of the $\hat{N}$ minima, and have not found a minimum twice. The probability for this to happen is

$$P = \frac{\hat{N}(\hat{N}-1)...(\hat{N}-n+1)}{\hat{N}^n},$$

if all $\hat{N}$ minima are equally probable. Clearly, $\hat{N} \geq n$, but a much stronger statement about $\hat{N}$ is possible if we require that the probability P to find our result have some value substantially different from zero, say, a. Using Stirling's formula, this leads to

$$0 \leq \ln P - \ln a \approx (\hat{N} - n) \ln \left[\frac{\hat{N}}{\hat{N} - n} \right] - n - \ln a. \tag{3.11}$$

The smallest value of $\hat{N}$ satisfying Eq. 3.11 can be easily found numerically. For the parameters $[\hat{\epsilon}_0, \hat{\epsilon}_1] = [-302, -300]$, $n = 281$, and $a = 0.1$ we find $\hat{N} \geq 17241$. The dependence on the confidence level (1–a) is rather weak, e.g., $a = 0.001$ yields $\hat{N} \geq 5810$.

From the lower bound of $\hat{N}$, it is easy to find one for N_0. We have

$$\hat{N} = \int_{\hat{\epsilon}_0}^{\hat{\epsilon}_1} \mathrm{d}\epsilon G(\epsilon) = \frac{N_0}{\sqrt{2\pi\sigma^2}} \int_{\hat{\epsilon}_0}^{\hat{\epsilon}_1} \mathrm{d}\epsilon e^{-\frac{(\epsilon-\epsilon_0)^2}{2\sigma^2}} = \frac{N_0}{2} \left(\mathrm{erfc}(\hat{x}_1) - \mathrm{erfc}(\hat{x}_0)\right), \tag{3.12}$$

where

$$\hat{x}_0 = \frac{\epsilon_0 - \hat{\epsilon}_0}{\sqrt{2}\sigma}, \qquad \hat{x}_1 = \frac{\epsilon_0 - \hat{\epsilon}_1}{\sqrt{2}\sigma}.$$

With the above parameters ($a = 0.1$) this leads to

$$N_0 \geq \frac{2\hat{N}}{\mathrm{erfc}(\hat{x}_1) - \mathrm{erfc}(\hat{x}_0)} = 10^{19.2} \quad \text{(BMLJ65)}.$$

If we had the computer time to obtain more configurations in $[\hat{\epsilon}_0, \hat{\epsilon}_1]$, the lower bound would increase as long as minima are still found only once. For example, $n = 1000$ and $n = 10000$ would give $N_0 > 10^{20.3}$ and $N_0 > 10^{22.3}$, respectively.

Exhaustive Sampling Method. A very direct way of finding the number N_0 of minima will now be described. The starting point is the insight that knowledge of the mean basin volume $\langle\Omega\rangle_G$ is equivalent to knowing N_0; since the total volume of configurational space V^N is known, we have[2] $N_0 N_A! N_B! = V^N / \langle\Omega\rangle_G$. The mean basin volume, in turn, follows from the mean volume of energy shells within basins, i.e.,

$$\langle\Omega\rangle_G = \int \mathrm{d}\zeta \, \langle\Omega(\zeta)\rangle \,, \tag{3.13}$$

where $\zeta(x) \equiv V(x) - V(\xi(x))$ is the energy elevation with respect to the ground of the instantaneous basin[3] and

$$\langle\Omega(\zeta)\rangle = \frac{1}{N_0 N_A! N_B!} \int_{\Omega_{\mathrm{conf}}} \mathrm{d}x \delta(\zeta(x) - \zeta).$$

Up to now, these are trivial relations, and the choice of $\zeta(x)$ is in no way unique. However, the advantage of $\zeta(x)$ as the relevant parameter is that the limit of $\langle\Omega(\zeta)\rangle$ for small elevations $\zeta \to 0$ is known since one deals with small vibrations around

[2]The contribution from the crystalline structures is assumed to be small, since they are by far less numerous than the amorphous packings. The fraction of V^N consisting of crystalline basins is given by the probability that by minimizing a random configuration in V^N, one ends up in a crystalline minimum. In our simulations, this has never happened within more than 10^4 quenches. Thus, the fraction of crystalline configurations is much less than 10^{-4}.

[3]not to be confused with the friction coefficient ζ of chapter 2 or the transition state ζ of chapter 5

minima. In other words, the limit of $\zeta \to 0$ can be recovered within harmonic approximation ($V(x) - V(\xi(x)) = \sum_{\nu=1}^{Nd-d} \frac{1}{2}\lambda_\nu x_\nu^2$),

$$\langle \Omega(\zeta) \rangle \to \left\langle \int_{\mathbb{R}^{Nd-d}} \mathrm{d}x \delta \left(\sum_{\nu=1}^{Nd-d} \frac{1}{2}\lambda_\nu x_\nu^2 - \zeta \right) \right\rangle, \quad \zeta \to 0$$

For a given basin i, the integral can be evaluated,

$$\begin{aligned}
&\int_{\mathbb{R}^{Nd-d}} \mathrm{d}x \delta \left(\sum_{\nu=1}^{Nd-d} \frac{1}{2}\lambda_{i,\nu} x_\nu^2 - \zeta \right) = \\
&= \prod_\nu \left(\frac{2}{\lambda_{i,\nu}} \right)^{1/2} \int \mathrm{d}x \delta(x^2 - \zeta) = \prod_\nu \left(\frac{2}{\lambda_{i,\nu}} \right)^{1/2} S_{Nd-d} \int_0^\infty \mathrm{d}r r^{Nd-d-1} \frac{\delta(r - \zeta^{1/2})}{2r} \\
&= \prod_\nu \left(\frac{2\pi}{\lambda_{i,\nu}} \right)^{1/2} \frac{1}{\Gamma(\frac{Nd-d}{2})} \zeta^{(Nd-d-2)/2} = \frac{Y_i \zeta^{(Nd-d-2)/2}}{\Gamma(\frac{Nd-d}{2})},
\end{aligned}$$

where the expression for the surface of the $(Nd-d)$-dimensional unit sphere was used,

$$S_{Nd-d} = \frac{2\pi^{(Nd-d)/2}}{\Gamma(\frac{Nd-d}{2})}.$$

Hence, for small arguments, $\Omega(\zeta)$ is solely determined by the mean vibrational partition function,

$$\langle \Omega(\zeta) \rangle \to \frac{\langle Y \rangle_G \zeta^{(Nd-d-2)/2}}{\Gamma(\frac{Nd-d}{2})}, \quad \zeta \to 0 \tag{3.14}$$

This is the crucial point of the method, since the function $\langle \Omega(\zeta) \rangle$ can be specified from simulations only up to an overall multiplicative constant.

The main numeric task now is to compute $\langle \Omega(\zeta) \rangle$ from runs at different temperatures. Again, as for $G(\epsilon)$, the idea is to sample ζ in overlapping windows and to construct $\langle \Omega(\zeta) \rangle$ by matching the reweighted histograms by appropriate vertical shifts, i.e.,

$$\ln \langle \Omega(\zeta) \rangle = \ln p(\zeta; T) + \beta\zeta + \text{const.} \tag{3.15}$$

Note that this reweighting requires a special kind of configurational sampling, namely

$$p(\zeta; T) \propto \int \mathrm{d}x \delta(\zeta(x) - \zeta) \exp\left(-\beta\zeta(x)\right) \neq \int \mathrm{d}x \delta(\zeta(x) - \zeta) \exp\left(-\beta V(x)\right). \tag{3.16}$$

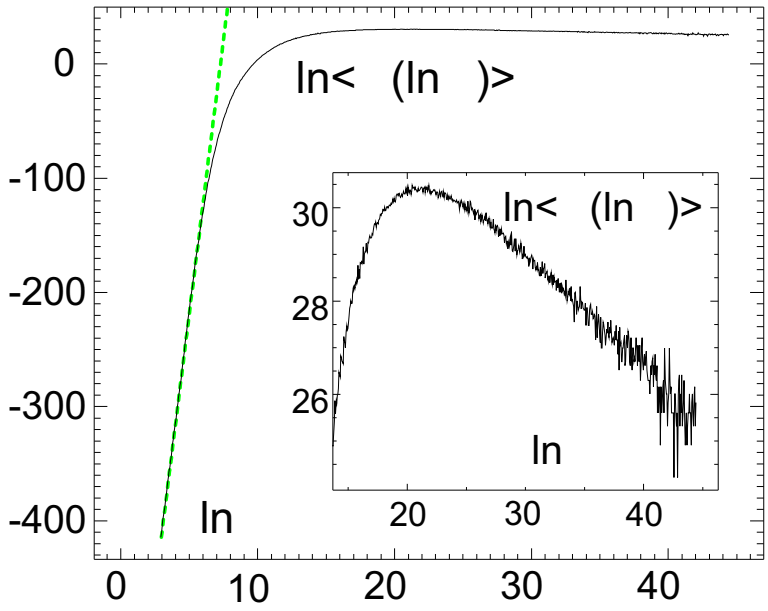

Figure 3.8: The volume on the energy shell ζ, averaged over basins, for the BMLJ65 system. The function is constructed by matching reweighted histograms in overlapping windows ($T = 0.30$, 0.40, 0.45, 0.50, 0.60, 0.80, 1, 1.5, 2, 3, 4, 5, 10, 15, 20, 40, 50, 70, 100, 400, 1000, 4000, 10000, 100000, 1000000, and $T = \infty$). Overall normalization is provided by the behavior for small ζ (dashed line), i.e. $\ln \langle \Omega(\ln \zeta) \rangle = \ln \langle Y \rangle_G - \ln \Gamma(\frac{Nd-d}{2}) + \frac{Nd-d}{2} \ln \zeta$, see Eq. 3.14. Note the relation $\langle \Omega(\ln \zeta) \rangle = \zeta \langle \Omega(\zeta) \rangle$. Inset: Magnification of the maximum of $\langle \Omega(\ln \zeta) \rangle$, which is entirely covered by the $T = \infty$ run.

The sampling becomes trivial at high temperatures where $\zeta(x) \approx V(x)$ (e.g., $T \geq T_{\text{trivial}} = 1000$, where $\langle V(x) - \zeta(x) \rangle / \langle V(x) \rangle < 2\%$), i.e., the energy of minima is negligible as compared to $V(x)$. In this regime, it suffices to use ordinary MD simulation, and record potential energies. At low T, a different strategy must be used to obtain $p(\zeta; T)$. We apply Metropolis dynamics with the elevation 'potential' $\zeta(x)$, where frequent minimizations ensure to have the correct $\zeta(x)$. If minimizations are too scarce, many Metropolis steps rely on a wrong $V(\xi(x))$, resulting in questionable distributions $p(\zeta; T)$. Minimization every thousand for the lowest, and every ten Metropolis steps for the highest temperatures turned out to be sensible.

If, finally, the distributions $p(\zeta; T)$ have been calculated for sufficiently many temperatures, reweighted and matched according to Eq. 3.15, and the resulting master curve has been normalized with the help of Eq. 3.14, only the integral of Eq. 3.13 remains to be performed. As seen from Fig. 3.8 for the BMLJ65 system, a broad maximum at very high energies is the relevant part of the integral. For this

example, the result is $\langle\Omega\rangle = 10^{14.2\pm1.1}$, which, with $V^N = 10^{112.6}$, leads to[4]

$$N_0 = \frac{V^N}{N_A!N_B!\,\langle\Omega\rangle_G} = 10^{20.7\pm1.1}. \tag{3.17}$$

The minimum requirement $N_0 > 1$ is thus fulfilled. Very interestingly, the present value of N_0 is only slightly larger than the lower bound of $10^{19.2}$, which, by a completely different argument, has been derived at the beginning of this section. There we have found that in the interval $\epsilon \in [-302, -300]$, there are more than 10^4 minima. From Eqs. 3.12 and 3.17, we find this number to be ca. 5×10^5.

Finally, the growth parameter (Stillinger, 1999; Wallace, 1997), is calculated to be

$$\alpha = N^{-1} \ln N_0 = 0.73 \pm 0.04 \qquad \text{(BMLJ65)}. \tag{3.18}$$

Comparison with Thermodynamic Integration. A different approach to the calculation of N_0 has recently been discussed in the literature (Sciortino et al., 1999; Mossa et al., 2002; Sastry, 2001; Scala et al., 2000; Sastry, 2000). The main

[4]The error results from the statistical error in the distributions $p(\ln\zeta;T)$. In every step of reweighting and matching the overlapping parts of $\ln\Omega(\ln\zeta)$, the uncertainty of the maximum of $\Omega(\ln\zeta)$ increases. Consider the distributions $p(\ln\zeta;T)$ and $p(\ln\zeta;T')$ at two nearby temperatures. Assume that the corresponding histograms overlap by M bins. In the limit of infinitely long sampling, we would recover the true distributions above, or, equivalently, the probabilities p_i and p'_i in the bin at ζ_i, $i = 1, ...M$. Due to the finite simulation time, our estimates $\tilde{p}_i = n_i/n$ and $\tilde{p}'_i = n'_i/n'$ exhibit some statistical error, i.e.

$$\tilde{p}_i = p_i + \delta_i, \qquad \tilde{p}'_i = p'_i + \delta'_i$$

(noisy quantities aquire the tilde). Here n_i is the number of counts in bin i and $n = \sum_{i=1}^{M} n_i$. On average, the statistical noise has the strength $\overline{\delta_i^2} = p_i(1-p_i)/n \approx \tilde{p}_i/n$ and $\overline{\delta_i'^2} \approx \tilde{p}'_i/n'$, assuming an underlying poissonian distribution of events. Assuming further that n is large enough to have $\sqrt{\overline{\delta_i^2}} \ll p_i$, we can approximate $\ln\tilde{p}_i + \beta\zeta_i \approx l_i + \Delta_i$, where $l_i \equiv \ln p_i + \beta\zeta_i$ and $\Delta_i \equiv \delta_i/\tilde{p}_i$ (analogously the primed quantities). Matching l_i and l'_i is achieved by estimating the vertical shift $v = l_i - l'_i$ from the noisy $\tilde{l}_i$'s,

$$\tilde{v} = \frac{1}{M}\sum_{i=1}^{M}(\tilde{l}_i - \tilde{l}'_i),$$

which for $\Delta_i \to 0$ coincides with v. What is the uncertainty in the estimator $\tilde{v}$? A simple calculation, involving uncorrelated Δ_i, Δ'_j, yields

$$\mathrm{Var}(\tilde{v}) = \overline{\tilde{v}^2 - v^2} = \frac{1}{M^2}\sum_i(\overline{\Delta_i^2} + \overline{\Delta_i'^2}) = \frac{1}{M^2}\sum_i(1/n_i + 1/n'_i),$$

where we have used $\overline{\Delta_i^2} \approx 1/n\tilde{p}_i = 1/n_i$. Each time such two overlapping histograms are matched, the overall error in the curve increases by the amount $\sqrt{\mathrm{Var}(\tilde{v})}$.

step is to compute the partition function $Z(T)$ or, equivalently, the entropy via thermodynamic integration from a known reference state. Equipped with $Z(T)$, one can invert Eq. 3.7 to find the number density of minima,

$$\ln G(\epsilon) = \ln p(\epsilon; T) + \beta\epsilon - \ln \langle Y|\epsilon\rangle_G + \ln Z(T) - \frac{Nd-d}{2} \ln T, \tag{3.19}$$

where we work within the harmonic approximation. This fixes the total number of minima, since $N_0 = \int \mathrm{d}\epsilon G(\epsilon)$. In the above-cited works, starting from a high-temperature (T_0), low-density (N/V_0) state, one compressed the system until the required volume V_1 of the supercooled liquid was reached. Subsequently, one cooled along the isochore down to $T = T_1$. The procedure is depicted in Fig. 3.9. The partition function at the state point (V_1, T_1) follows with the help of the relations

$$\left(\frac{\partial \ln Z}{\partial V}\right)_T = \beta p(V,T), \quad \text{and} \quad \left(\frac{\partial \ln Z}{\partial \beta}\right)_V = -E(V,T),$$

$$\ln Z(V_1,T_1) = \ln Z(V_0,T_0) + \beta_0 \int_{V_0}^{V_1} \mathrm{d}V p(V,T_0) - \int_{\beta_0}^{\beta_1} \mathrm{d}\beta E(V_1,T). \tag{3.20}$$

Note that we write $E(V,T)$ instead of $\langle V(x)\rangle$ for potential energy here, in order to avoid confusion with volume.

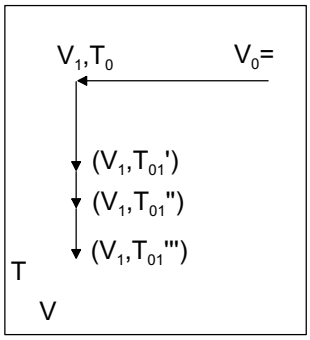

Figure 3.9: Thermodynamic integration path, circumventing the liquid/gas first-order transition.

We start with the evaluation of the first integral. Measuring pressure in a computer simulation is most easily done with the help of the Clausius virial function (Hansen and McDonald, 1990),

$$\mathcal{P}_{\text{ex}} = \frac{1}{Vd} \sum_i \boldsymbol{x}_i \cdot \boldsymbol{F}_i,$$

where $\boldsymbol{F}_i$ is the sum of interparticle forces acting on particle i. $\mathcal{P}_{\text{ex}}$ specifies the excess pressure over the ideal gas, so we have

$$p = \frac{Nk_{\text{B}}T}{V} + \langle \mathcal{P}_{\text{ex}} \rangle .$$

The expression for $\mathcal{P}_{\text{ex}}$ can be cast into a more convenient form, using the interparticle distances and forces,

$$\mathcal{P}_{\text{ex}} = \frac{1}{Vd} \sum_{i<j} \boldsymbol{x}_{ij} \cdot \mathbf{F}_{ij}.$$

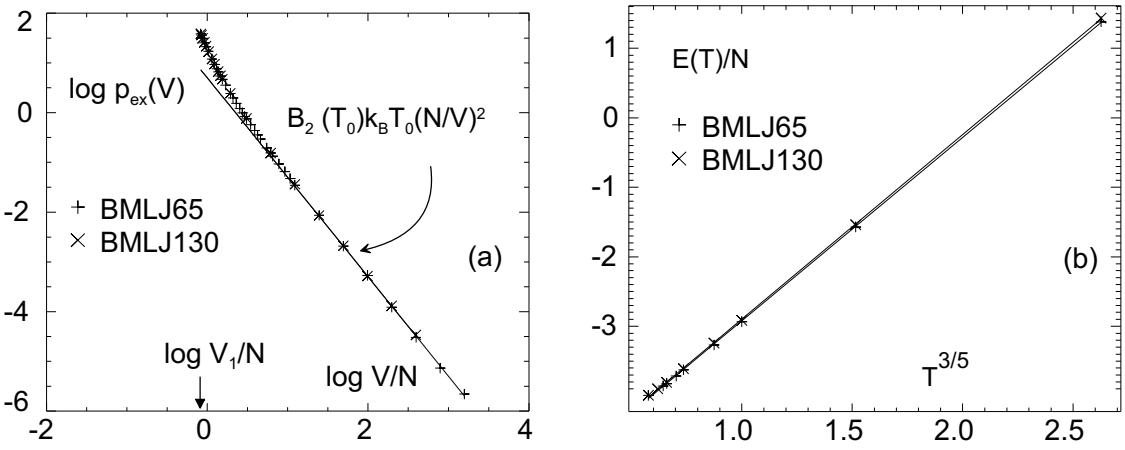

Figure 3.10: Simulation data for the thermodynamic integration in Eq. 3.20. (a) Excess pressure $p_{\rm ex} = p - Nk_{\rm B}T/V$ over V/N in a double-logarithmic plot. The straight line corresponds to the first correction to ideal-gas behavior, described by the second virial coefficient $B_2(T)$. (b) Temperature dependence of the mean potential energy $E(T)/N \equiv \langle V(x)\rangle /N$. Lines are fits of the form $E(T) = a + bT^{3/5}$. Note that the data of BMLJ65 and BMLJ130 practically coincide.

In Fig. 3.10a, $p(V, T_0)$ is shown for the BMLJ65 and the BMLJ130 system as a function of V/N. They are identical, as expected when finite-size effects are absent. In the limit of small density or large volume, we may use the virial expansion ($p_{\rm ex} = \langle \mathcal{P}_{\rm ex}\rangle$),

$$\frac{\beta p_{\rm ex}}{\rho} = \sum_{i=2}^{\infty} B_i(T)\rho^{i-1},$$

to find the volume dependence of $p(V, T)$. We see from the figure that towards high volume, $p_{\rm ex}(V, T_0)$ approaches quickly the term $B_2(T_0)k_{\rm B}T_0\left(\frac{N}{V}\right)^2$, which is the first correction to the ideal-gas behavior. The second virial coefficient $B_2(T_0)$ can be calculated from the two-particle potential, which, for the present Lennard-Jones mixture, is $B_2(T_0) = 1.0038$. For the identical BMLJ system, yet different cutoff procedure, a significantly smaller value of 0.53 has been found (Sciortino et al., 1999). From the data for $p_{\rm ex}(V, T_0)$, we can now calculate the partition function at the point (V_1, T_0). We obtain

$$\begin{aligned} \ln Z(V_1, T_0) &= -108.3 \pm 0.7 \qquad \text{(BMLJ65)}, \\ \ln Z(V_1, T_0) &= -218.5 \pm 2.5 \qquad \text{(BMLJ130)}. \end{aligned} \tag{3.21}$$

The factor of two between these figures is in agreement with an extensive scaling of free energy, already at these small system sizes.

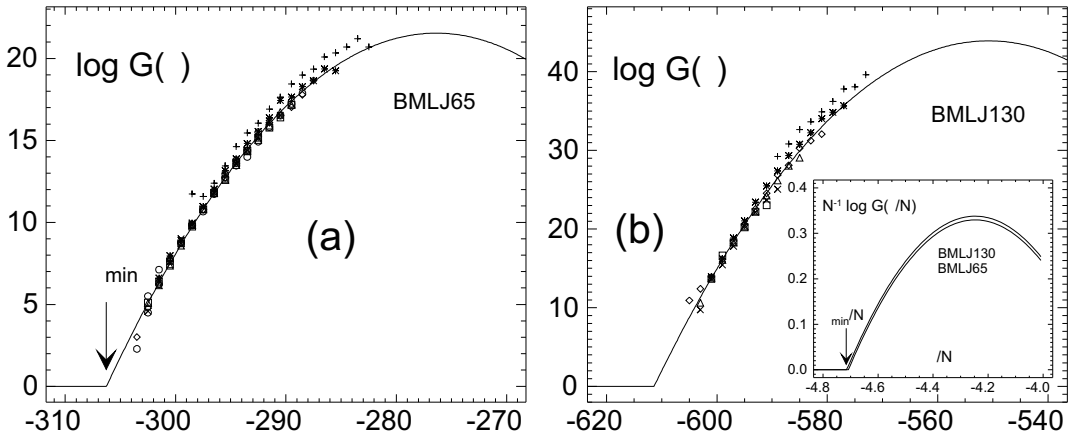

Figure 3.11: Number density of minima $G(\epsilon)$, computed via Eq. 3.24 from simulation runs (a) of the BMLJ65 at $T = 0.4, 0.435, 0.45, 0.466, 0.48, 0.5$, and 0.6. At $\epsilon_{\min} \approx -306$, the gaussian description breaks down. (b) Number density of minima of the BMLJ130, computed from $T = 0.4, 0.435, 0.45, 0.5$, and 0.6. In (a) and (b), data for $T \geq 0.8$ (+) do not fall onto the master curve. Inset: Number density of minima of BMLJ65 and BMLJ130, on a per-particle basis.

We will now consider the second integral of Eq. 3.20. Here, we need the mean potential energy $E(V,T)$ along the isochore $V = V_1$. In the literature, by means of classical density functional theory, it was concluded that the temperature dependence of $E(V,T)$ should be described by $a + bT^{3/5}$ for a large family of simple liquids (Rosenfeld and Tarazona, 1998). This functional form has indeed proved very successful in describing the numerical data on $E(V,T)$, see the above cited literature. The present case is no exception, as demonstrated in Fig. 3.10b. Although for $T < 1$ a linear law works well, too, it is not able to cover the whole temperature range up to $T_0 = 5$. From the two fit parameters a and b, we can calculate the second integral in Eq. 3.20,

$$\begin{aligned} &\int_{\beta_0}^{\beta_1} \mathrm{d}\beta (a + b\beta^{-3/5}) = a(\beta_1 - \beta_0) + \frac{5}{2} b \left(\beta_1^{2/5} - \beta_0^{2/5} \right), \\ &a = -361.4 \pm 0.3, \quad b = 171.5 \pm 0.3 \qquad \text{(BMLJ65)}, \\ &a = -718.8 \pm 0.8, \quad b = 341.2 \pm 0.9 \qquad \text{(BMLJ130)}. \end{aligned} \tag{3.22}$$

After Eq. 3.1, the partition function (the configurational part) of the ideal gas is $Z_{\mathrm{IG}} = N \ln V - \ln N_A! - \ln N_B!$. In the limit $V_0 \to \infty$, we may replace $\ln Z(V_0, T_0)$

in Eq. 3.20 by the ideal gas term, so we finally find

$$\ln Z(V_1, T_1) = N \ln V_1 - \ln N_A! - \ln N_B! + \\ + \beta_0 \int_{V_0}^{V_1} \mathrm{d}V \mathcal{P}_{\mathrm{ex}}(V, T_0) - a(\beta_1 - \beta_0) - \frac{5}{2} b \left(\beta_1^{2/5} - \beta_0^{2/5} \right). \tag{3.23}$$

We now use these results to calculate N_0. Instead of using Eq. 3.19 directly, we work with the reweighted distribution function (compare Eq. 3.9),

$$\ln G(\epsilon') = \ln \left\langle \delta(\epsilon' - \epsilon) Y^{-1} e^{\beta\epsilon} \right\rangle_T + \ln \tilde{Z}(T). \tag{3.24}$$

In contrast to section 3.1, we now have in hands the normalization factor. The expectation value in Eq. 3.24 can be computed via regular simulations and $\tilde{Z}(T) = T^{-(Nd-d)/2} Z(T)$. Thus, for temperatures where the harmonic approximation holds, we are able to calculate the absolute value of $G(\epsilon)$. For the BMLJ65 and BMLJ130 systems, $G(\epsilon)$ is shown in Fig. 3.11(a) and (b), respectively. At temperatures $T \leq 0.6$, all reweighted distributions fall nicely onto a master curve, whereas for $T \geq 0.8$ the normalization does not work anymore due to anharmonic effects, see reference (Sastry, 2000). Note that the section of $T = 0.8$ would fit well to the master curve if vertical shifting was allowed. We now fit gaussians to the data at $T \leq 0.6$, yielding the complete $G(\epsilon)$. The number of minima can then be calculated from $N_0 = \max G(\epsilon) \sqrt{2\pi\sigma^2}$. We obtain[5]

$$\begin{aligned} N_0 &= 10^{22.4 \pm 0.8} \qquad \text{(BMLJ65)}, \\ N_0 &= 10^{45.0 \pm 2.5} \qquad \text{(BMLJ130)}. \end{aligned} \tag{3.25}$$

The result for the BMLJ65 agrees within error bars with $N_0 = 10^{20.7 \pm 1.1}$ as produced by the Exhaustive Sampling Method above. In our opinion, this is quite reassuring, since the calculation of N_0 was carried out in two completely different ways.

Within error bars, the number of distinct minima in the BMLJ130 system is just the square of the BMLJ65 number of distinct minima. This quantity therefore displays the trivial scaling with system size expected from combinations of non-interacting subsystems. Once again, these results corroborate our statement that the BMLJ65 exhibits to a great extend the bulk properties of a BMLJ system, i.e. it is free of major finite-size effects. Finally, we find for the growth parameter $\alpha = N^{-1} \ln N_0$,

$$\begin{aligned} \alpha &= 0.79 \pm 0.03, \qquad \text{(BMLJ65)} \\ \alpha &= 0.80 \pm 0.04, \qquad \text{(BMLJ130)}. \end{aligned} \tag{3.26}$$

[5]The errors from Eq. 3.21 and Eq. 3.22 accumulate to ca. 1.8 (BMLJ65) and 5.7 (BMLJ130). Devision by $\ln 10$ then yields the errors in Eq. 3.25.

3.3 Configurational Entropy.

The perfect crystal has no remaining structural disorder except for the vibrations of atoms around the lattice positions. In the PEL language this means only the basin of the crystalline minimum is populated.[6] Clearly, the supercooled liquid has a higher degree of structural disorder. Yet, from the preceeding analysis of minima population, we know that the set of accessible minima shrinks tremendously upon decreasing temperature. Starting from the definition of Shannon entropy (appendix C.2), configurational and vibrational parts of the entropy may be separated by use of the basin populations $p_i(T)$ and the distribution $p(x|i;T)$ of vibrations in a basin i,

$$\begin{aligned} S &= -\int_{\Omega} \mathrm{d}x p(x) \ln\left[p(x)u\right] \\ &= -\sum_i \int_{\Omega_i} \mathrm{d}x p(x,i) \ln\left[p(x,i)u\right] = -\sum_i \int_{\Omega_i} \mathrm{d}x p_i p(x|i) \ln\left[p_i p(x|i)u\right] \\ &= -\sum_i p_i \ln p_i - \sum_i p_i \int_{\Omega_i} \mathrm{d}x p(x|i) \ln\left[p(x|i)u\right] \equiv S_c + S_{\mathrm{vib}}. \end{aligned} \tag{3.27}$$

Note that the reference volume, u, appears in both S and S_{vib}, whereas the configurational entropy is free of this arbitrariness. The fact that $S_c(T)$ is well defined is indispensable for the check of the Adam-Gibbs equation, see below.

Calculating $S_c(T)$ directly via thermodynamic integration. In the last section, we obtained the partition function from thermodynamic integration. Thus, the total entropy can be computed with the help of the relation

$$S(T) = \frac{1}{T}(E(T) - F(T)) = k_{\mathrm{B}}(\beta E(T) + \ln Z(T)), \tag{3.28}$$

where $E(T)$ is the average potential energy and $F(T)$ is the free energy at temperature T. We now only need to know $\langle S_{\mathrm{vib}}(T)\rangle$. In harmonic approximation, the vibrational entropy of a given basin i is (compare Eqs. C.1 and 3.3)

$$S_{\mathrm{vib},i} = \frac{(Nd-d)k_{\mathrm{B}}}{2} + \frac{1}{2}\sum_\nu \ln\left(\frac{2\pi k_{\mathrm{B}}T}{\lambda_{\nu,i}}\right) = \frac{(Nd-d)k_{\mathrm{B}}}{2}(1 + \ln k_{\mathrm{B}}T) + \ln Y_i, \tag{3.29}$$

where ν runs over all $3N-3$ non-zero eigenvalues of the Hessian matrix in the minimum. As we have seen in the last section, this is a good approximation below $T = 0.8$. In order to estimate $S_{\mathrm{vib}}(T)$ (by averaging Eq. 3.29 over all minima),

[6] Of course, due to particles permutations, there exist $N_A!N_B!$ such minima in configuration space.

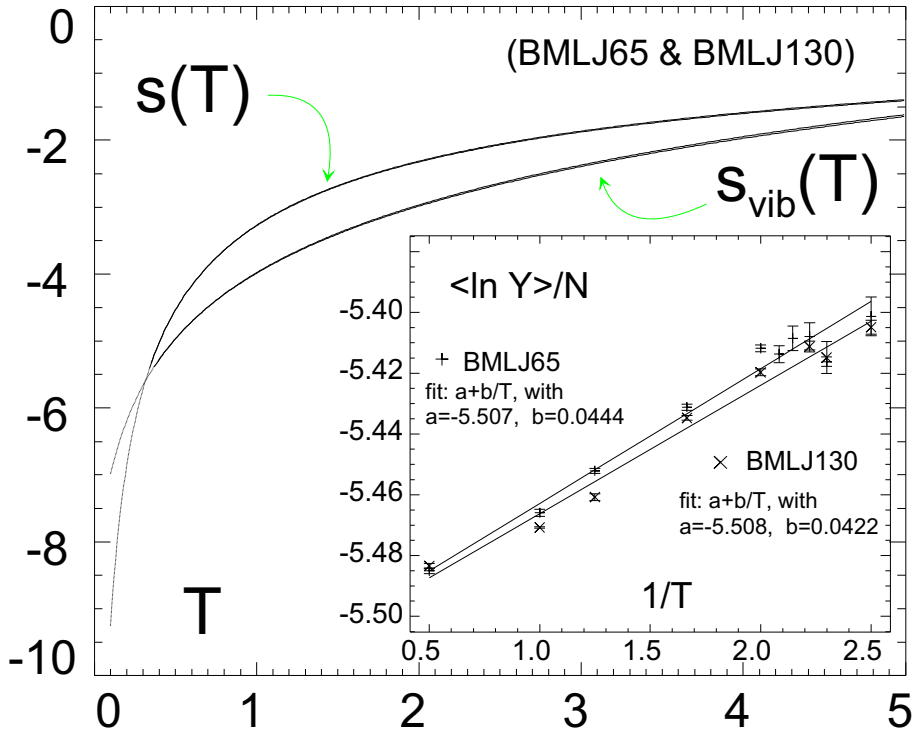

Figure 3.12: Total entropy per particle $s(T) = S(T)/N$ and vibrational entropy in harmonic approximation, $s_{\rm vib}(T) = S_{\rm vib}(T)/N$. Data for $N = 65$ and $N = 130$ are shown, they are nearly identical. Inset: $\langle \ln Y|T\rangle = s_{\rm vib}(T) - \frac{Nd-d}{2N}(1 + \ln k_{\rm B}T)$ versus $1/T$ for $N = 65$ and $N = 130$. When plotted versus $1/T$, data can be fitted by linear functions, parameters are given in the figure.

we have to compute $\langle \ln Y(T)\rangle$ from the simulation. Results for the BMLJ65 and BMLJ130 systems are shown in the inset of Fig. 3.12. For convenience, we plot this quantity versus $1/T$, where data is nearly linear over the present temperature range. From the fits plus the first term in Eq. 3.29, we compute $S_{\rm vib}(T)$. In Fig. 3.12, we show $s(T) \equiv S(T)/N$ and $s_{\rm vib}(T) \equiv S_{\rm vib}(T)/N$ for the BMLJ65 and BMLJ130 systems. The fact that the entropies are less than zero is not a problem, since, as said above, these entropies can only be specified up to a constant, the unit volume u. As can be seen, the temperature dependence of $s_{\rm vib}(T)$ is dominated by $(1+\ln k_{\rm B}T)$, so that the relatively low accuracy of the fits to $\langle \ln Y\rangle$ is not troublesome. From the difference $s(T) - s_{\rm vib}(T)$, we obtain the configurational entropy, see Fig. 3.14, curve (i) (curves (ii)-(iv) will be discussed in the next paragraph). The configurational entropies of the BMLJ65 and BMLJ130 are practically identical. They vanish at the 'Kauzmann temperature' $T_{\rm K} \approx 0.3$ in conformance with the analysis of Sastry (Sastry, 2000) and Sciortino et al. (Sciortino et al., 1999) for the standard BMLJ system. Above $T \approx 1.35$, $S_c(i)$ drops again, similarly to the behavior found

by Sciortino and coworkers (Sciortino et al., 1999). This is caused by the breakdown of the harmonic approximation for S_{vib}, because we know that S_c should increase monotonously in the BMLJ: The population of minima at $T = \infty$ (see Fig. 3.4) is still located left of the maximum of $G(\epsilon)$, so that a decrease of $S_c(T)$ with increasing T is not possible.

Calculation of $S_c(T)$ from $G(\epsilon)$. One may partly circumvent the limitation of the harmonic approximation by the use of $G(\epsilon)$, obtained in the last section, in conjunction with the distribution $p(\epsilon; T)$, taken *directly* from the simulation.

In the literature, we find the expression, $S_c(T) = \int \mathrm{d}\epsilon p(\epsilon; T) \ln G(\epsilon)$, for the configurational entropy ((Sastry, 2001), adapted to our notation). It is however incomplete. This can be seen by a simple argument[7]: Assume that $G(\epsilon)$ is constant and that the distribution $p(\epsilon; T)$ becomes more and more concentrated around some ϵ_0 upon cooling. As the consequence, $S_c(T)$ should decrease, though this is not reflected in the above formula, which yields a constant $S_c(T)$. Instead, the correct formula would be $S_c(T) = \int \mathrm{d}\epsilon p(\epsilon; T) \ln(G(\epsilon)/p(\epsilon; T))$, if no other parameters (like Y) are involved.

In what follows, we give a detailed derivation of $S_c(T)$ in terms PEL parameters. With Eq. 3.4, we write

$$\begin{aligned} S_c &= -\sum p_i \ln p_i \\ &\approx -\int \mathrm{d}\epsilon \int \mathrm{d}Y \sum_i \delta(\epsilon - \epsilon_i)\delta(Y - Y_i) p_i \ln\left(\frac{Y e^{-\beta\epsilon}}{\tilde{Z}(T)}\right) \\ &= \int \mathrm{d}\epsilon \int \mathrm{d}Y\, p(\epsilon, Y; T) \ln\left(\frac{G(\epsilon, Y)}{p_{\text{harm}}(\epsilon, Y; T)}\right), \end{aligned} \tag{3.30}$$

where $G(\epsilon, Y)$ is the number density of minima with properties ϵ, Y. In the step from the first to the second line, we made use of the harmonic approximation, Eq. 3.4, for the *second* p_i, and introduced integrals over delta functions. To arrive at the third line, we used $p(\epsilon, Y; T) = \sum_i \delta(\epsilon - \epsilon_i)\delta(Y - Y_i)p_i$ and the trivial relation

$$p_{\text{harm}}(\epsilon, Y; T) \equiv \sum_i \delta(\epsilon - \epsilon_i)\delta(Y - Y_i)\frac{Y_i e^{-\beta\epsilon_i}}{\tilde{Z}(T)} = \frac{Y e^{-\beta\epsilon}}{\tilde{Z}(T)} G(\epsilon, Y).$$

'Configurational disorder' thus results from the distribution over both energies ϵ and vibrational partition functions Y.

Clearly, the expression for $S_c(T)$, Eq. 3.30, is not very convenient. From section 3.1, we know that $G(\epsilon)$ has a strong dependence on ϵ. We therefore separate

[7] Even more simple would be to check the units: Since $G(\epsilon)$ is one over energy, we cannot take the logarithm without compensation.

the disorder within ϵ from the disorder within Y. We write

$$G(\epsilon, Y) = G(Y|\epsilon)G(\epsilon)$$

and

$$p_{\text{harm}}(\epsilon, Y; T) = p(Y|\epsilon)p_{\text{harm}}(\epsilon; T),$$

where

$$\int \mathrm{d}Y G(Y|\epsilon) = 1$$

and

$$p_{\text{harm}}(Y|\epsilon) = \frac{YG(Y|\epsilon)}{\int \mathrm{d}Y Y G(Y|\epsilon)}.$$

Thus,

$$\begin{aligned} S_c &= \int \mathrm{d}\epsilon p(\epsilon; T) \ln\left(\frac{G(\epsilon)}{p_{\text{harm}}(\epsilon; T)}\right) + \int \mathrm{d}\epsilon \mathrm{d}Y p(\epsilon, Y; T) \ln\left(\frac{G(Y|\epsilon)}{p(Y|\epsilon)}\right) \\ &\approx \int \mathrm{d}\epsilon p(\epsilon; T) \ln\left(\frac{G(\epsilon)}{p(\epsilon; T)}\right) + \int \mathrm{d}\epsilon p(\epsilon; T) \ln \int \mathrm{d}Y Y G(Y|\epsilon) - \int \mathrm{d}\epsilon \mathrm{d}Y p(\epsilon, Y; T) \ln Y \\ &= \int \mathrm{d}\epsilon p(\epsilon; T) \ln\left(\frac{G(\epsilon)}{p(\epsilon; T)}\right) + \int \mathrm{d}\epsilon p(\epsilon; T) \left(\ln \left\langle Y^{-1}|\epsilon\right\rangle_T - \left\langle \ln Y^{-1}|\epsilon\right\rangle_T\right) \\ &\equiv S_c^{(1)} + S_c^{(2)}, \end{aligned} \tag{3.31}$$

where $\langle Y|\epsilon\rangle_G = 1/\langle Y^{-1}|\epsilon\rangle_T$ has been used.

The first term of $S_c(T)$ is the disorder with regard to the property 'ϵ', whereas the remaining disorder, due to the variation of Y, has been incorporated into the second term. The advantage of this representation is that anharmonicities are partly accounted for by $p(\epsilon; T)$.

Essentially, $S_c^{(2)}(T)$ is the mean width[8] of the distributions $p(\ln Y|\epsilon; T)$. Clearly, if all Y's at constant ϵ were equal, $S_c^{(2)}(T)$ would vanish. A comparison of $\ln\langle Y^{-1}|\epsilon\rangle_T$ with $\langle \ln Y^{-1}|\epsilon\rangle_T$ is given in Fig. 3.13. As can be seen, the integrand of $S_c^{(2)}(T)$ is constant, and we find[9] $S_c^{(2)}(T) = 1.9 \pm 0.3$. It is only a minor correction to the first term, $S_c^{(1)}(T)$, as we will see.

[8] If $p(\ln Y|\epsilon; T)$ is gaussian with mean $\ln Y_0$ and width s, one calculates

$$\ln\langle Y|\epsilon\rangle_G = -\ln\langle Y^{-1}|\epsilon\rangle_T = \ln Y_0 - \frac{1}{2}s^2 = \langle \ln Y|\epsilon\rangle_T - \frac{1}{2}s^2.$$

[9] error estimated

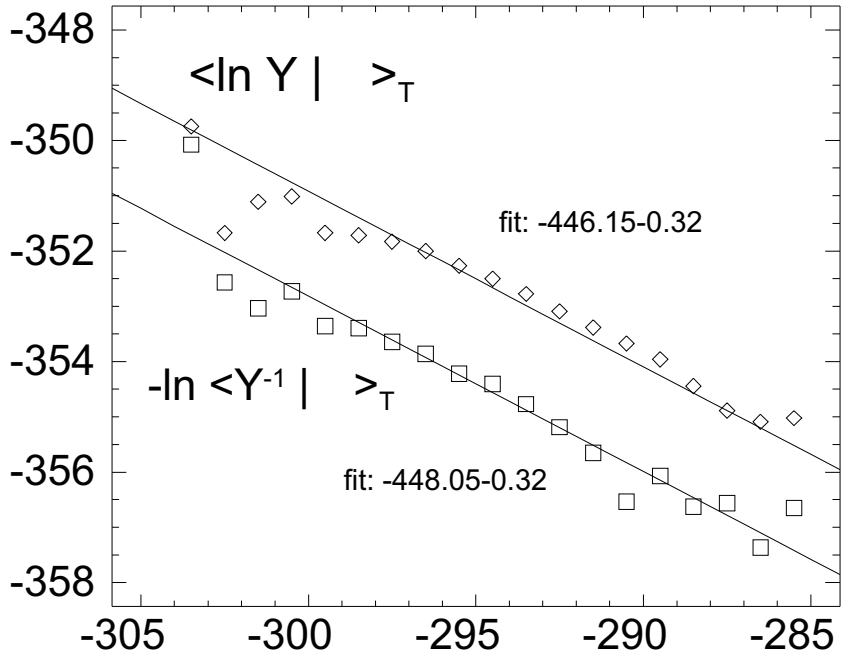

Figure 3.13: Comparison of two different averages of the vibrational partition function. Here, $\langle \ln Y|\epsilon\rangle_T$ is the canonical average of $\ln Y$ (see Eq. 3.3) at fixed energy and $-\ln\langle Y^{-1}|\epsilon\rangle_T$ is the average of Y over minima with energy ϵ. Note that, in harmonic approximation, these conditional averages are temperature independent.

Given the gaussian $G(\epsilon)$ (Eq. 3.10), $S_c^{(1)}(T)$ can be easily evaluated. The best way is to use $p(\epsilon;T)$ from the simulations and integrate over ϵ numerically. The result is shown in Fig. 3.14, curve (ii).

We can also start from Eq. 3.7 within harmonic approximation. In this case, $S_c^{(1)}(T)$ is given by the parameters characterizing $G(\epsilon)$ and $G_{\rm eff}(\epsilon)$. The analytic expression can be found in appendix C.5, Eqs. C.15 and C.16. The corresponding curve is shown in Fig. 3.14 (curve (iii)). In this computation of $S_c(T)$, the existence of a lower end of the PEL, $\epsilon_{\rm min}$ (given by $G(\epsilon_{\rm min}) = 1$, see Eq. 3.10), has been incorporated. Evidently, the cutoff influences the distributions $p(\epsilon;T)$ at low temperatures. *The consequence is that the vanishing of $S_c(T)$ at T_K is avoided.* In contrast, $S_c(T)$ obtained directly from thermodynamic integration vanishes at a temperature $T_{\rm K} \approx 0.3$, as suggested by curve (i). If the presence of the cutoff is ignored ($\epsilon_{\rm min} = -\infty$), we find the same configurational entropy as from thermodynamic integration (curve (iv)). *Thus, the extrapolation of the fit $E(T) = a + bT^{3/5}$ towards low temperatures (Sciortino et al., 1999) seems to be equivalent to ignoring the lower PEL cutoff (Sastry, 2001), both of which lead to the wrong result $S_c(T_K) = 0$, $T_K \approx 0.3 > 0$.*

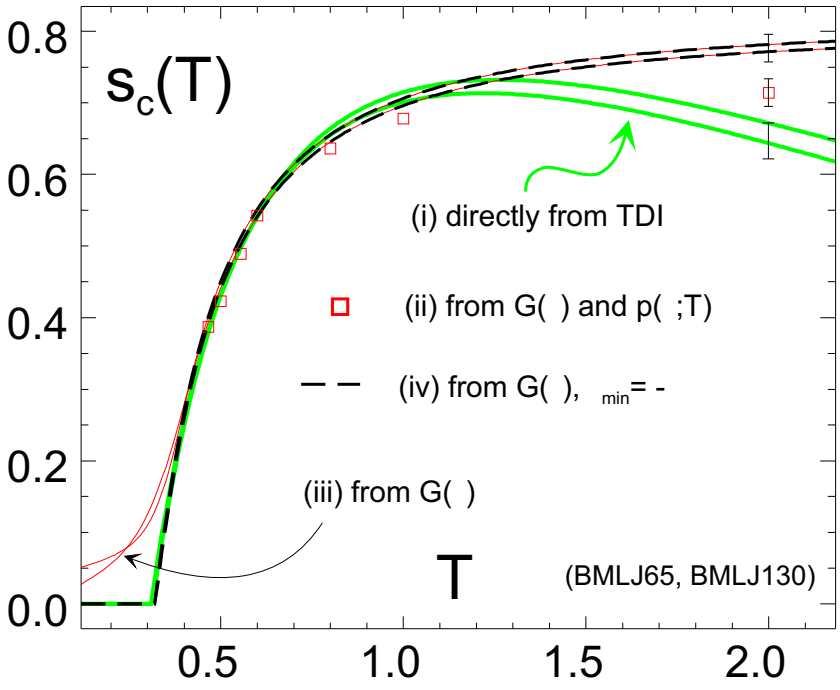

Figure 3.14: Configurational entropy per particle, computed in different ways (results for BMLJ65 and BMLJ130), (i) directly from the partition function after thermodynamic integration, Eqs. 3.28 and 3.29, (ii) from the gaussian $G(\epsilon)$ with $p(\epsilon;T)$ from simulation, Eq. 3.31, and (iii,iv) from $G(\epsilon)$ and $G_{\rm eff}(\epsilon)$, with and without lower PEL cutoff $\epsilon_{\rm min}$. The following cutoffs have been used in the calculation of curves (ii) and (iii): $\epsilon_{\rm min} = -306$ in the BMLJ65 and $\epsilon_{\rm min} = -612$ in the BMLJ130. Typical error bars are shown at $T = 2$.

Comparing all predictions for $S_c(T)$ (curves (i)-(iv)), we find that they practically coincide for $T_c = 0.45 < T < 3T_c = 1.35$. Above $3T_c$, anharmonic contributions disturb the calculations: for curves (i), (iii), and (iv), we worked completely within harmonic approximation, whereas in curve (ii), anharmonicities are partly accounted for by using the full $p(\epsilon;T)$ directly from the simulations. Thus, the latter curve should be taken most seriously.

We have also included the data for the BMLJ130 in Fig. 3.14, which show the same behavior. If we assume that a large system behaves essentially as the composition of small, independent subsystems (which is further verified in chapter 6), we can conclude that the avoidance of a vanishing configurational entropy at some temperature $T_{\rm K} > 0$ is no matter of the small system size of the BMLJ65.

Chapter 4

Dynamics: From Hopping to Diffusion

One major goal with respect to the dynamics of structural glass formers is a quantitative understanding of the molecular slowing down upon cooling. We have already seen that the energy landscape picture is useful for describing static properties below $2T_c$. Henceforth, our goal shall be an understanding of *dynamics* from the PEL perspective. Taking the practical viewpoint, average transport quantities like the diffusion coefficient or the viscosity are of greatest interest. Here, we concentrate on the long-time diffusion coefficient given by the Einstein relation

$$D(T) = \lim_{t\to\infty} \frac{\langle (x(t) - x(0))^2 \rangle}{6Nt}, \tag{4.1}$$

which describes the mean-square displacement of a particle during a long time t,

$$\left\langle (\boldsymbol{x}_i(t) - \boldsymbol{x}_i(0))^2 \right\rangle \approx 6Dt.$$

It is well known that $D(T)$ can also be written in terms of the inherent dynamics trajectory $\xi(t)$ instead of $x(t)$ (Schrøder et al., 2000). The simple reason is that the size of basins is limited, implying that the difference $\xi(t) - x(t)$ does not contribute to Eq. 4.1 in the long-time limit. Thus, it is sufficient to consider the hopping motion $\xi(t)$ among minima, neglecting the more or less complicated vibrations $x(t) - \xi(t)$ around them.

Based on these arguments, we will provide a link between the average dynamics of the system (as given by $D(T)$, section 4.1)) and the statistics of hopping events in the PEL. From the above it is clear that such a link exists, but its quantitative formulation could become more or less complicated. When studying the dynamics in terms of hopping between PEL minima (section 4.2), we will find strong correlations within groups of minima, which constitute superstructures in the PEL (metabasins).

It will then turn out that the hopping between whole metabasins can be related to $D(T)$ very easily (section 4.3), in contrast to a single-basin description (section 4.5).

It is important to note that we will use the visited PEL minima merely as a reduced description of the trajectory that was chosen by the system, as the 'milestones', so to speak (Fig. 4.1). Normally, the term 'hopping' is used to describe the *rare, activated jumps* between configurations. In this chapter, by 'hopping' we will mean something more general (i.e. moving from one basin to another), without referring to the physical mechanism behind this. Later, in chapter 5, we will trace back the temperature dependence of residence times in stable metabasins to the local PEL structure.

We finally remark that our approach is complementary to the real-space investigations of single-particle hopping via computer simulations (Miyagawa and Hiwatari, 1991; Allegrini et al., 1999). Since we consider hopping in configuration space, we have the advantage of incorporating the full many-particle effects (Keyes and Chowdhary, 2001).

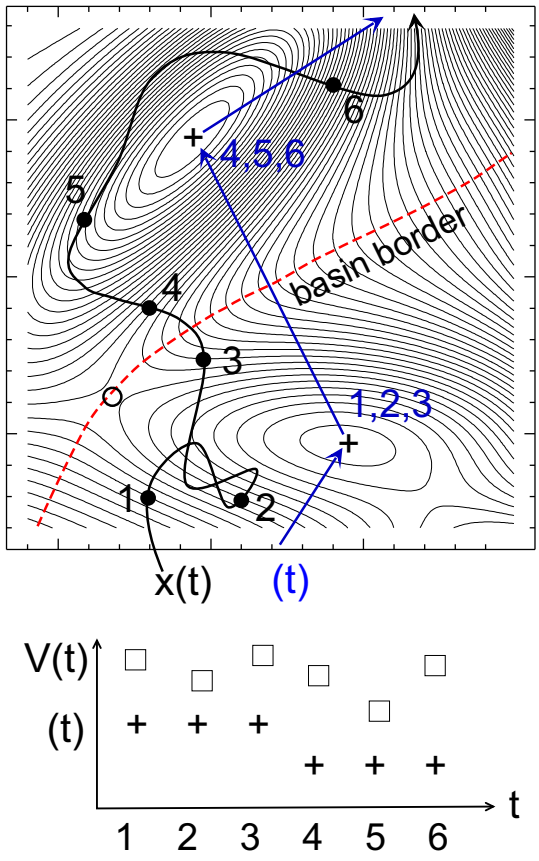

Figure 4.1: Sketch of the mapping from the real trajectory, $x(t)$, to the minima, $\xi(t)$.

4.1 The Long-Time Diffusion Coefficient.

The mean-square displacement. We first describe how $D(T)$ is extracted from the simulations. The mean-square displacement

$$\left\langle r^2(t)\right\rangle = \frac{1}{N}\left\langle (x(t)-x(0))^2\right\rangle = \frac{1}{N}\sum_i \left\langle (\boldsymbol{x}_i(t)-\boldsymbol{x}_i(0))^2\right\rangle \tag{4.2}$$

is shown in Fig. 4.2 for different temperatures in the BMLJ65. The brackets in Eq. 4.2 indicate the canonical average over different initial conditions at temperature T. By fitting the data with the expected long-time behavior $\langle r^2(t)\rangle = 2dD(T)t$, we obtain the diffusion coefficient $D(T)$. A measure for the accuracy of $D(T)$ is the

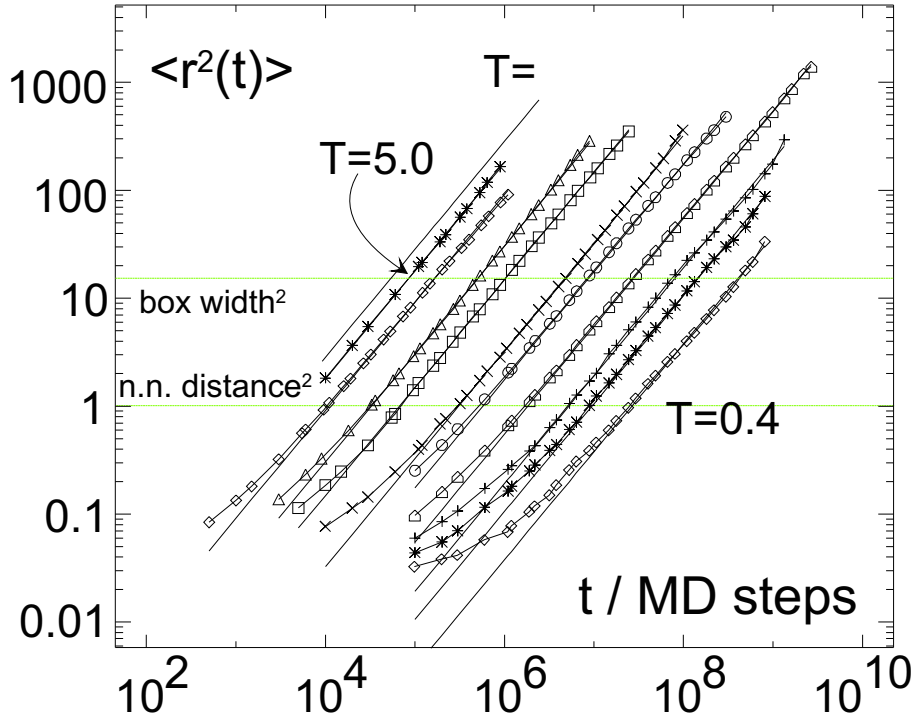

Figure 4.2: Mean-square displacement for the BMLJ65 (average is over A and B particles), at temperatures $T = \infty$, 5, 2, 1, 0.8, 0.6, 0.555, 0.5, 0.45, 0.435, and 0.4. Time is given in units of MD steps which is $\Delta t = 1/T$ in reduced units. The $T = \infty$ line corresponds to free diffusion. The short-time regime of $\langle r^2(t) \rangle$ is not shown from technical reasons (equidistant storage of particle configurations). The straight lines are fits to the long-time behavior $\langle r^2(t) \rangle \propto t$. For a comparison of distances, the typical next-neighbor distance and the box width are given.

number of independent initial configurations in the above average, which in turn is proportional to the total runtime. Alternatively, one may consider the distances traveled by the particles: generally, after covering a distance of the order of a next-neighbor separation, a particle is assumed to have structurally relaxed. This notion is supported by Fig. 4.2, since $\langle r^2(t) \rangle \propto t$ for $t > \tau_{\text{cage}}$ (where $\langle r^2(\tau_{\text{cage}}) \rangle \equiv 1$), which means that subsequent displacements on the timescale of τ_{cage} are approximately uncorrelated. In other words, after the cage formed by the surrounding particles has been broken and a new one has been formed, a particle has lost its memory and the further dynamics will essentially be uncorrelated from the past. We see in Fig. 4.2 that all simulation runs are long enough to contain many τ_{cage}'s. For instance, the total runtime at $T = 0.5$ is greater than $1000\tau_{\text{cage}}$. At $T = 0.4$, the run is still longer than $30\tau_{\text{cage}}$, which allows every particle to travel more than the length of the simulation box. One might intuitively think that this is sufficient for a

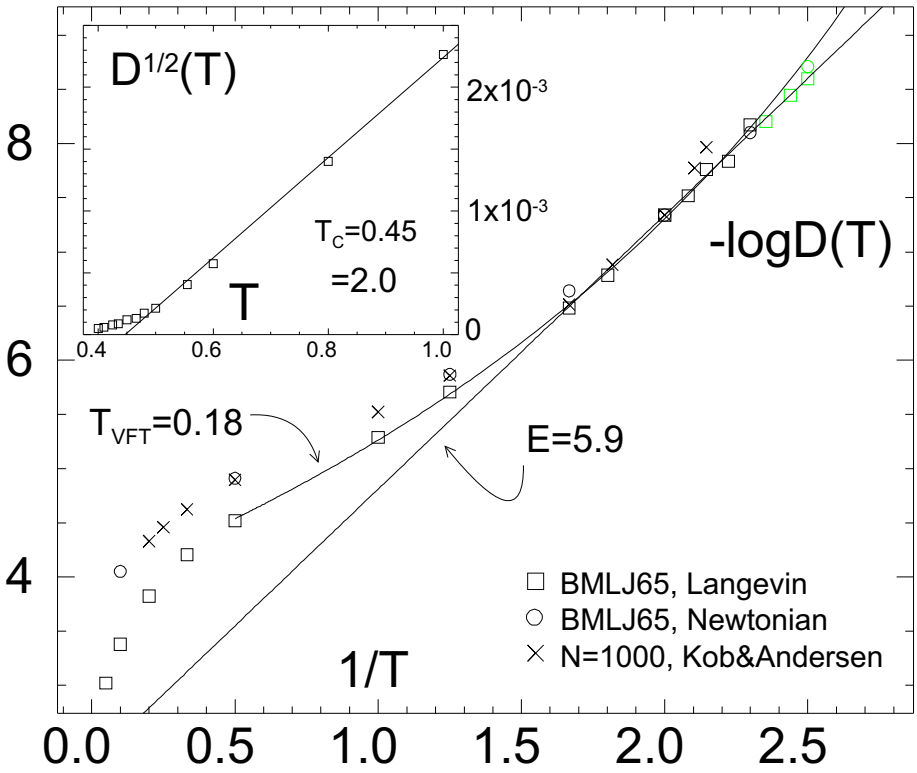

Figure 4.3: Arrhenius plot of the diffusion coefficient $D(T)$ for the BMLJ65 (average is over A and B particles). At the three lowest temperatures, error bars are unknown, which is indicated by a lighter color of the corresponding data points. Apparently, $D(T)$ becomes Arrhenius-like when approaching $T_c = 0.45 \pm 0.01$ from above, with an apparent activation energy of $\Delta E = 5.9 \pm 0.3$ (straight line). The curved line is a Vogel-Fulcher fit ($D(T) \propto \exp(-A/(T - T_{\mathrm{VFT}}))$), yielding $T_{\mathrm{VFT}} = 0.18$. For comparison, the results of Newtonian dynamics simulations (Kob and Andersen, 1995) have been included ($\times$). To better see the difference between Newtonian and Langevin dynamics we separately performed Newtonian dynamics simulations for the BMLJ65 ($\circ$). Kob's and our data from Newtonian dynamics simulations were multiplied by some constant to fall onto the Langevin dynamics at $T = 0.5$. Inset: Determination of the mode-coupling temperature T_c, according to the power law $D(T) \propto (T - T_c)^{\gamma}$. If we assume $\gamma = 2$, $D^{1/2}(T)$ should be linear in T and vanish at T_c.

thorough sampling of configuration space. However, we will see later on (section 5.5) that simulation runs for $T < 0.435$ are probably too short, due to the existence of some very rare but extremely long-lived metabasins. We therefore exclude data for $T < 0.435$ from deeper quantitative analysis.

The diffusion coefficient $D(T)$ for the BMLJ65 is shown in Fig. 4.3. In the limit of high temperatures, it is clear that $D(T) \rightarrow D_0 = k_{\mathrm{B}}T/m\zeta$: Firstly, because

the attractive part of the interaction potential, being of the order of ϵ_{AA} is not relevant at high temperatures, since $\epsilon_{AA} \ll k_{\mathrm{B}}T$. (A consequence is that only the repulsive part of the interaction is relevant there, implying that the BMLJ resembles more and more a soft-sphere system upon heating.) Secondly, the repulsive part ($\propto\ r^{-12}$) of the potential is probed at smaller and smaller distances r, due to the large thermal energy. The consequence is that the effective size of particles shrinks upon heating, which means that the distance where particle interactions disturb the free diffusion becomes smaller and smaller.

We are mainly interested in the regime of low temperatures. For $T \leq 2.0$, we observe the typical non-Arrhenius behavior of fragile glass formers, i.e. a positive curvature of $D(T)$ in the Arrhenius plot. A standard parameterization of such data is given by

$$D(T) \propto \exp\left(-\frac{A}{T - T_{\mathrm{VFT}}}\right).$$

This celebrated fit formula is due to Vogel, Fulcher, and Tammann (Vogel, 1921; Fulcher, 1925; Tammann and Hesse, 1926). As can be seen from the figure, it is able to fit the whole set of data, except for the three points of lowest temperatures ($T < 0.435$). If the latter points are correct, we would have a crossover around $T = 0.6$ from a non-Arrhenius to an Arrhenius $D(T)$. At present, however, the error bars of the data at $T < 0.435$ are unknown. As will be discussed in section 5.5, there are some indications that the $D(T)$ at these temperatures is overestimated due to insufficient statistics. Thus, the $D(T)$ below $T = 0.435$ should be considered with reservation.

Mode-coupling theory (MCT) predicts the power law $D(T) \propto (T - T_c)^{\gamma}$ (Götze and Sjogren, 1992), where the exponent γ is typically of the order of two (Kob and Andersen, 1995). To determine T_c, we therefore plot $D^{1/2}(T)$ versus T, see Fig. 4.3, inset. This yields the MCT 'critical' temperature $T_c = 0.45 \pm 0.01$. Below $T = 0.5$, we find deviations from the power-law prediction of MCT towards larger $D(T)$. For instance, $D(T)$ does not vanish at T_c. This failure of the MCT prediction is generally attributed to 'activated processes' which are not included in MCT but become relevant near and below T_c. We will later discuss this aspect in detail.

We have chosen the Lennard-Jones system of (Kob and Andersen, 1995), in short, KA, since it is one of the most widely studied super-cooled model liquids. The changes made to the potential were necessitated by the need of small systems. As we have seen in section 2, the reduced cutoff in conjunction with the continuity conditions results in changes which are not small. It is therefore not obvious how much our BMLJ differs from the one of Kob and Andersen. Three sources of deviations are present: the different interparticle potentials, the system size (KA:

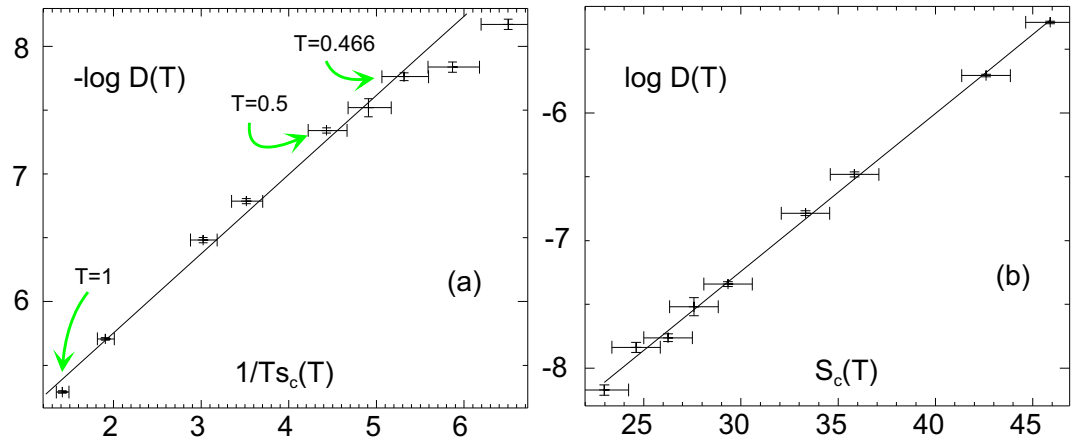

Figure 4.4: (a) Adam-Gibbs plot to check the relation $D(T) \propto \exp(-\frac{A}{Ts_c(T)})$ in the BMLJ65. Note the deviations from the straight line at $T \leq 0.45$. (b) Test of the relation $D(T) \propto \exp(BS_c(T))$. The straight line corresponds to $B = 0.285$.

$N = 1000$, here: $N = 65$), and the different type of dynamics (KA: Newtonian, here: Langevin dynamics). In Fig. 4.3, we have included the KA data of $D(T)$. The overall behavior is quite similar to that of the BMLJ65. At high T, the temperature dependence of the KA system is larger than that found in our BMLJ65 with Langevin dynamics. To check the influence of the different dynamics, we also show results for Newtonian dynamics of the BMLJ65 in Fig. 4.3. We now find an high-T behavior similar to KA. A clear difference to the KA system remains: while the BMLJ65 displays Arrhenius behavior[1] below $T = 0.6$, a markable increase in apparent activation energy is found by KA below $T = 0.5$. At the present stage, it is not clear if the continued non-Arrhenius behavior found by KA is the more generic one.

Adam-Gibbs plot. For completeness, we now test the Adam-Gibbs (AG) relation for the diffusion coefficient,

$$D(T) \propto \exp(-\frac{A}{Ts_c(T)}), \tag{4.3}$$

(see section 1.2). As we see from Fig. 4.4(a), $\log D(T)$ is approximately linear in $1/Ts_c$ between $T = 0.466$ and $T = 1$. However, an overall, slight curvature is clearly present in this temperature regime. For larger temperatures (not shown in the figure) and for $T < 0.466$, we find stronger deviations from the straight line. The breakdown of the AG relation for high temperature has also been observed

[1] apart from the uncertainty within the $T < 0.435$ data (see section 5.5)

in experiment (Richert and Angell, 1998). There, however, one has found deviations from the AG relation already above $1.6T_{\mathrm{K}}$. What concerns low temperatures, agreement with Eq. 4.3 has been found down to T_{g}, experimentally and in simulations (Saika-Voivod et al., 2001; Scala et al., 2000; Starr et al., 2001). For a very similar BMLJ system, Eq. 4.3 has also been verified (Sastry, 2001). The origin of the low-temperature deviations from the AG relation which we see in Fig. 4.4(a) should therefore be clarified. Here we have to restrict ourselves to noting that our value of the growth parameter ($\alpha \approx 0.8$) is smaller than the one found by Sastry ($\alpha \approx 0.9$). If we used $\alpha = 0.9$, the data points at $T < 0.466$ would much better fall on the straight line with the others.

Interestingly, the relation $D(T) \propto \exp(BS_c(T))$ with $B \approx 0.3$ is much better fulfilled than the AG relation, see Fig. 4.4(b). We do not attempt to give a physical interpretation of this, here.

4.2 Metabasin Hopping.

Some information about the waiting time distribution (WTD) has already been gained from the analysis of hopping processes of single particles in real space via computer simulations (Miyagawa and Hiwatari, 1991; Allegrini et al., 1999). In contrast, we consider hopping in configuration space, with the advantage of incorporating the full many-particle effects. We shall study the statistics of hopping events between PEL minima and, more importantly, between superstructures of them (metabasins).

Time series of minima. As demonstrated in (Büchner and Heuer, 2000), the time series of potential energies $\epsilon(t) = V(\xi(t))$ reflects well the character of dynamics in the super-cooled state. For $T = 0.435$, $\epsilon(t)$ is shown in Fig. 4.5 from which we note an interesting structure in $\epsilon(t)$: The system is trapped in some stable configurations for long times during which a small number of minima is visited over and over again (e.g. between MD steps 425×10^6 and 475×10^6). Typically, one or more low-lying minima are dominant in such groups of minima, and jumps to other minima possess large (backward) correlations. Obviously, this behavior reflects the dynamics within superstructures of minima which, following (Stillinger, 1995) we call *metabasins* (MBs).

One may imagine that minima of long-lived MBs are organized in funnel-like structures so that the system is stuck there for a long time. This seems to be a general construction principle of energy landscapes near stable configurations: The search for the native state in the process of protein folding, for instance, seems to

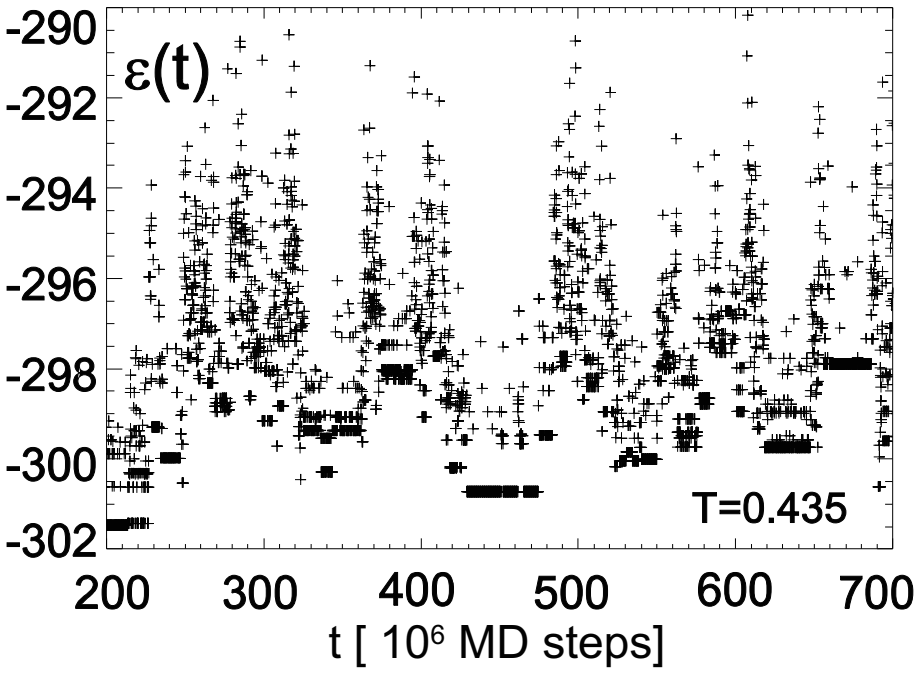

Figure 4.5: The time series of minima energies measured for the BMLJ65 at $T = 0.435$. The distance between minimizations is 10^5 MD Steps. The length of the total run is 2×10^9 MD Steps, the time window covering a quarter of the total run.

be guided by strong correlations on the PEL, generally pictured as huge folding funnels (Bryngelson et al., 1995). In the case of small clusters, similar funnel-like structures can be observed around the ground states (Ball et al., 1996). For glass formers, the existence of MBs has also been known for some while. After Stillinger had conjectured their presence in glasses, they were indeed found in computer simulations (Büchner and Heuer, 2000; Giovambattista et al., 2002b). What concerns the relation to experiment with glass formers it has been argued that the occurrence of β-relaxation at low temperatures is due to the MB substructure of the PEL (Stillinger, 1995). This is supported by the real-space signature of MBs found by Middleton and Wales. From the occurrence (or not) of particle-neighbor changes, they divide IS transitions into diffusive and non-diffusive ones (Middleton and Wales, 2001).

Interval bisection. All this indicates that MBs are the relevant, elementary building blocks of the PEL. Fortunately, it turns out that the hopping between them can be extracted from simulation data more easily than that between single basins. The simple reason is that all *elementary* hopping events have to be resolved for a complete description of dynamics. If we considered single basins, all IS transitions

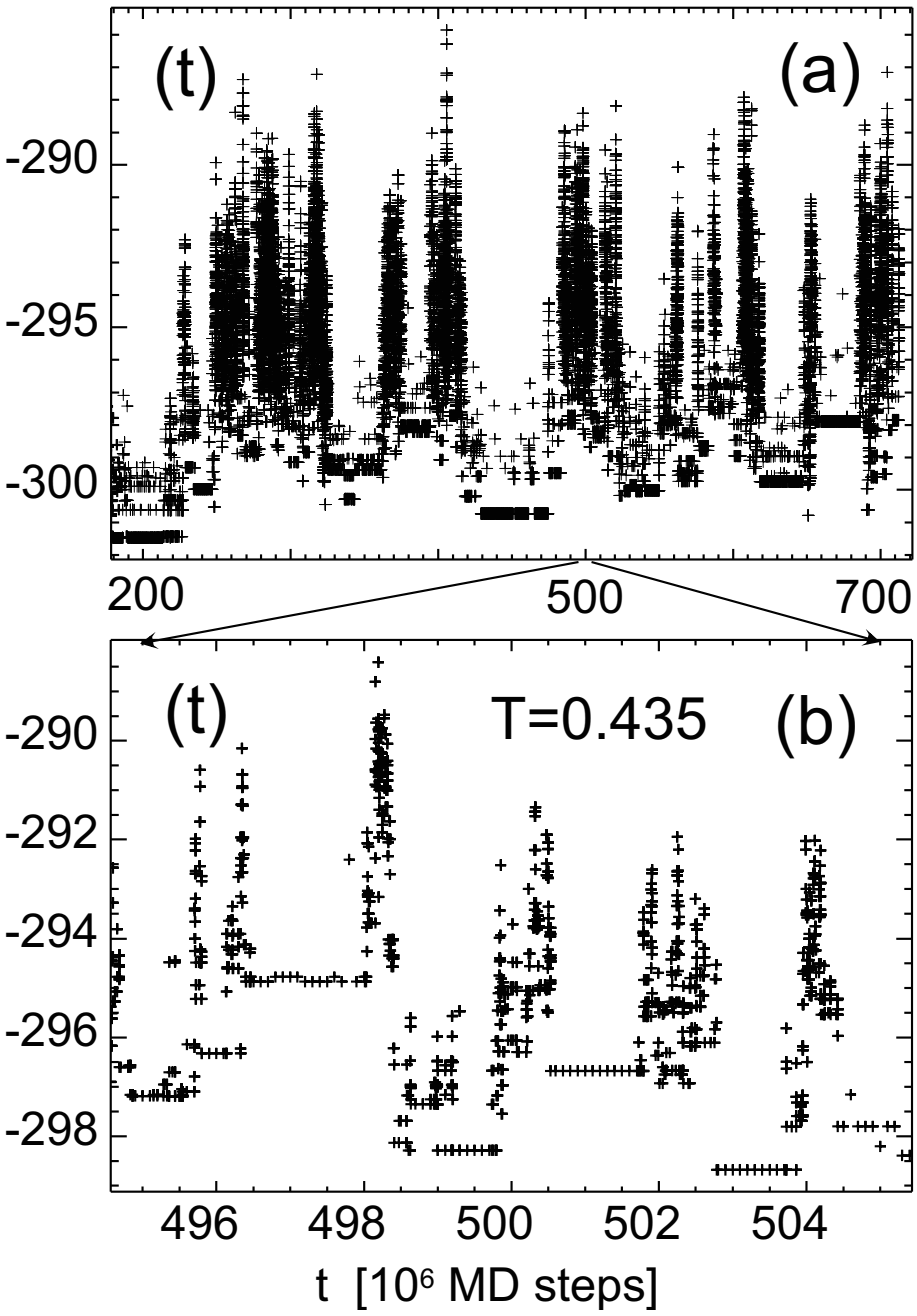

Figure 4.6: Time series of minima energies after applying interval bisection to the data of Fig. 4.5. (a) Time window as in Fig. 4.5, (b) magnification by a factor of fifty. Note that no interval bisection is carried out within the MBs known from Fig. 4.5.

would have to be detected. We would thus be forced to minimize $x(t)$ after every MD step. This is normally prohibited by computer time: For the BMLJ65, e.g., one minimization takes between three and five seconds on a DEC XP 1000 machine. To cover a typical low-temperature simulation run of 10^9 MD steps, we would therefore

need more than 10^6 hours! This time exceeds every PhD thesis. Thus, a description of dynamics on the basis of single-basin hopping is not very promising. We therefore turn to techniques for resolving *MB hopping* now.

Simulation runs like the one shown in Fig. 4.5 are between 10^8 and 10^{10} MD steps long. During a run, minimization is typically performed every 10^4 to 10^6 MD steps. We denote these configurations by $\xi(t_i)$. The advantage of introducing MBs now is that the back-and-forth jumps, which at low temperatures are especially numerous, do not have to be resolved. If the same minimum is found for times t_i and t_j, we need not care about transitions in the meantime. This is a clear computational advantage. If, in contrast, $\xi(t_i) \neq \xi(t_{i+1})$, one or more transitions have happened in the time interval $[t_i, t_{i+1}]$. A priori, we do not know whether $\xi(t_{i+1})$ is the direct successor of $\xi(t_i)$, or if other minima have been visited additionally. Therefore, further minimizations in such time intervals are necessary.

For reasons of efficiency, we apply a straightforward interval bisection method (IBM), which locates all relevant transitions with an accuracy of 1 MD step. Provided that $\xi(t^{(0)}_{\rm start}) \neq \xi(t^{(1)}_{\rm start})$,

(a) set $t^{(0)} \leftarrow t^{(0)}_{\rm start}$, $t^{(1)} \leftarrow t^{(1)}_{\rm start}$,
(b) reconstruct the trajectory $x(t)$ at time $t^{(2)} = (t^{(0)} + t^{(1)})/2$,
(c) calculate $\xi(t^{(2)})$,
(d) if $\xi(t^{(2)}) = \xi(t^{(0)})$, set $t^{(0)} \leftarrow t^{(2)}$, else set $t^{(1)} \leftarrow t^{(2)}$,
(e) repeat (b)-(d) until $t^{(1)} - t^{(0)} = 1$ MD step.

Note that in the end, $\xi(t^{(0)}) = \xi(t^{(0)}_{\rm start})$, per construction. However, if $\xi(t^{(1)}_{\rm start})$ is not the direct successor of $\xi(t^{(0)}_{\rm start})$, we have $\xi(t^{(1)}) \neq \xi(t^{(1)}_{\rm start})$. Repeated application[2] of the interval bisection to a simulation run $x(t)$ finally gives a set of transition times t'_i. The times t'_i have the properties $\xi(t'_i) \neq \xi(t'_i + \delta t)$ (i.e., an IS transition occurs at time t_i) and $\xi(t'_i + \delta t) = \xi(t'_{i+1})$ (i.e., a basin is entered at t'_i and left at t'_{i+1}). In this way, the jumps $\xi(t'_i) \rightarrow \xi(t'_i + \delta t)$ are guaranteed to form a contiguous trajectory.

In Fig. 4.6 we show the series of energies, $\epsilon(t'_i)$, after the IBM has been applied to the equidistant configurations of Fig. 4.5. One can see that in the regions of rapid transitions, many intermediate minima were detected. Since the very short-lived minima are often high-energetic, this yields many minima above -290, which

[2]From the technical point of view, the reconstruction of the trajectory at some arbitrary point is straightforward. In the case of Langevin dynamics, the random number generator has to be reset to the initial state, i.e. the random state has to be saved in addition to a configuration, in the same way as the momenta must be memorized in the case of Newtonian dynamics.

were not present in Fig. 4.5. Note, however, that unresolved IS transitions may be present between the initial t_i and t_{i+1}. This may happen if the lifetime of minimum $\xi(t_i)$ is interrupted by a visit to some third minimum ($\xi(t_i) \to \xi' \to \xi(t_i)$). If the residence in the basin of the third minimum is short enough, it may be overseen during the IBM. As already discussed, it is exactly such back- and forth hopping which is removed by the MB construction. Thus, if such an event is not detected, this will not harm the MB lifetimes. Although computationally demanding, the IBM most efficiently resolves the relevant details of MB hopping.

Metabasin lifetime construction. The strong correlations between groups of minima will lead us to a precise definition of MBs in section 5.3, based on the probabilities of returning to a previous minimum. To obtain these return probabilities, we will need some more sophisticated simulation techniques, including repeated starts from certain minima. This kind of analysis will be necessary for the determination of MB depths.

Here, for computing MB lifetimes[3], we will take a more pragmatic view. From a given MD run and the corresponding minima (e.g. Fig. 4.6), the lifetimes of MBs can be obtained through the following algorithm (Büchner and Heuer, 2000).

(a) determine the intervals $[t_i^*, t_i^\dagger]$ where t_i^* is the time of the first and $t_i^\dagger$ the time of the last occurrence of minimum $\xi(t_i^*)$,

(b) any two intervals $(t_i^* < t_j^* < t_i^\dagger < t_j^\dagger)$ with an overlap of less than fifty percent (i.e. $(t_j^* - t_i^\dagger)/\max\{(t_i^\dagger - t_i^*), (t_j^\dagger - t_j^*)\} < 50\%$) are cut so that the new intervals fulfill $[t_i^*, t_i^\dagger] \cap [t_j^*, t_j^\dagger] = \emptyset$, either by setting $t_i^\dagger = \max\{t|\xi(t) = \xi(t_i^*),\ t < t_j^*\}$ or $t_j^* = \min\{t|\xi(t) = \xi(t_j^\dagger),\ t > t_i^\dagger\}$ (randomly, with equal probability), new intervals $[\min\{t|\xi(t) = \xi(t_i^*),\ t > t_j^*\}, \max\{t|\xi(t) = \xi(t_i^*),\ t > t_j^*\}]$ or $[\min\{t|\xi(t) = \xi(t_j^\dagger),\ t < t_i^\dagger\}, \max\{t|\xi(t) = \xi(t_j^\dagger),\ t < t_i^\dagger\}]$ are introduced, respectively,

(c) any two intervals overlapping by more than fifty percent are combined to $[t_i^*, t_i^\dagger] \cup [t_j^*, t_j^\dagger]$,

(d) intervals $[t_j^*, t_j^\dagger]$ are deleted if there is some $[t_i^*, t_i^\dagger]$ with $[t_j^*, t_j^\dagger] \subset [t_i^*, t_i^\dagger]$

(e) the lifetimes of MBs are defined by the intervals after step (d),

(f) the MB configuration ξ_{MB} is defined as the lowest minimum visited during the MB lifetime, ϵ_{MB} being its energy.

A few comments on the procedure are in order. Time intervals in (a) are determined by the interval bisection method which yields the time of transitions from one minimum to another with an accuracy of one MD step. Step (b) is motivated

[3]We use 'lifetime' as a synonym for 'residence time' or 'waiting time' inside a basin or metabasin.

by the observation that recrossings of a basin border during a transition are very probable. If we ignored this fact, i.e. combined all overlapping intervals in step (c), we would merge nearly all intervals and end up with unphysically long MBs. The choice of fifty percent mutual overlap in steps (b) and (c) is a bit arbitrary. However, we found that the results for MB lifetimes are not very susceptible to taking values other than fifty percent. Step (c) itself and step (d) are the realization of the MB concept, since back-and-forth motion is removed. It is important to note that, different from (Büchner and Heuer, 2000), we will treat all MBs on the same footing here, no matter if they are short-lived or long-lived. We stress again that the MB lifetime construction rests upon single trajectories, which only partially reflect the configuration space topology. For the computation of lifetimes, though, this poses no serious problem, see the discussion in section 5.3.

We find that the metabasin lifetimes, τ, range from a few MD steps to many millions of them. This large span can only be covered with the help of the interval bisection method. The distribution of lifetimes will be denoted $\varphi(\tau, T)$. For the following considerations, its expectation value, $\langle\tau(T)\rangle$, will be a key quantity.

4.3 From Hopping to Diffusion.

One major advantage of analyzing metabasins rather than basins is that the simplistic picture of a random walk in configuration space will be better fulfilled on the level of metabasins rather than basins since direct back- and forth correlations among minima are already taken into account. Thus, at a given temperature, one may hope that dynamics can be expressed by a typical jump distance and the mean lifetime of MBs. Upon changing temperature, however, both of them might vary. Interestingly, as we shall show in this section, the spatial aspects of MB hopping are fairly temperature independent below $2T_c$. As the consequence, the whole temperature dependence is contained in the average waiting time $\langle\tau(T)\rangle$. This will lead to a simple description of diffusion as has been expressed in phenomenological models, see (Zwanzig, 1983; Monthus and Bouchaud, 1996; Odagaki et al., 1994).

As said above, the temperature dependence of the diffusion coefficient may generally be related to spatial and temporal aspects of hopping, as expressed by the relation

$$D(T) = \frac{a^2(T)}{6N\,\langle\tau(T)\rangle}. \tag{4.4}$$

With this ansatz, we anticipate the important role of the MB mean waiting time and collect the spatial details of hopping in an *effective* jump length $a(T)$. The latter involves (i) the average jump distance, (ii) correlations of jump lengths with waiting

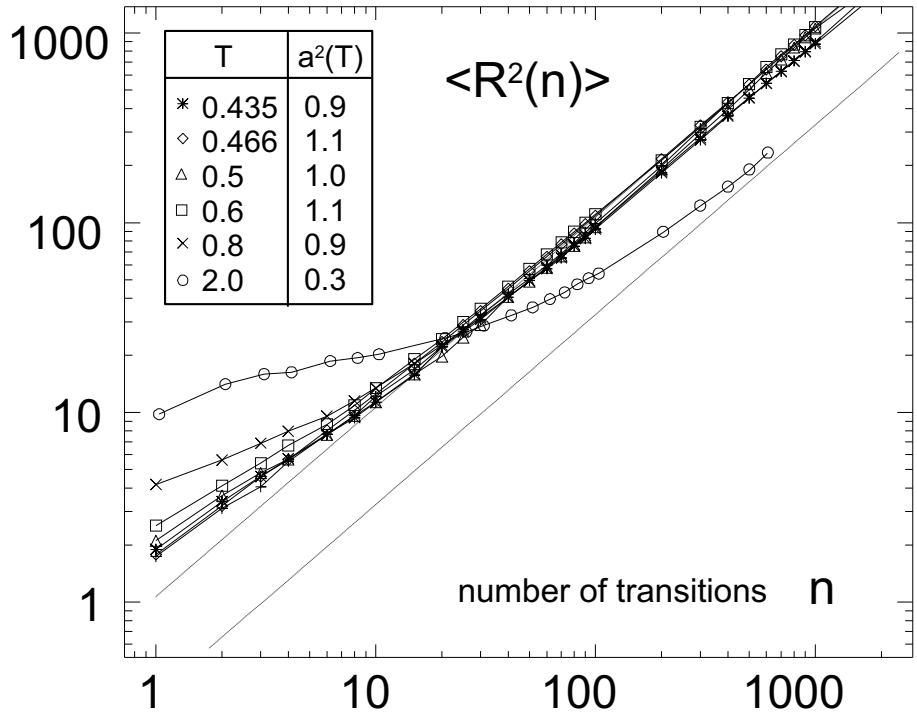

Figure 4.7: Squared displacement $\langle R^2(n)\rangle$ after n metabasin jumps for the temperatures $T = 0.4, 0.435, 0.466, 0.5, 0.6, 0.8$, and 2.0. We have included lines of slope 1.

times, and (iii) directional correlations of successive jumps. To our knowledge this decomposition into spatial and temporal contributions has not been systematically implemented within the PEL framework so far. A priori it is not clear to which degree the temperature dependence of $a(T)$ is relevant; see, e.g., (Vardeman and Gezelter, 2001; Schulz, 1998).

Our goal is to find an expression for the effective jump length $a(T)$ of Eq. 4.4. The key idea is to introduce the squared distance $\langle R^2(n)\rangle$ after n jumps (Maass et al., 1995), averaged over different realizations. This quantity is purely spatial since it does not involve any time scale. In the limit of large n one obtains[4] due to the central limit theorem $\lim_{n\to\infty}\langle R^2(n)\rangle/\langle\xi^2_{\mathrm{MB}}(n\,\langle\tau\rangle)\rangle = 1$ where $\langle\xi^2_{\mathrm{MB}}(n\,\langle\tau\rangle)\rangle$ is the average squared displacement[5] after time $n\,\langle\tau\rangle$. Thus,

$$D(T) = \lim_{n\to\infty}\frac{\langle\xi^2_{\mathrm{MB}}(n\,\langle\tau\rangle)\rangle}{6Nn\,\langle\tau\rangle} = \left[\lim_{n\to\infty}\frac{\langle R^2(n)\rangle}{6n}\right]\frac{1}{N\,\langle\tau\rangle} \tag{4.5}$$

where the first factor may be identified as $a^2(T)/6$. Note that both factors are

[4]To some, this may seem an obvious relation. Those who need a more strict derivation of Eq. 4.5 are referred to appendix C.3.

[5]Strictly speaking, we should write $\left\langle\left(\xi_{\mathrm{MB}}(t) - \xi_{\mathrm{MB}}(0)\right)^2\right\rangle$ for the displacement which is a bit clumsy, so we abbreviate it by $\left\langle\xi^2_{\mathrm{MB}}(t)\right\rangle$ as long as the meaning is clear.

independent of system size because IS transitions are localized ($\langle R^2(1)\rangle = O(1)$) and mean waiting times decrease with system size ($\langle\tau\rangle = O(1/N)$). We may now calculate $a(T)$ from the simulations, results are shown in Fig. 4.7. The most important observation is that $a(T)$ is temperature independent for $T \leq 2T_c = 0.9$. Interestingly, this is not affected by the variation of the elementary jump width $\langle R^2(1)\rangle$, which increases with temperature, a fact that was recently observed by Schulz et. al. (Schulz et al., 2001). A possible explanation for this might be found in the increasing population of higher-order stationary points (Angelani et al., 2000a) upon heating, which provokes many of the so-called 'bookkeeping' IS transitions (Keyes and Chowdhary, 2001). On the one hand, the minima visited in this way are known to be the more distant from each other the higher the index of the stationary points, resulting in a larger $\langle R^2(1)\rangle$. On the other hand, stronger backward correlations are found for these bookkeeping transitions, so that the same long-time limit $\lim_{n\to\infty} \langle R^2(n)\rangle /6n$ is recovered.

In any event, the constancy of $a(T)$ in the landscape-influenced regime $T \leq 2T_c$ implies that the temperature dependence of $D(T)$ follows alone from $\langle\tau(T)\rangle$, i.e.

$$D(T) \propto \langle\tau(T)\rangle^{-1}. \tag{4.6}$$

This simple picture breaks down above the landscape-influenced regime, $T > 2T_c$, where, probably, the explored regions of configuration space have a completely different structure. It has to be noted that the constancy of $a(T)$ for $T < 2T_c$ relies heavily on our resolution of *all elementary* MB transitions leading to relaxation. This might explain the discrepancy of our results with that of related studies (Schulz et al., 2001), which find jump distances that increase with temperature.

A further insight from Fig. 4.7 is that the dynamics on the level of metabasins is basically a random walk except for minor back-correlations for $n \leq 5$. As expected from Fig. 4.5, massive correlations are present between *single* basins, as will be shown in section 4.5, the consequence being a significant deviation from the relation $\langle R^2(n)\rangle \propto n$. More importantly, we will see that $a(T)$ would strongly depend on temperature, if we used single basins rather than MBs in the above investigation. It remains unclear why for a very small LJ system (N=32) the correlations among adjacent basins are irrelevant for $T \approx T_c$ (Keyes and Chowdhary, 2001), and why intra- rather than inter-basin dynamics is deemed to be the key to the understanding of diffusion (Keyes and Chowdhary, 2002).

We can check the relation $D(T) \propto 1/\langle\tau(T)\rangle$ within our simulations. Figure 4.8 shows that, for $T \leq 1$ it is indeed well fulfilled. As expected, we find the deviation for $T = 2$.

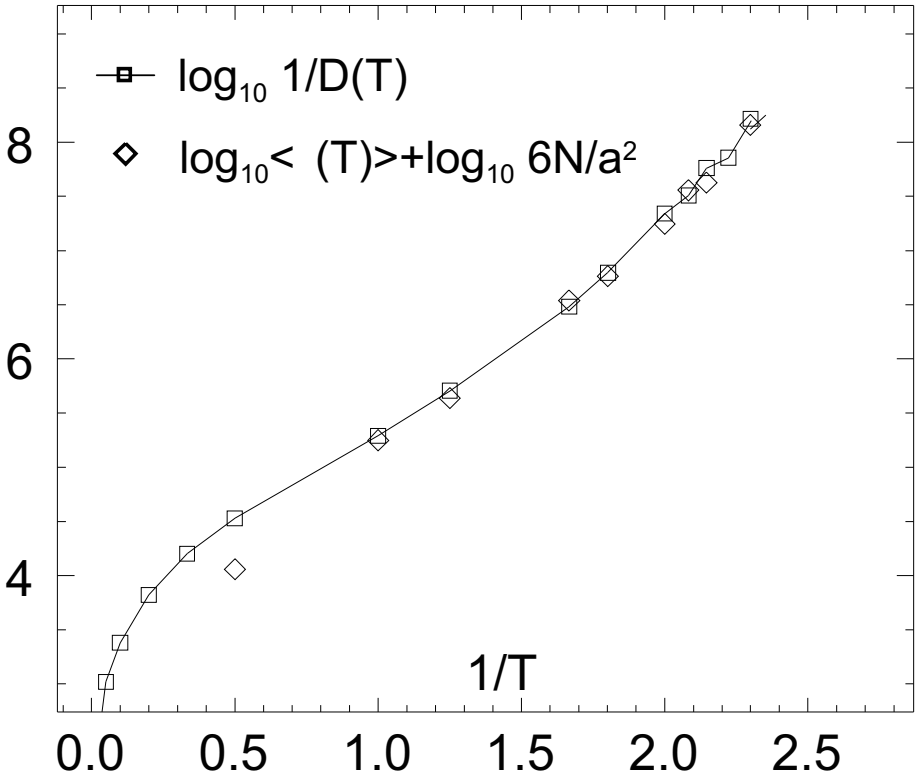

Figure 4.8: Arrhenius plot of the inverse one-particle diffusion coefficient $1/D(T)$ versus the MB mean waiting time $\langle\tau(T)\rangle$ multiplied by a constant ($a^2 = 1.0$). Error bars are of the order of the symbol size.

4.4 Waiting Time Distributions.

In this section, we discuss the properties of the waiting time distributions (WTDs), $\varphi(\tau, T)$. Some information about WTDs has already been gained from the analysis of hopping processes of single particles in real space via computer simulations (Miyagawa and Hiwatari, 1991; Allegrini et al., 1999). In these works, a definition of lifetimes is given by the requirement that a particle move some distance larger than δ before it is said to have relaxed. The choice of δ, though arbitrary, has a great influence on the WTDs (e.g. on their long-time decay). Furthermore, due to the single-particle description, collective effects are not accounted for: If, for instance, a particle and its neighbors move collectively into the same direction by more than δ, all of them are considered as relaxed, although at least the central particle has not at all left its cage. Due to the many-particle aspect of the PEL and the presence of well-defined basins, our WTDs do not have these drawbacks.

Figure 4.9 shows $\varphi(\tau, T)$ for some temperatures $T \leq 1$. For short τ, all curves exhibit a power-law behavior with exponent $-1/2$, similarly to (Michele and Lep-

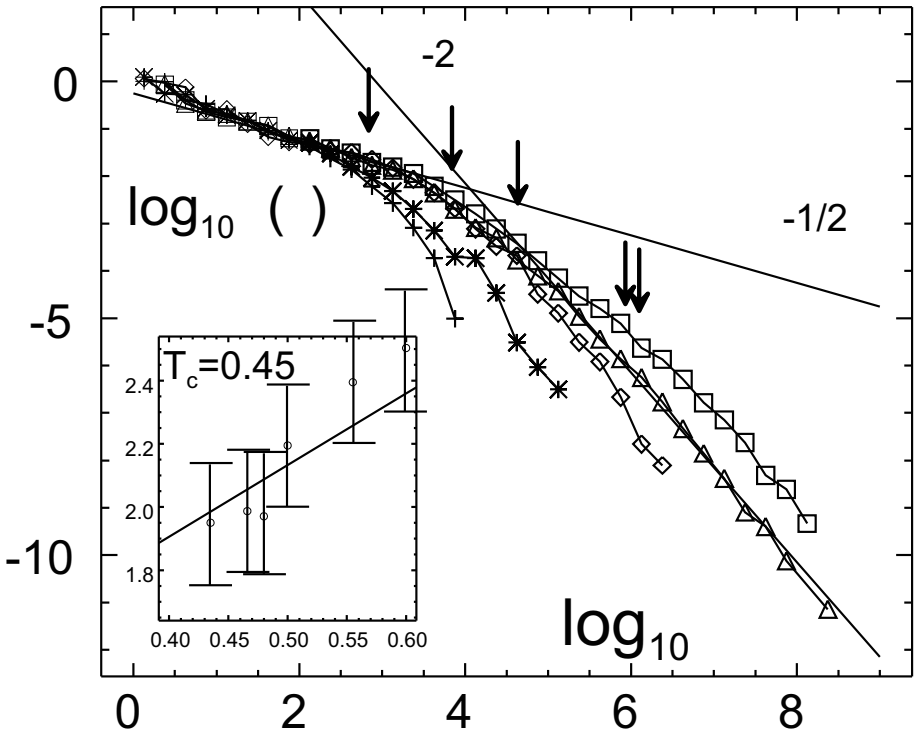

Figure 4.9: Distributions of waiting times, $\varphi(\tau, T)$, for $T = 1.0, 0.8, 0.6, 0.5$, and 0.435 (from left to right). Curves have been shifted to overlap for small τ. Lines corresponding to algebraic decays with exponents 0.5 and 2 are shown as guides to the eye. The arrows mark $\tau^*(T)$, i.e. the waiting time with the property $\int_{\tau^*(T)}^{\infty} \mathrm{d}\tau\varphi(\tau)\tau = 0.9\,\langle\tau\rangle$. Inset: Power-law exponent $\alpha(T)$ from fits to the long-time decay. Within the possible accuracy, $\alpha(T) \approx T/T_x + 1$, with $T_x \approx T_c = 0.45$.

orini, 2001). At larger τ a crossover to a faster decay can be observed, which again is compatible with a power-law, $\varphi(\tau, T) \propto \tau^{-\alpha(T)}$.

For $T = 0.435$, e.g., one finds $\alpha \approx 2.0$ for which the expectation value $\langle\tau\rangle$ would diverge. However, the behavior $\varphi(\tau) \propto \tau^{-\alpha}$ cannot extend to infinitely large τ. Due to the finite number of metabasins in the system, there exists a maximum effective barrier $E_{\max}$, giving rise to an exponential cutoff at some minimum rate $\gamma_{\min}$. This crossover to exponential decay at very large times is not seen in our data. One might therefore ask where this crossover should be found and, more importantly, if there is missing some relevant part of the long-time tail of $\varphi(\tau; T)$, in the sense of contributing significantly to $\langle\tau(T)\rangle_{\varphi}$. In the latter case, a more thorough sampling of the PEL would be necessary to find the correct $\langle\tau(T)\rangle_{\varphi}$, meaning that our present runs are too short. This is an important issue, which, after Eq. 4.6, concerns the accuracy of $D(T)$ and the equilibration of our runs in general. We shall show in section 5.5, how such questions can be answered. The result will be that for our

simulations at $T \geq 0.435$, the contribution from the unseen long-time tail of $\varphi(\tau; T)$ is small.

Dominance of the large τ's. It is now interesting to ask which part of $\varphi(\tau)$ dominates the mean waiting time $\langle \tau(T) \rangle_{\varphi}$. On the one hand, the majority of valleys is short lived, but these are weighted only by a small τ. On the other hand, the long-lived states are rare, but contribute a large τ. The slow decay of the WTDs now leads to the important observation that $\langle \tau \rangle$ is dominated by the contributions from large τ (see arrows in Fig. 4.9). For example at $T = 0.435$, 90% of $\langle \tau \rangle$ are made up by the six percent longest waiting times (i.e. 224 out of 3993 metabasins), with lifetimes greater than 0.5×10^6 MD Steps. Hence, only the very stable metabasins are of statistical relevance for the temperature dependence of the diffusion coefficient. This may come as a surprise because one might intuitively think that the diffusion coefficient and thus $\langle \tau \rangle$ is dominated by the fast particles. We note that our result is in qualitative agreement with the approach of Wolynes and Xia who regard the relaxation of long-lived local structures as the time-determining step (Xia and Wolynes, 2001).

Bouchaud's trap model. Interestingly, the algebraic decay of the WTDs follows for some theoretical models of diffusion with built-in traps. Bouchaud and coworkers discuss a model where relaxation is a consequence of activated jumps out of traps with depths E and distribution function $\rho(E)$ (Monthus and Bouchaud, 1996). In the exponential case $\rho(E) \propto e^{-E/T_x}$, they find WTDs $\varphi(\tau, T)$ with algebraic decay for long τ

$$\varphi(\tau, T) \propto \tau^{-(T/T_x+1)}.$$

(Details of Bouchaud's model can be found in appendix D.) As said above, our data is compatible with an algebraic long-time decay - which does not mean that all alternative forms can be excluded (see the recent paper by Bouchaud et al., where a detailed comparison of WTDs in a binary Lennard-Jones system with that of trap models can be found (Denny et al., 2002)). Within the possible accuracy, though, the exponent $\alpha(T)$ agrees with that of Bouchaud's model if we choose $T_x = 0.45 = T_c$, see the inset of Fig. 4.9.

Does this mean that the basic assumptions of the trap model hold for the BMLJ65? The main assumption in the model is that the depths and lifetimes are related one-to-one, by $\gamma(E) = \gamma_0 \exp(-\beta E)$. In the notation of chapter 5, this means $E_{\text{app}}(E) = \mathrm{d} \ln \langle \tau | E \rangle / \mathrm{d}\beta = E$. Alternatively, this can be expressed by the temperature independence of the distribution of visited traps, i.e. $\varphi(E; T) = \rho(E)$.

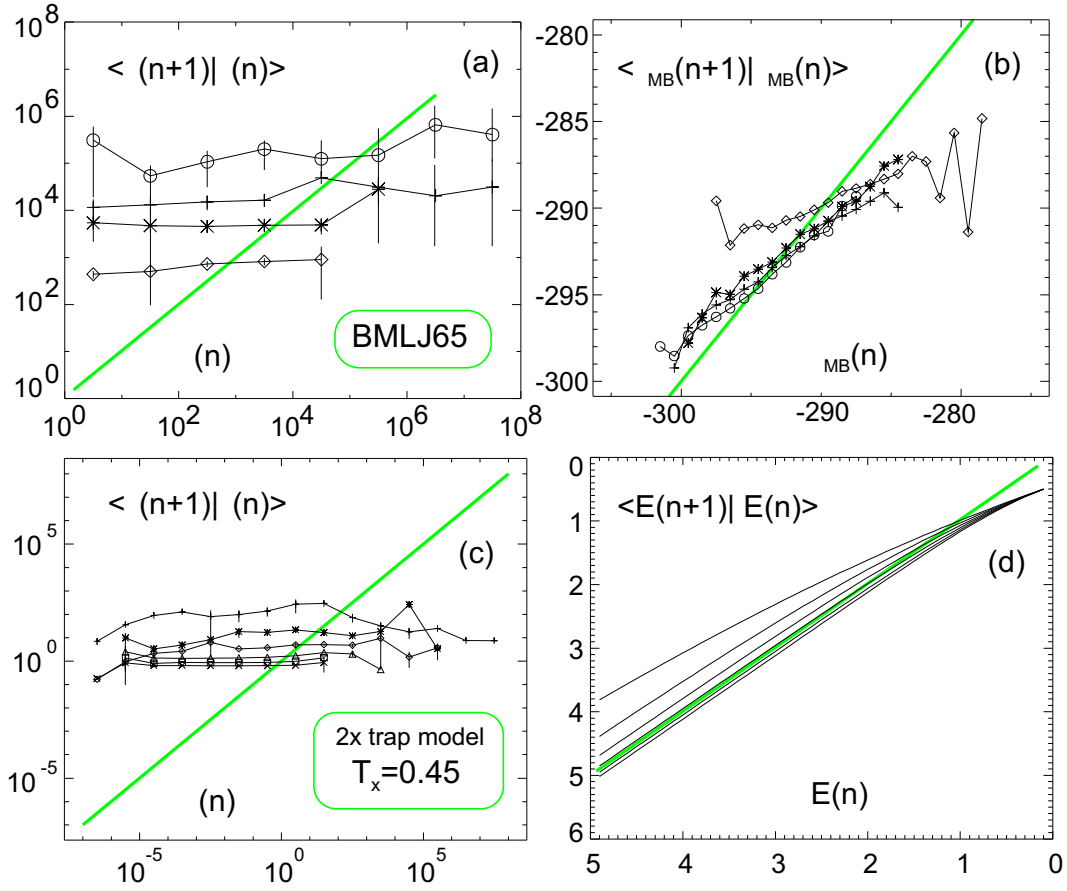

Figure 4.10: (a) Average subsequent MB waiting time $\langle \tau_{(n+1)} | \tau_{(n)} \rangle$, as a function of $\tau_{(n)}$ in the BMLJ65. Temperatures are $T = 0.435, 0.5, 0.6$, and 0.8 from top to bottom. (b) Average subsequent MB energy $\langle \epsilon_{\mathrm{MB}}(n+1) | \epsilon_{\mathrm{MB}}(n) \rangle$, *vs.* $\epsilon_{\mathrm{MB}}(n)$, for the same temperatures as in (a), from bottom to top. For comparison, (c) and (d) show the corresponding quantities for a system comprised of two independent trap models à la Bouchaud ($T_x = 0.45$). Temperatures are $T = 0.33, 0.4, 0.5, 0.667, 1.0$, and 2.0, from top to bottom in (c) and vice versa in (d). Auxiliary lines of slope one have been included.

Neither of these features is found in the BMLJ65, see section 5.1. An explanation for these findings could be the fact that the BMLJ65 is not a completely correlated entity, i.e. subsystems may sometimes relax independently. This leads to a weaker dependence of $E_{\mathrm{app}}(E)$ of E. Thus, the reason for the good agreement of the power-law exponents $\alpha(T)$ between the trap model and the BMLJ65 remains to be clarified. Finally we mention that also the trapping diffusion model (Odagaki et al., 1994) predicts a similar temperature dependence of $\alpha(T)$.

Correlations among subsequent MBs. As stressed above, the MB construction is devised to eliminate trivial back-and-forth correlations among IS transitions which are irrelevant for structural relaxation. We have seen that this works quite well in that the sequence of hops between MBs is near to a random walk. For reasons of completeness, we shall report further results in this connection: First, it is interesting to check for correlations between the lifetimes of subsequent MBs. For this purpose, we calculate the mean lifetime $\langle \tau_{(n+1)} | \tau_{(n)} \rangle$ of MB (n+1), as a function of the preceding $\tau_{(n)}$. As depicted in Fig. 4.10(a), this kind of correlation is absent, independently of temperature. Second, it is obvious to check for statistical interdependence among MB energies, $\epsilon_{\mathrm{MB}}(n)$. Again, we compute the average $\epsilon_{\mathrm{MB}}(n+1)$ as a function of $\epsilon_{\mathrm{MB}}(n)$, see Fig. 4.10(b). The strong correlations which we find are striking. The results obtained so far might have produced the impression that the choice of what MB to visit next is independent of the preceding one (like in the trap model). That this is not true is not a drawback of our MB approach - it rather reflects a deeper principle of PEL structure: Since (hopefully) our BMLJ65 is not a completely correlated entity, we expect that different parts of the system decouple to a certain extent. Stated otherwise, different parts of the system may relax independently - at least to some degree. To put this into perspective, we note that the 'string-like' motion, found in larger BMLJ systems, mostly comprises clusters of less than 10 particles (Donati et al., 1998). Taking this for granted, we immediately recognize that a single MB jump (say, corresponding to one of the above strings) cannot lead to a completely uncorrelated point in configuration space. Although dynamic backward correlations towards former MBs are essentially absent, the structure of the new MB is correlated with that of the former MB, which is what we find in Fig. 4.10(b).

To gain a better understanding of what is going on, we compare our findings with Bouchaud's trap model. We mimic the quasi-decoupled regions in our BMLJ65 by combining two independent copies of the trap model. The waiting times, $\tau(n)$, of the combined system are given by the time spans where neither of the copies makes a hop. In Fig. 4.10(c), we see the correlation of subsequent waiting times (which we computed numerically for this model, since the analytic solution seemed too lengthy). As in the BMLJ65, no correlations among waiting times can be found. The energy correlations can easily be computed analytically,

$$\langle E(n+1) | E(n) \rangle_{\varphi} = T_x - T + \frac{E(n)}{1 - e^{-\beta E(n)}},$$

where $E(n)$ is the total energy of both copies, see Eq. D.13. As shown in Fig. 4.10(d), we find similarly strong correlations of subsequent energies as in the BMLJ65. Thus, as the conclusion, the lacking correlations between MB waiting times and their

presence with respect to energies, can be explained by the fact that parts of the BMLJ65 relax quasi-independently.

Probably, a more quantitative study of the observed correlations in Fig. 4.10(a),(b) would yield a much deeper comprehension of PEL topology than we can provide here.

4.5 All this does not work with single basins.

We noted above that MBs are very suitable for numerical study since we may use interval bisection to locate the MB transitions. When dealing with single basins, in contrast, one has to minimize very frequently to resolve all IS transitions, including the numerous back-and-forth hops within MBs. Here we would like to demonstrate that this is not only numerically expensive, but also unprofitable for the comprehension of diffusion.

For three temperatures ($T = 0.5, 0.6$, and 0.8), we generated time series of minima over periods of 10^7 MD steps, with a spacing of 10 MD steps[6]. In this way, we find nearly all elementary IS transitions, including those within MBs. We now carry out the same analyses as we before did with MBs.

Average squared displacement after n jumps. Again, $\langle R^2_{\text{basin}}(n;T)\rangle$, provides some information about the spatial aspect of hopping, now between single basins. In Fig. 4.11, we see $\langle R^2_{\text{basin}}(n;T)\rangle$ calculated for jumps between basins, compared with the respective $\langle R^2(n;T)\rangle$ between MBs for the same set of temperatures. Two important differences are evident: (i) The subdiffusive regime for basins is much more pronounced than for MBs. (ii) The quantity $a^2_{\text{basin}}(T) = \lim_{n\to\infty} \langle R^2_{\text{basin}}(n)\rangle /6n$ depends on temperature, in contrast to the MB $a^2(T)$ (also compare Fig. 4.7).

The explanation for (i) is obvious from what we understand so far about the nature of MBs. Due to the frequent back-and-forth hops within MBs, one expects a long subdiffusive regime of $\langle R^2_{\text{basin}}(n)\rangle$. Since the number of intra-MB transitions increases with the lifetime of a MB, the subdiffusive regime grows upon cooling. This leads to the decrease of $a^2_{\text{basin}}(T)$. The back-and-forth jumps can nicely be seen in the oscillations of $R^2_{\text{basin}}(n)$ at small n. The growing importance of such motion towards low temperatures is also clearly visible.

Is evident from Fig. 4.11 that Eq. 4.6 cannot be valid on the single-basin level. This is directly demonstrated in Fig. 4.12: As expected, the mean basin waiting time has a too weak dependence on temperature to reproduce $D(T)$ up to a constant. Since part of the temperature dependence is contained in $a^2_{\text{basin}}(T)$, we have no

[6]The total runtime was ca. one month for each temperature on a DEC XP1000.

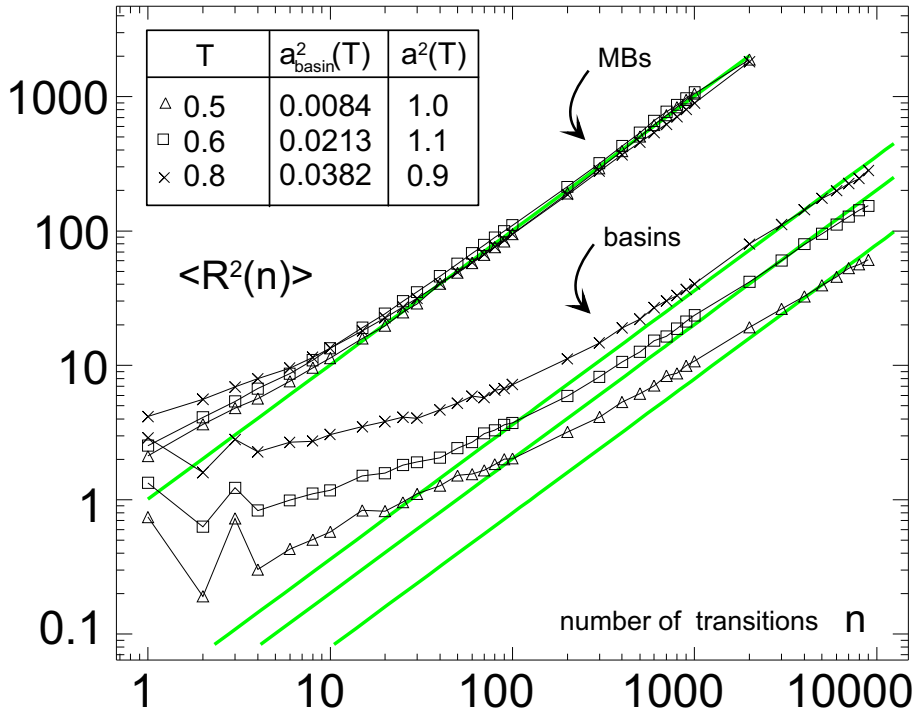

Figure 4.11: Squared displacement after n single-basin jumps for the temperatures $T = 0.5, 0.6$, and 0.8 (lower curves). The upper curves correspond to MBs jumps (copied from Fig. 4.7). Data stem from runs with high-frequent minimization (every 10 MD steps). Lines of slope 1 have been included.

contradiction to Eq. 4.5, which is valid for basins as well as MBs. Thus, although computationally demanding, the single-basin waiting times are not very useful for the comprehension of $D(T)$.

Single-basin *vs.* **MB WTDs - the short-time decay.** It is also instructive to consider the single-basin WTDs, see Fig. 4.13. Here we are interested in their short-time behavior, which follows a power law with exponent 3/2, for all temperatures. We would like to show that this finding can be related to the recrossings of basin borders.[7] If the system moves from one basin to another, it has to overcome some barrier between them. Having reached the top of such a barrier, the forces dragging the system back to the old basin or stirring it towards the new one become small. Thus, motion in the very vicinity of the (high-dimensional) basin border is quasi free along the direction perpendicular do the border. Since we use Langevin's equations of motion, this results in a dynamics which is close to free diffusion along that one

[7]The possibility of having some very small basins could be excluded as an explanation for the short τ by a more detailed analysis of entry and exit points on the basin borders.

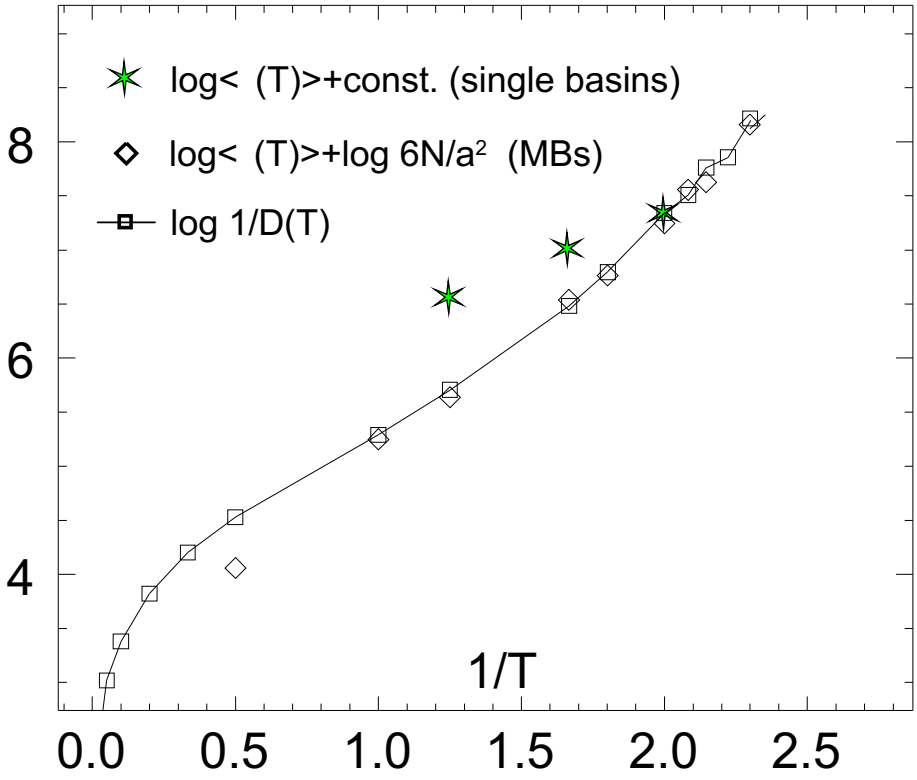

Figure 4.12: Arrhenius plot of the inverse one-particle diffusion coefficient $1/D(T)$ and the mean single-basin waiting time, multiplied by a constant. For comparison, we have included the mean MB waiting times, multiplied by a constant ($a^2 = 1.0$). Error bars are of the order of the symbol size.

direction in configuration space. It is then clear that recrossings of basin borders are highly probable, leading to a number of short visits to the basins of either side of the border. For one-dimensional diffusion along some coordinate y, starting in the origin, the first-passage times τ for the point y are distributed according to (Hughes, 1995)

$$\psi(\tau; y) = \frac{1}{(4\pi D\tau)^{3/2}} \exp\left(-\frac{y^2}{4D\tau}\right).$$

Evaluating this expression at $y = 0$, we obtain the distribution of first-return times, which is proportional to $\tau^{-3/2}$.

The fact that the single-basin WTDs are not normalizable is annoying. It is due to the assumption of an idealized, mathematical diffusion process, whose trajectory is a fractal object[8]. As the consequence of the $\tau^{-3/2}$ decay, we should find shorter

[8]In the real world, in contrast, one should introduce a lower cutoff time scale where self-similarity stops. Therefore, it would be interesting to study the WTDs in a Newtonian dynamics

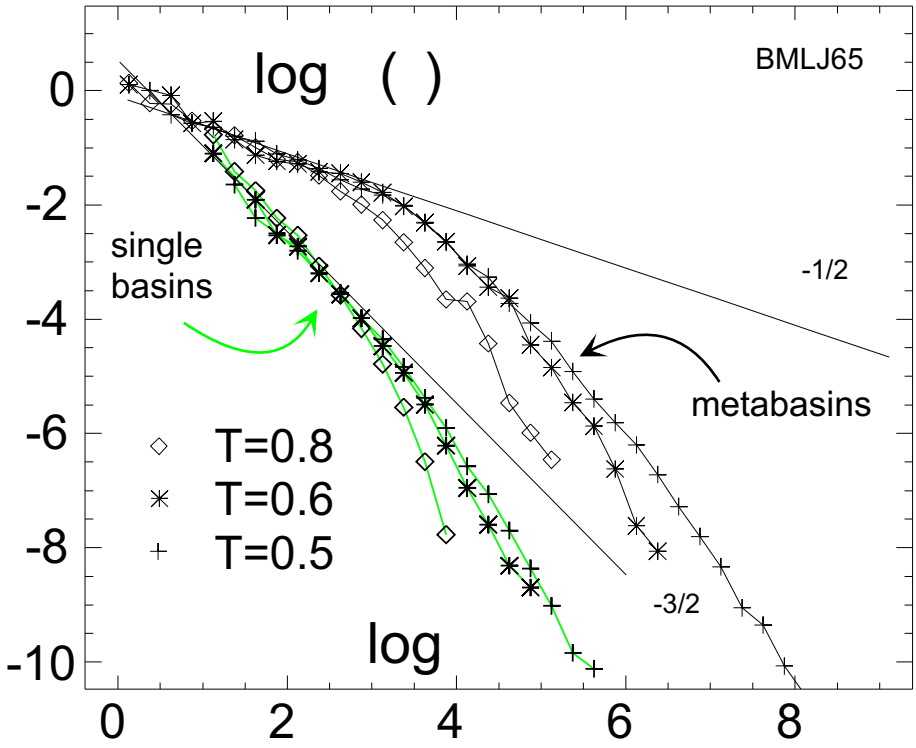

Figure 4.13: Distribution of metabasin and single-basin waiting times for the BMLJ65 at $T = 0.5, 0.6$, and 0.8. Auxiliary lines corresponding to power-laws have been included.

and ever shorter basin residence times by using smaller elementary time steps in our simulations. The basin $\langle\tau\rangle_\varphi$ therefore depends on our integration time step, too! This renders the single-basin description even less attractive. On the level of MBs, again, no problems arise: Since the WTDs decay approximately as $\tau^{-1/2}$ at short times, extremely short waiting times do not contribute much to the average $\langle\tau\rangle_\varphi$ and also the normalization is uncritical.

The MB WTDs of the BMLJ65, determined from the simulation runs with high-frequent minimization, are shown in Fig. 4.13(a). The most important observation is that they are identical to the WTDs depicted in Fig. 4.9, which were computed with the help of the interval-bisection technique. Thus –as expected on the level of MBs– high-frequent minimizations do not yield any new information.

We finally note that, at the moment, we do not have a strict explanation for the short-time behavior $\propto \tau^{-1/2}$ of the MB WTDs. At this point, we can only state that the slower decay is very plausible since the MB construction eliminates the back-and-forth motion on basin borders, so that much less of the extremely short waiting times occur.

---

simulation, where - in contrast to our Langevin dynamics - the short-time regime is purely ballistic.

Chapter 5

From PEL Structure to Hopping

Looking for a quantitative link of bulk diffusion $D(T)$ to PEL properties, we have investigated hopping dynamics on the PEL in great detail in chapter 4. A priori, temporal and spatial aspects of hopping events had to be considered, the former in the shape of the waiting time distribution (WTD) of jumps, the latter by the jump lengths and directions, and correlations thereof. We found that strong backward correlations of jumps arise from the organization of minima into superstructures, which we have called metabasins (MB). MBs were identified with the help of a straightforward algorithm such that close-by minima between which the system performs several back- and forth jumps are identified as a single MB. Then, indeed, hopping among MBs was found to be close to a random walk with a distribution $\varphi(\tau;T)$ of MB waiting times. Motivated by this fact, we have expressed $D(T)$ in the simple form,

$$D(T) = \frac{a^2}{6N\,\langle\tau(T)\rangle}, \tag{5.1}$$

with the mean waiting time $\langle\tau(T)\rangle$ and the *effective* jump length $a(T)$. With this ansatz, we anticipated that waiting times would carry the major part of the temperature dependence. Indeed, $a(T)$ turned out to be constant for $T < 2T_c$, which is why we have dropped the argument of $a(T)$ here. Eq. 5.1 constitutes an important step towards the understanding of diffusion in supercooled liquids: It suffices to look for the physics behind MB waiting times, spatial details of hopping being expressed by a single constant.

On might wonder whether there is much use in expressing one dynamical quantity by another. However, the MB waiting times are especially pertinent for an analysis in the PEL spirit. The reason for this can be understood at the simple example of relaxation in a one-dimensional double-well potential: We consider the behavior at low temperatures where there is a time-scale separation between vibrational motion and relaxation from one well to the other. We may then use

transition-state theory to compute the rates from the barrier height and the local vibrational properties of the stationary states only (Hänggi et al., 1990). More complicated, non-local information on the shape of the potential is not needed. Transferred to the high-dimensional case of our BMLJ liquid, we shall predict MB lifetimes from local PEL properties, too, most notably, from barrier heights. If there were an additional temperature dependence of jump lengths, we would have to include the sizes of MBs into our analysis. Evidently, this would render the overall picture much more complicated. Instead, the results of chapter 4 indicate that the notion of random jumps between traps of equal size is quite appropriate.

As a consequence of the slowly decaying WTDs, the mean value $\langle\tau(T)\rangle$ has been found to be dominated by the few, very long waiting times. In other words, the temperature dependence of $D(T)$ follows alone from the durations of trapping in the very stable MBs. These results were obtained for the small binary Lennard-Jones mixture of $N = 65$ particles. For a macroscopic system, which, due to its dynamic heterogeneity (Sillescu, 1999), contains many slow and fast subsystems in parallel, this implies the dominance of slow regions in the temperature dependence of $D(T)$.

The logical continuation along this line of thinking is to relate MB lifetimes to the PEL topography. The most prominent characteristics of a MB is, of course, its energy ϵ_{MB}, which is defined as the lowest energy of all its constituent minima. It is then natural to introduce the mean MB lifetime $\langle\tau(\epsilon_{\mathrm{MB}};T)\rangle$ at constant ϵ_{MB}. Knowledge of $\langle\tau(\epsilon_{\mathrm{MB}};T)\rangle$, together with the population of MBs,

$$p(\epsilon_{\mathrm{MB}};T) = \langle\delta(\epsilon_{\mathrm{MB}}(t) - \epsilon_{\mathrm{MB}})\rangle_T\,,$$

is sufficient to calculate $\langle\tau(T)\rangle$ and thus $D(T)$, as we will show now. We write

$$\langle\tau(T)\rangle = \int \mathrm{d}\epsilon_{\mathrm{MB}}\,\langle\tau(\epsilon_{\mathrm{MB}};T)\rangle\,\varphi(\epsilon_{\mathrm{MB}};T), \tag{5.2}$$

where $\varphi(\epsilon_{\mathrm{MB}};T)$ is the distribution of MBs visited at temperature T. We will see that this decomposition can be achieved by a detailed analysis of the hopping dynamics. Since $p(\epsilon_{\mathrm{MB}};T)$ denotes the probability that at a given time the system is in a MB with energy ϵ_{MB}, it is proportional to $\varphi(\epsilon_{\mathrm{MB}};T)$ and the time $\langle\tau(\epsilon_{\mathrm{MB}};T)\rangle$ the system remains in MBs of this energy. With the appropriate normalization one gets

$$p(\epsilon_{\mathrm{MB}};T) = \frac{\langle\tau(\epsilon_{\mathrm{MB}};T)\rangle}{\langle\tau(T)\rangle}\varphi(\epsilon_{\mathrm{MB}};T). \tag{5.3}$$

From Eqs. 5.1, 5.2 and 5.3, it immediately follows the representation

$$D(T) = \frac{a^2}{6N}\left\langle\frac{1}{\langle\tau(\epsilon_{\mathrm{MB}};T)\rangle}\right\rangle_T. \tag{5.4}$$

Here, $\langle ... \rangle_T$ denotes the canonical time average (w.r.t. $p(\epsilon_{\mathrm{MB}}; T)$), while $\langle ... \rangle$ is the average over MBs. Hence,

$$\{\langle \tau(\epsilon_{\mathrm{MB}}; T) \rangle \,,\; p(\epsilon_{\mathrm{MB}}; T)\} \rightarrow \langle \tau(T) \rangle \rightarrow D(T), \tag{5.5}$$

where the second implication has been established in chapter 4. For temperatures $T < 2T_c$, the population $p(\epsilon_{\mathrm{MB}}; T)$ is nearly identical to $p(\epsilon; T)$, as we will see in section 5.1. The latter distribution has been extensively discussed in chapter 3. It is a purely static quantity that can be derived from the approximately gaussian number density $G_{\mathrm{eff}}(\epsilon)$. Thus, the population of MBs,

$$p(\epsilon_{\mathrm{MB}}; T) \approx p(\epsilon; T) \propto G_{\mathrm{eff}}(\epsilon) e^{-\beta\epsilon}, \qquad T < 2T_c \tag{5.6}$$

can be expressed by three parameters describing the global PEL structure. In the present chapter, we focus on $\langle \tau(\epsilon_{\mathrm{MB}}; T) \rangle$, our goal being to deduce it from the local barriers around MBs. If this succeeds, we have established the following connection,

$$\text{local + global PEL structure} \rightarrow \text{long-time dynamics},$$

which, in our opinion, pushes the understanding of diffusion in supercooled liquids a step further.

We proceed as follows. Firstly, we extract mean MB lifetimes from ordinary simulations, in order to have in hands the quantities of interest (section 5.1). We start with the relaxation from four single, randomly selected MBs. By an exhaustive sampling of these MBs, we will be able to get some first insights into MB topology. Then, many MBs of fixed energy are considered and their lifetimes $\langle \tau(\epsilon_{\mathrm{MB}}; T) \rangle$ are calculated. Secondly, we relate MB lifetimes to PEL structure, by quantifying the MB depths, or effective barriers, which determine the temperature dependence of $\langle \tau(\epsilon_{\mathrm{MB}}; T) \rangle$ (section 5.3). The physical scenario which will emerge from the results of this chapter implies that MBs can be regarded as traps, surrounded by high barriers. From exhaustive explorations of PEL connectivity (Doye and Wales, 2002) it turned out that due to the high dimensionality of configuration space the number of escape paths from every minimum is enormous. Thus, one may anticipate that the effective barrier to leave a specific MB results as a complex superposition of individual escape paths. Therefore, enormous numerical effort is required to quantify their multitude for many different MBs.

Note that the whole analysis will be carried out in the spirit of activated barrier crossing. The extent to which this is present in supercooled liquids is quite disputed in literature. However, we will show that for temperatures in the landscape-influenced regime below $2T_c$, the apparent activation energy

$$E_{\mathrm{app}}(\epsilon_{\mathrm{MB}}; T) = \frac{\mathrm{d}}{\mathrm{d}\beta} \ln \langle \tau(\epsilon_{\mathrm{MB}}; T) \rangle \,, \tag{5.7}$$

can indeed be identified with PEL barriers much larger than k_BT which the system encounters when leaving a MB. Thus, together with Eq. 5.4, we will find that the activated escape out of deep traps is the physical mechanism behind diffusion.

To our knowledge, such a connection between dynamics and PEL barriers has never been established for a fragile glass former. In contrast, for SiO_2, the apparent activation energy of diffusion below T_c could be related to the simple breakage of $Si-O$ bonds (McMillan et al., 1994; Horbach and Kob, 1999).

The organization of the chapter is as follows. Section 5.1 deals with the computation of apparent activation energies from relaxation dynamics. The corresponding energy barriers will be addressed in section 5.3, after introducing our technique for finding transition states (section 5.2). In section 5.4, we independently demonstrate that barriers and associated reaction paths indeed govern relaxation. Finally, we discuss further aspects of our results in section 5.6. All data given in this chapter stem from the BMLJ65.

5.1 Activation Energies from Metabasin Lifetimes.

As noted above, the temperature dependence of $D(T)$ is dominated by the long-lived MBs. Generally, these are low-lying MBs, i.e. deep traps in the PEL. Since different MBs differ in their stability, a statistical treatment will be needed. As a first step, however, we restrict ourselves to the investigation of single MBs. Afterwards, we address the general behavior of MBs at given depth ϵ_{MB}. This will not only involve the mean lifetimes $\langle\tau(\epsilon_{\mathrm{MB}};T)\rangle$, but also the distribution over MBs at temperature T, $\varphi(\epsilon_{\mathrm{MB}};T)$.

Activation Energies for Single MBs. The relaxation times computed in this section do not stem from regular, linear simulation runs, but are obtained by artifically placing the system in a specific MB and waiting for its escape ('escape runs'). The algorithm for the MB lifetime construction (cf. section 4.2) implicitly assumes that MBs finally have been left. In other words, the algorithm may not be used to determine the time where to stop the simulation due to successful escape. Fortunately, we can avoid running into this paradoxical situation by judging from an independent criterion whether an escape has been completed: if the distance of the instantaneous minimum to the starting position is greater than $d_{\max} = 4$, returning to the original basin can practically be excluded (see section 5.3 for a justification of $d_{\max} = 4$). Then, by applying the MB construction algorithm to the escape run, we obtain the lifetime of the MB.

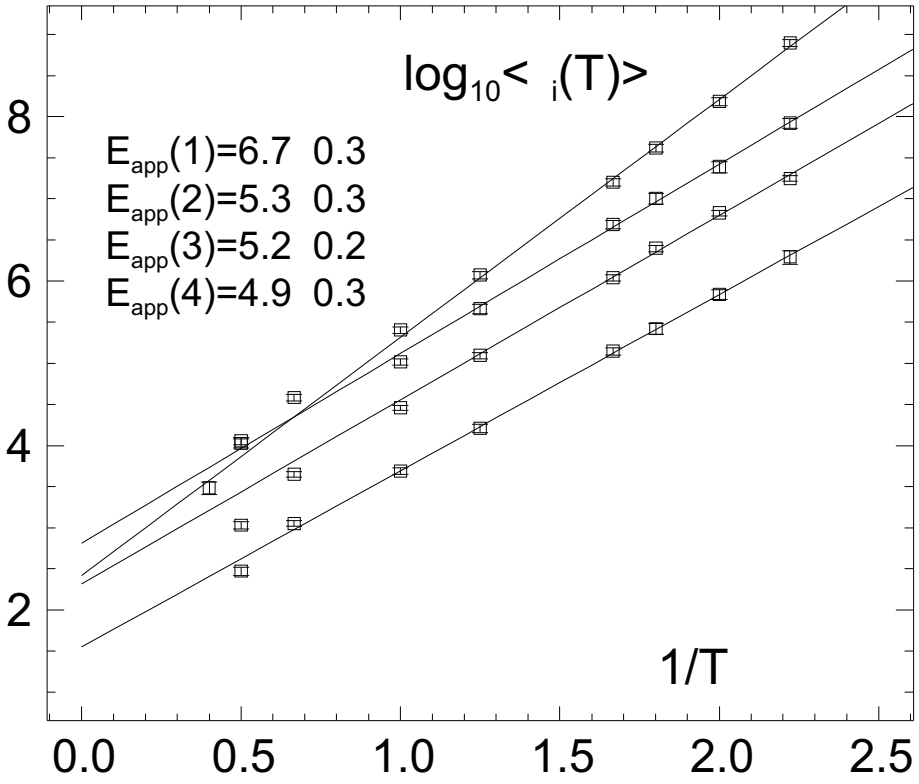

Figure 5.1: Mean lifetimes of four low-lying, randomly selected metabasins, computed from repeated escape runs ($\epsilon_{\mathrm{MB}} = -301.64, -300.47, -300.16$, and -300.74, from top to bottom). The number of runs are 85,59,175, and 105, from top to bottom. Arrhenius fits work well in the temperature range $T \leq 1 \approx 2.2T_c$, the corresponding activation energies are given in the figure. Curves have been shifted vertically by $0.5(4 - i)$ orders of magnitude for better inspection.

We analyzed four low-lying ($\epsilon_{\mathrm{MB}} < -300$), randomly selected MBs in greater detail. By repeated starts from the bottom of the MBs, we computed the mean lifetimes $\langle \tau_i(T) \rangle$ as a function of temperature. From Fig. 5.1, we see that the relaxations from all MBs follow nicely an Arrhenius law. We note that, due to starting at minima, a short intra-basin equilibration time[1] has been subtracted from the raw $\langle \tau_i(T) \rangle$.

The fact that an Arrhenius form of $\langle \tau(\epsilon_{\mathrm{MB}}; T) \rangle$ is observed indicates that the barriers do not change any further upon lowering temperature. Put differently, MBs serve as traps surrounded by barriers with heights around $E_{\mathrm{app}}(i) = \mathrm{d} \ln \langle \tau_i(T) \rangle / \mathrm{d}\beta$. We will see in section 5.3 that this is indeed correct. Since $E_{\mathrm{app}}(i)/k_{\mathrm{B}}T_c > 10$, this

[1]Starting from the bottom of different basins at $t = 0$, we computed the potential energy autocorrelation function, $\langle \delta V(0) \delta V(t) \rangle / \langle \delta V(0)^2 \rangle$. Its decay yields the relaxation time $\tau_{\mathrm{mol}} \approx 40$, which turns out to be temperature independent.

implies a strongly activated dynamics near T_c.

Activation Energies *vs.* **MB energies.** As a further step, we analyze the mean relaxation time from MBs with the same energy, $\langle\tau(\epsilon_{\rm MB};T)\rangle$; see Eq. 5.2. Clearly, the low $\epsilon_{\rm MB}$ are not populated at high temperatures so that regular simulation does not yield $\langle\tau(\epsilon_{\rm MB};T)\rangle$ over a wide temperature range. We therefore artificially place the system in the desired MBs (in the lowest minima $\epsilon_{\rm MB}$ thereof) and measure the escape times as a function of temperature. Averaging over many different MBs, we obtain $\langle\tau(\epsilon_{\rm MB};T)\rangle$. Results are shown in Fig. 5.2 as a function of $\epsilon_{\rm MB}$. Below $T=1$, all relaxation times display Arrhenius behavior. Thus, the apparent activation energies $E_{\rm app}(\epsilon_{\rm MB};T)$, Eq. 5.7, are temperature independent. In the following we will therefore omit the second argument. Thus, we can write

$$\langle\tau(\epsilon_{\rm MB};T)\rangle = \tau_0(\epsilon_{\rm MB})e^{\beta E_{\rm app}(\epsilon_{\rm MB})}. \tag{5.8}$$

As expected, the properties of MBs as expressed by $E_{\rm app}(\epsilon_{\rm MB})$ significantly depend on their ground state energy $\epsilon_{\rm MB}$.

We can interpret $E_{\rm app}(\epsilon_{\rm MB})$ as the mean effective depth of MBs at $\epsilon_{\rm MB}$. No deeper traps than $\epsilon_{\rm MB}\approx -302$ have been found (compare Fig. 3.2). A simple statement for the depths of traps would follow if the rims of all traps were at the same level $\epsilon_{\rm th}$. The consequence would be $E_{\rm app}(\epsilon_{\rm MB})=\epsilon_{\rm th}-\epsilon_{\rm MB}$, for all $\epsilon_{\rm MB}<\epsilon_{\rm th}$. This simple scenario is ruled out by the data, see Fig. 5.2(b). Actually, a more complicated energy dependence of $E_{\rm app}(\epsilon_{\rm MB})$ is expected from the very fact that the system - despite its small size - is not a completely cooperative unit.

The fact that we still observe Arrhenius-like relaxation in Fig. 5.2 indicates that the variation of trap depths at constant $\epsilon_{\rm MB}$ is not large, compare $E_{\rm app}(i)$ from Fig. 5.1. Otherwise, $E_{\rm app}(\epsilon_{\rm MB};T)$ would increase upon decreasing temperature, due to the more and more dominant, extremely deep traps. In contrast, trap depths at constant $\epsilon_{\rm MB}$ seem to be rather well defined by $\epsilon_{\rm MB}$, which suggests the existence of some underlying topological principle.

As seen from Fig. 5.2(c), the pre-factor $\tau_0(\epsilon_{\rm MB})$ has no strong dependence on $\epsilon_{\rm MB}$. From high energies, it decreases at most an order of magnitude and seems to level off below $\epsilon_{\rm MB}=-297$. Hence, for the range of energies that dominate $\langle\tau(T)\rangle$ at low temperatures, it can be considered constant within error bars, see below. In contrast to $E_{\rm app}(\epsilon_{\rm MB})$, we will not be able to deduce $\tau_0(\epsilon_{\rm MB})$ from PEL structure. Its weak variation is therefore quite fortunate.

Population of MBs. We will now analyze the second factor of the integrand in Eq. 5.2, $\varphi(\epsilon_{\rm MB};T)$. The distributions are shown in Fig. 5.3(a). The variation of

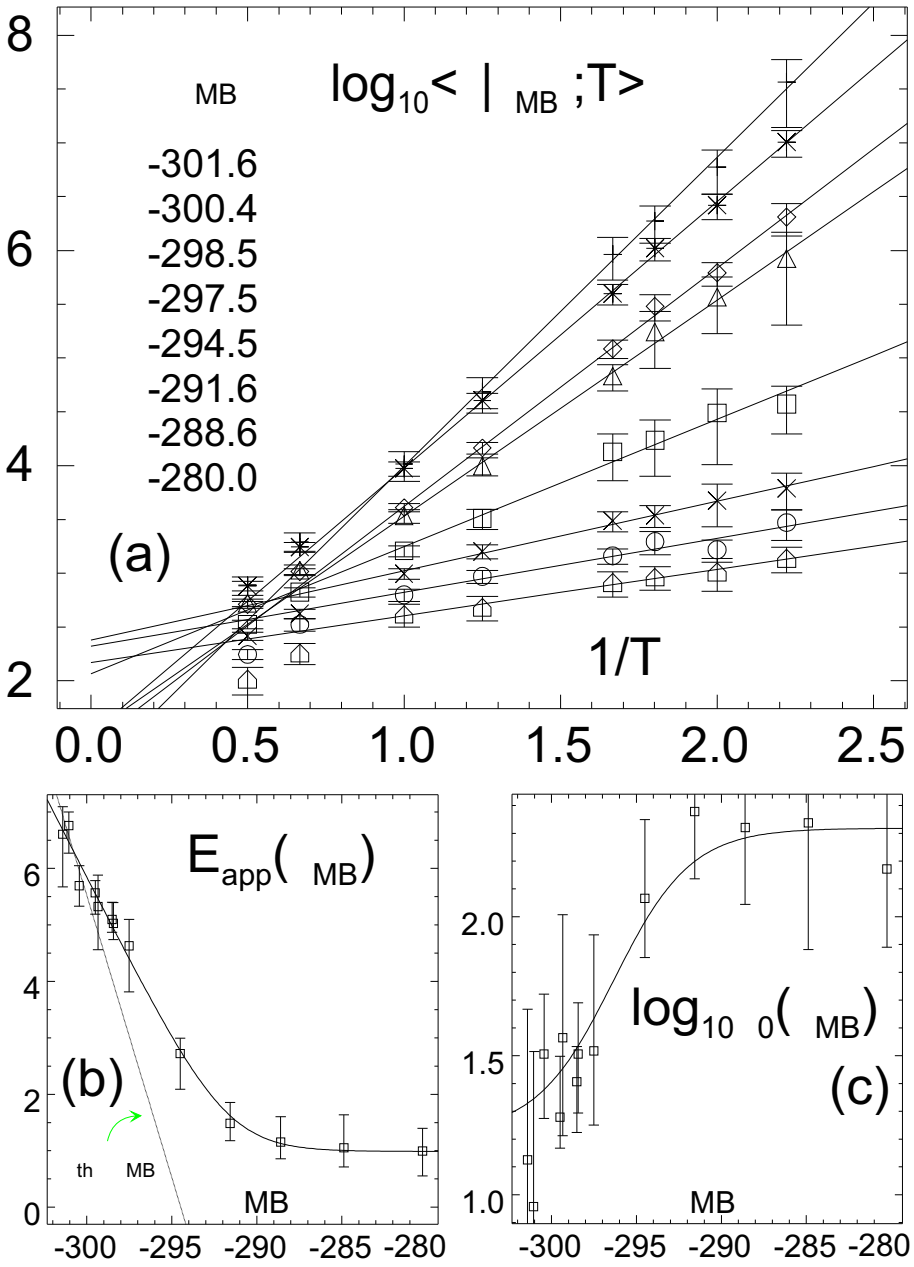

Figure 5.2: (a) Arrhenius plot of mean MB lifetimes $\langle\tau(\epsilon_{\rm MB};T)\rangle$, for different $\epsilon_{\rm MB}$. A MB equilibration time of $\tau_{\rm mol} = 40$ was subtracted. Straight lines are fits of the form Eq. 5.8. (b) apparent activation energies $E_{\rm app}(\epsilon_{\rm MB})$. (c) pre-factors $\tau_0(\epsilon_{\rm MB})$. Curved lines are interpolations of the data.

$\varphi(\epsilon_{\rm MB};T)$, as given by its mean value (Fig. 5.3(b)), is much weaker than the variation of $p(\epsilon_{\rm MB};T)$. After Eq. 5.3, this is because the MB residence times $\langle\tau(\epsilon_{\rm MB};T)\rangle$ contain a certain part of the temperature dependence of $p(\epsilon_{\rm MB};T)$. From Eqs. 5.3

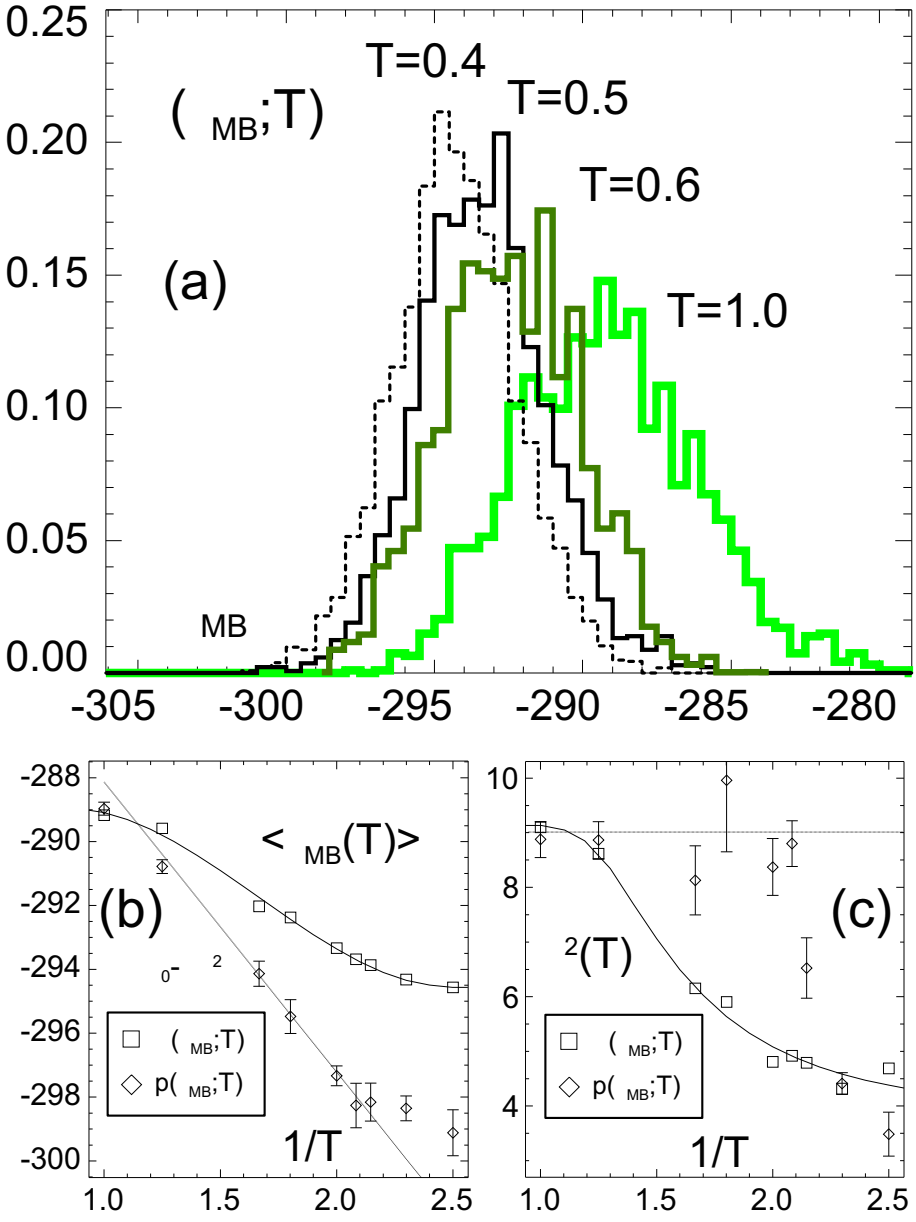

Figure 5.3: (a) distribution $\varphi(\epsilon_{\rm MB};T)$ of MB energies, for four temperatures. (b) Mean energies, from $\varphi(\epsilon_{\rm MB};T)$ and from $p(\epsilon_{\rm MB};T)$. (c) Variances of the distributions φ and p. Polynomial fits to the data are shown in (b) and (c). Straight lines are predictions for p from an ideally gaussian distribution $G_{\rm eff}(\epsilon_{\rm MB})$ (mean ϵ_0, variance σ^2). The deviations from the gaussian prediction at the lowest T are probably caused by insufficient statistics, as discussed in section 5.5.

and 5.8, one concludes[2] that the constancy of the distribution $\varphi(\epsilon_{\rm MB};T)$ is equivalent

[2]We assume that the distribution of MB energies follows from that of the single basins, i.e. $p(\epsilon_{\rm MB};T) \approx \exp(-\beta\epsilon_{\rm MB})G_{\rm eff}(\epsilon_{\rm MB})/z(T)$ (Eq. 5.6), where $z(T) = \int {\rm d}\epsilon_{\rm MB} \exp(-\beta\epsilon_{\rm MB})G_{\rm eff}(\epsilon_{\rm MB})$.

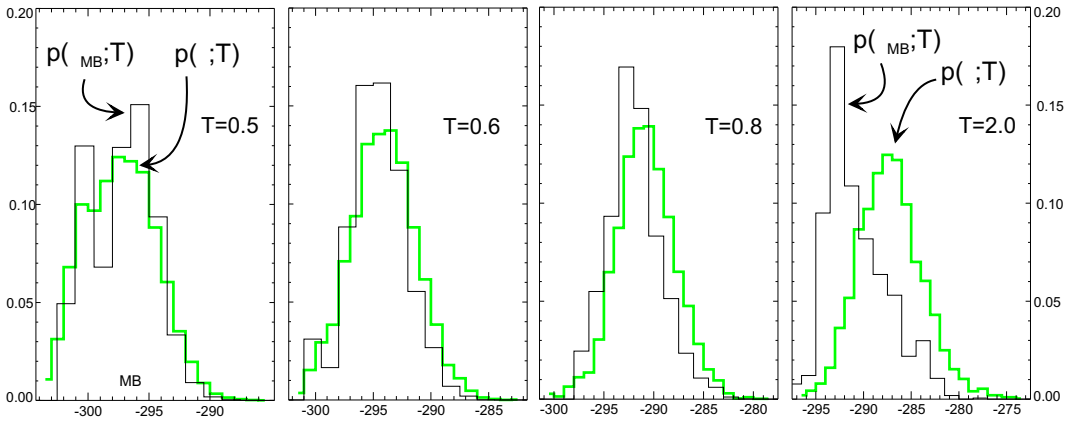

Figure 5.4: Population of MBs energies, $p(\epsilon_{\mathrm{MB}};T)$, compared with the single-basin $p(\epsilon;T)$.

to having $E_{\mathrm{app}}(\epsilon_{\mathrm{MB}}) = \epsilon_{\mathrm{th}} - \epsilon_{\mathrm{MB}}$, with some constant ϵ_{th}. This simple relation arises, for instance, in Bouchaud's trap model (see appendix D). There, the rims of all traps lie at the same height, namely, zero. In the BMLJ65, $E_{\mathrm{app}}(\epsilon_{\mathrm{MB}})$ shows a different behavior (Fig. 5.2(b)), so that the residual temperature dependence of $\varphi(\epsilon_{\mathrm{MB}};T)$ has to be expected.

What concerns $p(\epsilon_{\mathrm{MB}};T)$, it turns out that $p(\epsilon_{\mathrm{MB}};T)$ is nearly identical to the distribution of minima, $p(\epsilon;T)$, within the landscape-influenced/dominated regime (i.e. for $T < 2T_c$). In Fig. 5.4, we see that at $T = 2$, $p(\epsilon_{\mathrm{MB}};T)$ is shifted to the left with respect to $p(\epsilon;T)$. Already at $T = 0.8$, both distributions nearly agree, whereas at still lower temperatures they can be considered identical within statistical error. Here we give a plausible explanation for these findings, noting that a deeper statistical investigation of the basin-MB relation would be necessary to back (or not) the following argument. Since the energy of a MB is defined as that of its lowest minimum, the mapping from basins to MBs transfers the weights of the elevated minima of a MB to its lowest one, which lies at ϵ_{MB}. This explains the shift between $p(\epsilon_{\mathrm{MB}};T)$ and $p(\epsilon;T)$. First consider the case of low temperatures, say $T < 2T_c$. At high ϵ_{MB}, no pronounced MBs are observed (Fig. 4.5), so that the transition from basins to MBs has little effect. Considering a deep MB with generally many minima, we have seen that the population is concentrated around

---

After Eq. 5.3, the T-independence of $\varphi(\epsilon_{\mathrm{MB}};T)$ is equivalent to

$$0 = \frac{\mathrm{d}}{\mathrm{d}\beta}\left(\ln p(\epsilon_{\mathrm{MB}};T) + \ln\langle\tau(T)\rangle - \ln\langle\tau(\epsilon_{\mathrm{MB}};T)\rangle\right) = -\epsilon_{\mathrm{MB}} + \frac{\mathrm{d}}{\mathrm{d}\beta}\left(-\ln z(T) + \ln\langle\tau(T)\rangle\right) - E_{\mathrm{app}}(\epsilon_{\mathrm{MB}}).$$

Thus, $E_{\mathrm{app}}(\epsilon_{\mathrm{MB}}) = f(T) - \epsilon_{\mathrm{MB}}$, with an ϵ_{MB}-independent function $f(T)$. Since $E_{\mathrm{app}}(\epsilon_{\mathrm{MB}})$ does not depend on temperature, this function must be a constant which we denote ϵ_{th}.

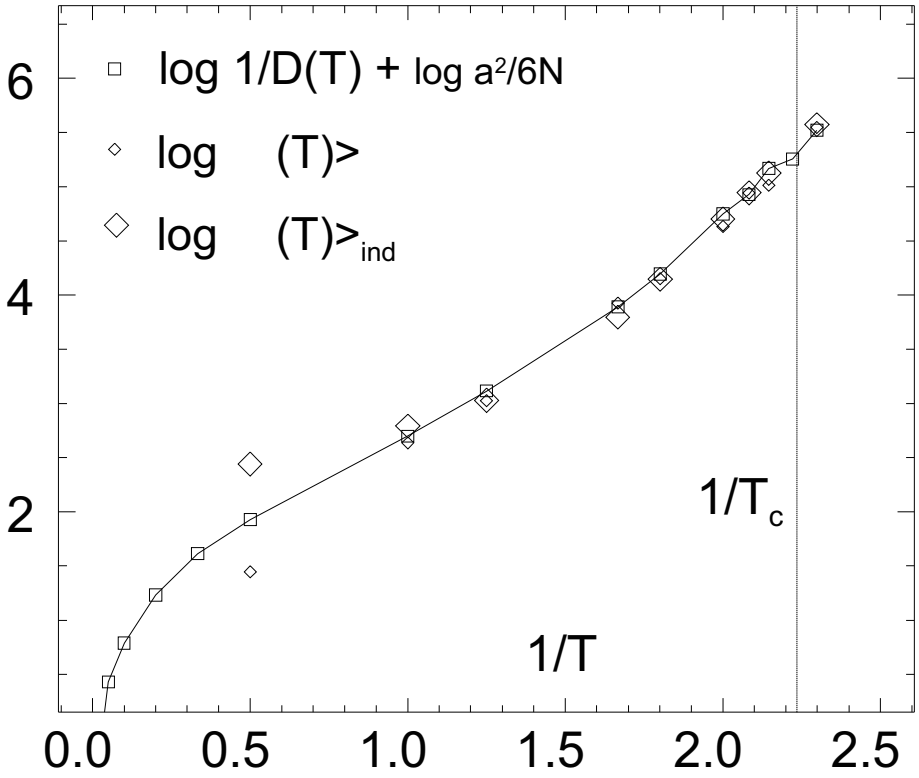

Figure 5.5: Arrhenius plot of the mean waiting time $\langle\tau(T)\rangle$ versus the indirectly determined counterpart, $\langle\tau(T)\rangle_{\rm ind}$. For comparison, we also show the inverse one-particle diffusion coefficient $1/D(T)$ multiplied by a constant ($a^2 = 1.0$), see chapter 4. Error bars are of the order of the symbol size.

$\epsilon_{\rm MB}$. Again, switching from basins to metabasins does not produce dramatical changes in the distributions. This is why $p(\epsilon_{\rm MB};T)$ and $p(\epsilon;T)$ agree at low T. At higher temperatures, in contrast, the elevated minima of MBs become populated, so that the transition from basins to MBs transfers more weight to the bottom of the MBs. In this way, one may understand the larger deviation between $p(\epsilon_{\rm MB};T)$ and $p(\epsilon;T)$ seen in Fig. 5.4, at $T = 2$.

As a consistency check, we use the data from Fig. 5.2 and 5.3 to reproduce $\langle\tau(T)\rangle$ indirectly via Eqs. 5.2 and 5.8 (denoted $\langle\tau(T)\rangle_{\rm ind}$). The match with $\langle\tau(T)\rangle$ is not completely trivial since the data for $\langle\tau(T)\rangle$ and $\varphi(\epsilon_{\rm MB};T)$ were gathered from a linear simulation run, while $\langle\tau(\epsilon_{\rm MB};T)\rangle$ results from selected MBs of certain $\epsilon_{\rm MB}$, where the system has been artificially placed. As shown in Fig. 5.5, the agreement of $\langle\tau(T)\rangle$ and $\langle\tau(T)\rangle_{\rm ind}$ is good for $T \leq 1$ within the possible accuracy. Note that there is no free fit parameter between them. The deviation at $T = 2$ can be explained by the fact that $\langle\tau(\epsilon_{\rm MB};T)\rangle$, above $T = 1$, and especially for the high $\epsilon_{\rm MB}$, departs from Arrhenius behavior (see Fig. 5.2(a)), so that the parametrization of Eq. 5.8 is

no longer valid.

So far, all barriers or trap depths have been derived indirectly, from the temperature dependence of waiting times. A link to the PEL structure is still lacking. For instance, the activation energies $E_{\rm app}(i)$ of this section are expected to reflect the local topography of the selected MBs. Indeed, they can be identified from the barriers of escape paths, as will be demonstrated in section 5.3.

5.2 Non-Local Ridge Method for Finding Transition States.

First of all, the barriers between *neighboring* minima are of interest. These are known once we have in hands the corresponding transition states (TSs).

We now describe how to determine those from the simulation, by what we call the (non-local) ridge method. The principle idea is that TSs are local minima of basin borders. They can be pictured as the lowest points of mountain ridges on the PEL. If the system crosses a basin border at time t, the steepest descent path starting from $x(t)$ should end up in a TS, see (Ionova and Carter, 1993). In practice, however, the descent will deviate from the ridge due to numerical error, finally ending up in one of the minima $\xi_0 \equiv \xi(t-)$ or $\xi_1 \equiv \xi(t+)$. As a way out, we let the system perform two descents in parallel, on either side of the basin border, as schematically depicted in Fig. 5.6. More specifically, if a transition happened at time t, interval bisection yields the configurations $x(t) \equiv y_0$ and $x(t + 1 \text{ MD step}) \equiv y_1$. From these, by further interval bisection on the straight line between y_0 and y_1, the distance to the border may be further reduced if necessary, resulting in two configurations, again called y_0 and y_1. Close as they are, they still belong to different basins. If we now let descend y_0 and y_1 in parallel, they first move along the ridge towards the transition state until they finally bend off to their respective minima. This separation is clearly not wanted, so from time to time we reduce their distance by interval bisection. After a few iterations (descents+interval bisection) the vicinity of the transition state is reached in most cases. We then use a short minimization of the auxiliary potential $\tilde{V} = \frac{1}{2}|F(x)|^2$ followed by a few steps of Newton-Raphson type, which bring the search for the TS to a quick convergence. Besides a vanishing force, the resulting configuration ζ has a Hessian matrix with one negative eigenvalue. After small displacements along the corresponding eigenvector, one reaches the adjacent minima via steepest descent. This yields the reaction path (RP) $\zeta(s)$, where s is a curvilinear parameter. We set $\zeta(0) = \zeta$, $\zeta(s_0) = \xi_0$, and $\zeta(s_1) = \xi_1$, where $s_0 < 0$ and $s_1 > 0$.

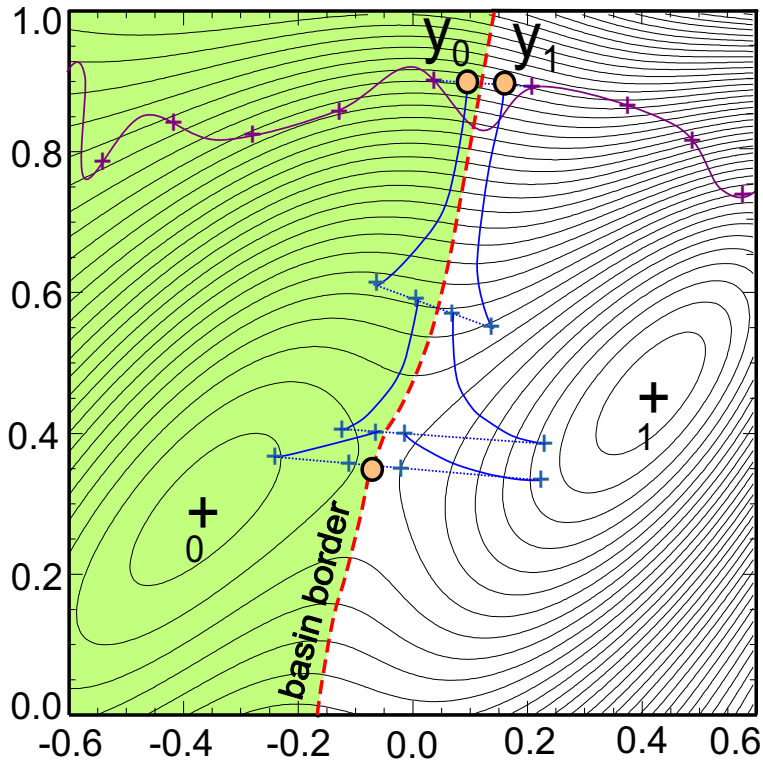

Figure 5.6: Sketch of the TS search with the ridge method.

It can happen, though, that no saddle between y_0 and y_1 is found, but that the interval bisection locates a third minimum. The basin border splits into two at this point, and no direct saddle between the initial and final minimum is available. Thus, we also have to split the descent along the basin border into two processes and then continue separately. If the two descents are successful without further bifurcations, we are finished and have the optimum reaction path which takes a detour via a third minimum. In such a situation, the RP is clearly not very useful. It has to be stressed that bifurcations are no artifacts of the ridge method, but a topological feature of some basin borders on the PEL. Fortunately, as a signature of strong anharmonicity, they are quite rare and happen to occur only in the high-energetic regions of the PEL. For the escapes from long-lived MBs, they are of no importance.

A similar algorithm is described in the literature (Ionova and Carter, 1993), which, instead of minimization and interval bisection, uses local maximization between y_0 and y_1 to prevent the configurations from moving apart. Although computationally less expensive, this method is not appropriate for our purpose. As an effect of the high dimensionality, the local shape of the PEL around y_0 and y_1 gives no direct clue to the membership to basins. When descending, one may thus loose

the important property of y_0 belonging to the basin of ξ_0 and y_1 belonging to that of ξ_1. This effect has indeed been reported in (Ionova and Carter, 1993).

In the literature, plenty of methods exist dealing with the computation of transition states. For our purpose, however, each of them has some kind of drawback, which we briefly discuss now. One kind of them starts from the knowledge of the initial and final minimum (Elber and Karplus, 1987; Matro et al., 1994; Deaven et al., 1996; Angelani et al., 2000b). Common to the latter methods is that, after a more or less educated guess for an initial trial RP, one iteratively improves the RP according to some prescription, e.g., the minimization of an action functional. Two sources of erroneous results have to be addressed in this connection. First, the two minima in question have to be true neighbors. This can only be verified by locating two points close to the basin border, e.g. by interval bisection of the initial trial path. The numerical cost is not small; for our ridge method, for instance, about one third of the calculation time is consumed by fixing y_0 and y_1 (depending on the minimization interval of the original MD run). Second, the iterative path optimization may become stuck in a local extremum, due to an unfortunate choice of the initial path.

The other kind of TS search methods start from an initial minimum and climb up to a transition state guided by the shape of the PEL. Just walking against the force, however, would be a fatal strategy, as one can see by turning the PEL upside down: ending up in a TS is numerically impossible, since one quickly runs into one of the PEL singularities (two or more identical particle positions). Eigenvector-following algorithms (Wales, 2001) overcome this defocusing of steepest ascent paths by walking into the direction of negative local PEL curvature. The 'activation-relaxation technique' by Mousseau and coworkers, in contrast, steps against the force in the direction leading away from the minimum, while descending the PEL perpendicular to that direction (Barkema and Mousseau, 1996). A drawback of the latter methods is that the choice for the next TS to mount is not well under control. From the minimum, a starting direction is chosen, either by purely random displacements or by some hard-sphere-like particle moves (Doye and Wales, 2002). Unfortunately, the number of escape directions from a minimum is generally very large (at least $O(Nd)$ as we found in the BMLJ65, see also (Doye, 2002)), whereas the majority of those is dynamically inaccessible at low T. Hence, eigenvector-following and activation-relaxation techniques yield many TSs which only negligibly contribute to relaxation rates. Striving for the simulation of low-temperature hopping dynamics based on these methods (Hernandez-Rojas and Wales, 2001; Mousseau, 2000; Ball and Berry, 1999), one may therefore suffer a considerable reduction of efficiency. In our point of view, this renders straightforward molecular simulation rather competitive for

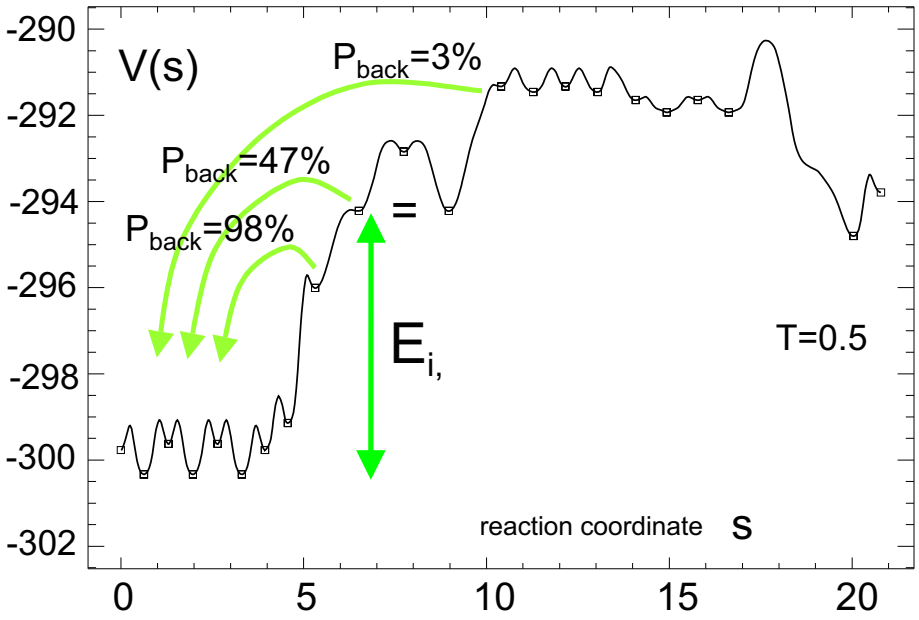

Figure 5.7: Potential energy along the reaction path $\zeta(s)$, which was calculated from the dynamics during 10^5 MD Steps, at the end of a typical MB of life span 8×10^6 MD Steps in the BMLJ65. The mapping of s to time is non-linear. The small barriers for $s < 5$ belong to fast intra-MB transitions. p_{back} denotes the probability of returning to the bottom of the MB. As a comparison, the potential energy at that temperature ($T = 0.5$) fluctuates around -249.3 ± 6.1!

many purposes.

Furthermore, we mention two complementary means of studying energy barriers. The 'lid' algorithm, proposed by Schön and coworkers (Wevers et al., 1999), is able to find upper bounds for the depths of single basins. By performing random walks below different potential energy thresholds and by regular minimizations, one is able to compute the elevation necessary for transitions to neighboring minima. From a more theoretical perspective, Schulz has specified a relation between transition rates and the overlap of vibrations in neighbouring basins (Schulz, 1998).

Finally, we remark that in the field of supercooled liquids, another method for locating *general stationary states* (saddles) has become quite fashionable. One defines the auxiliary potential $\tilde{V} = \frac{1}{2}|F(x)|^2$ and looks for its local minima. A detailed discussion of this method and a comparison to the ridge method is given in section 7.3.

5.3 Energy Barriers from PEL Topology.

Return Probabilities and Metabasin Definition. With the tools of interval bisection and TS search, we are now in the position to analyze the escapes from MBs in full detail. When a MB is left, we first resolve all minima visited during the escape. Second, all corresponding TSs and, if desired, reaction paths are calculated. An example is shown in Fig. 5.7. The successive RPs were spliced together to a long, multi-minima RP $\zeta(s)$. One might take the energy profile, $V(\zeta(s))$, depicted in the figure, for one of the common cartoons of a PEL. However, it rests upon real data. Berry and coworkers have produced similar charts for the relaxation of small atomic clusters towards their global minima (Ball et al., 1996; Ball and Berry, 1999). For $s < 5$ one can see the typical back-and-forth hopping among the ground minima of the MB. Obviously, the corresponding barriers are not large compared to $k_{\mathrm{B}}T = 0.5$. The escape starts at $s = 5$. The first minimum reached is very unstable as expected from the small backward barrier. Indeed, if we repeatedly start in this minimum and perform a number of short simulation runs (here: 99) with different random numbers, the system will return to the bottom of the MB with probability $p_{\mathrm{back}} = 98\%$ and leave the range of attraction only rarely. Thus, the escape is far from being complete at this stage. Going to the next minimum, the return probability decreases, but does not drop to zero. We say that the system is free if p_{back} is smaller than 50%. As the outcome of this investigation, we obtain the energy barrier surmounted before the first minimum with $p_{\mathrm{back}} < 50\%$ was reached, see below. The exits from other long-lived MBs mostly look the same as in the example, while the escape in one jump is not common. In other words, MBs usually have the form of a funnel with some ledges on the walls (Stillinger, 1995; Middleton and Wales, 2001). Minima with $p_{\mathrm{back}} > 50\%$ are said to belong to the MB. This criterion is reminiscent of the definition of dynamic bottlenecks introduced by Chandler and coworkers (Bolhuis et al., 2002).

An interesting property of a MB is its diameter d. It is defined as the maximum distance between its minima. For the MBs found in the simulation at $T = 0.5$, the distribution of diameters is depicted in Fig. 5.8. The delta-peak from single-minimum MBs has been omitted. No MB with $d > d_{\mathrm{max}} = 4$ has been found. As a consequence, if a minimum has a distance larger than d_{max} to some MB minimum, we can safely assume $p_{\mathrm{back}} \ll 50\%$. This criterion has already been used in section 5.1.

Based on these insights, we can now provide a more complete description of MBs (Fig. 5.9). First, the ground state of a MB has to be identified (kernel minimum), since the definition of p_{back} rests upon it. At low enough temperatures, the kernel minimum will certainly be visited during the MB lifetime, due to the very low barriers among the minima on the bottom of the MB. Second, for minima beyond the distance d_{max} from the kernel, we set p_{back} to zero. Third, the probability p_{back} for

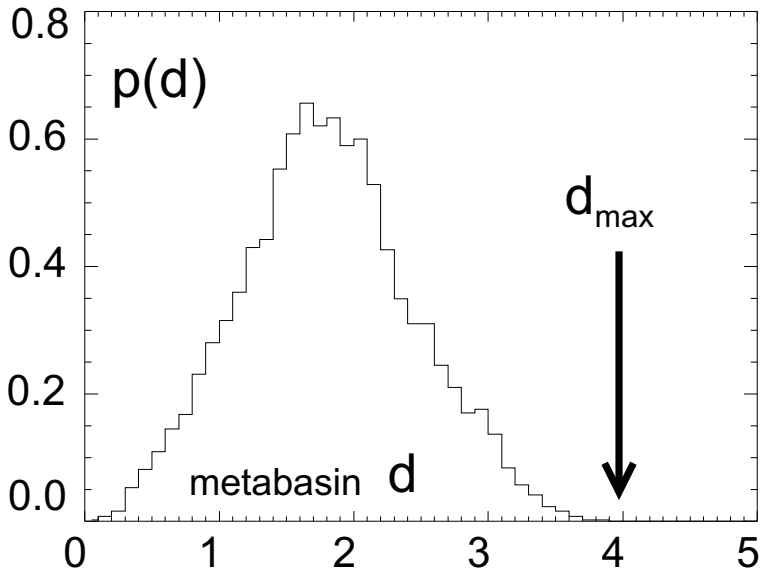

Figure 5.8: Distribution of MB diameters, d, defined as the maximum distance between all minima that were visited during a MB lifetime ($T = 0.5$, BMLJ65). The delta-peak from single-minimum MBs has been omitted.

returning to the kernel before reaching a distance greater than $d_{\max}$ can be assigned to every remaining minimum and -in principle- be computed by simulation. To this end, one repeatedly starts in the minimum and checks if a recurrence to the kernel occurs. Fourth, the minima with $p_{\text{back}} > 50\%$ are defined as the MB.

Please bear in mind that p_{back} will in general depend on temperature, since it is defined by the dynamics at a given T. Correlations among minima are expected to increase towards lower temperatures, implying that MBs are no static concept but rather grow with decreasing T. In Fig. 5.7, e.g., the minimum at $s \approx 6.5$ has the 'critical' value of $p_{\text{back}} \approx 47\%$ at $T = 0.5$. Although we do not know the details of PEL connectivity around this minimum, the small backward barrier suggests that the minimum would exceed $p_{\text{back}} = 50\%$ for still lower temperatures, thus joining the MB. However, we may also conceive some situations where a critical $p_{\text{back}} \approx 50\%$ is quite insusceptible to temperature changes. This is the case if backward and forward barriers are of about the same size. We will come back to that issue later.

We further note that the explicit computation of p_{back} can be extremely expensive. This is mainly the case when p_{back} is small, and complete escapes beyond $d_{\max}$ have to be awaited. However, the exact value of p_{back} is of no great interest. In fact, it suffices to know whether $p_{\text{back}} < 50\%$ or $p_{\text{back}} > 50\%$. This decision can often be reached to a high confidence with few trials.

The MB lifetime algorithm in section 4.2 is based on the detection of back-and-

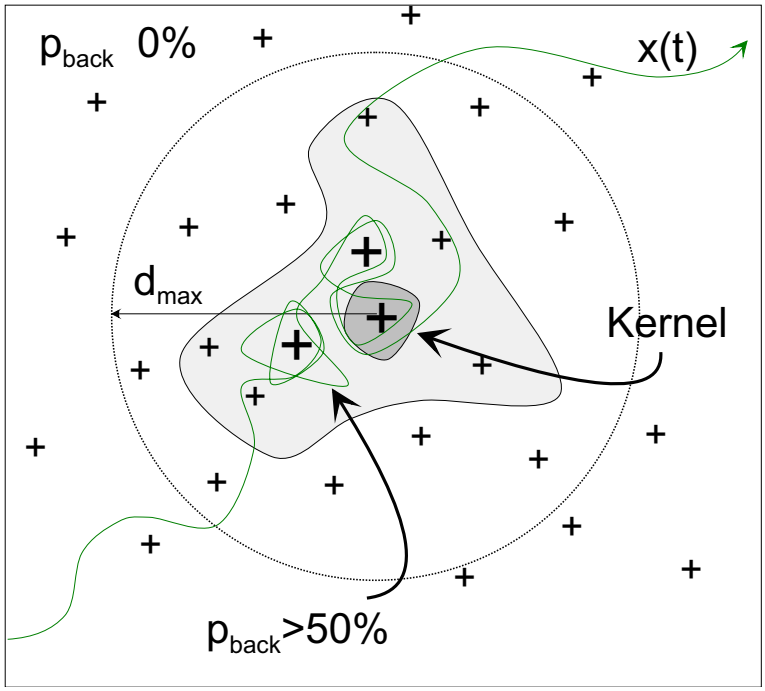

Figure 5.9: Sketch of the configuration space around a MB, crosses representing minima. Large crosses are the highly populated minima on the bottom of the MB. The shaded area comprises minima of high return probability to the kernel minimum ($p_{\text{back}} > 50\%$). By definition, these constitute the MB. The bent line is the system trajectory $x(t)$ entering and finally leaving the MB.

forth jumps between minima. One mostly observes the dominant minima on the bottom of the MBs, whereas the more elevated members are only weakly populated, see Fig. 5.9. If MB lifetimes are to be read from a simulation run, it suffices to notice when the set of dominant MB minima has been left, since the visits to the elevated minima at the end of the MB lifetime happen quite rapidly. Thus, the algorithm of section 5.1 reduces the MB to the most populated minima, which is sufficient for the purpose of lifetime calculation from a given simulation run. In contrast, for the *prediction* of MB relaxation behavior as pursued in this section, the minima close to the rim of MBs are of special interest. Their elevations from the bottom of the MB give the depth of the MB.

Barriers for Metabasin Relaxations. In the spirit of the above remarks, we will now carry out a systematic investigation of the energy barriers overcome when escaping MBs. The goal is to recover the apparent activation energies computed in section 5.1 from PEL topology.

The mean lifetime $\langle \tau_i \rangle$ of MB i can be expressed in terms of escape rates $\gamma_{i,\alpha}$ of

different relaxation channels α,

$$\langle \tau_i \rangle^{-1} = \sum_{\alpha} \gamma_{i,\alpha}. \tag{5.9}$$

In general, each $\gamma_{i,\alpha}$ reflects a multi-minima escape path

$$\xi_0 \xrightarrow{\zeta_{01}} \xi_1 \xrightarrow{\zeta_{12}} \xi_2 \ \ldots \ \xi_{M-1} \xrightarrow{\zeta_{M-1,M}} \xi_M \tag{5.10}$$

as the one shown in Fig. 5.7. Here ξ_0 is the kernel minimum ($\xi_a \neq \xi_0$, $a > 0$) and ζ_{ab} is the TS for $\xi_a \to \xi_b$. Suppose that the number M of jumps in the sequence Eq. 5.10 is large enough to completely quit the MB's range of attraction, i.e., $p_{\text{back}}(M) \approx 0$. For the escape shown in Fig. 5.7, e.g., $M \geq 7$ would be fine.

We further take for granted that the rates for single barrier crossings follow quantitatively -via transition state theory- from the height of barriers, $E_{ab} = V(\zeta_{ab}) - V(\xi_a)$ (the energy difference between the minimum ξ_a and the TS between a and b). Hence, rates g_{ab} for single transitions $\xi_a \to \xi_b$ are characterized by

$$g_{ab} \propto e^{-\beta E_{ab}}. \tag{5.11}$$

A justification for this assumption, even for temperatures above T_c, will be given in section 5.4.

Generally, the probability of upward jumps is small at low T. Hence, climbing out of a MB in a back-and-forth fashion (e.g., $\xi_a = \xi_{a+2}$ and $\xi_{a+1} = \xi_{a+3}$) is not probable. (This is reminiscent of the fact that the activated crossing of single potential barriers happens on a short time scale, i.e. in a rather straight way.) In contrast, *excursions* from the main path may happen. As shown in Fig. 5.7, the minimum at $s = 6.5$ is revisited at $s = 9$ after taking a look at another minimum ($s \approx 8$). The latter does not appear again later on. Clearly, running into such 'dead ends' should not contribute to the escape rate via the successful main path. We therefore eliminate such excursions from the sequence of minima, Eq. 5.10. From these remarks we take the liberty of assuming that no minimum appears more than once along the escape path,

$$\xi_a \neq \xi_b, \quad a \neq b. \tag{5.12}$$

We are now interested in the contribution of the path, Eq. 5.10, to the total escape rate, Eq. 5.9. Particularly, we have to consider the question of how many single transitions are relevant for the escape process. The probability to jump from minimum ξ_a to ξ_{a+1} is $g_{a,a+1}/g_a$, where g_a denotes the inverse lifetime of minimum ξ_a. The rate of escape via a longer pathway now is given by the rate of the first

jump times the probability that the minima ξ_a $(a = 1, ...M)$ are visited in correct order thereafter,

$$\gamma_{i,\alpha} = g_{01}\frac{g_{12}}{g_1}\frac{g_{23}}{g_2}...\frac{g_{M-1,M}}{g_{M-1}}. \tag{5.13}$$

In this expression, we have neglected the residence times in the elevated MB minima (ξ_1, ξ_2, ...) during the escape, which, at sufficiently low temperatures, are short as compared to the total MB lifetime. With the help of Eq. 5.11 one calculates

$$-\frac{\mathrm{d}}{\mathrm{d}\beta}\ln\gamma_{i,\alpha} = E_{01} + \sum_{a=1}^{M-1} p_{\mathrm{ret}}(a)(E_{a,a+1} - E_{a,a-1}), \tag{5.14}$$

where $p_{\mathrm{ret}}(a) = g_{a,a-1}/g_a$ is the probability to jump back to minimum $a-1$ from minimum a. In the derivation of Eq. 5.14, we have neglected a term proportional to $E_{a,a+1}$ minus the average barrier when jumping from a to a neighbouring minimum other than $a-1$. This term strictly vanishes when performing the final summation in Eq. 5.9. Moreover, we made use of Eq. 5.12.

One possibility for calculating activation energies from Eq. 5.14 would be to consider the complete paths, Eq. 5.10, where $p_{\mathrm{back}}(M) \approx 0$, and determine all terms in the sum of Eq. 5.14. However, an accurate computation of all the desired $p_{\mathrm{ret}}(a)$'s would even be more costly than the determination of the point where p_{back} changes from above to below 50%. We therefore use the following approximation of Eq. 5.14, which is in conformance with our previous definition of MBs: Let $m(T)$ be the first minimum along the path, Eq. 5.10, where $p_{\mathrm{back}} < 50\%$. Then, for all $a < m(T)$, we set $p_{\mathrm{ret}}(a)$ to unity, while for $a \geq m(T)$ (i.e. outside the MB), we let $p_{\mathrm{ret}}(a) = 0$. Thus,

$$\begin{aligned} -\frac{\mathrm{d}}{\mathrm{d}\beta}\ln\gamma_{i,\alpha} \approx E_{i,\alpha} &\equiv E_{01} + \sum_{a=1}^{m-1}(E_{a,a+1} - E_{a,a-1}) \\ &= \epsilon_{m-1} - \epsilon_0 + E_{m-1,m}, \end{aligned} \tag{5.15}$$

where $m = m(T)$. In this way, the terms $a < m(T)$ in Eq. 5.14 are given higher weights, whereas those of $a \geq m(T)$ are neglected. We will dwell on the quality of this approximation later on; for a more thorough discussion see (Saksaengwijit et al., 2002).

Note that, due to the temperature dependence of p_{back}, energy barriers $E_{i,\alpha}$ generally increase upon cooling: At high temperatures, in contrast, correlations among minima are small, such that MBs (even the low-lying) consist of only one minimum. This effect is included in Eq. 5.15 by the temperature dependence of $m(T)$.

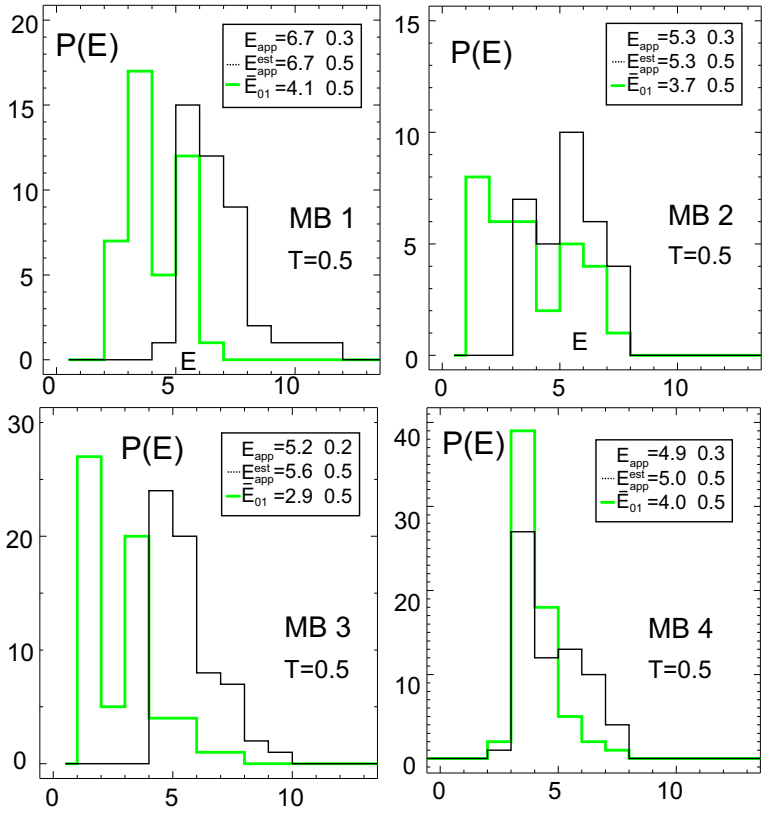

Figure 5.10: Bold curves: Histograms of barriers $E_{i,\alpha(k)}$ overcome when escaping single MBs ($i = 1, 2, 3, 4$ at $T = 0.5$). Light curves: Respective histograms of barriers E_{01} from first jumps. Apparent activation energies $E_{\mathrm{app}}(i)$, mean barriers $E_{\mathrm{app}}^{\mathrm{est}}(i)$, and mean barriers from first jumps $\bar{E}_{01}$ are given in the figure.

Single Metabasins. We now relate the lifetimes of the single, selected MBs (cf. section 5.1) to PEL barriers. By repeated starts from these MBs, the local PEL topography is sampled thoroughly, yielding sets of typical escape pathways. Whenever a MB is left, we locate the transitions by interval bisection and obtain the corresponding TSs with the help of the ridge method. Then, p_{back} is calculated for the minima visited, until for the first time, $p_{\mathrm{back}} < 50\%$. Finally, the barrier $E_{i,\alpha(k)}$ is computed according to Eq. 5.15, where $\alpha(k)$ denotes the escape path chosen at the kth escape. The histograms of barriers are shown in Fig. 5.10, for the four MBs of Fig. 5.1, at $T = 0.5 = 1.1T_c$. Due to the slow dynamics at this temperature, the computation of p_{back} was rather expensive. Nevertheless, the statistics should be sufficient for a reasonable estimate of the apparent activation energy. To this end, we express $E_{\mathrm{app}}(i)$ of MB i in terms of the contributions $E_{i,\alpha}$,

$$\frac{\mathrm{d}}{\mathrm{d}\beta} \ln \langle \tau_i \rangle \approx \langle \tau_i \rangle \sum_{\alpha} E_{i,\alpha} \gamma_{i,\alpha} = \sum_{\alpha} p_{i,\alpha} E_{i,\alpha} \equiv E_{\mathrm{app}}^{\mathrm{est}}(i), \tag{5.16}$$

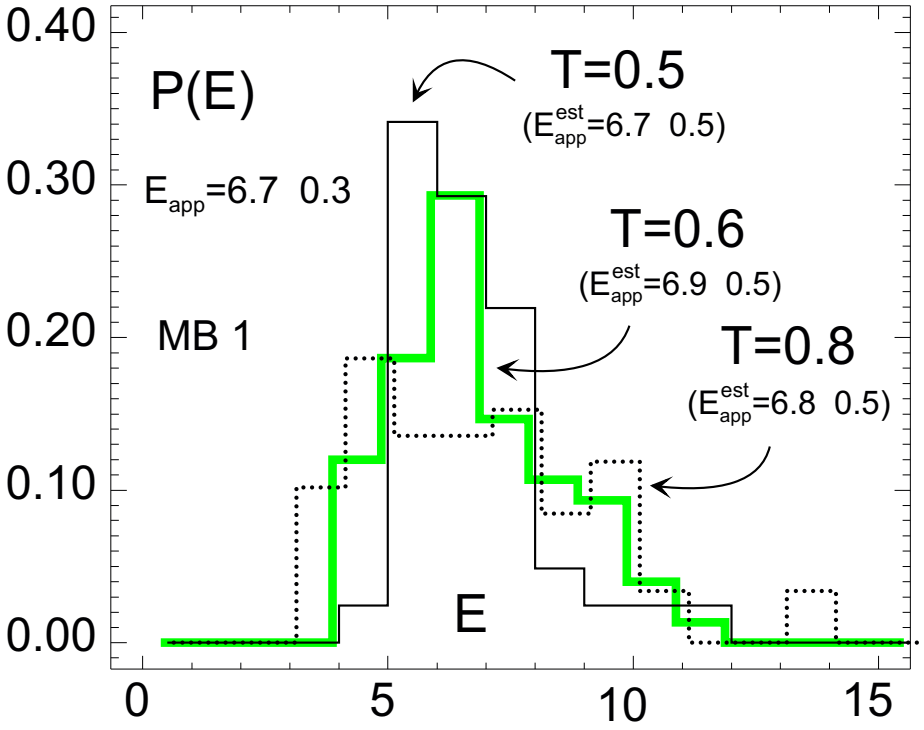

Figure 5.11: Normalized histograms of barriers $E_{1,\alpha(k)}$ overcome when escaping MB 1, for $T = 0.5, 0.6$, and 0.8. The numbers of contributing barriers are 42, 72, and 59, respectively. Estimated apparent activation energies, $E_{\rm app}^{\rm est}(1;T)$, are given in the figure.

where Eqs. 5.9 and 5.15 have been used. Thus, the barriers $E_{i,\alpha}$ are weighted by the probabilities $p_{i,\alpha} = \gamma_{i,\alpha}/\sum_\alpha \gamma_{i,\alpha}$ that the escape happens via pathway α. Note that the $E_{i,\alpha(k)}$ correspond to the pathways that were *chosen* by the system, i.e. they are already weighted correctly by $p_{i,\alpha(k)}$, compare Eq. 5.16. Therefore, $E_{\rm app}^{\rm est}(i)$ is just the average of the $E_{i,\alpha(k)}$. The values of $E_{\rm app}(i)$ and $E_{\rm app}^{\rm est}(i)$, given in Fig. 5.10, are in good agreement. Also shown in Fig. 5.10 is the distribution of first barriers, E_{01}, belonging to the step $\xi_0 \to \xi_1$. Evidently, the neglect of the multi-minima nature of escapes leads to a considerable underestimation of apparent activation energies.

We now continue the discussion of the temperature dependence of barriers $E_{i,\alpha}(T)$. At the example of MB 1 from Fig. 5.10, we have carried out the above program for two other temperatures, $T = 0.6$ and 0.8. The obtained distributions of barriers, $P(E_{i,\alpha})$, are shown in Fig. 5.11. We find that the estimates for the apparent activation energy ($E_{\rm app}^{\rm est}(1;T=0.6) = 6.9 \pm 0.5$ and $E_{\rm app}^{\rm est}(1;T=0.8) = 6.8 \pm 0.5$) remain in good agreement with $E_{\rm app}(1) = 6.7 \pm 0.3$ from section 5.1. The distributions of barriers, however, grow narrower with decreasing temperature. Single, high barriers, contributing to the right wing of the distribution, become inaccessible

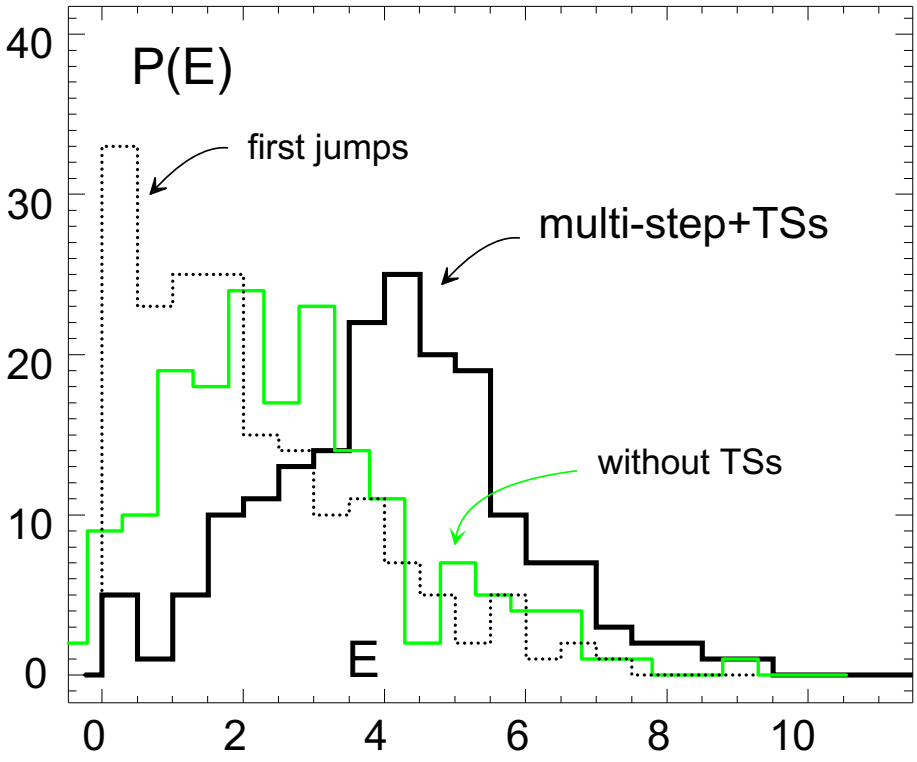

Figure 5.12: Histogram of barriers from a regular MD run at $T = 0.5$ (bold). Neglecting the contributions of transition states, we naturally find smaller barriers, as shown by the histogram of $\epsilon_m - \epsilon_{\mathrm{MB}}$ (light line). The barriers E_{01} from only the first jumps are given by the dotted line.

at low T, i.e., the relative weights $p_{i,\alpha}$ of the corresponding escapes become small. This suppression of high barriers at low T is a trivial effect.

More interesting is the vanishing of small barriers upon cooling, i.e., of the barriers $E < 5$ in the figure. Naively, one would expect these to dominate the escape rate at low T. However, due to the stronger backward correlations (increased p_{back}), jumps over these barriers eventually do not suffice anymore to escape. As described above, the respective escape paths, $\xi_0 \to ... \to \xi_{m(T)}$, grow longer, and the barriers change to a different, mostly larger value.

Average over Metabasins. During our analysis of the MB lifetimes in section 5.1 the apparent activation energies $E_{\mathrm{app}}(\epsilon_{\mathrm{MB}})$ emerged as useful quantities. Although the above results already indicate that barrier hopping is the relevant motional mechanism, a clear-cut verification requires the comparison with the average barrier the system has to cross when leaving a MB of energy ϵ_{MB}.

For this purpose we now carry out a similar program as before, with many MBs

visited during an ordinary MD run. We concentrate on MBs with lifetimes of more than 10^5 MD steps (179 MBs) at $T = 0.5$. When such a MB is left, we locate the transitions by interval bisection and obtain the corresponding TSs by the ridge method. Then, we calculate p_{back} and identify the barrier $E_k \equiv E_{i(k),\alpha(k)}$ according to Eq. 5.15. The histogram of barriers is shown as the bold line in Fig. 5.12. For comparison, we also show the barriers minus the contribution of the TSs, $E_{(m-1)m}$. Ignoring multi-minima correlations, we further show the histogram of first barriers E_{01} of escapes. Evidently, the neglect of TSs or of backward correlations leads to much smaller barriers.

From the above barriers, we will now calculate estimates of apparent activation energies. When the average over lifetimes of different MBs is considered, each MB i acquires a weight φ_i corresponding to its probability of occurrence,

$$\langle \tau \rangle = \sum_i \varphi_i \langle \tau_i \rangle .$$

At fixed ϵ_{MB}, the analog to Eq. 5.16 can then be derived

$$\frac{\mathrm{d}}{\mathrm{d}\beta} \ln \langle \tau(\epsilon_{\mathrm{MB}}; T) \rangle \approx \sum_i \frac{\langle \tau_i \rangle \varphi_i}{\langle \tau(\epsilon_{\mathrm{MB}}; T) \rangle} \sum_\alpha p_{i,\alpha} E_{i,\alpha}, \tag{5.17}$$

where summation goes over MBs of energy ϵ_{MB}. As in Eq. 5.16, the barriers in Eq. 5.17 are weighted according to their probability of occurrence, but, additionally, with the respective MB lifetimes.

In Eq. 5.17 we have neglected terms stemming from the variation of the φ_i's with temperature. This is justified, since the φ_i's belong to the same ϵ_{MB}. Their relative weights will only vary if these MBs differ considerably in their barrier heights. As already stated above, however, MBs of the same energy seem to be fairly uniform regarding this property. For the finite sample of MBs visited during an MD run, Eq. 5.17 then takes the form

$$E_{\mathrm{app}}^{\mathrm{est}}(\epsilon_{\mathrm{MB}}) = \frac{\sum \tau_k E_k}{\sum \tau_k}, \tag{5.18}$$

where summation goes over MBs of energy ϵ_{MB}. Again, the correct weighting is implicit here. This expression converges to the right-hand side of Eq. 5.17 in the limit of infinitely long sampling. In Fig. 5.13 we show the values of $E_{\mathrm{app}}^{\mathrm{est}}(\epsilon_{\mathrm{MB}})$, determined in this way. They perfectly agree with the apparent activation energies, derived from the analysis of relaxation times at different temperatures. Thus, we have a clear-cut proof that the apparent activation energies $E_{\mathrm{app}}(\epsilon_{\mathrm{MB}})$ are indeed related to barriers on the PEL and thus reflect activated dynamics significantly above T_c. This again demonstrates that we not only deal with the right order of barrier sizes, but we also *quantitatively* link PEL topography to dynamics.

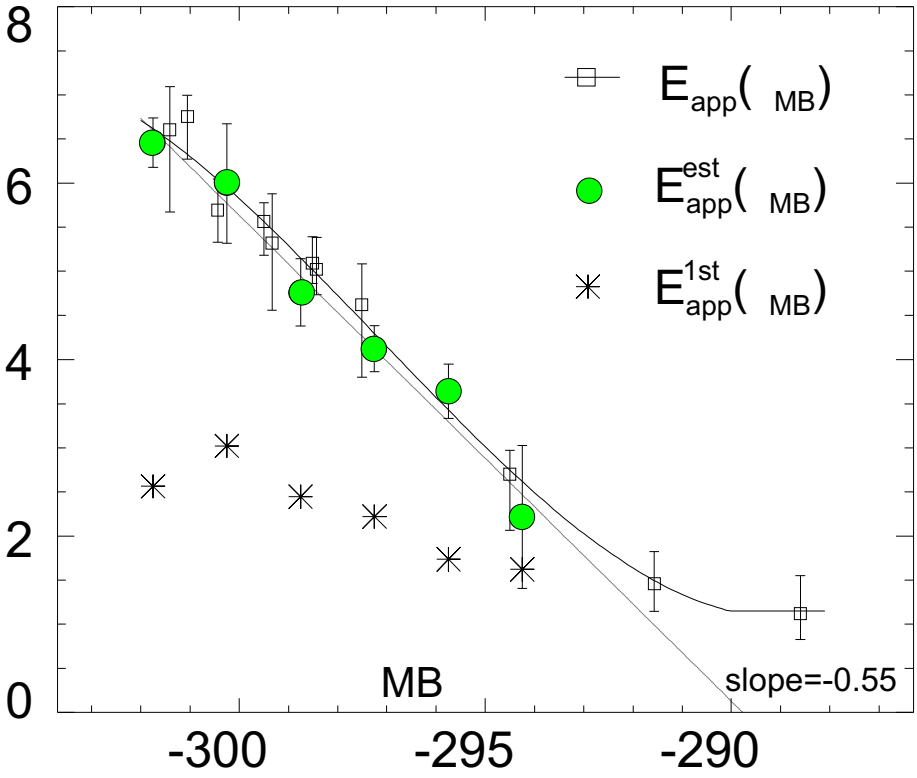

Figure 5.13: $E_{\rm app}(\epsilon_{\rm MB})$ (Fig. 5.2) vs. estimated $E^{\rm est}_{\rm app}(\epsilon_{\rm MB})$ from PEL barriers. Considering only the first jumps of escapes, we find a much smaller estimate ($E^{\rm 1st}_{\rm app}(\epsilon_{\rm MB})$). Data stem from a regular MD run at $T = 0.5$, where MBs of lifetime greater than 10^5 MD steps were analyzed (179 MBs, see Fig. 5.12).

For comparison, we have included the apparent activation energy which results if only the first transitions of escapes, $\xi_0 \to \xi_1$, are considered ($E_{01} = V(\zeta_{01}) - \epsilon_0$). One ends up with much too small apparent activation energies. Again, multi-minima correlations turn out to be crucial for the characterization of MB depths.

In principle, the results of Fig. 5.13 may slightly change if all MBs rather than those with lifetimes larger 10^5 MD steps were considered. However, our analysis has clearly revealed (see, e.g., Fig. 5.1) that the depths of MBs of similar $\epsilon_{\rm MB}$'s only mildly vary. Thus, inclusion of MBs with smaller values of τ would not significantly change the apparent activation energies $E^{\rm est}_{\rm app}(\epsilon_{\rm MB})$.

Finally, we show that these results, in conjunction with $p(\epsilon_{\rm MB}; T)$, largely explain the behavior of the diffusion coefficient $D(T)$. This is a conceptually important step, since we link $D(T)$ to purely structural and thermodynamical quantities, see Eq. 5.5. The key is the mean lifetime $\langle \tau(\epsilon_{\rm MB}; T) \rangle$ of MBs at energy $\epsilon_{\rm MB}$, which is parametrized by $\tau_0(\epsilon_{\rm MB})$ and $E_{\rm app}(\epsilon_{\rm MB})$ (Eq. 5.8). The former, $\tau_0(\epsilon_{\rm MB})$, however, has not been deduced from PEL properties. Its variation with MB energy is not

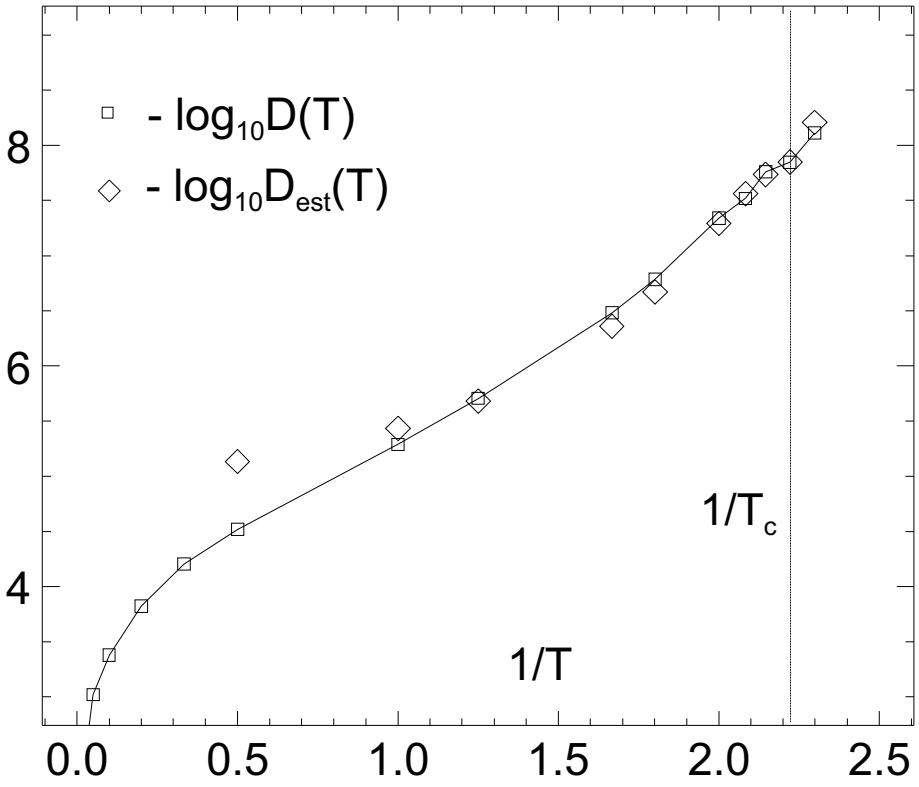

Figure 5.14: Comparison of the inverse diffusion coefficient, $1/D(T)$, with the prediction $1/D_{\rm est}(T)$ from Eq. 5.19, $\tau_0 = 200$.

strong (Fig. 5.2(c)), so we can hope that setting it to a constant will be a good approximation. Thus, Eq. 5.4 becomes

$$D(T) \approx \frac{a^2}{6N\tau_0} \int {\rm d}\epsilon_{\rm MB} p(\epsilon_{\rm MB};T) e^{-\beta E^{\rm est}_{\rm app}(\epsilon_{\rm MB})} \equiv D_{\rm est}(T). \tag{5.19}$$

The estimated diffusion coefficient derived from this expression is shown in Fig. 5.14. The agreement of $D(T)$ with our estimate is satisfactory below $T = 1$. The deviation at $T = 2$ is due to the depart of $\langle \tau(\epsilon_{\rm MB};T) \rangle$ from Arrhenius behavior for $T > 1$, see Fig. 5.2(a).

5.4 Barrier Crossing.

When making use of Eq. 5.11, we presumed that the barriers $V(\zeta_{ab}) - V(\xi_a)$ in fact govern the temperature dependence of rates. The excellent agreement between $E_{\rm app}(\epsilon_{\rm MB})$, determined from dynamics, and the $E^{\rm est}_{\rm app}(\epsilon_{\rm MB})$, from the analysis of the PEL, strongly indicates that this presumption is indeed true. We will show here in a very detailed way that at $T = 0.5 = 1.1T_c$, escapes from stable MBs are perfectly

activated. More precisely, two conditions are fulfilled, (i) the potential barriers are much larger than $k_{\mathrm{B}}T$, (ii) rates follow from the one-dimensional energy profile of the RP plus corrections from perpendicular curvatures.

We will check these conditions explicitly here by an analysis of escape dynamics out of MBs. We made the observation that during every escape from a stable MB, at least one single barrier larger than $6k_{\mathrm{B}}T$ must be surmounted. Moreover, this larger jump is mostly undertaken from one of the lowest minima of the MB, compare Fig. 5.7. From the repeated escape runs of section 5.1, we selected the most frequent ten transitions of that kind. From the respective TSs, ζ_l, we computed the RPs, denoted $\zeta_l(s)$, $l = 1...10$. We then investigated the motion within the MBs over a long period of the simulation where no escape had happened (10^7 MD steps in each MB). The goal was to observe how the system tries to climb the different RPs. To this end, we projected the instantaneous configuration $x(t)$ onto each of the RPs, according to

$$s_l(t) \equiv \left\{ s' : ||x(t) - \zeta_l(s')|| = \min_s ||x(t) - \zeta_l(s)|| \right\},$$

which means the point on the RP next to $x(t)$. Due to the long residences in the MBs, motion therein is largely equilibrated. Hence, if the potential energy profiles $V_l(s_l) = V(\zeta_l(s_l))$ along the reaction paths are of importance for the transition rates, we expect that the populations $p_l(s_l)$ of the RPs follow from Boltzmann's law[3]

$$p_l(s_l) \propto \exp\{-\beta V_l(s_l)\}\, Y_l^{\perp}(s_l) \equiv \exp\{-\beta F_l(s_l)\}. \tag{5.20}$$

The vibrations perpendicular to path l are accounted for by the harmonic partition function

$$Y_l^{\perp}(s_l) = \int \mathrm{d}y \exp\left\{ -\frac{\beta}{2} \sum \lambda_\nu y_\nu^2 \right\} \delta(y \cdot \hat{t}(s_l)),$$

where the origin $y = 0$ corresponds to the point $\zeta_l(s_l)$, λ_ν are the eigenvalues of the Hessian matrix, $H(s_l)$, y_ν the components of y along the eigenvectors, and $\hat{t}(s_l)$ is the tangent to the reaction path.

The upper inset of Fig. 5.15 shows an example of $p_l(s_l)$ and $F_l(s_l)/k_{\mathrm{B}}T$. The population of the reaction path follows nicely the prediction from its energy profile. For RPs with complicated shapes, this correspondence can be disturbed. The worst agreement of the considered RPs is shown in the second inset. Still, a clear correlation of RP population with energy is present. We compiled the results for all 10 RPs in Fig. 5.15 as a parametric plot of $-\ln p_l$ *vs.* $F_l/k_{\mathrm{B}}T$. Curves of slope

[3]Please do not confuse the free energy $F_l(s_l)$ defined here with the force vector $F(x)$.

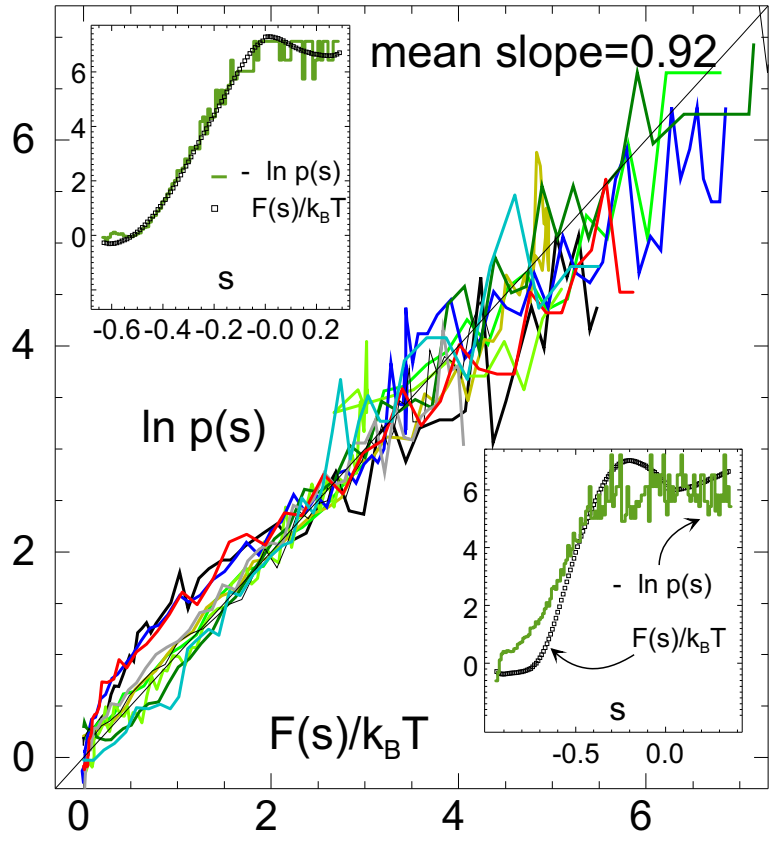

Figure 5.15: Parametric plot showing the correspondence, Eq. 5.20, of $-\Delta p_l(s_l) = -\ln p_l(s_l)+\text{const.}$ to the free energy profile $\Delta F_l(s_l)/k_\mathrm{B}T = F_l(s_l)/k_\mathrm{B}T+\text{const.}$, $l = 1...10$, $T = 0.5$, BMLJ65. All curves were shifted to start in the origin. Insets: comparison of the free energy profiles of two reaction paths with the population along the path.

one would result from a perfect equivalence of p_l to $F_l/k_\mathrm{B}T$, Eq. 5.20. Here, we find an average slope of 0.92. Since transition rates are proportional to the population of TSs, the implications of these results are obvious: MB jump rates follow from energy barriers. We finally note that the vibrational terms $\ln Y_l^{\perp}(s_l)$ are minor corrections to $\beta V(s_l)$.

5.5 Where is the PEL ground?

It is an interesting question how far down to low energies we can find amorphous minima. From the gaussian density $G(\epsilon)$, Eq. 3.10, we conclude that practically no minimum[4] should be present below $\epsilon_{\min}$, given by[5] $G(\epsilon_{\min}) = 1$. After Eq. 3.10, this

[4]In intervals of width $\mathrm{d}\epsilon = 1$ below $\epsilon_{\min}$, one finds less than one minimum, which is negligible.
[5]more correctly, $G(\epsilon_{\min}) = \epsilon_{\mathrm{AA}}^{-1}$

cutoff is[6]

$$\epsilon_{\min} = \epsilon_0 - \sigma\sqrt{2\alpha N - \ln 2\pi\sigma^2},$$

which in the BMLJ65 amounts to $\epsilon_{\min} \approx -306$. From the low-temperature $p(\epsilon;T)$ of Fig. 3.2, and its mean and variance in Fig. 3.7, a lower PEL cutoff at $\epsilon_{\min} = -302$ is indicated. However, we will show here that this value of $\epsilon_{\min}$ should not be inferred from the data presented in chapter 3, for the following reason. The fact that no minima are found below some $\epsilon_{\min}$ does not necessarily mean that they do not exist. They could also be extremely rare but, when encountered, contribute strongly to $p(\epsilon;T)$, due to their long lifetimes. This suggests that longer simulation runs could produce still lower minima and that the value of $\epsilon_{\min} = -302$ inferred in chapter 3 could be caused by an insufficient exploration of the PEL. After Fig. 3.2, this would affect the simulations at $T < 0.5$, where the cutoff becomes visible. Moreover, one should ask to what degree other quantities like $D(T)$ or $\langle\tau(T)\rangle$ would be affected by missing the very deepest MBs which contribute the largest waiting times. We shall see in this section that such questions can be answered by the PEL parametrization that we have obtained so far.

As $p(\epsilon_{\mathrm{MB}};T)$ and $p(\epsilon;T)$ are nearly identical below $2T_c$ (section 5.1), we may also use the gaussian parametrization of $p(\epsilon;T)$ (chapter 3) in conjunction with Eq. 5.3 to compute an estimate of $\varphi(\epsilon_{\mathrm{MB}};T)$,

$$\varphi_{\mathrm{est}}(\epsilon_{\mathrm{MB}};T) \propto \frac{p(\epsilon=\epsilon_{\mathrm{MB}};T)}{\langle\tau(\epsilon_{\mathrm{MB}};T)\rangle}, \qquad \epsilon_{\mathrm{MB}} > \epsilon_{\min}. \tag{5.21}$$

Here by $p(\epsilon=\epsilon_{\mathrm{MB}};T)$ we denote the population of *single* basins, evaluated at ϵ_{MB}. From Fig. 5.16, we see that this estimate is consistent with the $\varphi(\epsilon_{\mathrm{MB}};T)$ stemming directly from the metabasins found in the simulations (the ones also shown in Fig. 5.3). This is not only a consistency check. The $\varphi_{\mathrm{est}}(\epsilon_{\mathrm{MB}};T)$ computed in this way may also serve as an extrapolation of $\varphi(\epsilon_{\mathrm{MB}};T)$ towards lower MB energies that were not found within the simulations.

The case that the PEL is not sampled sufficiently within a given simulation run corresponds to a non-equilibrium situation. Unfortunately, there is no general means to test for equilibration. One rather has to check for all measured quantities whether the respective time averages become stationary within the limited simulation time. In this connection, one generally faces the problem that different quantities are differently sensitive to the finite sampling of phase space. In our case, e.g., good estimates of the average MB waiting times, $\langle\tau(T)\rangle$, seem to require a long equilibration. This is caused by the slowly-decaying WTDs, where the weight of

[6] more correctly, $\epsilon_{\min} = \epsilon_0 - \sigma\sqrt{2\alpha N - \ln(2\pi(\sigma/\epsilon_{\mathrm{AA}})^2)}$

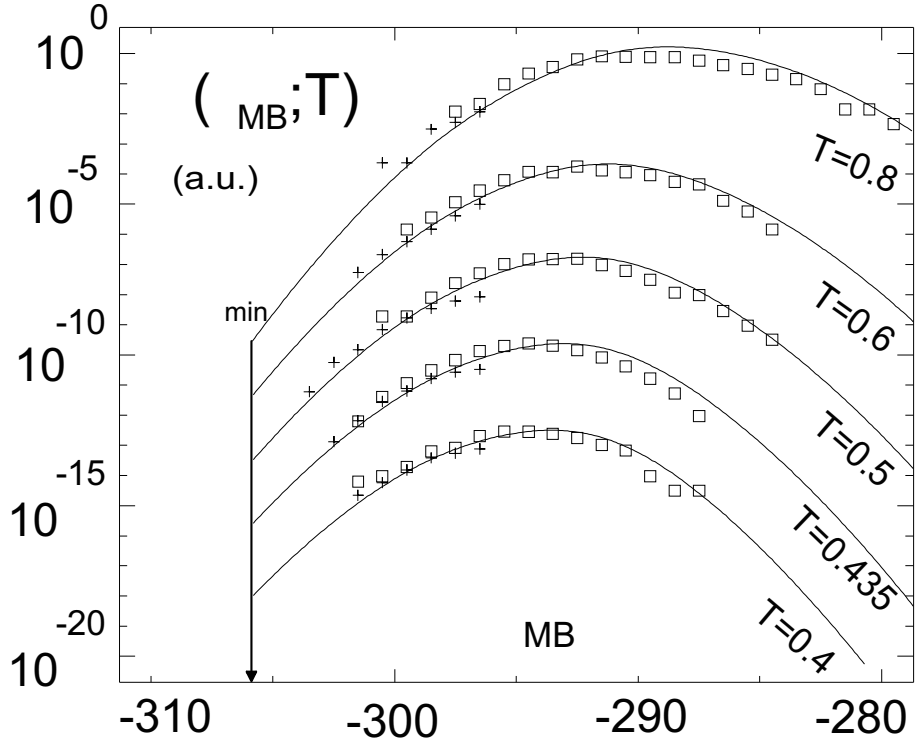

Figure 5.16: Estimated distribution of MB energies, $\varphi_{\rm est}(\epsilon_{\rm MB};T)$ (solid lines), compared with the distributions extracted directly from the simulations. For every temperature, data from long simulation runs with equidistant minimization (+) and from shorter runs with additional interval bisection (□) are shown. The long simulations encounter more of the deepest MBs, while they miss the fast, high-energetic MBs. These are discovered only in the shorter interval-bisection runs. Note that the solid-line curves of $\varphi_{\rm est}(\epsilon_{\rm MB};T)$ are no gaussians, since $E_{\rm app}(\epsilon_{\rm MB})$ is not linear in $\epsilon_{\rm MB}$ over the whole range of $\epsilon_{\rm MB}$; see Fig. 5.2(b). The mean lifetimes of MBs below -302 have been calculated by extrapolating $E_{\rm app}(\epsilon_{\rm MB})$ linearly down to lower energies and by keeping $\tau_0(\epsilon_{\rm MB})$ constant.

the rare but long waiting times is large. Other demanding quantities are the mean of the MB energies, or their variance, since again, low MBs are rare but long-lived. On the other hand, the distribution of MB energies encountered, $\varphi(\epsilon_{\rm MB};T)$, is less expensive, due to the lacking weighting with MB lifetimes; see Eq. 5.21. As shown in Fig. 5.16, the deep, long-lived MBs have a small weight in $\varphi(\epsilon_{\rm MB};T)$. Thus, averages with respect to $\varphi(\epsilon_{\rm MB};T)$ (e.g., $\langle\epsilon_{\rm MB}\rangle_{\varphi(\epsilon_{\rm MB};T)}$ or ${\rm Var}\varphi(\epsilon_{\rm MB};T)$) quickly become stationary. For simplicity, we therefore assume that right from the start of a simulation run, equilibrium with respect to $\varphi(\epsilon_{\rm MB};T)$ is already present, whereas 'aging' of the τ-weighted quantities like $\langle\tau(T)\rangle$ still has to be expected.

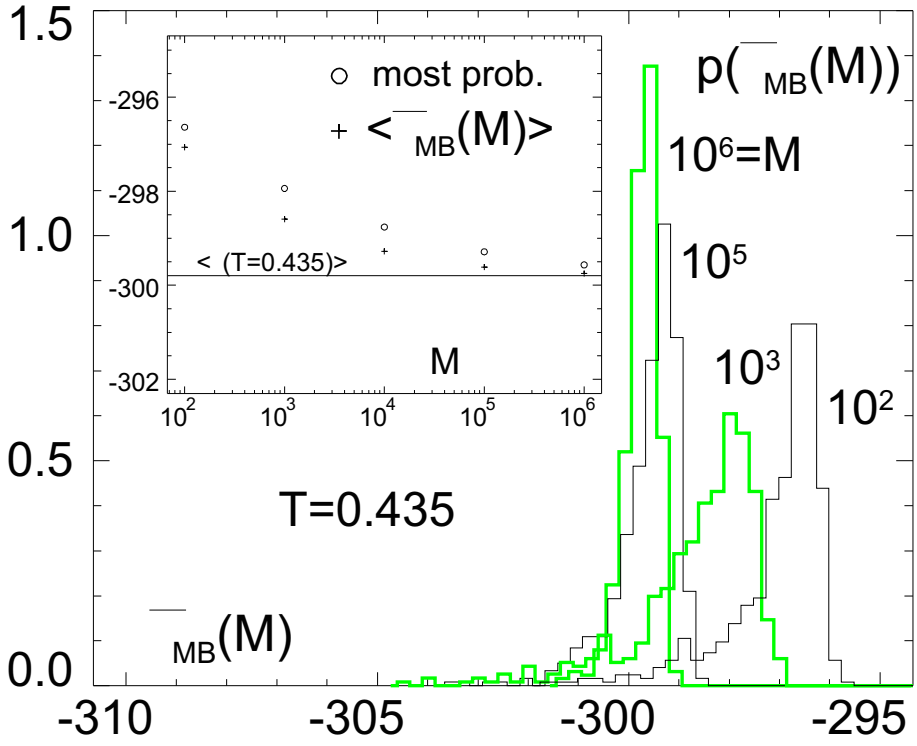

Figure 5.17: Distribution of the estimated average MB energy, $\bar{\epsilon}_{\mathrm{MB}}(M)$, after M draws from $\varphi_{\mathrm{est}}(\epsilon_{\mathrm{MB}};T)$, $T = 0.435$. For each M, 500 values of $\bar{\epsilon}_{\mathrm{MB}}(M)$ contribute to the corresponding histogram. Inset: Most probable and average value of $\bar{\epsilon}_{\mathrm{MB}}(M)$.

Average metabasin energy. We first check the influence of a finite simulation time on the average metabasin energy. We assume that the total simulation run corresponds to M times drawing a MB energy from $\varphi(\epsilon_{\mathrm{MB}};T)$, where M equals the total time of the run divided by $\langle\tau(T)\rangle$. For each ϵ_{MB} , using the parametrization of $\langle\tau(\epsilon_{\mathrm{MB}};T)\rangle$, we choose a random MB lifetime τ from the distribution $\gamma e^{-\gamma\tau}$, where $\gamma = \langle\tau(\epsilon_{\mathrm{MB}};T)\rangle^{-1}$. From this set of MBs, we calculate the estimated average MB energy,

$$\bar{\epsilon}_{\mathrm{MB}}(M) = \frac{\sum \epsilon_{\mathrm{MB}}\tau}{\sum \tau},$$

where the sum goes over the M MBs. How well does $\bar{\epsilon}_{\mathrm{MB}}(M)$ agree with the canonical expectation value $\langle\epsilon_{\mathrm{MB}}(T)\rangle$, which would be found in the limit $M \to \infty$? If M is too small, we expect that too few of the low MBs will be found, so that the true average is generally overestimated by a finite sample of MBs. To check this, we took 500 samples of M metabasins and each time calculated $\bar{\epsilon}_{\mathrm{MB}}(M)$. In Fig. 5.17 the histograms of $\bar{\epsilon}_{\mathrm{MB}}(M)$ are shown for different sample sizes M at $T = 0.435$. Evidently, for finite M, it is most probable to find a too large estimate $\bar{\epsilon}_{\mathrm{MB}}(M)$

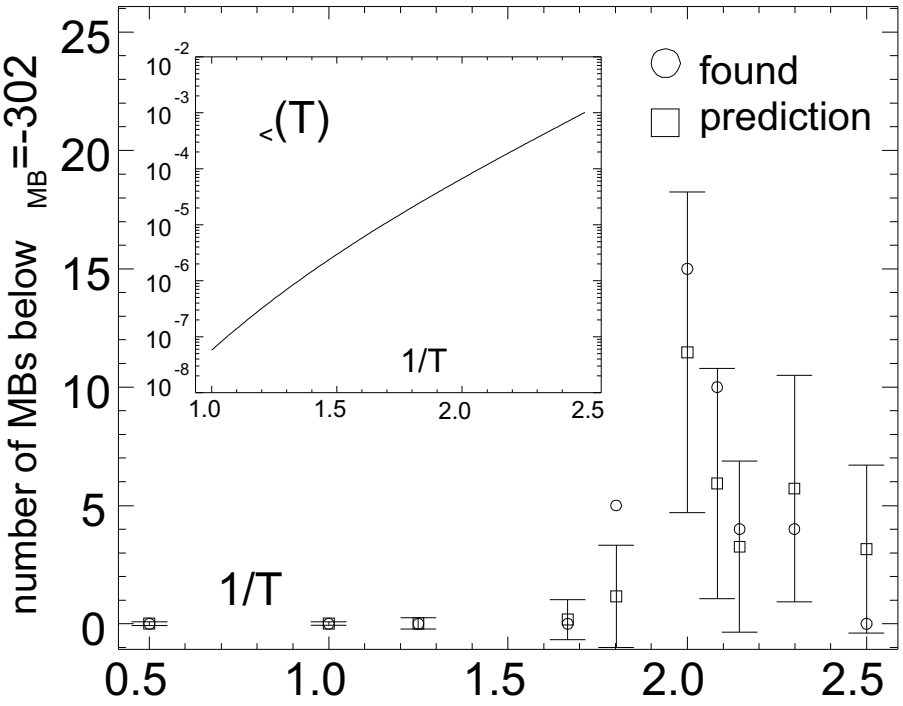

Figure 5.18: Number of MBs below $\epsilon_{\rm MB} = -302$ found in the BMLJ65 at different temperatures ($\circ$), compared to their expected number, $M\varphi_<$ ($\Box$). The error bars have the size $\sqrt{M\varphi_<(1-\varphi_<)}$. Inset: $\varphi_<(T)$ as defined in the text, *vs.* $1/T$.

of $\langle\epsilon_{\rm MB}(T)\rangle$. With increasing M, naturally, the expected error decreases. The $T = 0.435$ data presented in chapter 3 originated from a simulation run of approximately $M = 17000$ MBs. From the inset of Fig. 5.17, we find that such a simulation will most probably yield an estimate of $\langle\epsilon_{\rm MB}(T)\rangle$ which is about one energy unit too high. This is consistent with the value of $\langle\epsilon(T=0.435)\rangle$ reported in Fig. 3.7(a). As a further check, we performed a much longer simulation run at $T = 0.435$, corresponding to $M \approx 10^5$. As we saw in Fig. 3.7(a), this leads to a decreased estimate for the mean IS energy. From the above discussion and Fig. 5.17 this result is very plausible.

A similar analysis is possible for the variance of MB energies. The result is that $\mathrm{Var}p(\epsilon_{\rm MB};T)$ is even more susceptible to finite simulation lengths than $\langle\epsilon_{\rm MB}(T)\rangle$, which confirms the findings of Fig. 3.7(b).

Number of MBs found below $\epsilon_{\rm MB} = -302$. A further application of $\varphi_{\rm est}(\epsilon_{\rm MB};T)$ is to predict the number of low-lying MBs that we should find in some given simulation run. If the total length of the run is $M\,\langle\tau\rangle$, we should on average

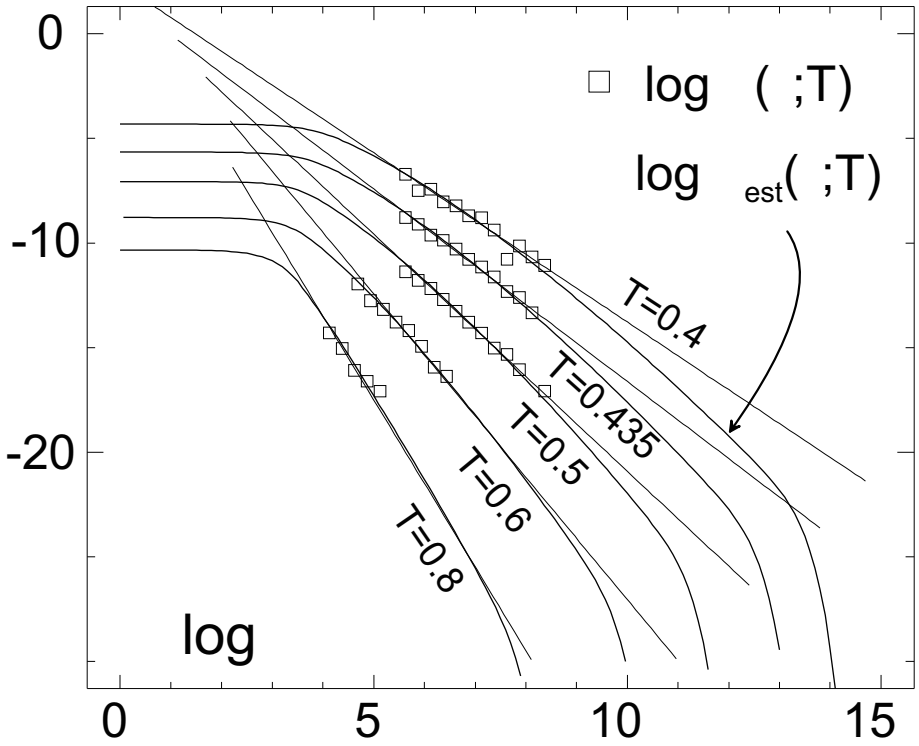

Figure 5.19: Estimated WTDs $\varphi_{\rm est}(\tau;T)$, from $\varphi_{\rm est}(\epsilon_{\rm MB};T)$ and $\gamma(\epsilon_{\rm MB}) = \langle\tau(\epsilon_{\rm MB};T)\rangle^{-1}$. For comparison, the long-time parts of the WTDs obtained directly from the simulations are also given. Straight lines are power-law fits.

encounter $M\varphi_<$ of such MBs, where

$$\varphi_<(T) = \int_{-\infty}^{-302} {\rm d}\epsilon_{\rm MB}\varphi_{\rm est}(\epsilon_{\rm MB};T)$$

is the probability to find a MB below $\epsilon_{\rm MB} = -302$ when drawing once from $\varphi_{\rm est}(\epsilon_{\rm MB};T)$. The inset of Fig. 5.18 shows $\varphi_<(T)$ *vs.* $1/T$. Again, we assumed that the amorphous minima extend down to $\epsilon_{\rm min} = -306$. The number of low MBs that were indeed found is depicted in the main panel of the figure and is compared to the prediction $M\varphi_<$. Despite $T = 0.555$, we find an agreement of figures within error bars.

Accuracy of the mean MB lifetime. In section 4.4, we have found that the waiting-time distributions of MBs near T_c attain power-law tails with exponents of about two. As noted there, the τ^{-2} behavior cannot persist in the limit $\tau \to \infty$, due to the finite (but large) set of MBs in the PEL. At very large τ, the deepest MB will dominate the WTD, leading to an exponential decay of $\varphi(\tau)$. However,

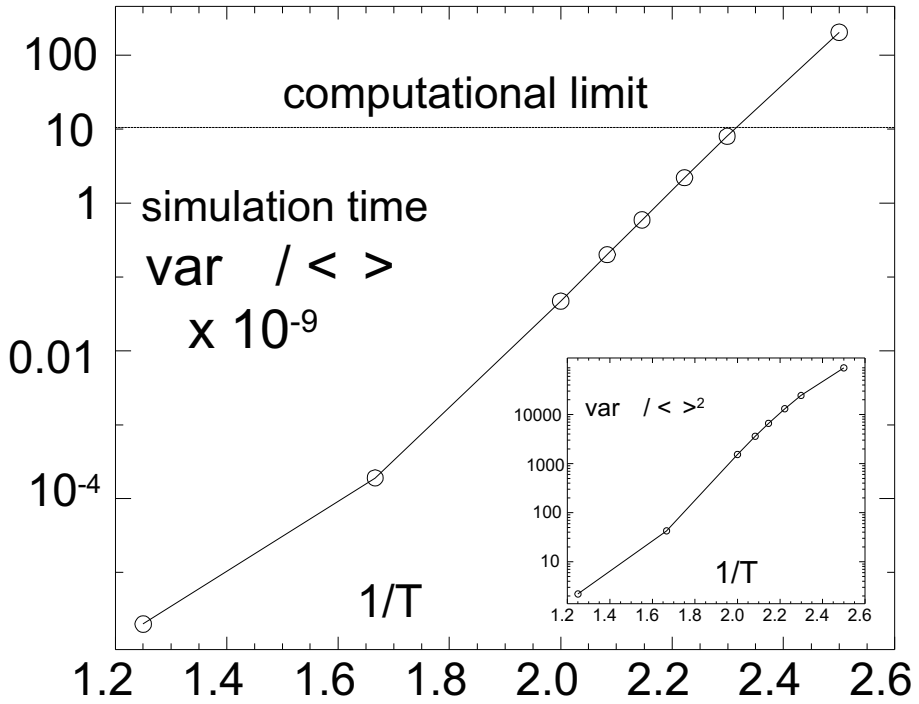

Figure 5.20: Total simulation time (in LJ units) needed to reach a relative accuracy of $\mathrm{Var}(\tau)/\langle\tau\rangle^2 < 1$, versus $1/T$. Inset: Relative variance of τ versus $1/T$. Here the computational limit is defined by a simulation length of one month on a single-processor machine (DEC XP1000).

this crossover to exponential decay has not been observed in the simulations. Thus, one might worry about the contribution of the missing, long τ's, which could significantly alter the value of $\langle\tau(T)\rangle$. We shall now estimate the complete distribution $\varphi_{\mathrm{est}}(\tau;T)$ from $\varphi_{\mathrm{est}}(\epsilon_{\mathrm{MB}};T)$ and $\gamma(\epsilon_{\mathrm{MB}}) = \langle\tau(\epsilon_{\mathrm{MB}};T)\rangle^{-1}$. The result is shown in Fig. 5.19 for different temperatures. The deviations from the power-law towards a faster decay start around $\log\tau \approx 8$, just outside the time window covered by our simulations. This indicates that much larger lifetimes than those already found in the simulations do not contribute strongly to $\langle\tau(T)\rangle$. We shall demonstrate this more quantitatively in the following.

Since MB lifetimes are mutually uncorrelated (Fig. 4.10), we can obtain an estimate τ_M of $\langle\tau(T)\rangle$ by drawing M times from $\varphi_{\mathrm{est}}(\tau;T)$. Since $\mathrm{Var}(\tau_M) = \mathrm{Var}(\tau)/(M-1)$, we need of the order of $M > \mathrm{Var}(\tau)/\langle\tau\rangle^2$ draws to obtain a relative accuracy of $\mathrm{Var}(\tau_M)/\langle\tau\rangle^2 < 1$. In the inset of Fig. 5.20, $\mathrm{Var}(\tau)/\langle\tau\rangle^2$ is shown versus $1/T$. At $T = 0.4$, for instance, we need of the order of 10^5 MBs to reach an acceptable accuracy of $\langle\tau\rangle$. As shown in the main panel of Fig. 5.20, the

total simulation time of $10^5 \langle\tau\rangle$ at this temperature[7] exceeds the limit of feasible calculations. In contrast, $T = 0.435$, which is slightly below T_c, can still be tackled.

5.6 Discussion.

For repeated relaxation from the same MB, we calculated the mean relaxation times $\langle\tau_i\rangle$ in section 5.1 and found Arrhenius behavior in all cases (Fig. 5.1). The simplest view is that the apparent activation energies $E_{\rm app}(i)$ from $\langle\tau_i\rangle$ correspond to the depths of these MBs, i.e. to the typical heights of barriers that surround the MBs. Indeed, this has been quantitatively confirmed for the four randomly selected, low-lying MBs (see Fig. 5.10). A direct conclusion from the constancy of $E_{\rm app}(i)$ is that the system does not find smaller and ever smaller barriers[8] upon decreasing T.

Although not of statistical relevance for the whole PEL, the results for the four single MBs give us a detailed picture of the local PEL topography. An important outcome is the variation of barrier heights with temperature, see Fig. 5.11. We have already discussed that low barriers grow upon cooling, due to enhanced multi-minima correlations (growing MBs), while unnecessarily high barriers are suppressed. Both effects seem to cancel, so that the mean barrier, $E_{\rm app}^{\rm est}(1)$, remains constant, leading to Arrhenius behavior below $T = 1$. This cancellation may be fortunate, at least we can offer no explanation for it, here. As depicted in Fig. 5.11, the distribution of barriers becomes more and more narrow when going from $T = 0.8$ to $T = 0.5$, but the mean value, i.e. $E_{\rm app}^{\rm est}(1)$, remains constant. The constant apparent activation energy of MB 1 down to $T = 0.45$ implies that the mean value of the distribution of barriers has not increased. We thus speculate that the growth of barriers due to increasing multi-minima correlations has essentially come to an end at $T \leq 0.5$. Although the temperature dependence of the barrier distribution has only been analyzed for a single MB, the constancy of apparent activation energies of the other three MBs and the temperature independence of $E_{\rm app}(\epsilon_{\rm MB})$ support this idea. Stated differently, the development of superstructures of minima seems to cease at some temperature above T_g. Expressed by $p_{\rm back}$, this means that no minimum with $p_{\rm back} < 50\%$ will surpass $p_{\rm back} = 50\%$ upon further cooling, thus being unable to join the MB in question. Hence, an escape sequence found at one temperature $T \leq 0.5$ has the same length at another one, i.e., from some temperature on, the minimum $\xi_{m(T)}$ remains at $p_{\rm back} < 50\%$ for $T \to 0$; we then say it terminates the sequence. It

[7] corresponding to approximately two years of computer time on a DEC XP1000

[8] In the infinite-dimensional random energy model (Derrida, 1981), for instance, the PEL topology of the BMLJ65 is therefore insufficiently represented. There, every minimum has some neighbors with arbitrarily close energy, which are favored by the Boltzmann factor at low temperatures. This causes $E_{\rm app}(i) \to 0$ for $T \to 0$.

is an interesting question under what circumstances such termination happens. A trivial example would be a 'transit' minimum with one backward and one forward exit, where taking the forward leads to a minimum with $p_{\rm back} \approx 0$. If the backward barrier was higher than the forward one, $p_{\rm back}$ would go to zero for $T \to 0$. On the other hand, the minima inside MBs generally feature growing $p_{\rm back}$'s upon cooling, because the energetic gain of returning becomes more and more attractive. Ideally, thus, for $T \to 0$, we would have $p_{\rm back} \to 1$ within MBs, and $p_{\rm back} \to 0$ outside. This provides a plausible, physical basis for computing barrier heights according to Eq. 5.15, at least in the limit $T \to 0$. Clearly, a more detailed investigation of the temperature dependence of $p_{\rm back}$ is necessary to back these conclusions.

Next, we analyzed the average relaxation times $\langle \tau(\epsilon_{\rm MB}; T) \rangle$ from MBs at fixed energy $\epsilon_{\rm MB}$. Again, they displayed Arrhenius behavior, with apparent activation energy $E_{\rm app}(\epsilon_{\rm MB})$ (see Fig. 5.2), which compared well with the prediction from PEL barriers (Fig. 5.13). In this connection, a recent paper (Grigera et al., 2002) is of interest. The authors use the auxiliary potential $\tilde{V} = \frac{1}{2}|F^2(x)|$ to compute general stationary states (saddles) in a binary soft-sphere mixture ($N = 70$). From the TSs among these saddles (index one, no shoulder), they perform steepest descents to obtain the connected minima. They define barriers as the energy difference ΔU from the TSs to the lower one of the connected minima $\epsilon = \min(\epsilon_0, \epsilon_1)$. Plotting the average $\overline{\Delta U}(\epsilon)$, they find a similar curve to our $E_{\rm app}(\epsilon_{\rm MB})$, Fig. 5.13, i.e., a strong increase of barriers towards lower energies. In contrast, when carrying out the same analysis for our BMLJ65, we found a nearly constant $\overline{\Delta U}(\epsilon)$, a curve close to the first barriers of escapes E_{01} shown in Fig. 5.13. We would have expected this result, since the multi-step nature of escapes in the BMLJ65 has clearly been demonstrated. On the other hand, the contrasting result of Grigera et al. would indicate that the soft-sphere PEL is not organized in multi-minima superstructures. However, as noted in section 2.1, it is not clear to what extent the results of Grigera et al. are blurred by the presence of crystalline configurations. A clarification of this point would be very useful.

The results shown in Fig. 5.14, obtained via Eqs. 5.4 and 5.8, demonstrate the use of the present chapter. From PEL barriers ($E_{\rm app}^{\rm est}(\epsilon_{\rm MB})$) and thermodynamics ($p(\epsilon_{\rm MB}; T)$) we are able to produce a reasonable estimate of dynamics. An overall proportionality factor $1/\tau_0$ remains as an adjustable parameter, since it could not be predicted from PEL structure. As discussed in section 5.1, one may use $p(\epsilon; T)$ for $p(\epsilon_{\rm MB}; T)$, since they are nearly identical. This is very convenient, because upon constructing $p(\epsilon; T)$, no information about dynamics is needed. The breakdown of the Arrhenius form of $\langle \tau(\epsilon_{\rm MB}; T) \rangle$, Eq. 5.8, above $2T_c$ limits our description to the temperatures $T \leq 2T_c$. In any event, we would not have dared to make

quantitative statements on the basis of the hopping picture above the landscape-influenced temperature regime.

Chapter 6

Finite-Size Effects

It is clear alone from the number of dimensions that the PEL of a large system will be more complex than that of a small system of the same kind. However, it is also clear that there should exist a critical system size from which on the growth in complexity becomes trivial: To see this most clearly, imagine a large system, say, a macroscopic sample of a supercooled liquid of one cubic centimeter. Clearly, its energy landscape will be less complicated than that of one liter of the same liquid. Due to negligible surface effects, though, the one liter will behave like thousand independent, single cubic centimeters. Thus, the PEL of the larger system factorizes into thousand PELs of much lower dimension, symbolically,

$$(1\mathrm{l}) \approx (1\mathrm{cm}^3) \otimes (1\mathrm{cm}^3) \otimes ... \otimes (1\mathrm{cm}^3).$$

In this chapter, we will study the influence of the system size on various static and dynamic properties of the supercooled binary Lennard-Jones liquid. In this way, we shall provide evidence that the results obtained in chapters 4 and 5 for a system as small as the BMLJ65 are also relevant for the bulk behavior. Systems of $N = 130, 260$, and 1000 particles will be investigated and compared to the BMLJ65. Especially, we shall demonstrate that the BMLJ130 behaves essentially like two non-interacting BMLJ65s,

$$(\mathrm{BMLJ130}) \approx (\mathrm{BMLJ65}) \otimes (\mathrm{BMLJ65}).$$

We will study static quantities in section 6.1 and turn to dynamic observables in section 6.2. Further aspects of our results are discussed in section 6.3.

6.1 Static properties.

Pair-correlation function. A first test for finite-size effects is to compare the distributions of interparticle distances $g_{ab}(r)$ for different system sizes. Here, we

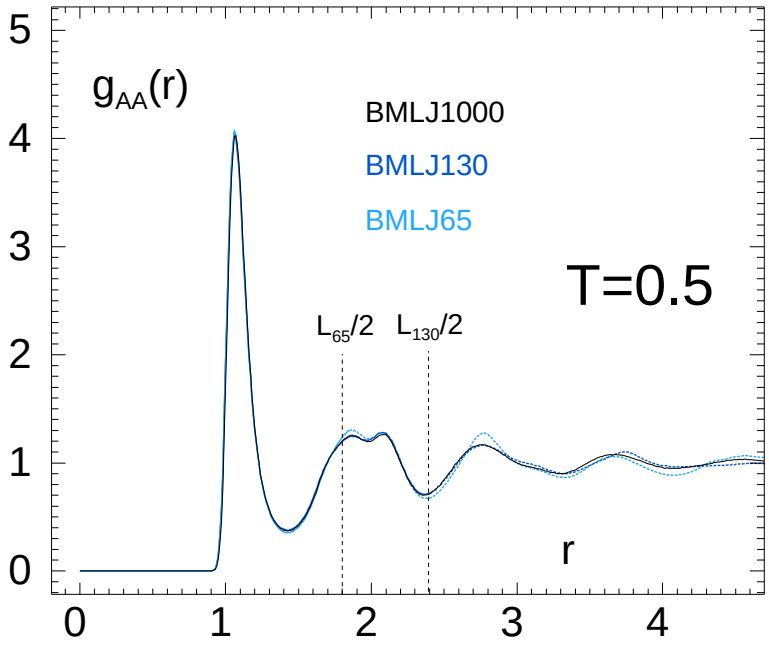

Figure 6.1: Pair-correlation function, $g_{AA}(r)$, between A particles, for $N = 1000, 130$, and 65. Periodic images of the simulation box have been used to compute $g_{AA}(r)$ for distances larger than half the box width, $r > L_N/2$ ($N = 130$ and 65).

restrict ourselves to the pair-correlation function of the A-particles, $g_{AA}(r)$, see Fig. 6.1. Within a simulation box of width L_N, we may only calculate $g_{ab}(r)$ for $r < L_N/2$. For larger values of r, periodic images of the simulation box must be used. We find that $g_{AA}(r)$ of the BMLJ65 is identical to the one of the BMLJ1000 for $r < L_{65}/2$. At larger distances, deviations from the bulk distribution can be seen. This is plausible, since the simple duplication of the simulation box can surely not reproduce all details of the long-ranged bulk correlations. Nevertheless, the oscillations corresponding to higher-order neighbor shells in the BMLJ1000 are also present in the duplicated BMLJ65. Similarly, the BMLJ130 matches the BMLJ1000 $g_{AA}(r)$ for $r < L_{130}/2$, whereas deviations for larger r already seem to be negligibly small.

Statistics of minima. We now turn to the question how the properties of the PEL are affected by changes in system size. The most prominent characteristics of a PEL minimum are its energy ϵ and vibrational partition function $T^{(3N-3)/2}Y$, see chapter 3. Since the number of PEL minima is large, a statistical treatment is needed. As a starting point, we analyze the mean energy of minima at temperature T, $\langle\epsilon(T;N)\rangle$, and their variance $\sigma^2(T;N)$. For systems composed of independent subsystems, $\langle\epsilon(T;N)/N\rangle$ and $\sigma^2(T;N)/N$ do not depend on system size. In

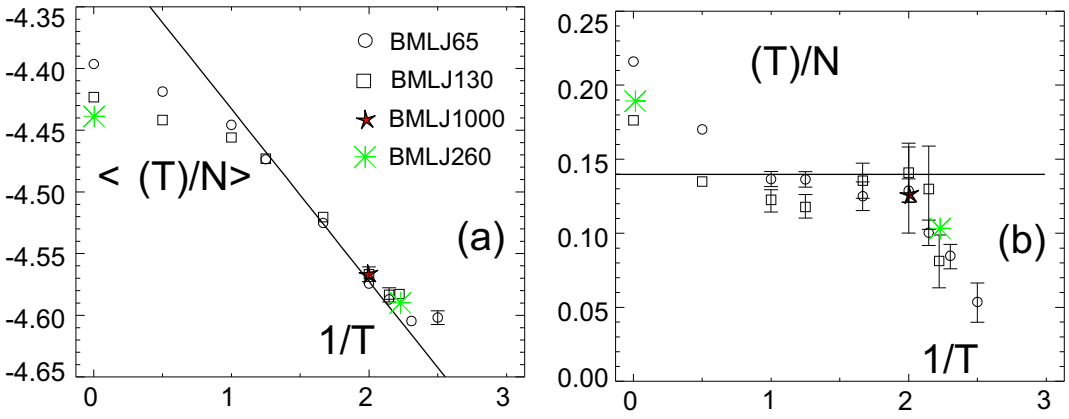

Figure 6.2: (a) Mean minimum energy per particle vs. $1/T$. Data of different system sizes are given. (b) Variance of minimum energies, also on a per-particle base, again vs. $1/T$. In (a) and (b), the straight lines are the predictions from a gaussian density of minima. At $1/T = 0$, minimizations were performed from configurations with random particle positions.

Fig. 6.2, these quantities are shown for $N = 65$ and $N = 130$, plus some data points of $N = 260$ and $N = 1000$. Concerning the mean energies, we find a good overall agreement of different system sizes. The maximum difference is about 1% between the BMLJ65 and the BMLJ260 at $T = \infty$. In the landscape-influenced regime below $T = 2T_c$, data for different N show a perfect match. A similar conclusion can be drawn from Fig. 6.2(b), where we see $\sigma^2(T)/N$. A systematically larger value is found for the BMLJ65 at high temperatures, as compared to the BMLJ130. For $T \leq 2T_c$, the difference is less than 20%, but more precise statements are prohibited by the statistical uncertainty of $\sigma^2(T)/N$ below $T = 0.6$. Thus, small but significant finite-size effects can be observed in this quantity.

We shortly comment on the deviations from the gaussian prediction at $T < 0.435$, as seen in Fig. 6.2(a) and below $T = 0.5$ in Fig. 6.2(b). As discussed in detail in section 5.5, our simulations below $T = 0.435$ were too short to sample the PEL thoroughly at the lowest energies. The result is an overestimation of $\langle \epsilon(T) \rangle$. Deviations in the variance of ϵ are even more pronounced if a simulation run is too short. This whole issue is directly related to the interplay between $\langle \tau(\epsilon_{\mathrm{MB}}; T) \rangle$ and the distribution of MBs sampled at a given temperature, $\varphi(\epsilon_{\mathrm{MB}}; T)$. Particularly important in this connection is the location of the lower PEL cutoff, ϵ_{min}.

Total number of minima and configurational entropy. A further check for the influence of system size on the energy landscape has already been can carried out in chapter 3. There, we have calculated the total number of PEL minima,

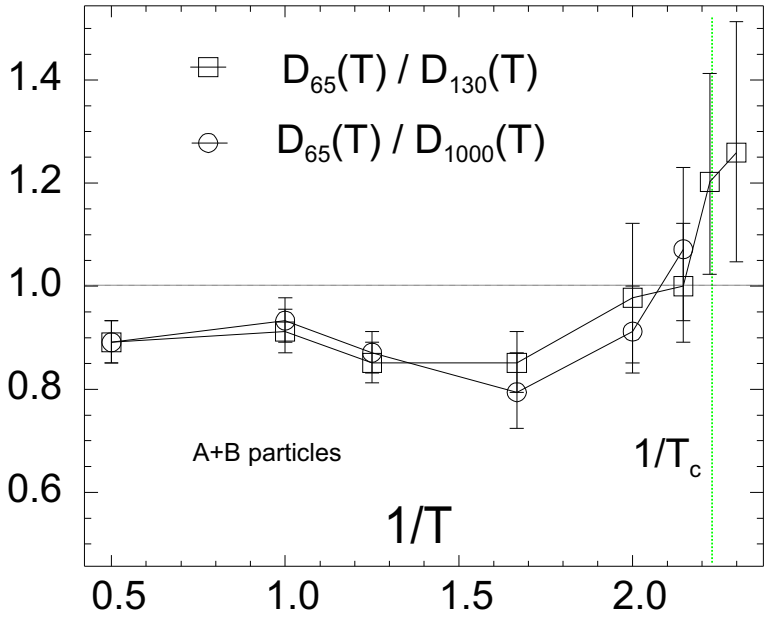

Figure 6.3: Ratios of diffusion coefficients $D_N(T)$ for three system sizes versus $1/T$.

$N_0(N)$ for $N = 65$ and $N = 130$ (Eq. 3.25). Within error bars, we have found $N_0(130) = (N_0(65))^2$, which is the trivial scaling behavior expected from combinations of non-interacting subsystems. Moreover, we have reached the same conclusion after calculating the configurational entropy per particle (Fig. 3.14): $S_c(T;N)/N$ turns out to be identical for $N = 65$ and $N = 130$ within statistical error.

6.2 Dynamic properties.

We now discuss the influence of system size on dynamics. Here, more drastic effects than in static quantities are to be expected: In fact, it is the most puzzling feature of the glass transition itself that a dramatic slowdown of molecular motion cannot be traced back to changes in static quantities easily.

Diffusion coefficients. We start with the long-time diffusion coefficient $D_N(T)$, defined by the Einstein relation. One finds that the $D_N(T)$ for $N = 65, 130$, and 1000 differ only very little. In Fig. 6.3, we see D_{65}/D_{1000} and D_{65}/D_{130} as functions of temperature. The difference between D_{65} and D_{1000} -we assume the latter to be identical to the bulk diffusion coefficient- is twenty percent or less above T_c. Since data for D_{1000} are not available below T_c, no such comparison is possible there. The fact that the BMLJ65 is systematically slower than the bulk is in qualitative agreement with results on soft spheres. In the latter systems, though, finite-size

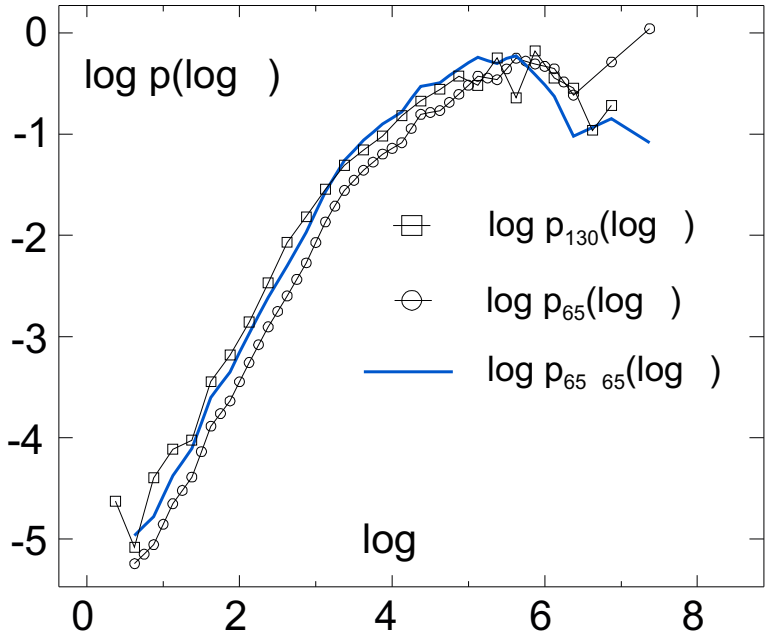

Figure 6.4: Distributions of MB lifetimes, $p(\log\tau)$ at $T = 0.5$. As discussed in the text, the distribution $p_{130}(\log\tau)$ should be reproducible from $p_{65}(\log\tau)$ by a special kind of convolution, Eq. 6.1. The corresponding function $p_{65\otimes65}(\log\tau)$ is given in the figure.

effects are much more pronounced (Kim and Yamamoto, 2000).

As reflected by D_{65}/D_{130}, the deviations are already present between $N = 65$ and $N = 130$. Below T_c, however, the BMLJ65 seems to become slightly faster than the BMLJ130. Since error bars are large for the two low-temperature data points, it is hard to judge whether this is a systematic effect that further increases upon cooling. In any event, in the temperature range studied, the overall variation of $D_N(T)$ is more than three orders of magnitude. Regarding the small deviation of the BMLJ65 relative to the BMLJ1000, finite-size effects in the long-time diffusion should be judged small.

Waiting-time distributions. As a more refined comparison of dynamics between different system sizes, we consider the distributions of MB lifetimes (waiting times), see chapter 4. At some arbitrary time of a simulation run, the probability to be in a MB of length τ is $p(\tau) = \sum_i \tau_i\delta(\tau-\tau_i)/\sum_i \tau_i$, where the τ_i's are the lifetimes found in the run. (Since the MB lifetimes span more than six orders of magnitude, our numerical computations will involve the distributions $p(\log\tau) = p(\tau)\tau\ln 10$ rather than $p(\tau)$.) The temperature dependence of $p(\tau)$ will be suppressed for notational convenience. Analogously to Eq. 5.3, we have the relation $p(\tau) = \tau\varphi(\tau)/\langle\tau\rangle$, where $\langle\tau\rangle = \int \mathrm{d}\tau\varphi(\tau)\tau$.

Guided by the idea that a BMLJ130 system is basically a duplication of two independent BMLJ65s, we may ask whether the distribution $p_{130}(\tau)$ of the larger system can be reproduced by some sort of convolution of the distribution $p_{65}(\tau)$ of the smaller one. (For a combined system, MB lifetimes are defined as the periods where neither of the subsystems relaxes.) Indeed, after a lengthy calculation (see appendix E), one finds for the duplicated system,

$$p_{65\otimes 65}(\tau) = -\frac{\mathrm{d}}{\mathrm{d}\tau}\int_{\tau}^{\infty}\mathrm{d}\tau' p_{65}(\tau')\int_{\tau}^{\infty}\mathrm{d}\tau'' p_{65}(\tau'')\left(1-\frac{\tau^2}{\tau'\tau''}\right). \tag{6.1}$$

This expression can be simplified and, upon using $p(\log\tau)$, it reads

$$p_{65\otimes 65}(\log\tau) = 2p_{65}(\log\tau)I(\tau) + 2\tau\tilde{I}(\tau)\left(\tilde{I}(\tau)\tau\ln 10 - p_{65}(\log\tau)\right), \tag{6.2}$$

where

$$I(\tau) = \int_{\tau}^{\infty}\mathrm{d}\tau' p(\tau') \quad \text{and} \quad \tilde{I}(\tau) = \int_{\tau}^{\infty}\mathrm{d}\tau' p(\tau')/\tau'.$$

In Fig. 6.4, we show $p_{65}(\log\tau)$, together with $p_{130}(\log\tau)$ at the temperature $T = 0.5$. The distribution resulting from the duplication, $p_{65\otimes 65}(\log\tau)$, is also given in the figure. It agrees reasonably with p_{130}. Thus, on the refined level of waiting-time distributions, we find further evidence that larger systems basically behave as consisting of non-interacting BMLJ65-type building blocks. Essentially, p_{130} is shifted to the left with respect to p_{65}. This is no wonder, because time intervals where both independent systems are inert, are generally shorter than the waiting times of a single system. For instance, the mean waiting times obey the relation

$$\langle\tau\rangle_{65} = 2\,\langle\tau\rangle_{65\otimes 65}\,,$$

which can be shown with the help of Eq. 6.1, see appendix E.

Metabasin depths. As discussed above, metabasins turn out as the relevant structures in the PEL for describing the slowdown of molecular motion in supercooled liquids. In chapter 5, we have reported on how the average lifetimes $\langle\tau|\epsilon_{\mathrm{MB}};T\rangle$ of MBs depend on their energies ϵ_{MB}. At some fixed ϵ_{MB}, we have found that $\langle\tau|\epsilon_{\mathrm{MB}};T\rangle$ is Arrhenius-like below $T \approx 2T_c$, leading to the parametrization

$$\langle\tau|\epsilon_{\mathrm{MB}};T\rangle = \tau_0(\epsilon_{\mathrm{MB}})e^{\beta E_{\mathrm{app}}(\epsilon_{\mathrm{MB}})}. \tag{6.3}$$

The apparent activation energy $E_{\mathrm{app}}(\epsilon_{\mathrm{MB}})$ shows a strong dependence on ϵ_{MB}, as soon as one drops below $\epsilon_{\mathrm{MB}}/N \approx -4.5$. This can be seen in Fig. 6.5 where $E_{\mathrm{app}}(\epsilon_{\mathrm{MB}})$ versus ϵ_{MB}/N is depicted both for $N = 65$ and $N = 130$.

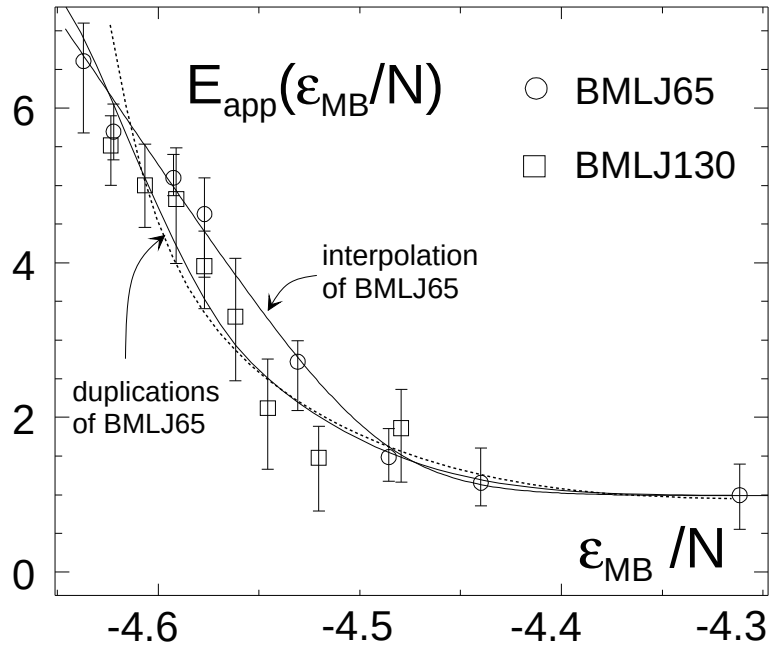

Figure 6.5: Apparent activation energies $E_{\rm app}(\epsilon_{\rm MB}/N)$ derived from mean lifetimes at fixed metabasin energy $\epsilon_{\rm MB}$ (Eq. 6.3). Data for $N = 65$ and $N = 130$ are shown versus $\epsilon_{\rm MB}/N$. The interpolation of the $N = 65$ data has been used to compute $E_{\rm app}$ for the union of two non-interacting BMLJ65, as described in the text. The result of this calculation is given in the figure (solid line). Three further duplications yield $E_{\rm app}$ for $N = 1040$ (dashed line).

Here we concentrate on the dependence of $E_{\rm app}(\epsilon_{\rm MB})$ on system size. As can be seen from Fig. 6.5, the activation energies $E_{\rm app}(\epsilon_{\rm MB}/N)$ of $N = 65$ and $N = 130$ are quite close. However, the $N = 130$ data for $\epsilon_{\rm MB}/N < -4.5$ show the tendency to fall slightly below that of $N = 65$. We shall show that this trend can be understood again in terms of a simple duplication of a BMLJ65. Hence, we are interested in the combination of two independent BMLJ65 systems. Consider a MB of energy $\epsilon_{\rm MB} = \epsilon^{(1)}_{\rm MB} + \epsilon^{(2)}_{\rm MB}$ in the combined system. Then assume that its average lifetime can be expressed through the lifetimes of both subsystems, i.e.

$$\langle\tau|\epsilon^{(1)}_{\rm MB}, \epsilon^{(2)}_{\rm MB}\rangle^{-1}_{65\otimes 65} = \langle\tau|\epsilon^{(1)}_{\rm MB}\rangle^{-1}_{65} + \langle\tau|\epsilon^{(2)}_{\rm MB}\rangle^{-1}_{65}\,. \tag{6.4}$$

Averaging $\left\langle\tau|\epsilon^{(1)}_{\rm MB}, \epsilon^{(2)}_{\rm MB}\right\rangle_{65\otimes 65}$ over the population of $\epsilon^{(1)}_{\rm MB}$ and $\epsilon^{(2)}_{\rm MB}$ at constant $\epsilon_{\rm MB}$ then yields $\langle\tau|\epsilon_{\rm MB}; T\rangle$ for the combined system[1]. The mean lifetimes produced in this way are again Arrhenius-like below $2T_c$ (data not shown here). Thus, data can again be fitted by a function of the form of Eq. 6.3, yielding $E_{\rm app}(\epsilon_{\rm MB})$ for the duplicated

[1]Here we assumed that $p(\epsilon_{\rm MB}; T) \approx p(\epsilon; T)$, as demonstrated in section 5.1.

BMLJ65. The result is shown in Fig. 6.5. Again, the artificial BMLJ65 duplication reproduces the observations for the real system of $N = 130$ particles.

Finally, we note that further duplication of the BMLJ65 leads to an interesting result: The activation energies from duplication nearly fall on top of each other for all $N \geq 130$ and $\epsilon_{\mathrm{MB}}/N > -4.6$. In Fig. 6.5, this is shown at the example of sixteen non-interacting BMLJ65s ($N = 1040$).

6.3 Discussion.

For several static and dynamic observables, we have verified the factorization property

$$\text{BMLJ130} \;\approx\; \text{BMLJ65} \;\otimes\; \text{BMLJ65}\;.$$

The BMLJ130, in turn, seems to be close to a bulk system. Some of the results presented here have already been obtained in earlier work for a very similar Lennard-Jones type system (Büchner and Heuer, 1999). Again, the conclusion can be drawn that binary Lennard-Jones systems of ca. 60 particles are a very good compromise between the desired smallness needed for our PEL investigations and the required absence of large finite-size related artifacts.

It is known from the study of cooperative length scales that they increase with decreasing temperature (Donati et al., 1999; Bennemann et al., 1999; Doliwa and Heuer, 2000). Thus, at some lower temperatures one might expect that 65 particles are no longer enough and finite-size effects become visible. For a similar Lennard-Jones system it has been shown that finite-size effects are reflected by the fact that the bottom of the PEL is frequently probed (Büchner and Heuer, 1999). From what we have learned so far, this should lead to an *enhancement* of diffusion, since deeper MBs - and thus larger $E_{\mathrm{app}}(\epsilon_{\mathrm{MB}})$ - are not available. In the present case still longer simulations at lower temperatures have to be performed to check whether also for $N = 65$ the PEL bottom can be reached; see section 5.5. Then the interesting question arises whether or not differences to the $N = 130$ system become visible.

In this connection, the simulation results of Kim and Yamamoto on the standard binary soft sphere mixture are of interest (Kim and Yamamoto, 2000). Comparing systems of $N = 108$ and 1000 particles above T_c, the authors find the small system to be up to an order of magnitude slower than the large one. These findings suggest a fundamental difference between the Lennard-Jones and the soft-sphere systems. Evidently, soft spheres exhibit a larger length scale of cooperative motion than do Lennard-Jones systems; see (Yamamoto and Onuki, 1998; Poole et al., 1998). We have seen in Fig. 6.3 that at $T > T_c$, the BMLJ65 is slower than the bulk

system, which is the same trend as reported by Kim and Yamamoto for soft spheres. However, this behavior changes below T_c since the diffusion of the BMLJ65 is slightly enhanced with respect to the bulk.

The results presented in this chapter suggest that the essential physics of the supercooled BMLJ is already contained in the system of $N = 65$ particles. For the temperatures under investigation here, as already noted, structures of collectively moving particles ('strings') have been reported in large systems (Donati et al., 1998). However, the size of these strings rarely exceeds ten particles, so that they may fit into our BMLJ65 as well. Preliminary results[2] show that the distributions of string sizes in the BMLJ65 are very similar to the ones reported by Donati et al. However, the length scale of correlated particle motion in large BMLJ systems (Poole et al., 1998) during typical structural relaxation times is relatively large. At the lowest temperatures under study ($T = 0.451$), Poole et al. find appreciable, pairwise correlations of mobile particles over up to five next-neighbor distances[3]. One would therefore think that a minimum simulation box of width ten is needed in order to avoid finite-size related artifacts. Apparently, this is in contradiction to the results of the present chapter where a box size of less than four has been used in the BMLJ65. As a conjecture, a possible resolution would be that large dynamical length scales at long observation times, consisting of a superposition of many single relaxation events (say, many different MB escapes), are only concomitants of the molecular slowing down. In other words, large-scale dynamical correlations are probably only indirectly related to the temperature dependence of the diffusion coefficient.

[2]Michael Vogel, unpublished.

[3]Poole et al. also report that the decay constants of the corresponding correlation functions are between 0.05 and 0.33, which seems to be wrong or -at least- misleading, when compared to their other results.

Chapter 7

The Molecular Slowing Down

The aim of the present chapter is to assemble the results obtained to far and to put them into a perspective with the current understanding of supercooled liquids, as can be found in the literature. In order to render the chapter self-contained, the essential steps in the argumentation will be repeated. For the reader who skipped the last chapters, thus, it might be convenient to find the main results in a nutshell.

The metabasin concept is at the heart of the present study. Following the pioneering work by Stillinger and Weber, we calculate the time series of inherent structure energies, $\epsilon(t)$, see Fig. 7.1(a). It is important to realize that the true potential energy of the system at time t, $V(t)$, lies far above $\epsilon(t)$: By the minimization procedure, the vibrational degrees of freedom -which contribute of the order of $3Nk_{\mathrm{B}}T/2$ to $V(t)$- are removed. For the temperature shown in Fig. 7.1, the mean value of $V(t)$ is located around $\langle V \rangle_T \approx -250$. In Fig. 7.1(a) one immediately recognizes that there are long time intervals during which the system jumps back and forth between a finite number of minima - the system is caught in some region of the PEL (compare Figs. 4.5 and 4.6). In real space this corresponds to a stable structure. In chapter 4, this observation gave rise to the notion of metabasins (MBs) as a way to group these strongly correlated inherent structures together. Then the total simulation run may be regarded as a continuous sequence of MB visits with individual waiting times τ. We denote the probability distribution of waiting times by $\varphi(\tau;T)$ and their average by $\langle \tau(T) \rangle$. Beyond $\varphi(\tau)$ we also introduce the distribution $p(\tau)$, expressing the probability that at a given time the present MB has a waiting time τ, i.e. $p(\tau;T) = \tau\varphi(\tau;T)/\langle \tau(T) \rangle$.

Interestingly, we observed in chapter 4,

$$D(T) = \frac{a^2}{6N \langle \tau(T) \rangle}, \qquad \text{for } T < 2T_{\mathrm{c}} \tag{7.1}$$

with a temperature-independent effective jump length ($a \approx 1.0$ in BMLJ units). Thus, the temperature dependence of $D(T)$ is *exclusively* determined by the average

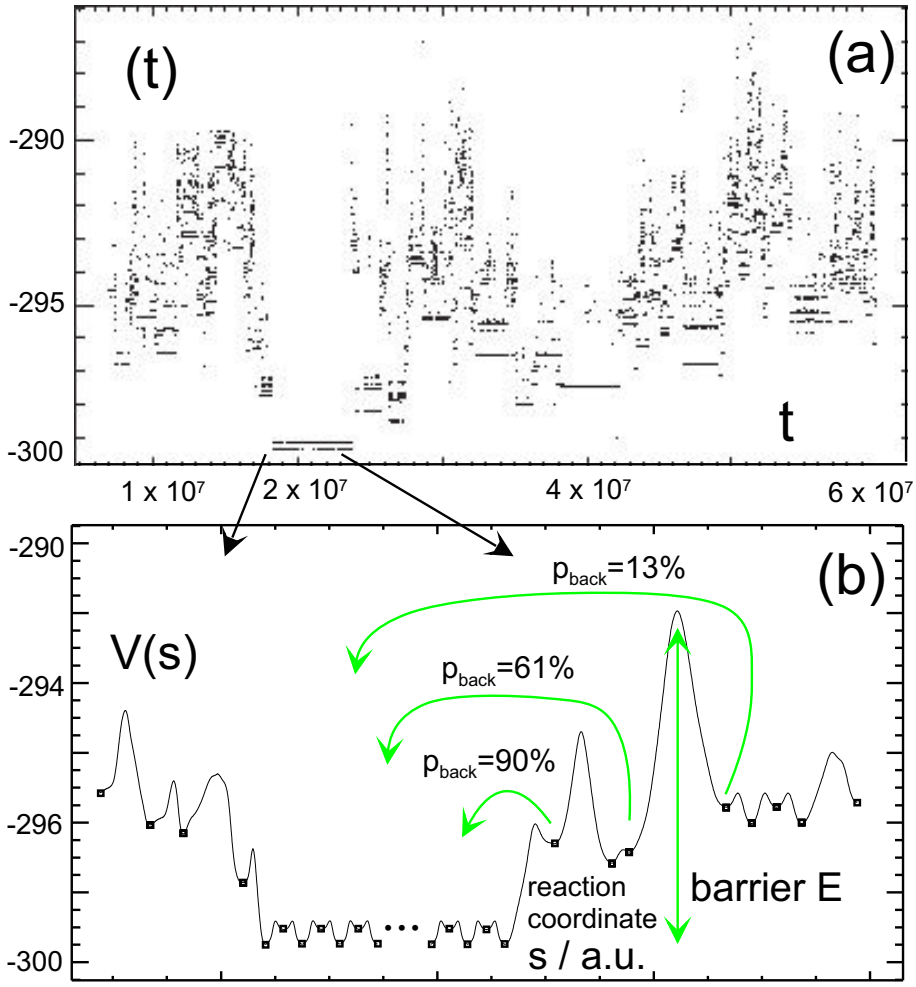

Figure 7.1: (a) The sequence of inherent structure energies $\epsilon(t)$ for $T = 1.1T_c$ in the BMLJ65 system. One can see the large time intervals during which the system is jumping between a finite number of inherent structures, thus giving rise to the notion of metabasins (MBs). (b) Detailed analysis of the transitions in one MB. The reaction path for every transition has been determined via an explicit transition-state search algorithm and the distance s is measured along the curvilinear reaction coordinate. Successive transitions are spliced together, leading to the potential energy profile $V(s)$. The quantity $p_{\rm back}$ denotes the probability to end up in the lowest minimum of the MB after starting from the corresponding minimum. All inherent structures with $p_{\rm back} > 0.5$ belong to the MB by definition. The barrier E (indicated by the arrow) is given by the difference between the ground state of the MB and the transition state which is necessary to reach the first inherent structure with $p_{\rm back} < 0.5$.

waiting time in the MBs whereas all spatial aspects of diffusion are temperature independent. Such a simple relation does not hold on the level of single inherent structures (section 4.5). In order to understand the temperature dependence of the

molecular slowing down on the basis of PEL structure, it is therefore sufficient to relate the average MB waiting time to the properties of the PEL regions that are explored at different temperatures.

At the example of the BMLJ65 model glass former, we show in section 7.1 that two types of MBs exist: some allowing for quasi-free motion on the PEL (liquid-like), the others acting as traps (solid-like). In this framework we obtain an intuitive description of the glass transition by analyzing the temperature dependence of their relative weights and their impact on dynamics. Especially, we identify a temperature -much above the glass transition- below which $D(T)$ is governed by activated hopping events out of the before-mentioned traps. As discussed in section 7.3, this is in contrast to the current understanding of the glass transition, where hopping is deemed to set in at much lower temperatures. The quantitative relation of these activated hops to the local PEL structure will be discussed before, in section 7.2.

7.1 Liquid-like and Solid-like Regions on the PEL.

The distribution $\varphi(\tau;T)$ is shown in Fig. 7.2(a), where waiting times for different temperature are reported over up to 8 orders of magnitude. By pure visual inspection, one identifies two different time regimes with a crossover at $\tau^* \approx 5000$, as indicated by the vertical line. In terms of energetics one expects that the long τ's arise from deep traps where the system is caught for long times. In the opposite limit one may imagine that there are quite shallow MBs which do not strongly confine the system so that it will mainly stay close to the high-dimensional boundary of MBs. Thus, short waiting times should correspond to just scratching a MB. To quantify this expectation we have calculated the angle α between the entry point of a MB, the inherent structure of this MB with the lowest energy and the exit point. The expectation value $\langle \cos\alpha \rangle_\varphi$ is shown in Fig. 7.2(b) as a function of τ. We see that short visits to MBs lead to small values of α, meaning that the system indeed merely scratches these MBs. For $\tau > \tau^*$, $\langle \cos\alpha \rangle_\varphi$ reaches a limiting value of 0.2. Hence, the entry and exit points are largely uncorrelated which should be the case after a long residence in a MB with many possible exits. The non-zero value of $\langle \cos\alpha \rangle_\varphi \approx 0.2$ indicates that residual correlations between MB entry and exit remain, also for long residences. The origin of those is not fully clear: After section 4.2, the dynamics between MBs is not completely a random walk, so that minor backward correlations are expected. On the other hand, an un-symmetric location of the lowest MB minimum (which serves as the point of the angle α) within

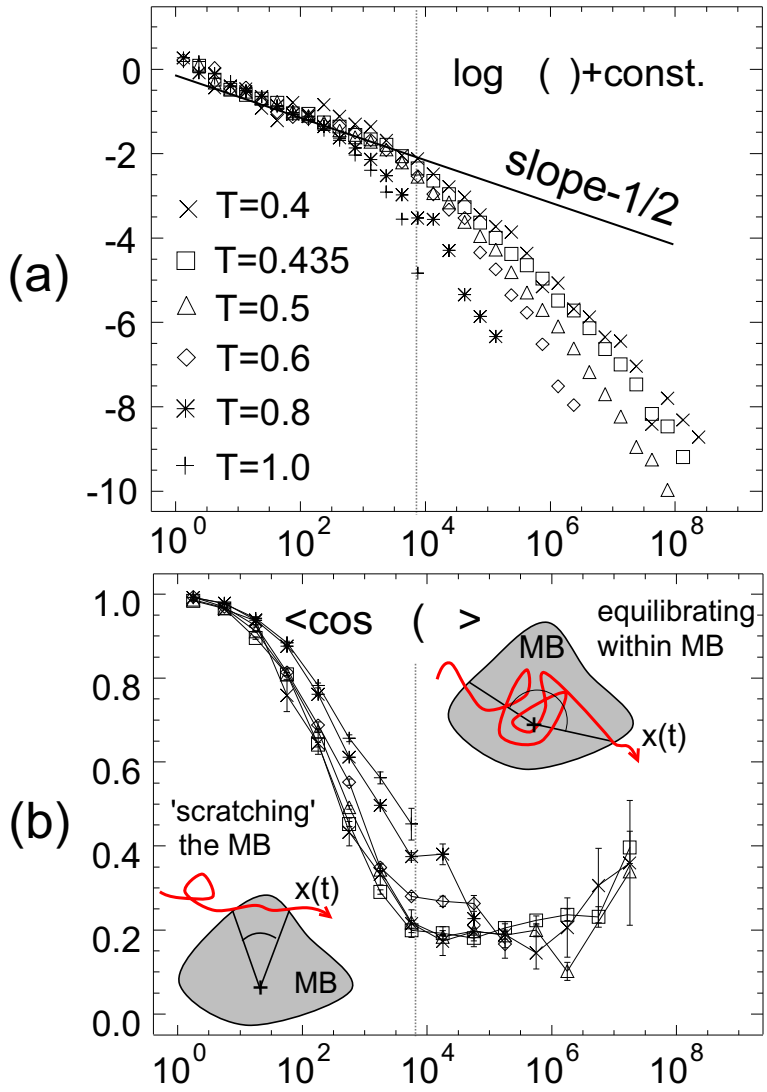

Figure 7.2: (a) The distribution $\varphi(\tau;T)$ of waiting times. By visual inspection, one can distinguish two different time regimes, indicated by the vertical line. (b) Average value of $\langle\cos\alpha\rangle$, where α is the angle between the entry point, the lowest inherent structure of the MB and the exit point. Again two time regimes with a temperature-independent crossover time $\tau^* \approx 5000$ can be identified.

the MB also leads to a non-zero $\langle\cos\alpha\rangle_\varphi$, even if entry and exit are uncorrelated[1]. Quantities related to $\langle\cos\alpha\rangle_\varphi$, like the distance in configuration space between MB entry and exit points as a function of τ, support the conclusion that the short MB

[1]This can be seen by a simple two-dimensional argument. Assume that the MB has the shape of a circle and that entry and exit points lie at some random, uncorrelated positions on the circle. If the lowest MB minimum is not at the center, but at some random position within the circle, the average cosine of the angle between these three points will be non-zero, too (ca. 0.1).

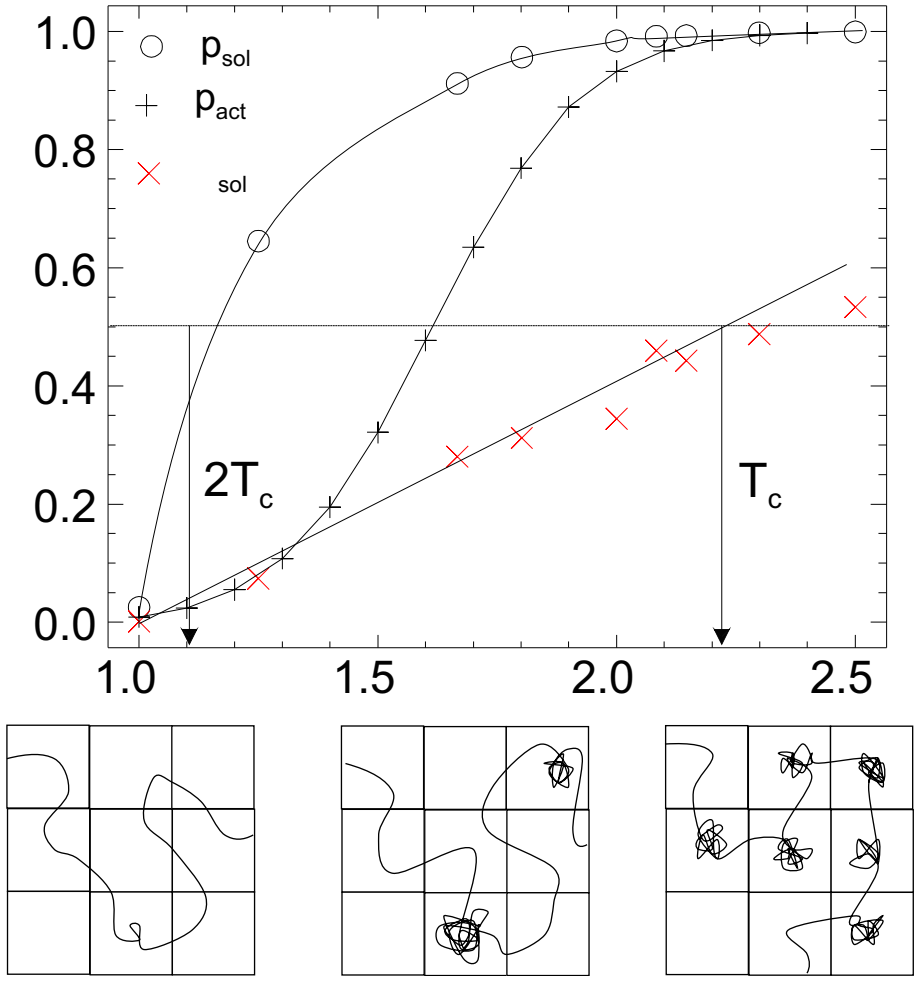

Figure 7.3: The temperature dependence of p_{sol} (the fraction of time spent in solid-like configurations), φ_{sol} (the fraction of solid-like configurations encountered during the time evolution), and p_{act} (a measure for the contribution of activated processes to the diffusion coefficient). In the lower part we depict schematic plots of the scenarios in the three temperature regimes. The squares stand for the different MBs.

visits ($\tau < \tau^*$) are completely different in nature from the long ones. Due to the difference in stability, we will call the MBs with $\tau > \tau^*$ *solid-like*, the other MBs *liquid-like*. This notation has been borrowed from two-state models where these two types of configurations have been postulated (Fischer et al., 2002).

In chapter 5, we quantitatively related the escape from solid-like structures to barriers in the PEL (see also section 7.2). For the liquid-like regions, this is not possible, since the corresponding MBs are too shallow, i.e. their depth is only of the order of $k_{\mathrm{B}}T$.

The very different properties of solid-like and liquid-like structures indicate that

the slowing down upon cooling may be rationalized in terms of an enhancement of solid-like contributions. This can be quantified in two different ways. Firstly, one may determine the number of solid-like vs. liquid-like configurations the system encounters during its dynamics in configuration space. The fraction of solid-like regions is given by $\varphi_{\rm sol} \equiv \int_{\tau^*}^{\infty} {\rm d}\tau\varphi(\tau)$, where $\varphi_{\rm sol} < 0.5$ implies that more liquid-like than solid-like configurations are visited. Secondly, we can specify the fraction of time spent in solid-like configurations. Using the distribution $p(\tau)$ this can be expressed as $p_{\rm sol} \equiv \int_{\tau^*}^{\infty} {\rm d}\tau\ p(\tau)$. Since

$$D^{-1}(T) \propto \langle\tau(T)\rangle = \int_0^{\tau^*} {\rm d}\tau\tau\varphi(\tau;T) + \int_{\tau^*}^{\infty} {\rm d}\tau\tau\varphi(\tau;T),$$

$p_{\rm sol} > 0.5$ implies that the time scale of dynamics is dominated by the escape from solid-like configurations. In Fig. 7.3 we show the temperature dependence of $\varphi_{\rm sol}$ and $p_{\rm sol}$. Three different temperature regimes can be distinguished (see the sketch in Fig. 7.3): For $T > 2T_{\rm c}$ both quantities are smaller than 0.5. Thus, the system behaves liquid-like. Interestingly, it is exactly the temperature regime for which the inherent structures no longer influence the thermodynamic properties of the system. Below $2T_{\rm c}$, $p_{\rm sol}$ is larger than 0.5. Thus, for $T < 2T_{\rm c}$ the temperature dependence of $D(T)$ is dominated by the escape from solid-like configurations. Finally, below a temperature close to $T_{\rm c}$, also $\varphi_{\rm sol}$ exceeds 0.5, i.e., we have a trap-to-trap motion.

7.2 From PEL Structure to Diffusion.

It is possible to go one step further and to characterize the escape mechanism from solid-like MBs in terms of the local PEL structure. This has been analysed in detail in chapter 5, where we have found that the mean residence time in MBs of energy $\epsilon_{\rm MB}$ is given by

$$\langle\tau(\epsilon_{\rm MB};T)\rangle = \tau_0(\epsilon_{\rm MB})e^{E_{\rm app}(\epsilon_{\rm MB})/k_{\rm B}T}, \quad \text{for } T < 2T_{\rm c}. \tag{7.2}$$

With regard to the complexity of MBs, the multitude of escape paths, and the multi-step nature of either of these paths, it is quite surprising that such a simple parameterization of $\langle\tau(\epsilon_{\rm MB};T)\rangle$ is possible and that even $\tau_0(\epsilon_{\rm MB})$ only weakly depends upon $\epsilon_{\rm MB}$. As discussed at length in chapter 5, the apparent activation energy $E_{\rm app}(\epsilon_{\rm MB})$ is a complex superposition of all barriers surrounding a MB. Since their relative weights change with temperature, is seems to be fortunate that $E_{\rm app}(\epsilon_{\rm MB})$ remains constant (see the discussion of Fig. 5.11 in section 5.3). At present, we cannot give an explanation for the constancy of $E_{\rm app}(\epsilon_{\rm MB})$, but only take it as

convenient enough for the parameterization of $\langle\tau(\epsilon_{\rm MB};T)\rangle$. The activation energy $E_{\rm app}(\epsilon_{\rm MB})$ is shown in Fig. 7.4(a). The deeper the MB lies in the PEL, i.e. the lower $\epsilon_{\rm MB}$, the higher the activation energy. In contrast, $\tau_0(\epsilon_{\rm MB})$ turns out to be basically independent of $\epsilon_{\rm MB}$ (see Fig. 5.2).

It is natural to check whether $E_{\rm app}(\epsilon_{\rm MB})$ indeed corresponds to the barrier heights around MBs (see section 5.3). To this end, we have analysed the entry and exit events of MBs in detail: For every individual transition between inherent structures we determined the respective transition state. We have then computed the potential energy profile, $V(s)$, along the ideal reaction path over the transition state, as a function of the curvilinear reaction coordinate s. Splicing these functions together, we obtain a multi-barrier energy profile $V(s)$ which gives a good impression of the PEL structure underlying the dynamics, see Fig. 7.1(b). One clearly observes the several back- and forth jumps in the MB, which cross only small barriers as compared to $k_{\rm B}T$. One also notes that the entry and exit events are given by a sequence of staircase-like steps rather than by a single transition. From these one can identify the barrier E that has been surmounted when escaping the MB, see Fig. 7.1(b). Averaging these barriers over all escapes one indeed recovers $E_{\rm app}(\epsilon_{\rm MB})$ (see Fig. 5.13). Thus, relaxation dynamics, as expressed through Eq. 7.2, is indeed stirred by the local barriers around MBs.

The consequences of these observations for the macroscopic dynamics have already been expressed in Fig. 5.14. Together with Eq. 7.1 we can estimate the diffusion coefficient (denoted $D_{\rm est}(T)$, Eq. 5.19) via

$$D_{\rm est}(T) = \frac{a^2}{6N\tau_0}\int d\epsilon_{\rm MB} p(\epsilon_{\rm MB},T) e^{-E_{\rm app}(\epsilon_{\rm MB})/k_{\rm B}T} \equiv D_0 \exp(-E_{\rm eff}(T)/k_{\rm B}T) \quad (7.3)$$

where the integral is written as $\exp(-E_{\rm eff}(T)/k_{\rm B}T)$. $E_{\rm eff}(T)$ can be interpreted as an effective activation energy at temperature T. $p(\epsilon_{\rm MB},T)$ denotes the probability to be in a MB of energy $\epsilon_{\rm MB}$ and is also plotted in Fig. 7.4(a). Eq. 7.3 expresses the average jump rate out of MBs as an integral over $\epsilon_{\rm MB}$, using the specific information about the average time scale to leave a MB with energy $\epsilon_{\rm MB}$. Note that the ingredients of the constant D_0, i.e. a and τ_0, have been obtained from the different simulations mentioned above. However, D_0 cannot be inferred directly from the local PEL structure. In the units of our simulation we have $D_0 \approx 1.2 \cdot 10^{-5}$. The validity of Eq. 7.3 is checked in Fig. 7.4(b) by comparing $D_{\rm est}(T)$ with the true diffusion coefficient $D(T)$.

The r.h.s of Eq. 7.3 contains information about the thermodynamics, i.e. the population of MBs as expressed by $p(\epsilon_{\rm MB},T)$, and information about local barriers via $E_{\rm app}(\epsilon_{\rm MB})$. Actually, it turns out that to a very good approximation $p(\epsilon_{\rm MB},T) \approx p(\epsilon,T)$ (Fig. 5.4), corresponding to the distribution of inherent struc-

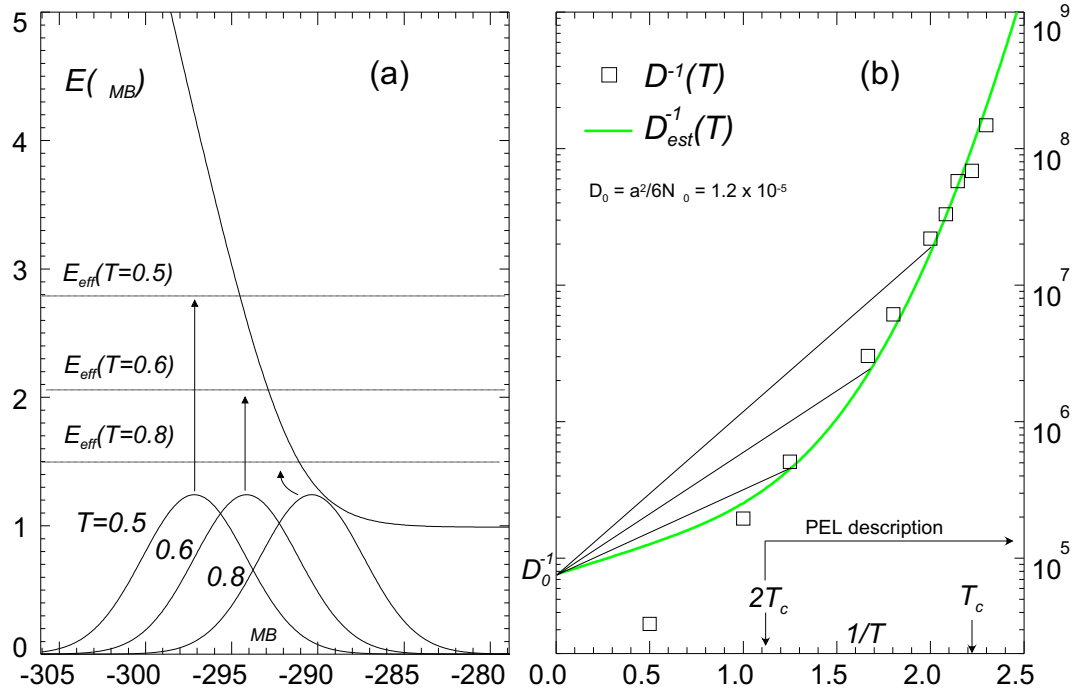

Figure 7.4: (a) The barrier height $E_{\rm app}(\epsilon_{\rm MB})$ and the population of MBs $p(\epsilon_{\rm MB}, T)$ for different temperatures. From these quantities, according to Eq. 7.1, we obtain an estimate for the diffusion coefficient, $D_{\rm est}(T) = D_0 \exp(-E_{\rm eff}(T)/k_{\rm B}T)$, with the effective barrier height $E_{\rm eff}(T)$. A comparison of the predicted with the true diffusion coefficient $D(T)^{-1}$ (squares) is shown in (b).

tures, which has been studied in great detail. Thus it is possible for $T < 2T_{\rm c}$ to predict the macroscopic dynamics from knowledge of the thermodynamics and the local barriers. Furthermore, Eq. 7.3 implies that the activation energy which is obtained from connecting $(0, D = D_0)$ and $(1/T, D(T))$ in an Arrhenius plot by a straight line can indeed be interpreted as the typical barrier height the system experiences at a given temperature. This non-trivial interpretation has just recently been confirmed experimentally by hyper-quench experiments (Angell et al., 2002).

Crossover to activated dynamics. With Eq. 7.3 we can also analyze the question in which temperature regime the diffusion coefficient is determined by activated processes. Here we denote a process as activated if the activation energy is larger than $5k_{\rm B}T$. Using Eq. 7.3 we may write $D(T) = D_{\rm act}(T) + D_{\rm rest}(T)$ where the first term denotes the integral over all $\epsilon_{\rm MB}$ for which $E_{\rm app}(\epsilon_{\rm MB}) > 5k_{\rm B}T$ and the second term the integral over the other MBs. The ratio $p_{\rm act} = D_{\rm act}(T)/D(T)$ is thus a measure for the relevance of activated processes. Its temperature dependence is also shown in Fig. 7.3. The crossover temperature for which $p_{\rm act} = 0.5$ is

close to $1.5T_c$. Thus, already significantly above T_c, the temperature dependence of the diffusion coefficient is dominated by activated processes. This is an additional information to our earlier observation that already far above T_c the escapes from solid-like configurations determine the mean MB lifetime.

To reduce a bit the reader's confusion concerning the relation of the quantities $p_{\rm sol}$ and $p_{\rm act}$, we note again that $p_{\rm sol}$ is the relative weight in $\langle\tau\rangle$ of *all* long waiting times ($\tau > \tau^*$). To $p_{\rm act}$, only the MBs with $E_{\rm app}(\epsilon_{\rm MB}) > 5k_{\rm B}T$, i.e. with $\tau_0(\epsilon_{\rm MB})\exp(\beta E_{\rm app}(\epsilon_{\rm MB})) > \min(\tau_0(\epsilon_{\rm MB}))\, e^5 \approx 5\times 10^3 = \tau^*$ contribute. Thus, at least, $p_{\rm act} \leq p_{\rm sol}$. At intermediate temperatures ($T \approx 1.5T_c$), however, the weight of MBs longer than τ^*, but with $E_{\rm app} < 5k_{\rm B}T$ is relatively large, so that $p_{\rm act}$ is significantly smaller than $p_{\rm sol}$.

7.3 Relation to Existing Work.

Instantaneous-normal-mode studies. We now discuss the relation of our work to the instantaneous normal mode approach (INM) which considers the number of 'diffusive modes', $f_{\rm diff}$, to be at the physical basis of diffusion (La Nave et al., 2000; La Nave et al., 2001; La Nave et al., 2002b; Chowdhary and Keyes, 2002). From the directions corresponding to negative eigenvalues of the Hessian $H(x(t))$ (unstable directions), one filters out the 'diffusive' directions. We do not discuss the procedure for doing so here, but merely remark that it is by no means unique. Considering the energy profile on the straight lines along the unstable directions, La Nave et al. observed extremely small barriers, indicating completely 'entropic' dynamics at the considered temperatures (La Nave et al., 2001). This conclusion, though reached for a model of supercooled water, is in contrast to our findings of the relevance of energetic barriers. A possible key to this apparent contradiction is that $f_{\rm diff}$ is directly related to the fraction of time spent in 'mobile' regions of configuration space. In contrast, we have concentrated on the durations of the stable, immobile structures. As the consequence of longer and longer residences in deep MBs, the mobile fraction becomes smaller and smaller. Thus, one observes a relation between $D(T)$ and $f_{\rm diff}(T)$, although it is the long trapping times which are the reason for the slowing down of dynamics.

To be more quantitative, let us assume that the average number of free directions is proportional to the fraction of time spent in the liquid regions of configuration space, i.e. $f_{\rm diff}(T) \propto p_{\rm liq}(T)$, where

$$p_{\rm liq} = 1 - p_{\rm sol} = \int_0^{\tau^*} {\rm d}\tau \frac{\tau\varphi(\tau)}{\langle\tau\rangle} = \frac{\varphi_{\rm liq}\langle\tau\rangle_{\rm liq}}{\langle\tau\rangle}.$$

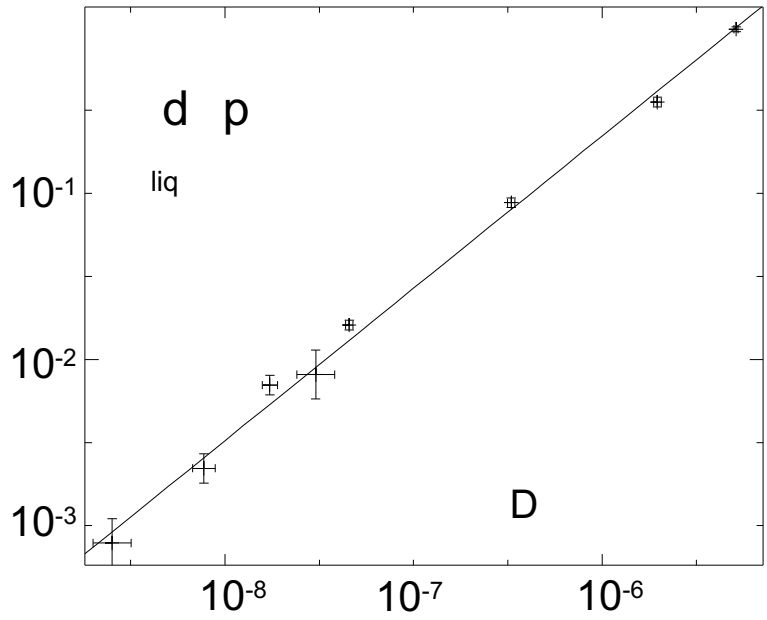

Figure 7.5: The fraction of time, $p_{\rm liq}(T)$, spent in MBs shorter than τ^*, parametrically plotted against $D(T)$.

Here $\langle\tau\rangle_{\rm liq}$ denotes the average lifetime of liquid-like configurations and $\varphi_{\rm liq} = 1-\varphi_{\rm sol}$. From Fig. 7.2(a) it is evident that $\langle\tau\rangle_{\rm liq}$ does not depend on temperature. Moreover, if $\varphi_{\rm liq} > 0.5$ (i.e. for $T > T_{\rm c}$), the main temperature dependence of $p_{\rm liq}$ stems from the denominator, i.e. $p_{\rm liq} \propto 1/\langle\tau\rangle$. Thus, one has $f_{\rm diff}(T) \propto p_{\rm liq}(T) \propto 1/\langle\tau(T)\rangle \propto D(T)$. We have explicitly checked the validity of this proportionality in Fig. 7.5. Thus, a strong correlation between $f_{\rm diff}(T)$ and $D(T)$, as found in the INM studies, is expected in the BMLJ65 system. Nevertheless, it remains correct that the diffusion coefficient is determined by the activated escape from the solid-like configurations rather than by the search of barrier-free modes.

The whole argument may be rationalized by a very simple model. Picture a random walk on a surface with traps which are of depth E. Despite the traps, the surface is flat. Escapes from traps are assumed to be given by the Arrhenius law, i.e. happen after a mean waiting time of $\tau_0 e^{\beta E}$. On top of the surface, no activation is needed to continue the walk, and we take the waiting times to be equal to the constant τ_0, there. If the surface is covered half by traps, the mean waiting time during the walk is $\langle\tau(T)\rangle = \tau_0(e^{\beta E}+1)/2$. Since the long-time diffusion coefficient follows $D \propto 1/\langle\tau\rangle$, we have $D \propto 1/(e^{\beta E}+1)$. The mobility on top of the surface is high, which would correspond to the presence of many unstable directions in the INM approach. For simplicity, we assume $f_{\rm diff} = 1$ on top of the surface and zero in the traps. Under these assumptions, we find on average, $f_{\rm diff}(T) = 1/(e^{\beta E}+1)$, which

is equal to the population of the top of the surface. Thus, the relation $D \propto f_{\text{diff}}$ arises, as in the INM analyses for supercooled liquids. It is clear from the model, however, that this connection is rather indirect: At low temperature, $D(T)$ is small due to the long trapping times, whereas $f_{\text{diff}}(T)$ is small since the population of the surface is low, both of which are determined by the trap depth E. Hence, the interrelation between $D(T)$ and $f_{\text{diff}}(T)$ as found in the instantaneous-normal-mode approach is of the kind: 'autumn leaves fall because they change their color.'

We further note that the MB concept is in no way implemented in the INM approach. Supercooled water, e.g., exhibits very pronounced MB correlations in the time series of minima, even for a 'large' system of 216 particles (Giovambattista et al., 2002b). Generally, fragile glass formers are expected to have a 'rugged' PEL, i.e. exhibit extensive superstructures of minima (Stillinger, 1995). In view of this insight, the success of INM analyses for the latter type of systems is quite surprising.

Higher-order stationary points ('saddles'). In the recent literature, much attention has been paid to the generalization of the inherent-structure concept to higher-order stationary points (Angelani et al., 2000a; Broderix et al., 2000). With the help of the auxiliary potential of the squared force, $\tilde{V}(x) = \frac{1}{2}|F(x)|^2$, one partitions the configurational space into a new set of basins, corresponding to the local minima of $\tilde{V}(x)$. Since $\tilde{V}(x)$ is never negative, all stationary points (i.e. configurations with vanishing forces) are absolute minima of $\tilde{V}(x)$. Thus, by minimizing $\tilde{V}(x)$ starting from equilibrium configurations, one can hope to find a representative set of stationary states, or 'saddles', that are populated at a given temperature. (Sometimes, these are fondly called italo saddles.) The number of negative eigenvalues of the Hessian matrix, $H(x)$, evaluated in a saddle configuration is defined as the saddle index n. Clearly, PEL minima correspond to $n = 0$ and transition states to $n = 1$. Generally, the saddle index is interpreted as a measure for the stability of the respective configuration: If n is large, the system has many possibilities to descend from the saddle, so that this will be an unstable configuration. Moreover, an equilibrium configuration which is located in the $\tilde{V}$-basin of a high-order saddle is expected to be as unstable as the saddle itself. This, in turn, should mean that the system is highly mobile in this region of configuration space. Thus, the study of the statistics of stationary points on the PEL should teach us more about the mobility of the system, which seems to be a promising advance[2].

[2]Recently, it became clear that most of the $\tilde{V}$-minima reached from equilibrium configurations are no stationary points, due to non-zero forces (Doye and Wales, 2002). Thus, most of them are no global but only local minima of $\tilde{V}$ ('false' saddles). The desired partitioning of configuration space into basins of saddles is therefore incomplete. Later on, some of the authors of the original saddle investigations could show that their initial findings remain valid because 'false' saddles,

In the above-cited works, Angelani and coworkers calculated the mean saddle index, $n(T) = \langle n(x) \rangle_T$, as a function of temperature for the BMLJ of $N = 1000$ particles. Interestingly, they found a linear relation of $n(T)$ with T covering a large range of temperatures. Moreover, $n(T)$ was found to vanish exactly at T_c, i.e.

$$n(T) \approx A(T - T_c), \qquad \text{for } T > T_c, \tag{7.4}$$

with some constant A, and $n(T) \approx 0$ below T_c. At $T = 1.1T_c$, for instance, an average index of $n(T) \approx 15$ was reported. These results were then interpreted as follows. Above T_c, the system has permanent access to high-order stationary points, giving rise to many unstable directions in configuration space. Thus, for diffusion to take place there is no need for traversing additional energy barriers by thermally activated processes. The system rather wanders around until it finds one of the unstable directions which then enables the relaxation to a neighboring part of configuration space. Below T_c, where $n(T) \approx 0$, these unstable directions are not available anymore, since the system now resides close to the PEL minima. Thus, after Angelani et al., thermally activated processes are relevant for relaxation only below T_c.

A priori, the *numerical results* of Angelani et al. do not contradict our findings. As we have seen in Fig. 7.1(b), the MB depth E is much larger than the typical barriers that are constantly crossed by the *intra*-MB dynamics. In time-averaged quantities, however, the latter barriers are predominant. Thus, it is no wonder that higher-order stationary points are constantly found above T_c. Since they merely connect inherent structures within the same MB, though, they are irrelevant for relaxation. Thus, it is the *interpretation* of Angelani et al. which goes too far, since it ignores the existence of metabasins.

In the following, however, we give a criticism of the $\tilde{V}$-saddles, which is serious in our opinion. In chapter 5, we demonstrated that the relaxation from MBs can be described correctly by taking into account the transition states that govern the single transitions along the multi-minima escape paths. These were located by the ridge method, as described in section 5.2. The advantage of the ridge method is that we definitely find the relevant barrier for a transition, i.e. a first order saddle on the basin border next to the point where the border was crossed (see Fig. 5.6). In contrast, by using the auxiliary potential $\tilde{V}$ as described above, we encounter two major drawbacks: First, as already said, one obtains higher-order saddles and, most frequently, non-stationary points ('false' saddles or shoulders). These configurations are of no use to us because for the calculation of reaction rates via transition state theory, we need 'true' first-order saddles. Second, and more importantly, the $\tilde{V}$

despite the non-zero forces, have the same properties as the 'true' saddles (Angelani et al., 2002).

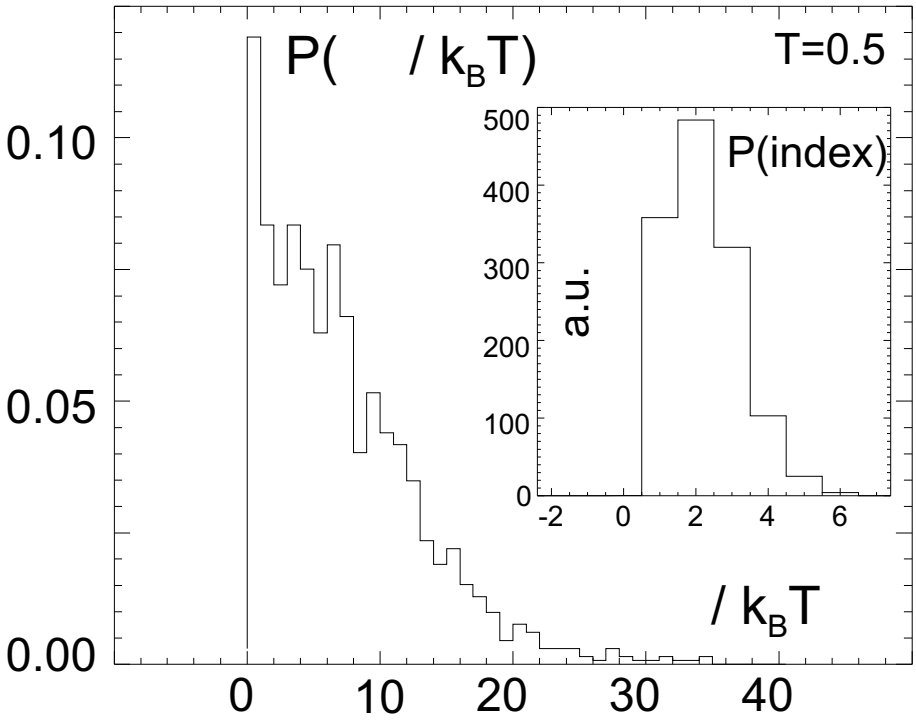

Figure 7.6: Comparison of transition states, obtained via the ridge method, with minima of the auxiliary potential $\tilde{V}$. Starting points for saddle computations lay close to basin borders. Main plot: histogram of $\tilde{V}$-saddle minus TS energies. Inset: histogram of indices of $\tilde{V}$-saddles.

minimization locates saddles, even if they are not kinetically accessible. This is because the expression $F^\dagger(x)H(x)F(x) = (\partial V(x))^\dagger \partial\tilde{V}(x)$ is not positive. Thus, the $\tilde{V}$-minimization can *climb up* to a saddle.

To shed more light on the second point and on the interrelation between TSs and $\tilde{V}$-saddles, we have minimized $\tilde{V}$ by steepest descent, starting only from configurations $x(t)$ near basin borders, i.e. we start from $x(t)$ only if $\xi(t) \neq \xi(t+1 \text{ MD step})$ (like y_0 in Fig. 5.6). In other words, we have calculated $\tilde{V}$-saddles exactly at transition times. If this yielded the correct TSs, our more time-consuming ridge method would clearly be useless. The energy difference $\Delta\epsilon = \epsilon_{\tilde{V}} - \epsilon_{\text{TS}}$ specifies the overestimation of the true barrier by the $\tilde{V}$-saddle. It may also happen that the index of the $\tilde{V}$-saddle is different from one. The distributions of $\Delta\epsilon$ and the index are shown in Fig. 7.6 (for $T = 0.5$). Obviously, the $\tilde{V}$-saddles considerably overestimate barriers and the correct TSs are only found very rarely. Moreover, most of the $\tilde{V}$-saddles have an index different from one, i.e. are no TSs at all. In turn, the energy of the TS is never undersold by a $\tilde{V}$-saddle. In conclusion, $\tilde{V}$-saddles turn out to have the undesired quality of being decorrelated from the relevant TSs, i.e., from the barriers

that control relaxation (see section 5.4[3]).

Population of Basin Borders. Since the preceeding paragraph may cast some doubts on the significance of $\tilde{V}$-saddles, we now want to discuss an alternative analysis of the way the population of minima versus unstable configurations evolves upon decreasing temperature. More specifically, we determine the population of basin borders,

$$p_{\mathrm{BB}}(T) = \frac{1}{Z(T)} \int \mathrm{d}\mathcal{B} \int \mathrm{d}x e^{-\beta V(x)} \delta(x - \mathcal{B}), \tag{7.5}$$

where integration is over the non-crystalline part of configuration space, also in the partition function $Z(T)$, and $\mathcal{B}$ runs over all basin borders of the PEL. This expression is impractical in numerical simulation; one may rather ask if, for some instantaneous configuration x, there is a basin border nearby. In this case, small random displacements (length $\delta \in \mathbb{R}$, direction $\omega \in \mathbb{R}^{Nd}$, $|\omega| = 1$) possibly lead into another basin, i.e. $\xi(x) \neq \xi(x + \omega\delta)$. This kind of PEL analysis has been carried out very recently (Fabricius and Stariolo, 2002). One calculates

$$p_{\mathrm{BB}}(T; \delta) = \langle P\left(\xi(x) \neq \xi(x + \omega\delta)\right) \rangle_{T,\omega}\,, \tag{7.6}$$

which is the probability that random disturbances $\omega\delta$ will cause crossings of basin borders at temperature T. The brackets denote the canonical average plus the average over the random directions ω. One obtains the behavior

$$p_{\mathrm{BB}}(T; \delta) \to \mathrm{const} \times p_{\mathrm{BB}}(T)\delta, \quad \delta \to 0 \tag{7.7}$$

(the constant is set to unity for convenience). The validity of Eq. 7.7 is demonstrated in the left inset of Fig. 7.7, where $p_{\mathrm{BB}}(T; \delta)/\delta$ has been calculated as a function of δ. We find that $p_{\mathrm{BB}}(T; \delta)/\delta$ is constant within statistical error below $\delta = 1.2$. As an orientation, the typical distance between neighboring minima is larger than 2.0, whereas intra-MB neighbors on average are less than 1.0 apart.

The main part of Fig. 7.7 shows results for $p_{\mathrm{BB}}(T)$ in an Arrhenius plot, with $\delta = 0.7$. Over the whole temperature range considered, $p_{\mathrm{BB}}(T)$ is Arrhenius-like. The apparent activation energy is ca. 1.8, which is small in comparison with the typical values observed for MB lifetimes. One reason for this lies in the multi-step

[3]In view of the results in section 5.4, it is a little surprising that the TS location with the help of the auxiliary potential $\tilde{V}$ is that unsuccessful. Since the RP population suits well the harmonic description of the RP, one expects that motion near the TS is quite harmonic, too. Minimizing $\tilde{V}$ in an harmonic potential directly yields the stationary state. Consequently, one should easily find the TS when starting from a configuration at $s \approx 0$. As shown here, this is not the case, so at least minor anharmonicities must be present.

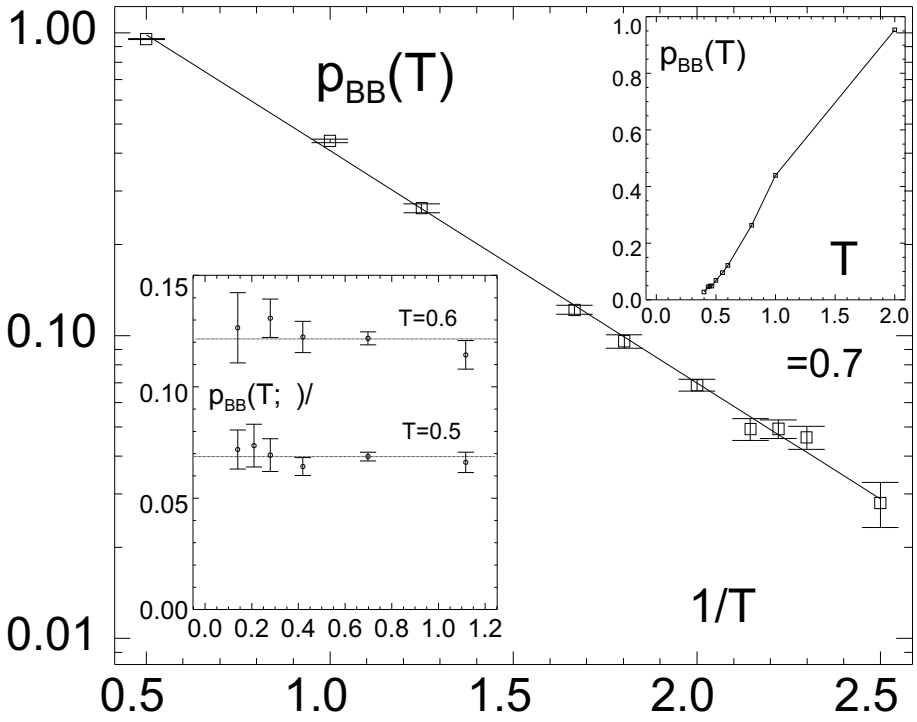

Figure 7.7: Population of basin borders, $p_{\mathrm{BB}}(T)$, obtained from disturbances of length $\delta = 0.7$, which corresponds to a displacement of ca. 0.09 per particle. Left inset: dependence on δ of $p_{\mathrm{BB}}(T)$, for $T = 0.5$ and $T = 0.6$. Right inset: $p_{\mathrm{BB}}(T)$ plotted linearly against T.

nature of MB escapes. Therefore, the temperature dependence becomes stronger if we impose the constraint of a minimum distance between neighboring minima (data not shown). In this way, we eliminate the fast intra-MB transitions, which have small barriers.

In any event, no indication for an abrupt change of relaxation mechanism could be observed in $p_{\mathrm{BB}}(T)$ when approaching and crossing[4] T_{c}. Stated differently, the data suggest that the increasing timescale separation upon cooling happens rather smoothly, with no distinctly new physics emerging near T_{c}. This is in qualitative agreement with the work of Schrøder et al., who use the incoherent scattering functions from hopping dynamics $\xi(t)$ to deal with the separation of intra- and inter-*basin* dynamics (Schrøder et al., 2000). There, the short-time decay of scattering functions (quantified by the so-called non-ergodicity parameter) is nothing else than a measure of the population of basin borders. Thus, there is no qualitative change around T_{c}.

[4]In a different graphical representation (see right inset) one might wrongly conclude that $p_{\mathrm{BB}}(T)$ disappears at some finite temperature.

Hopping and mode-coupling theory (MCT). From the fact that we could quantitatively relate MB lifetimes to PEL barriers below $2T_c$ and the results from section 5.4, we see that there exist activated barrier crossing events significantly above T_c. As shown in chapter 4, these escape processes from stable MBs determine the temperature dependence of the diffusion coefficient also above T_c. Thus, the general statement that hopping events are not relevant there (see, e.g. (Franosch and Götze, 1999)) is not correct for the BMLJ system. This implies that the ideal MCT can be applied to systems for which activated processes *determine* the time-scale of relaxation. Thus it seems that the theoretical description of the cage effect in terms of structural quantities, as done in MCT, works independently of whether the cage effect is purely entropic (like in hard-sphere systems) or is to a large degree based on barrier-crossing events.

7.4 Conclusion.

We conclude the thesis with a summary of the essential results and an outlook to possible further research.

Summary. The main purpose of this thesis was to shed more light on the molecular slowing down upon supercooling and glass formation. Within the energy landscape description, we have demonstrated that macroscopic *dynamic* quantities like the diffusion coefficient, $D(T)$, can be inferred from a local PEL analysis at temperatures below $2T_c$. The essential step has been to consider whole superstructures of many PEL minima (metabasins), rather than single minima. Metabasins are reminiscent of protein folding funnels (Bryngelson et al., 1995) or related structures in the energy landscape of small clusters (Ball et al., 1996). Their depths, as given by the surrounding energy barriers, directly determine the system's average residence time therein. As we have shown, the temperature dependence of the diffusion coefficient, $D(T)$, is dominated by the long residences in stable (solid-like) configurations for $T < 2T_c$. This might have come as a surprise, since, after the common view, the highly mobile particles are deemed to determine the temperature dependence of $D(T)$. The relation of $D(T)$ to the fraction of *liquid-like* configurations, as found in related computational studies, does not contradict our results. However, as we have shown, the reduction of liquid-like configurations upon cooling is merely a concomitant of the long trapping times in low-energy metabasins. Hence, the escape from long-lived MBs is the relevant process for a quantitative description of diffusion.

A second, unexpected observation was the dominance of activated processes much above T_c. On the one hand, it is clear that an *abrupt* cease of 'entropy-driven'

relaxation in favor of activated barrier crossing at T_c would be hard to justify. Hence, our finding that hopping sets in smoothly seems to be very plausible. On the other hand, the extent to which hopping is relevant -to our knowledge- has never been quantified before. Our finding that thermal activation becomes dominant upon cooling already below $1.5T_c$ might come as a surprise to some since after the general view, hopping sets in at T_c. We thus feel that the present study might remove some misunderstandings in this connection.

An essential point in this study was to consider small systems. In this way, we were able to reduce the energy-landscape complexity to the minimum needed for a realistic description of the bulk behavior. As we have argued, the existence of many quasi-independent subsystems in a large sample renders the corresponding PEL unnecessarily complicated. The main physics is already contained in a single subsystem. A quantitative check of this hypothesis has been presented in chapter 6. We have also demonstrated that, in principle, the same analyses are possible in larger systems. In much larger systems, however, besides the washed-out PEL information, one runs into serious technical problems arising from the many independent subsystems: Due to the much higher frequency of IS transitions (Eq. E.7) one has to reduce the elementary integration time step in order to obtain the same resolution of transitions as in a small system. In addition to the larger computational cost of larger systems, this renders such studies rather expensive. As we have discussed at length, though, no additional insights should be expected from much larger systems.

Outlook. From a purist's perspective, it would be more satisfactory to prove the 'factorization' of the PEL into that of small subsystems by starting from a macroscopic sample. However, this kind of study would require a much better understanding of PEL structure than we were able to gain here. For instance, one immediately encounters the serious problem of how to define the subsystems and on what time scale. A related aspect is the generalization of the MB concept to larger systems. The back-and-forth motion between minima, a characteristic of our MBs, will be strongly reduced in larger systems due to independently relaxing subsystems. Although one subsystem might remain immobile, this will be concealed by simultaneous relaxations in other regions of the system. Thus, clearly, the MBs of large systems should be defined locally in space. We feel that such investigations would constitute a formidable task.

We would now like to discuss a further possible extension of our work, which is related to the previous statements. The MB definition is devised to eliminate the information on trivial back-and-forth jumps within MBs. This strongly correlated

type of motion is reminiscent of the particles' rattling in the cages formed by their neighbors. Similarly, escaping from MBs seems to be equivalent to the breaking of cages and thus to structural relaxation. Of course, this speculation can only be verified by unveiling the *real-space* aspects of MB relaxation. A more general question along this line would be whether some of the collective phenomena found in supercooled liquids, e.g., string-like motion (Donati et al., 1998), can be traced back to energy-landscape features.

Another promising line of further research would be to strive for an understanding of the Adam-Gibbs relation, Eq. 1.3, from PEL principles. One might feel that this is not too far in reach since all ingredients of the relation can be determined in the PEL framework: the configurational entropy on the one side (see section 3.3), on the other side the barriers, $E_{\rm app}(\epsilon_{\rm MB})$, and the population of MBs (see chapter 5). Since the Adam-Gibbs relation is valid for the BMLJ, these quantities have to be related in a specific way. However, what we need to know is *why* this is so. Of course, this requires an understanding of $s_c(T)$ and $E_{\rm app}(\epsilon_{\rm MB})$ from more fundamental principles. For doing so, one will probably need to establish a link from the molecular architecture (i.e. interparticle potentials) to the PEL features specified above. In our opinion, this is one of the great challenges in this field of research.

Appendix A

Notation

A.1 Statistics.

The symbol $p(x, y, z, ...; C)$ is generally used for (probability) distributions of variables $x, y, z, ...$ under some condition C. An example is the probability $p(\epsilon, S_{\text{vib}}; T, N)$ of finding a system of size N in basins of minima with energy ϵ and vibrational entropy S_{vib} at temperature T. When there is no danger of confusion, parameters are omitted for convenience. Integrating out some variables $p(x, y, z, ...; C)$ leads to reduced distributions, e.g.

$$p(x) = \int \mathrm{d}y\mathrm{d}z...p(x, y, z, ...).$$

Averages of observables $A(x, y, z...)$ over distributions $p(x, y, z, ...)$ are denoted by

$$\langle A \rangle_p = \int \mathrm{d}x\mathrm{d}y\mathrm{d}z...A(x, y, z, ...)p(x, y, z, ...),$$

restricted averages by

$$\langle A|y \rangle_p = \frac{\int \mathrm{d}x\mathrm{d}z...A(x, y, z, ...)p(x, y, z, ...)}{\int \mathrm{d}x\mathrm{d}z...p(x, y, z, ...)} = \frac{\int \mathrm{d}x\mathrm{d}z...A(x, y, z, ...)p(x, y, z, ...)}{p(x, z, ...)}.$$

The index$_p$ is left out if it is convenient and if there is no danger of confusion.

Thermal averages in the canonical ensemble ($\beta = 1/k_{\text{B}}T$) result from the distribution

$$p(x; T) = \frac{e^{-\beta V(x)}}{Z(T)},$$

with $x \in \Omega_{\text{conf}}$ and the partition function $Z(T) = \int \mathrm{d}x \exp(-\beta V(x))$. The equivalence of configurational and time averages is assumed, i.e.

$$\langle A(x)\rangle_T = \frac{1}{Z(T)} \int \mathrm{d}x A(x) e^{-\beta V(x)} = \lim_{t\to\infty} \frac{1}{t} \int_0^t \mathrm{d}\tau A(x(\tau)),$$

where $x(\tau)$ is the system trajectory according to the equations of motion. This is a consequence of the ergodicity hypothesis, which tells us that in the limit of long observation times t, all regions of configuration space will be visited with frequency $\propto \exp(-\beta V(x))$. In this limit, the population of configuration space approaches the equilibrium distribution implying that the choice of the initial condition $x(0)$ is of no importance.

A.2 Symbols and Acronyms.

Acronyms.

BMLJ	binary mixture of Lennard-Jones particles
BMLJ65	BMLJ with $N = 65$
CRR	cooperatively rearranging region
IBM	interval-bisection method
IS	inherent structure = local PEL minimum
MB	metabasin
MCT	mode-coupling theory
PEL	potential energy landscape
SD	steepest descent
WTD	waiting-time distribution

Important symbols.

N	number of particles in the system
$\boldsymbol{x}_i$	position of particle i
$x = \{\boldsymbol{x}_1, ..., \boldsymbol{x}_N\}$	high-dimensional configuration vector
ξ	high-dimensional configuration of an IS
ϵ	energy of an IS
ϵ_{MB}	MB energy, i.e., the lowest IS within a MB
$V(x)$	total potential energy
$F(x)$	high-dimensional force vector
$H(x)$	Hesse matrix of $V(x)$
λ_ν	eigenvalues of $H(x)$
log	$\log_{10}$

Appendix B

System Specifications

B.1 Calculation of the Hesse Matrix.

For reasons of completeness, we give some further details on the calculations involving the interparticle potential, including the explicit computation of the Hesse matrix. The total potential energy is

$$V = \frac{1}{2}\sum_{i\neq j} V_{ij}(r_{ij}).$$

The total force on particle i is

$$F_i^\alpha = -\partial_i^\alpha V = \sum_{j\neq i} V'_{ij}(r_{ij})\frac{x_{ij}^\alpha}{r_{ij}},$$

where by $\alpha, \beta = 1, 2, 3$ we denote the components of vectors in real space and $x_{ij}^\alpha = x_j^\alpha - x_i^\alpha$. The Hessian is defined by

$$H_{ik}^{\alpha\beta} = -\partial_k^\beta F_i^\alpha.$$

In the calculation of $H_{ik}^{\alpha\beta}$, we differentiate between the two cases $k \neq i$ and $k = i$. In the case $k \neq i$ we have

$$\begin{aligned}
-H_{ik}^{\alpha\beta} = \partial_k^\beta F_i^\alpha &= \sum_{j\neq i} \partial_k^\beta \left(V'_{ij}(r_{ij})\frac{x_{ij}^\alpha}{r_{ij}} \right) = \partial_k^\beta \left(V'_{ik}(r_{ik})\frac{x_{ik}^\alpha}{r_{ik}} \right) \\
&= V''_{ik}(r_{ik})\frac{x_{ik}^\beta}{r_{ik}}\frac{x_{ik}^\alpha}{r_{ik}} + V'_{ik}(r_{ik})\left(\frac{\delta_{\alpha\beta}}{r_{ik}} + x_{ik}^\alpha \frac{-1}{r_{ik}^2}\frac{x_{ik}^\beta}{r_{ik}} \right) \\
&= V''_{ik}(r_{ik})(\hat{\boldsymbol{x}}_{ik} \otimes \hat{\boldsymbol{x}}_{ik})_{\alpha\beta} + \frac{V'_{ik}(r_{ik})}{r_{ik}}\left(\delta_{\alpha\beta} - (\hat{\boldsymbol{x}}_{ik} \otimes \hat{\boldsymbol{x}}_{ik})_{\alpha\beta}\right),
\end{aligned}$$

which means

$$H_{ij}^{\alpha\beta} = -\delta_{\alpha\beta}\frac{V'_{ij}(r_{ij})}{r_{ij}} + (\hat{\boldsymbol{x}}_{ij} \otimes \hat{\boldsymbol{x}}_{ij})_{\alpha\beta}\left[\frac{V'_{ij}(r_{ij})}{r_{ij}} - V''_{ij}(r_{ij}) \right], \tag{B.1}$$

and in the case $k = i$,

$$-H_{ii}^{\alpha\beta} = \partial_i^\beta F_i^\alpha = \sum_{j\neq i} \partial_i^\beta \left(V'_{ij}(r_{ij}) \frac{x_{ij}^\alpha}{r_{ij}} \right) = -\sum_{j\neq i} \partial_j^\beta \left(V'_{ij}(r_{ij}) \frac{x_{ij}^\alpha}{r_{ij}} \right) = \sum_{j\neq i} H_{ij}^{\alpha\beta}. \tag{B.2}$$

Thus, the Hessian has the helpful properties,

$$H_{ij}^{\alpha\beta} = H_{ji}^{\alpha\beta} = H_{ij}^{\beta\alpha}, \quad H_{ii}^{\alpha\beta} = -\sum_{j\neq i} H_{ij}^{\alpha\beta}.$$

B.2 Details of the BMLJ Potential.

The BMLJ potential is (compare Eqs. B.3, 2.3 and 2.4)

$$\begin{aligned} V(r) =& 4\epsilon \left[\left(\frac{\sigma}{r}\right)^{12} - \left(\frac{\sigma}{r}\right)^{6} \right] - 4\epsilon \left[\left(\frac{\sigma}{r_c}\right)^{12} - \left(\frac{\sigma}{r_c}\right)^{6} \right] \\ &+ \frac{12\epsilon}{r_c} \left[4\left(\frac{\sigma}{r_c}\right)^{12} - 2\left(\frac{\sigma}{r_c}\right)^{6} \right] (r - r_c), \end{aligned} \tag{B.3}$$

where

$$V^{\mathrm{LJ}\,\prime}(r) = -\frac{12\epsilon}{r} \left[4\left(\frac{\sigma}{r}\right)^{12} - 2\left(\frac{\sigma}{r}\right)^{6} \right]$$

has been used. For later use, we calculate

$$\begin{aligned} V'(r) &= -\frac{12\epsilon}{r} \left[4\left(\frac{\sigma}{r}\right)^{12} - 2\left(\frac{\sigma}{r}\right)^{6} \right] + \frac{12\epsilon}{r_c} \left[4\left(\frac{\sigma}{r_c}\right)^{12} - 2\left(\frac{\sigma}{r_c}\right)^{6} \right] \\ V''(r) &= \frac{12\epsilon}{r^2} \left[13 \cdot 4\left(\frac{\sigma}{r}\right)^{12} - 7 \cdot 2\left(\frac{\sigma}{r}\right)^{6} \right]. \end{aligned} \tag{B.4}$$

Depending on particle species, σ and ϵ have to replaced by σ_{ab} and ϵ_{ab}, $a, b \in \{\mathrm{A}, \mathrm{B}\}$. We drop the indices of species here for convenience. By $\boldsymbol{F}_{ij}(r)$, we define the force acting on particle i resulting from the interaction with particle j. It is given by

$$\boldsymbol{F}_{ij}(r) = \hat{\boldsymbol{x}}_{ij} V'_{ij}(r), \qquad \boldsymbol{x}_{ij} = \boldsymbol{x}_j - \boldsymbol{x}_i,$$

where the hat produces unit vectors. Explicitly, for the BMLJ with linear correction term at the cutoff, we have

$$\boldsymbol{F}_{ij}(r_{ij}) = -12\boldsymbol{x}_{ij} \left(\epsilon \left[4\frac{\sigma^{12}}{r_{ij}^{14}} - 2\frac{\sigma^6}{r_{ij}^8} \right] - \frac{1}{r_{ij}} \epsilon \left[4\frac{\sigma^{12}}{r_c^{13}} - 2\frac{\sigma^6}{r_c^7} \right] \right),$$

where again the indices at potential parameters were dropped.

From Eq. B.1, we find the Hessian matrix elements,

$$\begin{aligned} H_{ij}^{\alpha\beta} =& 24\epsilon\delta_{\alpha\beta}\left[2\frac{\sigma^{12}}{r^{14}} - \frac{\sigma^6}{r^8} - 2\frac{\sigma^{12}}{rr_c^{13}} + \frac{\sigma^6}{rr_c^7}\right] \\ & - 24\epsilon(\hat{\boldsymbol{x}}_{ij}\otimes\hat{\boldsymbol{x}}_{ij})_{\alpha\beta}\left[28\frac{\sigma^{12}}{r^{14}} - 8\frac{\sigma^6}{r^8} - 2\frac{\sigma^{12}}{rr_c^{13}} + \frac{\sigma^6}{rr_c^7}\right]. \end{aligned} \tag{B.5}$$

B.3 Simulation Runs.

Table B.1: Simulation runs of the BMLJ65. The step size invariably was $\lambda = 0.015$. Columns have the following meaning: '#save'-spacing of saved configurations (MD steps), '#configs'-number of saved configurations, '#steps'-total number of steps, 'τ_α'-structural relaxation time in MD steps, 'DT'-diffusion coefficient times temperature, '$\#\tau_\alpha$'-number of structural relaxation times covered in the run. See also next table.

token	T	#save	#configs	#steps	τ_α	DT	$\#\ \tau_\alpha$
h2	0.400	10^5	10^4	10^9	1.7×10^7	-8.20	59
j	0.410	10^5	10^4	10^9	10^7	-8.06	100
g	0.425	10^5	10^4	10^9	7.7×10^6	-7.83	130
e	0.435	10^5	26053	2.6×10^9	4.5×10^6	-7.81	578
eX	0.435	10^6	17752	1.8×10^{10}	5.0×10^6	-7.90	3600
l	0.450	10^6	1100	1.1×10^9	1.9×10^6	-7.49	579
a2	0.466	10^5	10^4	10^9	1.0×10^6	-7.43	1000
G	0.480	10^5	23653	2.4×10^9	9.1×10^5	-7.20	2637
D2	0.500	10^5	36835	3.7×10^9	3.9×10^5	-7.04	9487
H	0.555	10^5	4479	4.5×10^8	5.2×10^4	-6.53	8824
B2	0.600	10^4	10^4	10^8	2.5×10^4	-6.26	4000
A2	0.800	5000	5000	2.5×10^7	4.0×10^3	-5.61	6250
E2	1.000	3000	3000	9.0×10^6	1.5×10^3	-5.29	6000
F	2.000	500	3000	1.5×10^6	4.5×10^2	-4.82	3333
Tinf	∞		10^4				

Table B.2: Simulation runs of the BMLJ130. Again, step size $\lambda = 0.015$; see previous caption for more details. Note that at $T = \infty$, we performed no dynamics, but only used random configurations as starting points for minimizations.

token	T	#save	#configs	#steps	τ_α	DT	# τ_α
h	0.400	10^5	8245	0.8×10^9	2.3×10^7	-8.35	35
e2	0.435	10^5	10^4	10^9	5.3×10^6	-7.85	189
l	0.450	10^5	8630	0.9×10^9	2.0×10^6	-7.58	450
a2	0.466	10^5	4000	4.0×10^8	1.0×10^6	-7.43	400
D	0.500	10^4	10^4	10^8	3.3×10^5	-7.03	303
B2	0.600	10^4	5253	5.3×10^7	1.7×10^4	-6.19	3118
A2	0.800	5000	10^4	5.0×10^7	5.0×10^3	-5.54	10000
E	1.000	1000	10^4	1.0×10^7	1.7×10^3	-5.25	5882
F	2.000	500	1901	9.5×10^5	4.2×10^2	-4.77	2263
Tinf	∞		10^4				

Table B.3: Simulation runs of the BMLJ260, $\lambda = 0.015$.

token	T	#save	#configs	#steps	τ_α	DT	# τ_α
l	0.450	10^5	10^4	10^9	1.9×10^6	-7.99	526
Tinf	∞		3704				

Table B.4: Simulation runs of the BMLJ1000, $\lambda = 0.015$.

token	T	#save	#configs	#steps	τ_α	DT	# τ_α
l	0.450	10^4	8651	9.0×10^7	3.7×10^6	-7.84	24
D	0.500	5000	10^4	5.0×10^7	2.6×10^5	-7.00	192
B	0.600	5000	1000	5.0×10^6	1.3×10^4	-6.16	384
C	0.700	5000	2500	1.3×10^7	4.6×10^3	-5.75	2826
A2	0.800	5000	1525	7.6×10^6	2.5×10^3	-5.55	3050
E	1.000	1000	7304	7.3×10^6	1.6×10^3	-5.26	4562

B.4 Details of the BMSS70 Potential.

The BMSS potential is given by (see Cavagna et al. (Grigera and Parisi, 2001; Grigera et al., 2002))

$$V_{ab}^{\mathrm{SS}}(r) = \begin{cases} \left(\frac{\sigma_a+\sigma_b}{r}\right)^{12} + C_{ab} & , \text{if} \quad r < r_c \\ B_{ab}(A-r)^3 & , \text{if} \quad r_c < r < A \\ 0 & , \text{if} \quad r > A \end{cases} , \tag{B.6}$$

where $a, b \in \{A, B\}$ denote the particle species in an equimolar mixture. The parameters are

$$\begin{gathered} \frac{\sigma_A}{\sigma_B} = R = 1.2 \\ \sigma_A = \left(\frac{2}{4R^3 + 4 + (1+R)^3} \right)^{1/3} = 0.452683, \quad \sigma_B = 0.543219 \\ r_c = \sqrt{3}, \quad a = \frac{15 r_c}{13}, \\ B_{ab} = 169 \frac{(\sigma_a + \sigma_b)^{12}}{r_c^{15}}, \quad C_{ab} = -\frac{5}{13} \frac{(\sigma_a + \sigma_b)^{12}}{r_c^{12}}. \end{gathered} \tag{B.7}$$

The modifications to the simple r^{-12} potential are introduced for the sake of continuity at the cutoff r_c. We compute

$$V_{ab}^{\mathrm{SS}\,\prime}(r) = \begin{cases} -\frac{12}{r} \left(\frac{\sigma_a + \sigma_b}{r} \right)^{12} & , \text{if} \quad r < r_c \\ -3 B_{ab} (A - r)^2 & , \text{if} \quad r_c < r < A \\ 0 & , \text{if} \quad r > A \end{cases}, \tag{B.8}$$

and

$$V_{ab}^{\mathrm{SS}\,\prime\prime}(r) = \begin{cases} \frac{12 \cdot 13}{r^2} \left(\frac{\sigma_a + \sigma_b}{r} \right)^{12} & , \text{if} \quad r < r_c \\ 6 B_{ab} (A - r) & , \text{if} \quad r_c < r < A \\ 0 & , \text{if} \quad r > a \end{cases}. \tag{B.9}$$

The non-diagonal elements ($i \neq k$) of the Hessian are (Eq. B.1),

$$H_{ij}^{\alpha\beta}(r) = \begin{cases} 12 \left[\delta_{\alpha\beta} - 14 (\hat{\boldsymbol{x}}_{ij} \otimes \hat{\boldsymbol{x}}_{ij})_{\alpha\beta} \right] \frac{(\sigma_i + \sigma_j)^{12}}{r^{14}} & , \text{if} \quad r < r_c \\ 3 B_{ij} (A - r) \left[\delta_{\alpha\beta} \frac{A - r}{r} - (\hat{\boldsymbol{x}}_{ij} \otimes \hat{\boldsymbol{x}}_{ij})_{\alpha\beta} \left(\frac{A - r}{r} + 2 \right) \right] & , \text{if} \quad r_c < r < A \end{cases}. \tag{B.10}$$

Appendix C

Miscellaneous

C.1 Configurational Partition Function of an Harmonic Oscillator.

The potential is $V(x) = \frac{1}{2}\lambda x^2$, with spring constant λ. The (purely configurational) partition function can then be calculated,

$$Z = \int \frac{\mathrm{d}x}{u} e^{-\beta V(x)} = \left(\frac{2\pi k_\mathrm{B} T}{\lambda}\right)^{\frac{1}{2}},$$

where u, a reference length, has been set to unity. For M independent oscillators with constants λ_ν, we obtain

$$Z = \prod_\nu \left(\frac{2\pi k_\mathrm{B} T}{\lambda_\nu}\right)^{\frac{1}{2}} \equiv T^{\frac{M}{2}} Y.$$

By Y we denote the T-independent part of the partition function (Büchner and Heuer, 1999). From $F = -k_\mathrm{B} T \ln Z$, $U = -(\partial \ln Z/\partial\beta)$ and $F = U - TS$, we find

$$U = \frac{M k_\mathrm{B} T}{2} \quad \text{and} \quad S = \frac{M k_\mathrm{B}}{2} + \frac{1}{2}\sum_\nu \ln\left(\frac{2\pi k_\mathrm{B} T}{\lambda_\nu}\right). \tag{C.1}$$

Note that the inclusion of the kinetic part in the partition function leads to $U = M k_\mathrm{B} T$ and $S = M k_\mathrm{B} + \sum \ln(2\pi k_\mathrm{B} T\sqrt{m/\lambda_\nu})$.

C.2 A Comment on Entropy.

The canonical, configurational partition function is generally given by

$$Z = \int \frac{\mathrm{d}x}{u} e^{-\beta V(x)},$$

where x is a multi-dimensional vector and u a reference volume, e.g., the unit volume. Thus, the partition function is dimensionless. We now calculate the entropy via $S = \partial(k_{\mathrm{B}}T \ln Z)/\partial T$,

$$\begin{aligned} S &= k_{\mathrm{B}} \ln Z + k_{\mathrm{B}}T \int \mathrm{d}x \frac{1}{uZ} e^{-\beta V(x)} \frac{V(x)}{k_{\mathrm{B}}T^2} \\ &= k_{\mathrm{B}} \int \mathrm{d}x \frac{1}{uZ} e^{-\beta V(x)} \left(\ln Z + \beta V(x)\right) \\ &= -k_{\mathrm{B}} \int \mathrm{d}x p(x) \ln\left[p(x)u\right]. \end{aligned}$$

The last expression is the definition of Shannon entropy. Note that the entropy is only defined up to the volume element u, which naturally arises in a quantum-mechanic formulation of statistical mechanics. For classical systems as the ones under investigation here, no definition of u is preferred. Thus, thermodynamic quantities (like F or S) can only be specified up to a constant.

C.3 Derivation of Eq. 4.5.

Here we give a strict derivation of Eq. 4.5, i.e. of

$$\lim_{n\to\infty} \frac{\langle R^2(n)\rangle}{\langle \xi^2_{\mathrm{MB}}(n\,\langle\tau\rangle)\rangle} = 1, \tag{C.2}$$

under the following assumptions. The brackets denote the canonical average, $\langle ...\rangle = \langle ...\rangle_T$. The squared displacement after n MB jumps is defined as

$$R^2_x(n) = \xi^2_x(t_n), \qquad t_n = \sum_{i=1}^{n} \tau_i,$$

where, for convenience, we write $\xi(t) \equiv \xi_{\mathrm{MB}}(t)$ for the MB configuration at time t. The index x indicates that, before averaging, a quantity depends on the choice of time origin, i.e. on the starting configuration x. The τ_i's are the waiting times between MB jump $i-1$ and i. Note that $\langle\tau_1\rangle \neq \langle\tau\rangle_\varphi$, since the starting configuration is drawn from the canonical distribution, $p(x;T) = e^{-\beta V(x)}/Z(T)$. However, due to the lacking correlations among subsequent waiting times, we have $\langle\tau_2\rangle = \langle\tau_3\rangle = ... = \langle\tau\rangle_\varphi$. t_n is the time needed for n MB jumps. Thus, in the limit of (moderately) large n, $\langle t_n\rangle = n\,\langle\tau\rangle$. The essential assumption is that dynamics for long times is diffusive, i.e.

$$\lim_{t\to\infty} \frac{\xi^2_x(t)}{6Nt} = D_x = \mathrm{const}, \tag{C.3}$$

or

$$\lim_{t\to\infty}\left\langle\frac{\xi_x^2(t)}{6Nt}\right\rangle=\langle D_x\rangle=D, \tag{C.4}$$

where $D=D(T)$ is the diffusion coefficient. We have

$$\begin{aligned}R_x^2(n)-\xi_x^2(n\langle\tau\rangle)\leq&6ND_x(t_n-n\langle\tau\rangle)+|\xi_x^2(t_n)-6ND_xt_n|+|\xi_x^2(n\langle\tau\rangle)-6ND_xn\langle\tau\rangle|\\ \leq&\,6ND_x(t_n-n\langle\tau\rangle)+\epsilon(t_n+n\langle\tau\rangle),\end{aligned}$$

where the last inequality is due to Eq. C.3: For every given $\epsilon>0$, we can find an n_0 such that for all $n>n_0$, $|\xi_x^2(t_n)-6ND_xt_n|<\epsilon t_n$ and $|\xi_x^2(n\langle\tau\rangle)-6ND_xn\langle\tau\rangle|<\epsilon n\langle\tau\rangle$. By averaging, we find

$$\begin{aligned}\left|\left\langle R_x^2(n)-\xi_x^2(n\langle\tau\rangle)\right\rangle\right|&\leq|\langle 6ND_x(t_n-n\langle\tau\rangle)\rangle|+2\epsilon n\langle\tau\rangle\\ &\leq 6N\langle D_x|t_n-n\langle\tau\rangle|\rangle+2\epsilon n\langle\tau\rangle\\ &\leq 6N\left\langle D_x^2\right\rangle^{1/2}\left\langle(t_n-n\langle\tau\rangle)^2\right\rangle^{1/2}+2\epsilon n\langle\tau\rangle,\end{aligned} \tag{C.5}$$

where the last line stems from the Hölder inequality. Please note that $\langle D_x^2\rangle$ does not depend on n. Due to the central limit theorem, the variance of t_n is given by $n\mathrm{Var}(\tau)$, where $\mathrm{Var}(\tau)$ is the variance of the distribution $\varphi(\tau)$. Thus, the last line of Eq. C.5 can be written as

$$cn^{1/2}+2\epsilon n\langle\tau\rangle,$$

with some n-independent constant c. With this in mind we compute

$$\frac{|\langle R_x^2(n)-\xi_x^2(n\langle\tau\rangle)\rangle|}{\langle\xi_x^2(n\langle\tau\rangle)\rangle}<\left(2\epsilon+\frac{c}{n^{1/2}\langle\tau\rangle}\right)/\left(\frac{\langle\xi_x^2(n\langle\tau\rangle)\rangle}{n\langle\tau\rangle}\right). \tag{C.6}$$

Since the last denominator converges to $6ND$ for $n\to\infty$ (Eq. C.4), we are finished with the proof of Eq. C.2: For every $\tilde{\epsilon}>0$, we can find an n_1 such that the L.H.S. of Eq. C.6 is smaller than $\tilde{\epsilon}$ for all $n>n_1$.

To arrive at Eq. 4.5 from Eq. C.2 is trivial.

C.4 Useful Integrals.

We define

$$G(\epsilon)=\begin{cases}\frac{1}{I(\epsilon_{\min},0)}\frac{N_0}{\sqrt{2\pi\sigma^2}}\exp\left(-\frac{(\epsilon-\epsilon_0)^2}{2\sigma^2}\right) & ,\text{ if }\quad \epsilon>\epsilon_{\min}\\ 0 & ,\text{ if }\quad \epsilon<\epsilon_{\min}\end{cases}, \tag{C.7}$$

where

$$\begin{aligned} I(\epsilon_{\min},\beta) &\equiv \frac{1}{\sqrt{2\pi\sigma^2}} \int\limits_{\epsilon_{\min}}^{\infty} \mathrm{d}\epsilon e^{-\frac{1}{2\sigma^2}\left(\epsilon-(\epsilon_0-\beta\sigma^2)\right)^2} \\ &= \frac{1}{\sqrt{\pi}} \int\limits_{\left[\frac{\epsilon_{\min}-(\epsilon_0-\beta\sigma^2)}{\sqrt{2\sigma^2}}\right]}^{\infty} \mathrm{d}\epsilon e^{-\epsilon^2} = \frac{1}{2}\mathrm{erfc}\left(\frac{\epsilon_{\min}-(\epsilon_0-\beta\sigma^2)}{\sqrt{2\sigma^2}}\right) \end{aligned} \tag{C.8}$$

with the complementary error function (Abramowitz and Stegun, 1984),

$$\mathrm{erfc}(x) = \frac{2}{\sqrt{\pi}} \int\limits_{x}^{\infty} \mathrm{d}t e^{-t^2}. \tag{C.9}$$

Hence, $\mathrm{erfc}(\infty) = 0$, $\mathrm{erfc}(-\infty) = 2$. We also use $G_{\mathrm{eff}}(\epsilon)$ and $I_{\mathrm{eff}}(\epsilon_{\min},\beta)$, with the parameters

$$\epsilon_{0,\mathrm{eff}} = \epsilon_0 + b\sigma^2, \qquad \sigma_{\mathrm{eff}} = \sigma, \qquad N_{0,\mathrm{eff}} = N_0 e^{a+\frac{1}{2}b^2\sigma^2+\epsilon_0 b}, \tag{C.10}$$

where the constants a and b stem from the parametrization $\langle Y|\epsilon\rangle_G = e^{a+b\epsilon}$. The partition function is

$$Z(\epsilon_{\min},T) = \int\limits_{-\infty}^{\infty} \mathrm{d}\epsilon G_{\mathrm{eff}}(\epsilon) e^{-\beta\epsilon} = N_0 \frac{I_{\mathrm{eff}}(\epsilon_{\min},\beta)}{I_{\mathrm{eff}}(\epsilon_{\min},0)} \exp\left(-\beta\left(\epsilon_{0,\mathrm{eff}} - \frac{1}{2}\beta\sigma_{\mathrm{eff}}^2\right)\right). \tag{C.11}$$

The population of minima at temperature T is

$$p(\epsilon;T) = \frac{1}{Z(T)} e^{-\beta\epsilon} G_{\mathrm{eff}}(\epsilon) = \frac{1}{I_{\mathrm{eff}}(\epsilon_{\min},\beta)} \frac{1}{\sqrt{2\pi\sigma_{\mathrm{eff}}^2}} e^{-\frac{1}{2\sigma_{\mathrm{eff}}^2}\left(\epsilon-(\epsilon_{0,\mathrm{eff}}-\beta\sigma_{\mathrm{eff}}^2)\right)^2}. \tag{C.12}$$

The expectation value of ϵ is given by

$$\begin{aligned} \langle\epsilon\rangle - \epsilon_{0,\mathrm{eff}} + \beta\sigma_{\mathrm{eff}}^2 &= -\frac{\mathrm{d}}{\mathrm{d}\beta} \ln I_{\mathrm{eff}}(\epsilon_{\min},\beta) \\ &= \frac{\sigma_{\mathrm{eff}}}{\sqrt{2\pi} I_{\mathrm{eff}}(\epsilon_{\min},\beta)} \exp\left(-\frac{\left(\epsilon_{\min}-\epsilon_{0,\mathrm{eff}}+\beta\sigma_{\mathrm{eff}}^2\right)^2}{2\sigma_{\mathrm{eff}}^2}\right) \overset{\epsilon_{\min}\to-\infty}{\longrightarrow} 0. \end{aligned} \tag{C.13}$$

The variance is

$$\begin{aligned} &\left\langle\left(\epsilon-\langle\epsilon\rangle\right)^2\right\rangle - \sigma_{\mathrm{eff}}^2 = \left(-\frac{\mathrm{d}}{\mathrm{d}\beta}\right)^2 \ln I_{\mathrm{eff}}(\epsilon_{\min},\beta) \\ &= \frac{\sigma_{\mathrm{eff}}}{\sqrt{2\pi} I_{\mathrm{eff}}(\epsilon_{\min},\beta)} (\epsilon_{\min}-\epsilon_{0,\mathrm{eff}}+\beta\sigma_{\mathrm{eff}}^2) \exp\left(-\frac{(\epsilon_{\min}-\epsilon_{0,\mathrm{eff}}+\beta\sigma_{\mathrm{eff}}^2)^2}{2\sigma_{\mathrm{eff}}^2}\right) - \left(\langle\epsilon\rangle - \epsilon_{0,\mathrm{eff}} + \beta\sigma_{\mathrm{eff}}^2\right)^2 \\ &\overset{\epsilon_{\min}\to-\infty}{\longrightarrow} 0. \end{aligned} \tag{C.14}$$

Also needed will be

$$\begin{aligned}\left\langle \epsilon^2 \right\rangle &= \left\langle (\epsilon - \langle\epsilon\rangle)^2 \right\rangle + \langle\epsilon\rangle^2 \\ &= \sigma^2 + \text{Eq. C.14} + \left(\epsilon_0 - \beta\sigma^2 + \text{Eq. C.13}\right)^2 .\end{aligned}$$

C.5 Configurational Entropy from Gaussian Distributions.

We now calculate the first term of Eq. 3.31, i.e.

$$\int \mathrm{d}\epsilon p(\epsilon;T) \ln G(\epsilon) - \int \mathrm{d}\epsilon p(\epsilon;T) \ln p(\epsilon;T) \equiv I_1 + I_2.$$

We have

$$I_1 = \ln\left(\frac{1}{I(\epsilon_{\min},0)}\frac{N_0}{\sqrt{2\pi\sigma^2}}\right) - \frac{1}{2\sigma^2}\left(\left\langle\epsilon^2\right\rangle - 2\epsilon_0\langle\epsilon\rangle + \epsilon_0^2\right), \tag{C.15}$$

where the expectation values are given by Eq. C.13 and Eq. C.14. The second term, I_2, is constant as long as the lower end $\epsilon_{\min}$ of the PEL is not reached, since then, $p(\epsilon;T)$ is a gaussian with constant width. With the help of Eq. C.12 we calculate

$$I_2 = \ln\left(I_{\text{eff}}(\epsilon_{\min},\beta)\sqrt{2\pi\sigma^2_{\text{eff}}}\right) + \frac{1}{2\sigma^2_{\text{eff}}}\left(\left\langle\epsilon^2\right\rangle - 2(\epsilon_{0,\text{eff}} - \beta\sigma^2_{\text{eff}})\langle\epsilon\rangle + (\epsilon_{0,\text{eff}} - \beta\sigma^2_{\text{eff}})^2\right). \tag{C.16}$$

Appendix D

Bouchaud's Trap Model

Bouchaud and coworkers have introduced a very simple model for activated relaxation out of traps (Monthus and Bouchaud, 1996). The system is supposed to be found in traps of depths $E > 0$, which are distributed according to some $\rho(E)$. Escapes happen with rates $\gamma(E) = \gamma_0 \exp(-\beta E)$, after which a new depth is drawn from $\rho(E)$. We will deal with the special case of an exponential distribution here,

$$\rho(E) = \beta_{\mathrm{x}} e^{-\beta_{\mathrm{x}} E},$$

which is motivated by the fact that it reproduces the algebraic decays of waiting time distributions in the BMLJ65; see section 4.4. This choice of $\rho(E)$ causes the mean waiting time to diverge at $\beta = \beta_{\mathrm{x}}$, since traps of arbitrarily large depths exist. As argued in section 4.4, a truncated version ($E < E_{\max}$) of the trap model is more appropriate for a comparison with the BMLJ65. After compiling some properties of a single trap model, we will take a look at the parallel and independent operation of two of them.

D.1 Single System.

In the presence of a cutoff $E_{\max}$, we have

$$\rho(E) = \frac{\beta_{\mathrm{x}} e^{-\beta_{\mathrm{x}} E}}{1 - e^{-\beta_{\mathrm{x}} E_{\max}}}, \quad E \in [0, E_{\max}] \tag{D.1}$$

$$p(E;T) = \frac{\rho(E) e^{\beta E}}{\int_0^\infty \mathrm{d}E \rho(E) e^{\beta E}} = \frac{(\beta_{\mathrm{x}} - \beta) e^{-(\beta_{\mathrm{x}} - \beta) E}}{1 - e^{-(\beta_{\mathrm{x}} - \beta) E_{\max}}}, \tag{D.2}$$

where we assume $\beta < \beta_{\mathrm{x}}$. The distribution of visited traps is temperature independent, because there are no correlations between subsequent traps,

$$\varphi(E;T) = \varphi(E) = \rho(E). \tag{D.3}$$

We denote by $\varphi(\tau, E; T)$ the probability to find a waiting time τ in a trap E, $\varphi(\tau|E; T)$ being the conditional probability. Since the rate of escape from a trap E is $\gamma(E) \equiv \gamma_0 e^{-\beta E}$, we have $\varphi(\tau|E; T) = \gamma(E)e^{-\tau\gamma(E)}$, and thus,

$$\begin{aligned} \langle \tau(T) \rangle_\varphi &= \int_0^\infty \mathrm{d}E \varphi(E; T) \int_0^\infty \mathrm{d}\tau \varphi(\tau|E; T)\tau \\ &= \frac{\beta_\mathrm{x}}{\gamma_0(\beta_\mathrm{x} - \beta)} \frac{1 - e^{-(\beta_\mathrm{x}-\beta)E_\mathrm{max}}}{1 - e^{-\beta_\mathrm{x} E_\mathrm{max}}}. \end{aligned} \tag{D.4}$$

Clearly,

$$E_\mathrm{app}(E; T) \equiv \frac{\mathrm{d}}{\mathrm{d}\beta} \ln \langle \tau|E; T\rangle_\varphi = E, \tag{D.5}$$

where we defined $\langle \tau|E; T\rangle_\varphi = \int \mathrm{d}\tau \varphi(\tau|E; T)\tau$. The distributions p and φ are related by

$$p(\tau, E; T) = \frac{\tau\varphi(\tau, E; T)}{\langle \tau(T) \rangle_\varphi}, \tag{D.6}$$

which implies $1/\langle \tau \rangle_\varphi = \langle 1/\tau \rangle_p$, where subscripts φ and p denote respective averages. The average apparent activation energy is ($\beta > \beta_\mathrm{x}$)

$$E_\mathrm{app}(T) \equiv \frac{\mathrm{d}}{\mathrm{d}\beta} \ln \langle \tau(T)\rangle = -\frac{1}{\beta - \beta_\mathrm{x}} + \frac{E_\mathrm{max} e^{(\beta-\beta_\mathrm{x})E_\mathrm{max}}}{e^{(\beta-\beta_\mathrm{x})E_\mathrm{max}} - 1}, \tag{D.7}$$

which is the same expression for $\beta < \beta_\mathrm{x}$,

$$\frac{\mathrm{d}}{\mathrm{d}\beta} \ln \langle \tau(T)\rangle = -\frac{\mathrm{d}}{\mathrm{d}\beta} \ln(\beta_\mathrm{x} - \beta) + \frac{\mathrm{d}}{\mathrm{d}\beta} \ln(1 - e^{-(\beta_\mathrm{x}-\beta)E_\mathrm{max}}) = \frac{1}{\beta_\mathrm{x} - \beta} + \frac{-E_\mathrm{max} e^{-(\beta_\mathrm{x}-\beta)E_\mathrm{max}}}{1 - e^{-(\beta_\mathrm{x}-\beta)E_\mathrm{max}}}.$$

For $\beta_\mathrm{x} - \beta = \epsilon$, $\epsilon \to 0$, we obtain

$$\begin{aligned} E_\mathrm{app}(T) &= \frac{1}{\epsilon} + \frac{E_\mathrm{max}}{1 - e^{\epsilon E_\mathrm{max}}} \approx \frac{1}{\epsilon} + \frac{E_\mathrm{max}}{-\epsilon E_\mathrm{max} - \epsilon^2 E_\mathrm{max}^2/2} = \frac{1}{\epsilon} - \frac{1}{\epsilon} \frac{1}{1 + \epsilon E_\mathrm{max}/2} \\ &= \frac{1}{\epsilon} \frac{\epsilon E_\mathrm{max}/2}{1 + \epsilon E_\mathrm{max}/2} = \frac{E_\mathrm{max}}{2} \frac{1}{1 + \epsilon E_\mathrm{max}/2} \to \frac{E_\mathrm{max}}{2}. \end{aligned}$$

At very low temperatures, only the deepest traps contribute, i.e.

$$E_\mathrm{app}(T) \to E_\mathrm{max}, \qquad \text{for } \beta \to \infty$$

which follows directly from Eq. D.7.

The behavior of $\langle \tau(T)\rangle$ in these limiting cases is displayed in Fig. D.1 with parameters realistic to the BMLJ65 system. Evidently, the trap model is not able to reproduce the temperature dependence of $D(T)$ in the BMLJ65.

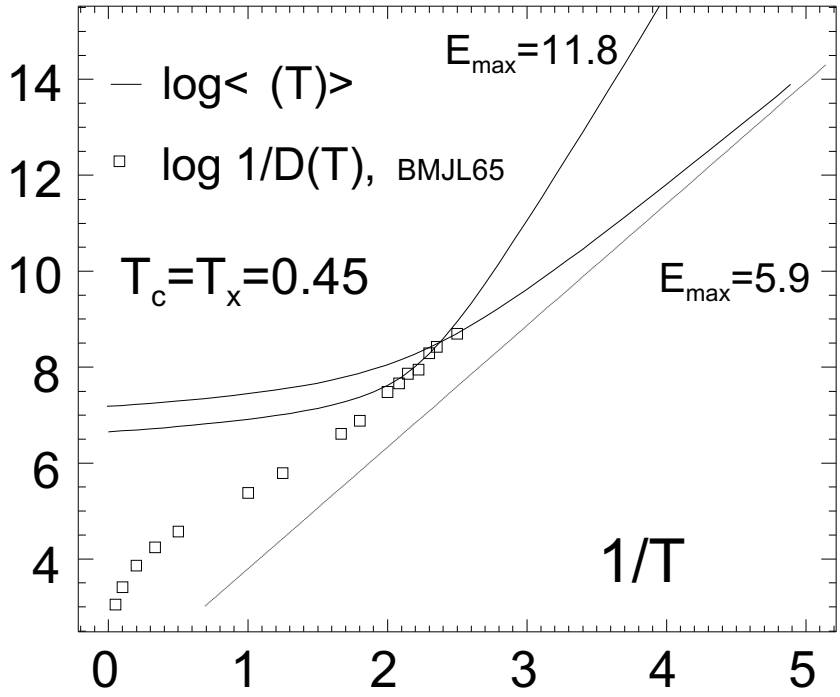

Figure D.1: Arrhenius plot of mean waiting times $\langle \tau(T) \rangle$, for parameters $E_{\max} = 5.9$ and $E_{\max} = 2 \times 5.9$, $T_x = 0.45$ in the trap model. For comparison, we show $1/D(T)$ of the BMLJ65. The auxiliary, straight line has the slope $5.9/\ln(10)$.

D.2 Combination of Two Independent Systems.

The distribution of traps $E = E_1 + E_2$, is

$$\begin{aligned} \rho_2(E) &= \int_{\max(0,E-E_{\max})}^{\min(E_{\max},E)} \mathrm{d}E_1 \rho(E_1)\rho(E-E_1) \\ &= \frac{\beta_{\mathrm{x}}^2}{(1-e^{-\beta_{\mathrm{x}}E_{\max}})^2} e^{-\beta_{\mathrm{x}}E} \times \\ &\times \left\{ \begin{array}{c} E \quad , E < E_{\max} \\ 2E_{\max} - E, \; E_{\max} < E < 2E_{\max} \end{array} \right\}, \end{aligned} \tag{D.8}$$

their population at temperature $T > T_x = 1/k_{\mathrm{B}}\beta_{\mathrm{x}}$ is

$$\begin{aligned} p_2(E;T) &= \int\limits_{\max(0,E-E_{\max})}^{\min(E_{\max},E)} \mathrm{d}E_1 p(E_1;T)p(E-E_1;T) \\ &= \frac{(\beta_{\mathrm{x}}-\beta)^2}{(1-e^{-(\beta_{\mathrm{x}}-\beta)E_{\max}})^2} e^{-(\beta_{\mathrm{x}}-\beta)E} \times \left\{ \begin{array}{c} E \quad\quad , E < E_{\max} \\ 2E_{\max}-E, \; E_{\max} < E < 2E_{\max} \end{array} \right\}. \end{aligned} \tag{D.9}$$

The mean waiting time in a trap of joint energy E is

$$\langle \tau | E;T \rangle_{\varphi} = 1/\left\langle \frac{1}{\tau} | E;T \right\rangle_p . \tag{D.10}$$

We calculate the latter expectation value,

$$\begin{aligned} & p_2(E) \left\langle \frac{1}{\tau} | E;T \right\rangle_p \\ &= \int\limits_{\max(0,E-E_{\max})}^{\min(E_{\max},E)} \mathrm{d}E_1 p(E_1)p(E-E_1) \int \mathrm{d}\tau \frac{1}{\tau} p(\tau | E_1, E-E_1) \\ &= \frac{(\beta_{\mathrm{x}}-\beta)^2}{(1-e^{-(\beta_{\mathrm{x}}-\beta)E_{\max}})^2} e^{-(\beta_{\mathrm{x}}-\beta)E} \int\limits_{\max(0,E-E_{\max})}^{\min(E_{\max},E)} \mathrm{d}E_1 \gamma(E_1, E-E_1). \end{aligned} \tag{D.11}$$

Here, the relation $p(\tau|E_1,E_2) = \tau\gamma^2(E_1,E_2)e^{-\tau\gamma(E_1,E_2)}$ has been used. Since $\gamma(E_1,E_2) = \gamma_0(e^{-\beta E_1} + e^{-\beta E_2})$, we find

$$\begin{aligned} & \langle \tau | E;T \rangle_{\varphi} = \\ &= \frac{\beta}{2\gamma_0} \left\{ \begin{array}{c} \frac{E}{1-e^{-\beta E}} \quad\quad , E < E_{\max} \\ \frac{2E_{\max}-E}{e^{-\beta(E-E_{\max})}-e^{-\beta E_{\max}}}, \; E_{\max} < E < 2E_{\max} \end{array} \right\}. \end{aligned}$$

Hence, the apparent activation energy becomes

$$\begin{aligned} & E_{\mathrm{app}}(E;T) = \frac{\mathrm{d}}{\mathrm{d}\beta} \ln \langle \tau | E;T \rangle_{\varphi} = \frac{1}{\beta} + \\ & + \left\{ \begin{array}{c} \frac{-E}{e^{\beta E}-1} \quad\quad , E < E_{\max} \\ \frac{(E-E_{\max})e^{\beta(2E_{\max}-E)}-E_{\max}}{e^{\beta(2E_{\max}-E)}-1}, \; E_{\max} < E < 2E_{\max} \end{array} \right\}. \end{aligned}$$

In the limit $T \to \infty$ this expression tends to $E/2$, while for $T \to 0$, one has $E_{\mathrm{app}}(E;T) \to (E-E_{\max})\theta(E-E_{\max})$.

Correlations of subsequent traps (cf. Fig. 4.10). Here, for simplicity, we assume $E_{\max} = \infty$. Since, generally, $\varphi(\tau) = \tau p(\tau)/\langle\tau\rangle$, we have (dropping the T argument)

$$\begin{aligned}\varphi(E_1, E_2) &= \langle\tau\rangle_2 \frac{p(E_1, E_2)}{\langle\tau|E_1, E_2\rangle} = \langle\tau\rangle_2 \gamma(E_1, E_2) p(E_1, E_2) \\ &= \langle\tau\rangle_2 \gamma_0 \left(e^{-\beta E_1} + e^{-\beta E_2}\right) (\beta_\mathrm{x} - \beta)^2 e^{-(\beta_\mathrm{x}-\beta)(E_1+E_2)}\end{aligned}$$

and

$$\varphi_2(E) = \frac{p_2(E)\,\langle\tau\rangle_2}{\langle\tau|E\rangle_2} = \frac{\beta_\mathrm{x}(\beta_\mathrm{x} - \beta)}{\beta}(1 - e^{-\beta E})e^{-(\beta_\mathrm{x}-\beta)E}, \tag{D.12}$$

which is the distribution of traps of joint energy $E = E_1 + E_2$ encountered at temperature T (at distributions and averages, no subscripts or subscripts '1' denote a single subsystem, subscripts '2' the combined system, if necessary). Hence, the average subsequent trap is

$$\begin{aligned}\varphi_2(E)\,\langle E'|E\rangle_2 &= \int_0^E \mathrm{d}E_1 \varphi(E_1, E - E_1) \times \\ &\times \frac{1}{\gamma_1 + \gamma_2}\left[\gamma_1\left(\int_0^\infty \mathrm{d}E_1' \varphi(E_1')E_1' + E - E_1\right) + \gamma_2\left(\int_0^\infty \mathrm{d}E_2' \varphi(E_2')E_2' + E_1\right)\right] \\ &= 2\gamma_0\,\langle\tau\rangle\,(\beta_\mathrm{x} - \beta)^2 e^{-(\beta_\mathrm{x}-\beta)E} \int_0^E \mathrm{d}E_1 e^{-\beta E_1}\left(\langle E\rangle_1 + E - E_1\right) \\ &= 2\gamma_0\,\langle\tau\rangle\,(\beta_\mathrm{x} - \beta)^2 e^{-(\beta_\mathrm{x}-\beta)E}\left\{(\langle E\rangle_1 + E)\frac{1}{\beta}(1 - e^{-\beta E}) + \frac{E}{\beta}e^{-\beta E} + \frac{1}{\beta^2}e^{-\beta E} - \frac{1}{\beta^2}\right\} \\ &= \frac{\beta_\mathrm{x}(\beta_\mathrm{x} - \beta)}{\beta} e^{-(\beta_\mathrm{x}-\beta)E}\left\{\langle E\rangle_1 (1 - e^{-\beta E}) + E - \frac{1}{\beta}(1 - e^{-\beta E})\right\},\end{aligned}$$

where we have used $\langle\tau\rangle_2 = \frac{1}{2}\langle\tau\rangle_1$, which holds in general, after Eq. E.7. The first line of the calculation expresses that either the first or the second copy may make a hop, with probabilities $\gamma_1/(\gamma_1 + \gamma_2)$ and $\gamma_2/(\gamma_1 + \gamma_2)$, respectively ($\gamma_i = \gamma(E_i)$). Thus, with Eq. D.12 and $\langle E\rangle_1 = 1/\beta_\mathrm{x}$,

$$\langle E'|E\rangle_2 = \frac{1}{\beta_\mathrm{x}} - \frac{1}{\beta} + \frac{E}{1 - e^{-\beta E}}. \tag{D.13}$$

Correlations between subsequent $\tau's$ are harder to calculate analytically. Hence, we compute them numerically (see chapter 4).

Appendix E

Waiting Times of a System Composed of Two Independent Subsystems

The goal of this chapter is to calculate the distribution of waiting times of a system which is comprised of two independent, identical subsystems with known WTD. This kind of information is useful to test whether a larger system behaves like two un-coupled smaller ones (see chapter 6). The notation we use is the following. By $\varphi(\tau)$, we denote the distribution of waiting times in the small systems. As before, the probability to find a certain waiting time (WT) at some arbitrary instance is $p(\tau) = \tau\varphi(\tau)/\langle\tau\rangle$. The corresponding distributions of the combined system aquire the index '2'. All averages $\langle ...\rangle$ are with respect to the φ-distributions here.

E.1 Distribution of Waiting Times.

Here we compute $p_2(\tau)$ from $p(\tau)$. At some instance (say, $t = 0$), the probability $p_>(\tau)$ to find a WT in the combined system larger than τ is given by the following expression:

$$p_>(\tau) = 2\int_{\tau}^{\infty} \mathrm{d}\tau_1 \frac{p(\tau_1)}{\tau_1} \int_{\tau}^{\tau_1} \mathrm{d}\tau_2 \frac{p(\tau_2)}{\tau_2} \int_{-\tau_1}^{0} \mathrm{d}s_1 \int_{-\tau_2}^{0} \mathrm{d}s_2 \theta(u(\tau_1, s_1, \tau_2, s_2) - \tau), \qquad \text{(E.1)}$$

where the 'overlap' u is defined in Fig. E.1 and $\theta(t) = 1$ if $t > 0$ and zero otherwise. (The waiting time of the combined system found at $t = 0$ is identical to u.) At $t = 0$, the probability to find the first system with WT τ_1 is given by $p(\tau_1)$. The start of this WT is specified by some $s_1 < 0$, over which we have to integrate. We then assume that the WT of the second subsystem is $\tau_2 < \tau_1$, starting at $s_2 < 0$.

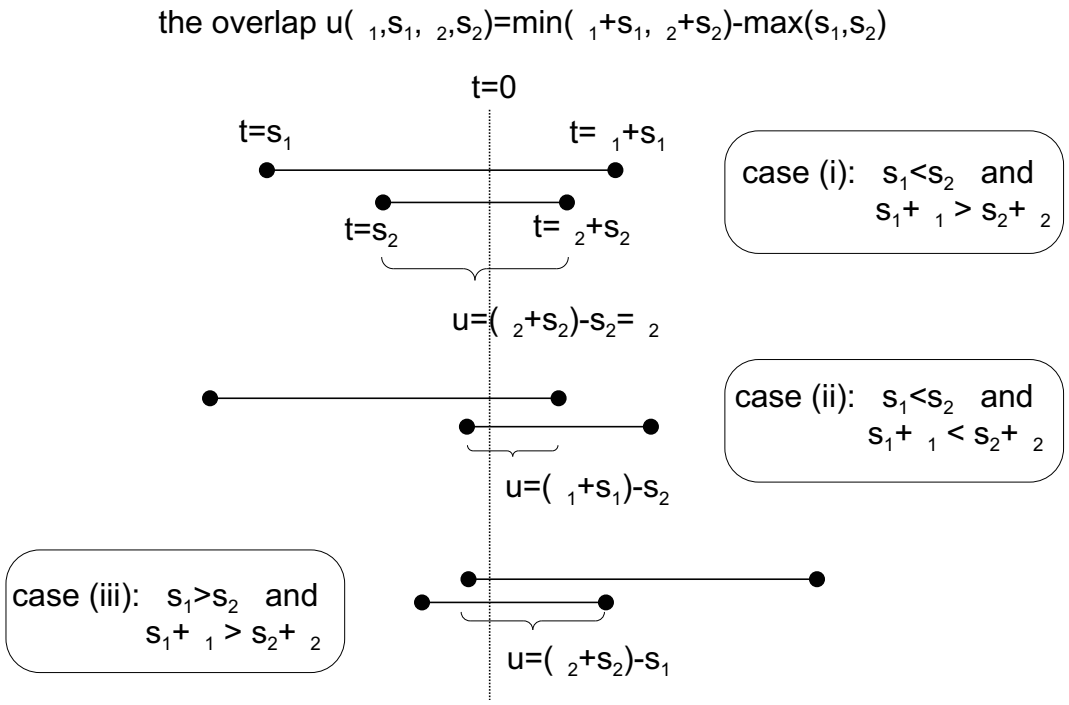

Figure E.1: Possible overlaps, where $\tau_2 < \tau_1$.

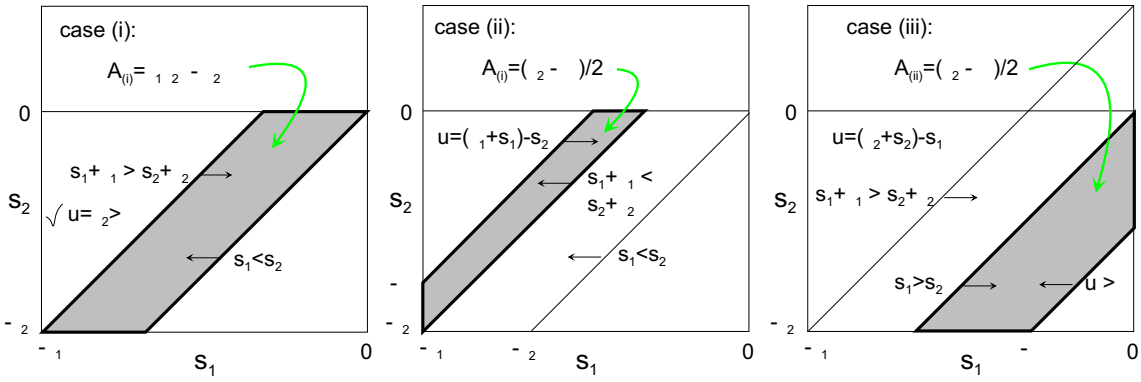

Figure E.2: Graphical illustration of the constraints in Fig. E.1.

The contribution of a pair τ_1, τ_2 to $p_>(\tau)$ is given by the fraction of overlaps larger than τ, i.e. the s-integrals divided by $\tau_1\tau_2$. Thus, Eq. E.1 has a direct intuitive meaning.

The different situations that may occur, depending on s_1 and s_2, are illustrated in Fig. E.1. We now look for the cases where the overlap of both WTs is larger than τ, i.e. where $\theta(u(\tau_1, s_1, \tau_2, s_2) - \tau) = 1$. We have to differentiate between the three

cases shown in Fig. E.1. Rather than doing this by massive case differentiation[1], we will obtain the result graphically. We are interested in the s-integrals corresponding to (i)-(iii). The given constraints on s_i can be pictured in the s_1-s_2 plane, as shown in Fig. E.2. The shaded areas correspond to the desired value of the s-integrals,

$$\begin{aligned} A_{(\mathrm{i})} &= \tau_1\tau_2 - \tau_2^2 \\ A_{(\mathrm{ii})} &= \frac{1}{2}(\tau_2^2 - \tau^2) = A_{(\mathrm{iii})}. \end{aligned} \tag{E.2}$$

With this in mind, Eq. E.1 can be rewritten as

$$\begin{aligned} p_>(\tau) &= \int_\tau^\infty \mathrm{d}\tau_1 \frac{p(\tau_1)}{\tau_1} \int_\tau^\infty \mathrm{d}\tau_2 \frac{p(\tau_2)}{\tau_2} \left(A_{(\mathrm{i})} + A_{(\mathrm{ii})} + A_{(\mathrm{iii})}\right) \\ &= \int_\tau^\infty \mathrm{d}\tau_1 p(\tau_1) \int_\tau^\infty \mathrm{d}\tau_2 p(\tau_2) \left(1 - \frac{\tau^2}{\tau_1\tau_2}\right). \end{aligned} \tag{E.3}$$

The distribution $p_2(\tau)$ is then obtained by differentiation,

$$p_2(\tau) = -\frac{\mathrm{d}p_>(\tau)}{\mathrm{d}\tau}. \tag{E.4}$$

E.2 Mean Waiting Time of the Combined System.

From Eqs. E.3 and E.4 we have

$$\begin{aligned} \frac{\tau\varphi_2(\tau)}{\langle\tau\rangle_2} = p_2(\tau) &= 2I(\tau)p(\tau) + 2\tau\tilde{I}(\tau)(\tilde{I}(\tau) - p(\tau)) \\ &= 2\frac{1}{\langle\tau\rangle}J(\tau)\frac{1}{\langle\tau\rangle}\tau\varphi(\tau) + 2\tau\frac{1}{\langle\tau\rangle}\tilde{J}(\tau)\left(\frac{1}{\langle\tau\rangle}\tilde{J}(\tau) - \frac{1}{\tau\varphi}\tau\varphi(\tau)\right) \\ &= \frac{2\tau}{\langle\tau\rangle^2}\left(J(\tau)\varphi(\tau) + \tilde{J}(\tau)^2 - \tilde{J}(\tau)\tau\varphi(\tau)\right) \end{aligned} \tag{E.5}$$

with the definitions

$$\begin{aligned} I(\tau) &= \int_\tau^\infty \mathrm{d}\tau' p(\tau'), \quad \tilde{I}(\tau) = \int_\tau^\infty \mathrm{d}\tau' \frac{p(\tau')}{\tau'} \\ J(\tau) &= \int_\tau^\infty \mathrm{d}\tau'\tau'\varphi(\tau'), \quad \tilde{J}(\tau) = \int_\tau^\infty \mathrm{d}\tau'\varphi(\tau'). \end{aligned}$$

[1] which costs about one night

Dividing Eq. E.5 by τ and integrating over τ yields

$$\frac{1}{\langle\tau\rangle_2} = \frac{2}{\langle\tau\rangle^2}\int_0^\infty \mathrm{d}\tau \left(J(\tau)\varphi(\tau) + \tilde{J}(\tau)^2 - \tilde{J}(\tau)\tau\varphi(\tau)\right). \tag{E.6}$$

If the integral equals $\langle\tau\rangle$, which is shown hereafter, it follows that

$$\langle\tau\rangle_2 = \frac{\langle\tau\rangle}{2}, \tag{E.7}$$

i.e. the mean waiting time of a combination of two independent systems is half the mean waiting time of one of them.

The three integrals in Eq. E.6 are abbreviated $A+B-C$. We calculate explicitly,

$$\begin{aligned} A &= \int_0^\infty \mathrm{d}\tau \int_\tau^\infty \mathrm{d}\tau_1 \tau_1 \varphi(\tau_1)\varphi(\tau) = \int_0^\infty \mathrm{d}\tau \left\{ \left[-\tau_1 \int_{\tau_1}^\infty \mathrm{d}\tau_1' \varphi(\tau_1') \right]_\tau^\infty + \int_\tau^\infty \mathrm{d}\tau_1 \tilde{J}(\tau_1) \right\} \varphi(\tau) \\ &= \int_0^\infty \mathrm{d}\tau\tau\tilde{J}(\tau)\varphi(\tau) + \int_0^\infty \mathrm{d}\tau\varphi(\tau)\int_\tau^\infty \mathrm{d}\tau_1 \tilde{J}(\tau_1) = C + \int_0^\infty \mathrm{d}\tau\varphi(\tau)\int_\tau^\infty \mathrm{d}\tau_1\tilde{J}(\tau_1). \end{aligned}$$

Therefore,

$$\begin{aligned} A - C &= \int_0^\infty \mathrm{d}\tau\varphi(\tau)\int_\tau^\infty \mathrm{d}\tau_1\tilde{J}(\tau_1) = \left[-\int_\tau^\infty \mathrm{d}\tau_2\varphi(\tau_2)\int_\tau^\infty \mathrm{d}\tau_1\tilde{J}(\tau_1) \right]_0^\infty + \int_0^\infty \mathrm{d}\tau\tilde{J}(\tau)(-\tilde{J}(\tau)) \\ &= -0 + 1\int_0^\infty \mathrm{d}\tau_1\tilde{J}(\tau_1) - \int_0^\infty \mathrm{d}\tau\tilde{J}(\tau)^2 = \langle\tau\rangle - B, \end{aligned}$$

where the relation

$$\int_0^\infty \mathrm{d}\tau\int_\tau^\infty \mathrm{d}\tau_1\varphi(\tau_1) = \int_0^\infty \mathrm{d}\tau\tau\varphi(\tau) = \langle\tau\rangle$$

has been used. Thus, $A + B - C = \langle\tau\rangle$, which proofs Eq. E.7.

Bibliography

Abramowitz, M. and Stegun, I. A. (1984). Pocketbook of mathematical functions. *Verlag Harri Deutsch*.

Adam, G. and Gibbs, J. H. (1965). On the temperature dependence of cooperative relaxation properties in glass-forming liquids. *J. Chem. Phys.*, 43(1):139.

Allegrini, P., Douglas, J. F., and Glotzer, S. C. (1999). Dynamic entropy as a measure of caging and persistent particle motion in supercooled liquids. *Phys. Rev. E*, 60(5):5714–5724.

Allen, M. P. and Tildesley, D. J. (1996). Computer simulation of liquids. *Oxford Science Publications, Oxford*.

Angelani, L., Leonardo, R. D., Ruocco, G., Scala, A., and Sciortino, F. (2000a). Saddles in the energy landscape probed by supercooled liquids. *Phys. Rev. Lett.*, 85(25):5356–5359.

Angelani, L., Leonardo, R. D., Ruocco, G., Scala, A., and Sciortino, F. (2002). Quasisaddles as relevant points of the potential energy surface in the dynamics of supercooled liquids. *J. Chem. Phys.*, 116(23):10297–10306.

Angelani, L., Parisi, G., Ruocco, G., and Viliani, G. (2000b). Potential energy landscape and long-time dynamics in a simple model glass. *Phys. Rev. E*, 61(2):1681–1691.

Angell, C. A. (1988). Structural instability and relaxation in liquid and glassy phases near the fragile liquid limit. *J. Non-Cryst. Solids*, 102(1-3):205–221.

Angell, C. A. (1995). Formation of glasses from liquids and biopolymers. *Science*, 267(5206):1924–1935.

Angell, C. A., Borick, S., and Wang, L. (2002). Electrospray techniques for the study of liquid energetics by hyperquenched glass calorimetry. *to be published*.

Ball, K. D. and Berry, R. S. (1999). Dynamics on statistical samples of potential energy surfaces. *J. Chem. Phys.*, 111(5):2060–2070.

Ball, K. D., Berry, R. S., Kunz, R. E., Li, F. Y., Proykova, A., and Wales, D. J. (1996). From topographies to dynamics on multidimensional potential energy surfaces of atomic clusters. *Science*, 271(5251):963–966.

Barkema, G. T. and Mousseau, N. (1996). Event-based relaxation of continuous disordered systems. *Phys. Rev. Lett.*, 77(21):4358–4361.

Bennemann, C., Donati, C., Baschnagel, J., and Glotzer, S. C. (1999). Growing range of correlated motion in a polymer melt on cooling towards the glass transition. *Nature*, 399(6733):246–249.

Bohmer, R., Chamberlin, R. V., Diezemann, G., Geil, B., Heuer, A., Hinze, G., Kuebler, S. C., Richert, R., Schiener, B., Sillescu, H., Spiess, H. W., Tracht, U., and Wilhelm, M. (1998). Nature of the non-exponential primary relaxation in structural glass-formers probed by dynamically selective experiments. *J. Non-Cryst. Solids*, 235:1–9.

Bolhuis, P. G., Chandler, D., Dellago, C., and Geissler, P. L. (2002). Transition path sampling: Throwing ropes over rough mountain passes, in the dark. *Annu. Rev. Phys. Chem.*, 53:291–318.

Bouchaud, J. P., Cugliandolo, L., Kurchan, J., and Mezard, M. (1996). Mode-coupling approximations, glass theory and disordered systems. *Physica A*, 226(3-4):243–273.

Broderix, K., Bhattacharya, K. K., Cavagna, A., Zippelius, A., and Giardina, I. (2000). Energy landscape of a lennard-jones liquid: Statistics of stationary points. *Phys. Rev. Lett.*, 85(25):5360–5363.

Bryngelson, J. D., Onuchic, J. N., Socci, N. D., and Wolynes, P. G. (1995). Funnels, pathways, and the energy landscape of protein-folding - a synthesis. *Proteins*, 21(3):167–195.

Büchner, S. and Heuer, A. (1999). Potential energy landscape of a model glass former: Thermodynamics, anharmonicities, and finite size effects. *Phys. Rev. E*, 60(6):6507–6518.

Büchner, S. and Heuer, A. (2000). Metastable states as a key to the dynamics of supercooled liquids. *Phys. Rev. Lett.*, 84(10):2168–2171.

Casalini, R., Capaccioli, S., Lucchesi, M., Paluch, M., Corezzi, S., and Rolla, P. A. (2002). Temperature and pressure behavior of the structural relaxation time in glass formers. *J. Non-Cryst. Solids*, 307:264–269.

Chowdhary, J. and Keyes, T. (2002). Conjugate gradient filtering of instantaneous normal modes, saddles on the energy landscape, and diffusion in liquids. *Phys. Rev. E*, 65(2):6125.

Cohen, M. H. and Grest, G. S. (1979). Liquid-glass transition, a free-volume approach. *Phys. Rev. B*, 20(3):1077–1098.

Cohen, M. H. and Turnbull, D. (1959). Molecular transport in liquids and glasses. *J. Chem. Phys.*, 31(5):1164–1169.

Comez, L., Fioretto, D., Kriegs, H., and Steffen, W. (2002). Temperature and pressure dependence of the alpha relaxation and configurational entropy of a prototype glass former. *Phys. Rev. E*, 66(3):2501.

Crisanti, A., Marinari, E., Ritort, F., and Rocco, A. (2001). A new method to compute the configurational entropy in spin glasses. *e-print cond-mat/0105391*.

Deaven, D. M., Tit, N., Morris, J. R., and Ho, K. M. (1996). Structural optimization of lennard-jones clusters by a genetic algorithm. *Chem. Phys. Lett.*, 256(1-2):195–200.

Debenedetti, P. G. and Stillinger, F. H. (2001). Supercooled liquids and the glass transition. *Nature*, 410(6825):259–267.

Denny, R. A., Reichman, D. R., and Bouchaud, J.-P. (2002). Trap model and slow dynamics in supercooled liquids. *e-print cond-mat/0209020*.

Derrida, B. (1981). Random-energy model - an exactly solvable model of disordered-systems. *Phys. Rev. B*, 24(5):2613–2626.

Doliwa, B. and Heuer, A. (2000). Cooperativity and spatial correlations near the glass transition: Computer simulation results for hard spheres and disks. *Phys. Rev. E*, 61(6):6898–6908.

Doliwa, B. and Heuer, A. (2002a). Energy barriers and activated dynamics in a supercooled lennard-jones liquid. *e-print cond-mat/0209139*.

Doliwa, B. and Heuer, A. (2002b). Finite-size effects in a supercooled liquid. *e-print cond-mat/0210121*.

Doliwa, B. and Heuer, A. (2002c). Hopping in a supercooled lennard-jones liquid: Metabasins, waiting time distribution, and diffusion. *e-print cond-mat/0205283*.

Donati, C., Douglas, J. F., Kob, W., Plimpton, S. J., Poole, P. H., and Glotzer, S. C. (1998). Stringlike cooperative motion in a supercooled liquid. *Phys. Rev. Lett.*, 80(11):2338–2341.

Donati, C., Glotzer, S. C., and Poole, P. H. (1999). Growing spatial correlations of particle displacements in a simulated liquid on cooling toward the glass transition. *Phys. Rev. Lett.*, 82(25):5064–5067.

Doye, J. P. K. (2002). Network topology of a potential energy landscape: A static scale-free network. *Phys. Rev. Lett.*, 88(23):8701.

Doye, J. P. K. and Wales, D. J. (2002). Saddle points and dynamics of lennard-jones clusters, solids, and supercooled liquids. *J. Chem. Phys.*, 116(9):3777–3788.

Ediger, M. D. (1996). Supercooled liquids and glasses. *J. Phys. Chem.*, 100(31):13200–13212.

Elber, R. and Karplus, M. (1987). A method for determining reaction paths in large molecules - application to myoglobin. *Chem. Phys. Lett.*, 139(5):375–380.

Ermak, D. L. and Yeh, Y. (1974). Equilibrium electrostatic effects on behavior of polyions in solution - polyion-mobile ion interaction. *Chem. Phys. Lett.*, 24(2):243–248.

Fabricius, G. and Stariolo, D. A. (2002). Distance between inherent structures and the influence of saddles on approaching the mode coupling transition in a simple glass former. *Phys. Rev. E*, 66(3):1501.

Fischer, E. W., Bakai, A., Patkowski, A., Steffen, W., and Reinhardt, L. (2002). Heterophase fluctuations in supercooled liquids and polymers. *J. Non-Cryst. Solids*, 307:584–601.

Franosch, T., Fuchs, M., Götze, W., Mayr, M. R., and Singh, A. P. (1997). Asymptotic laws and preasymptotic correction formulas for the relaxation near glass-transition singularities. *Phys. Rev. E*, 55(6):7153–7176.

Franosch, T. and Götze, W. (1999). Relaxation rate distributions for supercooled liquids. *J. Phys. Chem. B*, 103(20):4011–4017.

Frenkel, D. and Smit, B. (1996). Understanding molecular simulation. *Academic Press*.

Fulcher, G. S. (1925). *J. Am. Chem. Soc.*, 77:3701.

Gibbs, J. H. and DiMarzio, E. A. E. (1958). Nature of the glass transition and the glassy state. *J. Chem. Phys.*, 28(3):373–383.

Giovambattista, N., Buldyrev, S. V., Starr, F. W., and Stanley, H. E. (2002a). Connection between adam-gibbs theory and spatially heterogeneous dynamics. *e-print cond-mat/0209395*.

Giovambattista, N., Starr, F. W., Sciortino, F., Buldyrev, S. V., and Stanley, H. E. (2002b). Transitions between inherent structures in water. *Phys. Rev. E*, 65(4):1502.

Gleim, T., Kob, W., and Binder, K. (1998). How does the relaxation of a supercooled liquid depend on its microscopic dynamics? *Phys. Rev. Lett.*, 81(20):4404–4407.

Goldstein, M. (1969). Viscous liquids and glass transition - a potential energy barrier picture. *J. Chem. Phys.*, 51(9):3728–3728.

Götze, W. (1989). *in Liquids, Freezing and the Glass Transition, edited by J.P. Hansen, D. Levesque, and J. Zinn-Justin (North-Holland, Amsterdam, 1989)*.

Götze, W. and Sjogren, L. (1992). Relaxation processes in supercooled liquids. *Rep. Prog. Phys.*, 55(3):241–376.

Grigera, T. S., Cavagna, A., Giardina, I., and Parisi, G. (2002). Geometric approach to the dynamic glass transition. *Phys. Rev. Lett.*, 88(5):5502.

Grigera, T. S. and Parisi, G. (2001). Fast monte carlo algorithm for supercooled soft spheres. *Phys. Rev. E*, 63(4):5102.

Hänggi, P., Talkner, P., and Borkovec, M. (1990). Reaction-rate theory - 50 years after kramers. *Rev. Mod. Phys.*, 62(2):251–341.

Hansen, J. P. and McDonald, I. R. (1990). Theory of simple liquids. *Academic Press*.

Hernandez-Rojas, J. and Wales, D. J. (2001). Supercooled lennard-jones liquids and glasses: a kinetic monte carlo approach. *e-print cond-mat/0112128*.

Heuer, A. and Büchner, S. (2000). Why is the density of inherent structures of a lennard-jones- type system gaussian? *J. Phys.-Condes. Matter*, 12(29):6535–6541.

Horbach, J. and Kob, W. (1999). Static and dynamic properties of a viscous silica melt. *Phys. Rev. B*, 60(5):3169–3181.

Hughes, B. D. (1995). Random walks and random environments, vol. 1. *Clarendon Press, Oxford*.

Ionova, I. V. and Carter, E. A. (1993). Ridge method for finding saddle-points on potential-energy surfaces. *J. Chem. Phys.*, 98(8):6377–6386.

Jäckle, J. (1986). Models of the glass-transition. *Rep. Prog. Phys.*, 49(2):171–231.

Kauzmann, W. (1948). *Chem. Rev.*, 43:219.

Keyes, T. and Chowdhary, J. (2001). Inherent-structure dynamics and diffusion in liquids. *Phys. Rev. E*, 64(3):2201.

Keyes, T. and Chowdhary, J. (2002). Potential energy landscape and mechanisms of diffusion in liquids. *Phys. Rev. E*, 65(4):1106.

Kim, K. and Yamamoto, R. (2000). Apparent finite-size effects in the dynamics of supercooled liquids. *Phys. Rev. E*, 61(1):R44.

Kob, W. and Andersen, H. C. (1995). Testing mode-coupling theory for a supercooled binary lennard- jones mixture - the van hove correlation-function. *Phys. Rev. E*, 51(5):4626–4641.

Kob, W. and Barrat, J. L. (1997). Aging effects in a lennard-jones glass. *Phys. Rev. Lett.*, 78(24):4581–4584.

Kob, W., Donati, C., Plimpton, S. J., Poole, P. H., and Glotzer, S. C. (1997). Dynamical heterogeneities in a supercooled lennard-jones liquid. *Phys. Rev. Lett.*, 79(15):2827–2830.

La Nave, E., Mossa, S., and Sciortino, F. (2002a). Potential energy landscape equation of state. *Phys. Rev. Lett.*, 88(22):5701.

La Nave, E., Scala, A., Starr, F. W., Sciortino, F., and Stanley, H. E. (2000). Instantaneous normal mode analysis of supercooled water. *Phys. Rev. Lett.*, 84(20):4605–4608.

La Nave, E., Scala, A., Starr, F. W., Stanley, H. E., and Sciortino, F. (2001). Dynamics of supercooled water in configuration space. *Phys. Rev. E*, 64(3):6102.

La Nave, E., Stanley, H. E., and Sciortino, F. (2002b). Configuration space connectivity across the fragile-to-strong transition in silica. *Phys. Rev. Lett.*, 88(3):5501.

Lax, M. (1966). Classical noise .4. langevin methods. *Rev. Mod. Phys.*, 38(3):541.

Maass, P., Meyer, M., and Bunde, A. (1995). Nonstandard relaxation behavior in ionically conducting materials. *Phys. Rev. B-Condens Matter*, 51(13):8164–8177.

Matro, A., Freeman, D. L., and Doll, J. D. (1994). Locating transition-states using double-ended classical trajectories. *J. Chem. Phys.*, 101(12):10458–10463.

McMillan, P. F., Poe, B. T., Gillet, P., and Reynard, B. (1994). A study of SiO_2 high-temperature raman-spectroscopy. *Geochim. Cosmochim. Acta*, 58(17):3653–3664.

Mezard, M. and Parisi, G. (2000). Statistical physics of structural glasses. *J. Phys.-Condes. Matter*, 12(29):6655–6673.

Mezard, M., Parisi, G., and Virasoro, M. A. (1987). Spin glass theory and beyond. *World Scientific, Singapore.*

Michele, C. D. and Leporini, D. (2001). Viscous flow and jump dynamics in molecular supercooled liquids. i. translations. *Phys. Rev. E*, 63(3):6701.

Middleton, T. F., Hernandez-Rojas, J., Mortenson, P. N., and Wales, D. J. (2001). Crystals of binary lennard-jones solids. *Phys. Rev. B*, 64(18):4201.

Middleton, T. F. and Wales, D. J. (2001). Energy landscapes of some model glass formers. *Phys. Rev. B*, 64(2):4205.

Miyagawa, H. and Hiwatari, Y. (1991). Molecular-dynamics study of the glass-transition in a binary soft-sphere model. *Phys. Rev. A*, 44(12):8278–8288.

Monthus, C. and Bouchaud, J. P. (1996). Models of traps and glass phenomenology. *J. Phys. A-Math. Gen.*, 29(14):3847–3869.

Mossa, S., La Nave, E., Stanley, H. E., Donati, C., Sciortino, F., and Tartaglia, P. (2002). Dynamics and configurational entropy in the lewis-wahnstrom model for supercooled orthoterphenyl. *Phys. Rev. E*, 65(4):1205.

Mousseau, N. (2000). Cooperative motion in lennard-jones binary mixtures below the glass transition. *e-print cond-mat/0004356*.

Odagaki, T., Matsui, J., and Hiwatari, Y. (1994). Trapping diffusion-model for glass-transition and slow dynamics in supercooled liquids. *Physica A*, 204(1-4):464–481.

Poole, P. H., Donati, C., and Glotzer, S. C. (1998). Spatial correlations of particle displacements in a glass- forming liquid. *Physica A*, 261(1-2):51–59.

Reinsberg, S. A., Heuer, A., Doliwa, B., Zimmermann, H., and Spiess, H. W. (2002). Comparative study of the nmr length scale of dynamic heterogeneities of three different glass formers. *J. Non-Cryst. Solids*, 307:208–214.

Richert, R. and Angell, C. A. (1998). Dynamics of glass-forming liquids. v. on the link between molecular dynamics and configurational entropy. *J. Chem. Phys.*, 108(21):9016–9026.

Richert, R. and Blumen, A. (1993). Disorder effects on relaxational processes. *Springer-Verlag, Heidelberg*.

Rosenfeld, Y. and Tarazona, P. (1998). Density functional theory and the asymptotic high density expansion of the free energy of classical solids and fluids. *Mol. Phys.*, 95(2):141–150.

Russell, E. V. and Israeloff, N. E. (2000). Direct observation of molecular cooperativity near the glass transition. *Nature*, 408(6813):695–698.

Saika-Voivod, I., Poole, P. H., and Sciortino, F. (2001). Fragile-to-strong transition and polyamorphism in the energy landscape of liquid silica. *Nature*, 412(6846):514–517.

Saksaengwijit, A., Doliwa, B., and Heuer, A. (2002). Description of the dynamics in complex energy landscapes via metabasins: a simple model study. *submitted to Journal of Physics: Condensed Matter*.

Sastry, S. (2000). Evaluation of the configurational entropy of a model liquid from computer simulations. *J. Phys.-Condes. Matter*, 12(29):6515–6523.

Sastry, S. (2001). The relationship between fragility, configurational entropy and the potential energy landscape of glass-forming liquids. *Nature*, 409(6817):164–167.

Sastry, S., Debenedetti, P. G., and Stillinger, F. H. (1998). Signatures of distinct dynamical regimes in the energy landscape of a glass-forming liquid. *Nature*, 393(6685):554–557.

Scala, A., Starr, F. W., La Nave, E., Sciortino, F., and Stanley, H. E. (2000). Configurational entropy and diffusivity of supercooled water. *Nature*, 406(6792):166–169.

Schilling, R. and Scheidsteger, T. (1997). Mode coupling approach to the ideal glass transition of molecular liquids: Linear molecules. *Phys. Rev. E*, 56(3):2932–2949.

Schrøder, T. B., Sastry, S., Dyre, J. C., and Glotzer, S. C. (2000). Crossover to potential energy landscape dominated dynamics in a model glass-forming liquid. *J. Chem. Phys.*, 112(22):9834–9840.

Schulz, B. M., Trimper, S., and Schulz, M. (2001). Diffusion in phase space with molecular friction: A numerical study for undercooled liquids. *J. Chem. Phys.*, 114(23):10402–10410.

Schulz, M. (1998). Energy landscape, minimum points, and non-arrhenius behavior of supercooled liquids. *Phys. Rev. B*, 57(18):11319–11333.

Sciortino, F., Kob, W., and Tartaglia, P. (1999). Inherent structure entropy of supercooled liquids. *Phys. Rev. Lett.*, 83(16):3214–3217.

Sciortino, F., Kob, W., and Tartaglia, P. (2000). Thermodynamics of supercooled liquids in the inherent-structure formalism: a case study. *J. Phys.-Condes. Matter*, 12(29):6525–6534.

Sillescu, H. (1999). Heterogeneity at the glass transition: a review. *J. Non-Cryst. Solids*, 243(2-3):81–108.

Starr, F. W., Sastry, S., La Nave, E., Scala, A., Stanley, H. E., and Sciortino, F. (2001). Thermodynamic and structural aspects of the potential energy surface of simulated water. *Phys. Rev. E*, 63(4):1201.

Stillinger, F. H. (1995). A topographic view of supercooled liquids and glass-formation. *Science*, 267(5206):1935–1939.

Stillinger, F. H. (1999). Exponential multiplicity of inherent structures. *Phys. Rev. E*, 59(1):48–51.

Stillinger, F. H. and Weber, T. A. (1982). Hidden structure in liquids. *Phys. Rev. A*, 25(2):978–989.

Tammann, G. and Hesse, W. (1926). *Z. Anorg. Allg. Chem.*, 156:245.

Tracht, U., Wilhelm, M., Heuer, A., Feng, H., Schmidt-Rohr, K., and Spiess, H. W. (1998). Length scale of dynamic heterogeneities at the glass transition determined by multidimensional nuclear magnetic resonance. *Phys. Rev. Lett.*, 81(13):2727–2730.

Vardeman, C. F. and Gezelter, J. D. (2001). Comparing models for diffusion in supercooled liquids: The eutectic composition of the ag-cu alloy. *J. Phys. Chem. A*, 105(12):2568–2574.

Vogel, W. (1921). *Phys. Z*, 22:645.

Wales, D. J. (2001). Energy landscapes: From clusters to biomolecules. *Abstr. Pap. Am. Chem. Soc.*, 221.

Wallace, D. C. (1997). Statistical mechanics of monatomic liquids. *Phys. Rev. E*, 56(4):4179–4186.

Weber, T. A. and Stillinger, F. H. (1985a). Local order and structural transitions in amorphous metal- metalloid alloys. *Phys. Rev. B*, 31(4):1954–1963.

Weber, T. A. and Stillinger, F. H. (1985b). Local order and structural transitions in amorphous metal- metalloid alloys. *Phys. Rev. B*, 31(4):1954–1963.

Wevers, M. A. C., Schon, J. C., and Jansen, M. (1999). Global aspects of the energy landscape of metastable crystal structures in ionic compounds. *J. Phys.-Condes. Matter*, 11(33):6487–6499.

Xia, X. Y. and Wolynes, P. G. (2001). Microscopic theory of heterogeneity and non-exponential relaxations in supercooled liquids. *Phys. Rev. Lett.*, 86(24):5526–5529.

Yamamoto, R. and Onuki, A. (1998). Dynamics of highly supercooled liquids: Heterogeneity, rheology, and diffusion. *Phys. Rev. E*, 58(3):3515–3529.

Zwanzig, R. (1983). On the relation between self-diffusion and viscosity of liquids. *J. Chem. Phys.*, 79(9):4507–4508.

Burkhard Doliwa

The Dynamics of a Small Model Glass Former as Viewed from Its Potential Energy Landscape

Despite intensive research during the last decades, the theoretical understanding of supercooled liquids and the glass transition is still far from being complete. Besides analytical investigations, the so-called energy-landscape approach has turned out to be very fruitful. In the literature, many numerical studies have demonstrated that, at sufficiently low temperatures, all *thermodynamic* quantities can be predicted with the help of the properties of local minima in the potential-energy-landscape (PEL).

The main purpose of this thesis is to strive for an understanding of *dynamics* in terms of the potential energy landscape. In contrast to the study of static quantities, this requires the knowledge of barriers separating the minima. Up to now, it has been the general viewpoint that thermally activated processes ('hopping') determine the dynamics only below T_c (the critical temperature of mode-coupling theory), in the sense that relaxation rates follow from local energy barriers. As we show here, this viewpoint should be revised since the temperature dependence of dynamics is governed by hopping processes already below $1.5T_c$. At the example of a binary mixture of Lennard-Jones particles (BMLJ), we establish a quantitative link from the diffusion coefficient, $D(T)$, to the PEL topology. This is achieved in three steps: First, we show that it is essential to consider whole superstructures of many PEL minima, called metabasins, rather than single minima. This is a consequence of strong correlations within groups of PEL minima. Second, we show that $D(T)$ is inversely proportional to the average residence time in these metabasins. Third, the temperature dependence of the residence times is related to the depths of the metabasins, as given by the surrounding energy barriers.

We further discuss that the study of small (but not too small) systems is essential, in that one deals with a less complex energy landscape than in large systems. In a detailed analysis of different system sizes, we show that the small BMLJ system considered throughout the thesis is free of major finite-size-related artifacts.

Datum: 15. Dezember 2002
Betreuer: Prof. Andreas Heuer